DELIVERY OF ANTIMICROBIAL BIOMATERIALS THROUGH ADDITIVE MANUFACTURING

by

MORGAN ANDREW LOWTHER

A thesis submitted to
The University of Birmingham
for the degree of
DOCTOR OF PHILOSOPHY

School of Chemical Engineering
College of Engineering and Physical Sciences
The University of Birmingham
May 2022

UNIVERSITY OF
BIRMINGHAM

University of Birmingham Research Archive

e-theses repository

This unpublished thesis/dissertation is copyright of the author and/or third parties. The intellectual property rights of the author or third parties in respect of this work are as defined by The Copyright Designs and Patents Act 1988 or as modified by any successor legislation.

Any use made of information contained in this thesis/dissertation must be in accordance with that legislation and must be properly acknowledged. Further distribution or reproduction in any format is prohibited without the permission of the copyright holder.

Abstract

Reconstruction of hard tissues is increasingly challenged by post-operative bone and implant related infections. For low risk elective orthopaedic procedures such as joint replacements, 22 % of revision surgeries are motivated by infection. This clinical need is compounded with a growing incidence of bacterial resistance to antimicrobials, particularly antibiotics.

To tackle this, a biomaterials driven approach to reducing reliance on conventional antibiotics for infection management is needed. Inherently antimicrobial materials that do not rely upon conventional antibiotic chemistries offer a promising supplement to typical post operative prophylaxes. This thesis focusses on the formulation of antimicrobial materials, with a view to their delivery in additively manufactured implants.

First, an antimicrobial cement formulation is investigated. An injectable magnesium oxychloride cement (MOC) was formulated, and the effect of doping with Ag_3PO_4 as an antimicrobial agent considered. Whilst silver doped MOC showed sustained Ag release over 14 days and enhanced efficacy in vitro, undoped MOC also showed significant inherent antimicrobial behaviour. Preliminary studies of two-phase additively manufactured implants were made.

Second, novel Ti-Ag alloy microstructures were produced through laser powder bed fusion (L-PBF) additive manufacturing. Blended elemental feedstocks were manufactured with a range of laser parameters, with resulting microstructures ranging from highly segregated to homogenised. Statistical analysis demonstrated in-situ spread induced demixing of the powder blend, with varying Ag content across the build bed.

Finally, the possible mode of action of antimicrobial Ti-Ag alloys was assessed. Despite previous assertions that specific intermetallic phases dominate efficacy, high Ti_2Ag content alloys showed no statistically significant change in antimicrobial action versus control samples. This study further indicates the poorly understood nature of antimicrobial alloys, and the need for more in depth mechanistic investigations.

Together, this work contributes to the growing need for biomaterials driven approaches to infection prevention in hard tissue reconstruction.

To my great-great-great uncle, Stanley Melville.



"If Melville had a hobby it was assisting other people."

ACKNOWLEDGEMENTS

Whilst every doctorate is a deeply personal journey, none of the work in this thesis would have been possible alone.

First and foremost, thanks go to my supervisors, Dr. Sophie Cox and Prof. Liam Grover. Your unwavering support and guidance since you first gave me the opportunity to pursue this research have been invaluable.

Immense thanks go to the staff across the University of Birmingham, without whose expertise and assistance this work would not have been possible. Credit goes to Dr. Victor Villapun for assistance with mammalian and bacterial cultures, and to Dr. Luke Carter for numerous discussions of additive manufacturing. Special thanks go to Dr. Sam Cruchley in the School of Metallurgy and Materials, whose tireless troubleshooting and willingness to help got me going in the early stages of this research, and to Dr Alexander Knowles whose enthusiastic advice in Ti alloying was a great help in the latter stages. Dr. Sarah Kuehne and Dr. Rachel Sammons provided a fantastic grounding in bacteriological techniques to a complete novice.

The technical and administrative staff who enable research across the university have also been invaluable. Particular thanks to Daniel Wilmot, Dr Mark Taylor, and Elaine Mitchell, who helped keep labs running; and to Emma Lardner, without whom the entire endeavour of the Healthcare Technologies Institute would likely have crumbled. My colleagues within the HTI can take significant credit in lifting my spirits on countless occasions, and giving me confidence that collectively we might make the world a slightly better place through our work.

I acknowledge the EPSRC for funding (EP/P02341X/1) and thank the School of Chemical Engineering at the University of Birmingham for financial support. Funding for TEM was provided by the Henry Royce Foundation, via the Facilities PhD Access scheme - thanks to Dr. John Nutter for his expert eye in running the microscope.

Lastly, I could not leave without mentioning my partner, El, who has been a source of immense strength, even from the other side of the planet - you continue to inspire me to be, and do, better.

CONTENTS

1 Introduction **1**

1.1 Challenges to metallic endoprostheses . . . 2

1.1.1 Current strategies for implant associated infections . . . 3

1.2 Antimicrobial resistance . . . 5

1.2.1 Acquisition of antimicrobial resistance . . . 5

1.2.2 Biomaterials strategies for mitigation of AMR . . . 6

1.3 Inorganic antimicrobials . . . 8

1.3.1 Silver ions . . . 9

1.3.2 Metal compounds . . . 12

1.4 Additive manufacturing of implants . . . 13

1.4.1 In-situ alloying . . . 16

1.4.2 Two phase implants . . . 19

1.5 Aims and content of this research . . . 20

2 Formulation of an antimicrobial magnesium oxychloride cement **22**

2.1 Introduction . . . 24

2.2 Materials and methods . . . 29

2.2.1 Cement production and characterisation . . . 29

2.2.2 Cytotoxicity assessment . . . 34

2.2.3 Microbiological characterisation . . . 35

2.2.4 Release studies . . . 37

2.2.5 Two-phase implant model . . . 38

2.2.6 Statistical methodology . . . 40

2.3 Results . . . 41

2.3.1 Cement production and chemical characterisation . . . 41

2.3.2 Physical characterisation of cements . . . 43

2.3.3 Cytotoxicity assessment of cements . . . 50

2.3.4 Antimicrobial efficacy of cements . . . 50

2.3.5 Release characteristics . . . 51

2.3.6 Statistical analyses . . . 55
2.3.7 Two phase implant model . . . 56
2.4 Discussion . . . 57
2.5 Conclusion . . . 66

3 In-situ alloying of titanium and silver by laser powder bed fusion 67
3.1 Introduction . . . 69
3.2 Materials and methods . . . 74
3.2.1 Sample preparation . . . 74
3.2.2 Characterisation . . . 76
3.2.3 Image analysis . . . 78
3.2.4 Statistical analysis . . . 80
3.3 Results . . . 83
3.3.1 Powder characterisation . . . 83
3.3.2 As manufactured microstructure . . . 84
3.3.3 Physical characteristics . . . 91
3.3.4 Variation with build plate position . . . 94
3.3.5 Single track melting . . . 95
3.4 Discussion . . . 98
3.5 Conclusion . . . 106

4 Investigation of binary titanium silver alloy behaviour 107
4.1 Introduction . . . 109
4.2 Materials and methods . . . 115
4.2.1 Alloy production and sample preparation . . . 115
4.2.2 Physical and chemical characterisation . . . 118
4.2.3 Microbiological characterisation . . . 120
4.2.4 Release study . . . 121
4.2.5 Statistical methodology . . . 121
4.3 Results . . . 122
4.3.1 Alloy production . . . 122
4.3.2 Microstructural characterisation . . . 124
4.3.3 Bulk characterisation of alloys . . . 132
4.3.4 Antimicrobial efficacy of alloys . . . 137
4.4 Discussion . . . 138
4.5 Conclusion . . . 150

5 Conclusions and future work **151**
5.1 Antimicrobial magnesium oxychloride cements 151
5.2 Binary Ti-Ag alloys 153
5.2.1 Additive manufacture of Ti-Ag alloys 153
5.2.2 Antimicrobial response of Ti-Ag alloys 154
5.3 Overall conclusions 156

Appendix A: Mathematical derivations **205**
A.1 Solutions to Fick's Law 205
A.1.1 One dimensional case 205
A.1.2 Three dimensional case 206
A.2 Optical properties of materials 206

Appendix B: Design and specification of U-RBV reduced build ancillary **207**

LIST OF FIGURES

1.1 Suggested biomaterial driven approaches for reducing antimicrobial resistance; alternative antimicrobials to encourage reduced antibiotic usage, surface texture based antimicrobial strategies, and consideration of delivery systems design. Adapted from figure produced for Hall et al, Biomaterials Science, 2020. 7

1.2 Schematic of the Sil system, with proposed functionality of genes. The SilS sensor kinase responds to binding with silver ions, phosphorylating SilR, which in turn regulates expression of SilCFBA. Binding proteins chaperone silver to the SilCBA efflux pump, which removes ions from the cell. Adapted from Randall et al, Journal of Antimicrobial Chemotherapy, 2015. 11

1.3 Schematic showing the principles of powder bed fusion (PBF) additive manufacturing. a) Typical physical layout of PBF apparatus. Dosed powder is spread across a substrate and a cross section is thermally fused by a directed energy source. The build plate subsequently lowers, another layer of powder is spread, and is fused to the material below. b) Cross section of the build region. Unfused powder provides a degree of support to overhanging material, or support structures can be fused as appropriate. 15

1.4 Schematic visualising three approaches to adding therapeutic materials to an implant to achieve additional functionality; conventional addition of a coating, intercalation with an AM lattice structure, and inclusion of an internal reservoir through AM 19

2.1 Isothermal ternary phase diagram at 23 °C for MgO - $MgCl_2$ - H_2O. A dashed line shows the compositions achievable with a 4.0 M $MgCl_2$ brine, and where the PLR explored in this study lie. 27

2.2 Two phase implant models used for proof of concept. CAD models of Ti−6Al−4V cylinders with (a) 1 mm and (b) 2 mm diameter pores; PET cylinders with (c) 2 mm and (d) 4 mm diameter pores. 38

2.3 Effect of formulation chemistry upon cement phases formed; a) composition of cements based on the semi-quantitative method provided by Bruker Diffrac.Eva software. Reported crystallinity by mass according to software also shown; b) representative XRD patterns for 1.4 MgO powder to liquid ratios, with indexing of cement phases; c) colour change of 1.4 MgO to liquid ratio formulations after mixing, 2 hours of curing, and 48 hours exposure to light; d) real time quantification of extent of reaction. 42
2.4 Setting time (a) according to Gilmore needles method, with statistical comparisons made separately within initial and final setting time groups; visualisation of formulation flow (b) after 1 minute inversion in 1 mL cuvette; fraction of cement mass extruded (c) and peak extrusion force (d) from 1 mL syringes, where formulations marked with * exhibited syringe buckling prior to complete extrusion. Means that do not share letters are significantly different from one another. 44
2.5 Washout behaviour of $1.4\,g\,mL^{-1}$ formulations when immersed in water. Samples of MOC and MOC-Ag are shown after extrusion; immediately after immersion following 5, 45, or 90 minutes curing; and after 48 h of immersion. 45
2.6 Mechanical properties of cements cured for 48 hours at room temperature; (a) Typical compressive stress profile with key parameters labelled; (b) Ultimate compressive strength of cements; (c) Young's moduli; (d) strain energy density at failure; (e) Weibull plots for MOC and MOC-Ag, with best fit lines excluding outlier; (f) relative density of cements. 46
2.7 Example 2D XCT cross section of (a) MOC and (b) MOC-Ag at $1.4\,g\,mL^{-1}$ PLR; (c) Volume distribution of pore radii in MOC at $1.4\,g\,mL^{-1}$ PLR according to μXCT analysis, with log-normal fit. 47
2.8 Scanning electron micrographs of pores present in a) and b) MOC, with arrows indicating radial cracks from pores; c) and d) MOC-Ag cements, with arrows indicating crack diversion at the interface of Ag rich regions; e) EDS mapping of elements present around Ag rich regions in Ag_3PO_4 cement; f) SEM micrograph of Ag_3PO_4 reagent powder. 49
2.9 Cyotoxicity and viability assessment of MC3T3 cell cultures when exposed to cements for 24 h and 7 d; a) fraction of cells alive according to fluorescence microscopy; b) viability of cultures compared to control according to Alamar Blue assay. 50

2.10 Microbial assessment of cement formulations with *S. aureus* and *P. aeruginosa*; a) Zones of inhibition for both crushed and curing cements; b) response of LB broth cultures to incubation with cements, including MOC and MOC-Ag aged for 72 hours; c) 24 hour *S. aureus* growth curves in extracts from 72 hours aging at cement to broth ratio of $0.5\,\mathrm{g\,mL^{-1}}$ cement, and from 24 hours aging at a ratio of $0.14\,\mathrm{g\,mL^{-1}}$; d) 24 hour survival of *S. aureus* cultures in extracts from $0.14\,\mathrm{g\,mL^{-1}}$ cement to broth ratio release study. For planktonic cultures, dotted and dashed lines represent bacteriostasis and the minimum detectable level of viable bacteria, respectively. 52
2.11 Characteristics of release study media; a) pH, b) reactive oxygen species chemiluminescence assay, and background corrected concentrations of c) Mg, and d) Ag. The pH and chemiluminescence of control LB and PBS media are shown. For ICP data, LB and PBS blanks are substracted from sample measurements as part of the calibration process and as such are not displayed. 54
2.12 a) Zone of inhibition sizes measured around MOC-Ti two phase implants; b) concentration of bromothymol blue eluted from polymer two-phase implants. 56

3.1 Schematic showing the proposed model for generating non-equilibrium microstructures by in-situ alloying. Initially highly segregated microstructures are generated by SLM, and act as spherical diffusion couples. The possible microstructural evolution with heat treatment is shown schematically, with intermetallic formation and subsequent homogenisation. The current established Ti-Ag phase diagram is shown at right to contextualise the equilibrium phases. Phase diagram adapted from Dezellus et al, 2011. . 71
3.2 Example of a typical greyscale distribution from a backscatter SEM micrograph of a Ti-25Ag alloy sample. Increased electron yield from Ag due to its higher atomic number than Ti results in strong elemental contrast. Fitted Gaussian distributions for the bulk Ti matrix and Ag enriched phase are shown, with fully saturated and de-saturated values representing Ag and pore regions. 79
3.3 Diagram of the basic procedure for matching greyscale distributions for microstructures with different degrees of segregation and potentially variable imaging conditions. Once fitting of Gaussian distributions for each histogram has been performed, they are normalised to the same mean and standard deviation for the Ti matrix phase. This allows for a uniform threshold value to be applied to these scaled distributions. 80

3.4 Schematic describing the variables involved in analysing positional dependency of manufacturing. Each individual alloy composition and laser parameter defines a series of samples, which have specified positions on the printing substrate. Sample position, X, is defined relative to the substrate edge over which powder is first spread. A statistical model is required to assess the relative significance of the sample series, and the position, on each of the measured responses. 81
3.5 Schematic describing the parameters used in the linear fitting model for assessing quality control samples. Assuming a linear dependency of the response variable upon the position, an initial gradient and intercept of best fit are assigned to a series. Subsequent series may be compared by including parameters for the change in intercept, γ, and difference in gradient, δ. The implications of statistical significance for each parameter is described. . . . 82
3.6 Powder analyses of feedstocks, with a) range and b) cumulative particle size distributions of each powder with d10, d50, and d90 given; and SEM micrographs of c) Ti, d) Ag, and e) Ti-3Ag powders. The satellited and agglomerated nature of Ag is apparent, and the accumulation of fine Ti particles into Ag agglomerates is visible in e). 84
3.7 Optical micrographs of the a) top and b) side surface of additively manufactured Ag, showing highly porous and unmelted texture with large delamination perpendicular to the build direction. 85
3.8 Backscatter SEM micrographs of additively manufactured commercially pure titanium (cp-Ti). Each sample is labelled with linear energy density (E_d^L) values. Lack of fusion defects are visible, identifiable as pores with unmelted powder particles. As energy density increases, the apparent porosity of samples decreases. 87
3.9 Backscatter SEM micrographs of additively manufactured Ti-3Ag. Each sample is labelled with linear energy density (E_d^L) values. Small regions of high silver content are identifiable by higher brightness. Increasing energy density results in increased microstructural homogeneity, as indicated by fewer bright regions and greater uniformity of greyscale. 88

3.10 Backscatter SEM micrographs of additively manufactured Ti-10Ag. Each sample is labelled with linear energy density (E_d^L) values. Regions of high silver content are identifiable by higher brightness, with larger 200 µm silver regions present than the 30 µm particles in Ti-3Ag. Increasing energy density results in increased microstructural homogeneity, as indicated by fewer bright regions and greater uniformity of greyscale. Spherical Ti particles are visible entrapped within Ag rich regions, as marked. 89
3.11 Backscatter SEM micrographs of additively manufactured Ti-25Ag. Each sample is labelled with linear energy density (E_d^L) values. Lack of fusion defects are present at lower energy density, alongside regions of silver rich phase identifiable by higher brightness. At higher E_d^L, segregation and porosity decrease, indicated by more homogeneous brightness. 90
3.12 Relative density of samples compared to theoretical value of a binary mix of Ti and Ag, and porosity of samples based on SEM image analysis, versus linear energy density. Colour scales representing applied laser power and effective scanning speed are shown, to differentiate between scan parameters with the same linear energy density. 92
3.13 Composition of samples according to XRF, and microstructural segregation based on image analysis, versus linear energy density. Colour scales representing applied laser power and effective scanning speed are shown, to differentiate between scan parameters with the same linear energy density. 93
3.14 Variation of density, porosity, composition and microstructural segregation of Ti-Ag QC samples, versus location on build substrate in the direction of spreading. Values have been normalised relative to the distribution of each build. Linear regression lines of best fit are shown for each series, providing an indication of any trend in behaviour along the build plate. Statistical analysis of these linear fits can indicate whether trends are shared across series, indicating a behaviour that is inherent to the manufacturing process. 94
3.15 Stitched SEM micrographs of Ti-3Ag single and quad laser track melting tests, labelled with linear energy density. At 133 J m^{-1}, the surface texture of the plinth is notably pronounced, with single layer tracks difficult to distinguish from the underlying roughness. Contour regions show different surface texture to the plinth, visible as the outer 0.3 mm. 96

3.16 Surface profile measurements across Ti-3Ag single and quad laser track melting tests. A 2 mm wide height map across the centre of each sample is shown with a pseudocolour, with a line profile - shown by a dashed white line - represented below. Surface tracks are more easily distinguished from the underlying plinth roughness at higher energy density. 97
3.17 Model of thermal evolution in a homogeneous melt pool with an ideal interface to a fixed temperature substrate, for a pure a) Ti and b) Ag melts. Respective melting points are shown to indicate transit of solidification front as cooling time progresses. 101
3.18 a) Schematic of suggested formation mechanism of segregated microstructures observed in Ti-Ag blends. Silver rich agglomerations are packed within the predominantly Ti powder layer. Upon laser exposure, the low absorptivity of Ag results in temperatures that far exceed the melting point of Ag, but are similar to or below that of Ti. Combined with the rapid cooling observed in SLM, Ti particles solidify before homogenisation occurs, followed by solidification of the surrounding silver rich melt. b) Example powder particles, and c) resulting microstructure. Note the discrepancy in size of 5 µm Ti fines within the Ag rich agglomeration, versus the 15 to 45 µm Ti pockets in solidified microstructure. 103

4.1 Binary phase diagram for the Ti-Ag system. Adapted from Dezellus et al, 2011. 110
4.2 Summary of previously demonstrated antimicrobial Ti-Ag alloys, with the stated efficacy against *E. coli* and *S. aureus* shown. 112
4.3 Annotated section of Ti-Ag binary phase diagram, indicating the composition and heat treatments used to generate samples in this work. A brief description of each point is provided. 114
4.4 Particle size analysis of feedstocks, with a) range and b) cumulative size distributions; and SEM micrographs of c) cp-Ti, d) Ag-999, e) Ti-6Ag, f) Ti-10Ag, and g) Ti-25Ag powders. Accumulation of fine Ti particles onto Ag agglomerates is marked in d). 122
4.5 a) Oxygen content by inert gas fusion of alloys with base alloy powders shown, and b) composition of Ti-Ag alloys according to SEM-EDS with nominal target composition of 6, 10 and 25 wt% shown. A scale for the wt% of Ag is provided; note that this does not accurately represent the wt% of Si present. 123

4.6 SEM micrographs of Ti-6Ag, Ti-10Ag, and Ti-25Ag after at each stage of the heat treatment process. Scale bars are 20 µm. HIP samples comprise 100 µm Ag rich particles within a Ti matrix. Porosity is observed in Ti-10Ag, and dark precipitates are present in Ti-10Ag A2. 125
4.7 SEM micrographs of specific microstructural features of interest; a) and b) grain boundary precipitates in Ti-6Ag A2 indicating precipitation of Ti_2Ag as predicted by phase diagram; and low magnification comparison of Ti-25Ag c) A1 and d) A2, demonstrating that no major changes in microstructural features occurred on secondary ageing. 126
4.8 Composition of individual microstructural features according to SEM-EDS. A scale for the wt% of Ag is provided; note that this does not accurately represent the wt% of Si present. 127
4.9 Bright field STEM and TEM micrographs of grain boundary precipitates in Ti-6Ag A2. a) The presence of elongate precipitates along the length of boundaries are apparent. Both for b) individual 0.5 µm precipitates and c) 2.5 µm wide agglomerations of precipitates, clusters of smaller 30 nm precipitates are visible either side of the grain boundary. A precipitate-free denuded zone is present between the larger grain boundary particles and the nanoparticles. In d), a 2 µm long precipitate is shown to have an adjacent network of dislocations in the Ti matrix. 129
4.10 Bright field and HAADF STEM micrographs of Ti-25Ag A2. a) and b) Parallel lamellae of intermetallic precipitates are clearly distinguishable, with a network of dislocations spanning between adjacent lamallae. These dislocations are shown at higher magnification in c) and d) 130
4.11 Indexed SAED patterns for a) Ti-6Ag A2 and b) Ti-25Ag A2, with best fitting phase considering spot locations and systematic absences. Two reciprocal lattice vectors are labelled to clarify orientation. 131
4.12 Quantitative maps of TEM-EDS analysis for a) and b) Ti-6Ag A2, and c) Ti-25Ag A2. Composite map colour scale has been chosen to visually differentiate between TiAg and Ti_2Ag intermetallics. 132
4.13 Indexed XRD patterns of materials. Markers for reference patterns are shown at the expected 2θ values, allowing the assignment of phases to relevant peaks. Peaks correlating with Ti, TiAg, and Ti_2Ag are observed in all HIP samples, with intermetallic peaks subsequently missing in the HOM state, confirming that samples are in solid solution. Ti_2Ag diffraction peaks are clearly present in the Ti-25Ag A1 and A2 states, however are not distinguishable in Ti-6Ag and Ti-10Ag. 135

4.14 Measured XPS spectra of cp-Ti, and Ti-25Ag HOM and A2. Survey data a) indicates similar behaviour across all three materials, with the presence of Ag 3d and 3s the most notable change. Peaks for b) C 1s, c) O 1s and d) Ti 2p show only minor variations. Si spectra e) indicated no contamination. Slight shifts in the oxidation states of f) Ag are observed, but with Ag_2O remaining the dominant oxidation state for both HOM and A2 states. . . . 136
4.15 Response of *S. aureus* cultures to the surface of alloys after a) 4 h culture, compared to cp-Ti, and b) after 24 h culture for select samples. 137
4.16 Concentration of Ti and Ag in LB broth eluent after ageing alloy samples for 15 d at 35 °C. Eluent of Ti-10Ag in the as-HIPed and homogenised state were not assessed due to microbial contamination. Control samples of cp-Ti, Ag, and an LB blank are included for comparison. Samples marked * were excluded due to microbial contamination. 138
4.17 Schematic of possible mechanisms for inactivation of antimicrobial behaviour in Ti-Ag alloys. 144
4.18 Pourbaix diagrams for a) Ag and b) Cu at 35 °C in aqueous conditions, with a Cl^- concentration of 0.06 M. Metal concentration was set at 5×10^{-5} M. Dashed lines represent the region of stability for water. 147

LIST OF TABLES

1.1 Examples of additively manufactured bioactive alloys, showing the wide range of base systems and fraction of therapeutic material included. 18

2.1 Reference spectra used for indexing and quantification of phases in XRD, including parameters used for calculation of diffraction peak area in the Diffrac.EVA software for calculation of ξ 30
2.2 Estimated values of fracture toughness (K_1) for samples based on volume weighted mean pore radius. 48
2.3 Statistical parameters for 2-way ANOVA of data, with the formulation type (MOC/MOC-Ag), PLR, and the interaction of these two variables considered. 55
2.4 Comparison of the phases measured in unmodified MOC by XRD, with anticipated composition from stoichiometry. 60

3.1 Laser parameter spaces previously explored for manufacture of c=cp-Ti and pure Ag by SLM. Scan speeds and powers for cp-Ti are notably lower than those used to manufacture other Ti alloys, with recommended values provided by Renishaw of 200 W and 1500 $\mathrm{mm\,s^{-1}}$ for Ti-6Al-4V. 73
3.2 Additional parameters that must be defined for manufacturing via selective laser melting, and the fixed values chosen for all experiments in this work. 75
3.3 Sequence of polishing procedures used to prepare metallographic specimens with the Struers Tegramin-25 automated rotary preparation machine. . . . 77
3.4 ANOVA statistical comparison of density, porosity, composition and microstructural segregation relative to position within the build bed, the specific series (i.e. laser parameters and composition), and the interaction of position with series. These variables are labelled β, γ, and δ as per the model described in equation 3.6. Significance is labelled such that $0 < *** < 0.001 < ** < 0.01 < * < 0.05 < . < 0.1 < < 1$. Parameters have been rounded to two significant figures for ease of display. 95

3.5 Optical constants of Ti and Ag at 1070 nm, and the implied reflectance and penetration depth for normally incident radiation from vacuum. Calculations assume Fresnel regime reflectivity and Beer-Lambert regime attenuation (see Appendix §A.2). 98
3.6 Reported thermal conductivity κ, specific heat capacity c_p and density ρ for species in the Ti-Ag binary system at respective melting points, and estimated thermal diffusivity α. Note that estimates of thermal diffusivity in liquid neglect any considerations of convection. *Data for thermal conductivity of liquid Ag taken at 1373 K. 100
3.7 Arrhenius type diffusion coefficients for species in the Ti-Ag binary system. The maximal diffusion coefficient D_0, and activation energy Q, are provided for each of the relevant matrices. 102

4.1 Parameters used in previous bacteriological assessments of antimicrobial Ti-Ag alloys. 113
4.2 Parameters of heat treatments used for samples 116
4.3 Sequence of polishing procedures used to prepare samples for bacteriological testing. 117
4.4 Reference files used for indexing of TEM SAED patterns. 118
4.5 Reference patterns used for identification and indexing of alloy phases in XRD. 119
4.6 Ratio of phases present in Ti-6Ag A2, Ti-10Ag A2, and Ti-25Ag A1 and A2. The expected proportion according to phase diagram is present for nominal and measured composition, alongside the imaged phase ratio by SEM. 126
4.7 Vickers hardness of polished samples at loading of 100 g force. Due to inhomogeneity at the length scale of indentations for samples in the HIP state, separate indentations were made for intermetallic particles and the Ti matrix phase. Groupings are presented based on Tukey statistical comparison, with samples that do not share letters significantly different from one another. 133
4.8 Statistical parameters for 2-way ANOVA of hardness data, with the alloy composition and heat treatment state considered. Results are presented both for all samples, and excluding samples in the HIP state due to the significant inhomogeneity at the length scale of indentations. 134

LIST OF ACRONYMS AND ABBREVIATIONS

AM additive manufacturing

ANOVA analysis of variance

AMR antimicrobial resistance

bcc body centred cubic

BSE backscattered electron

BTB bromothymol blue

CFU colony forming units

cp-Ti commercially pure titanium

DED direct energy deposition

DSC differential scanning calorimetry

EBM electron beam melting

E. coli Escherichia coli

EDM electrical discharge machining

EDS energy-dispersive X-ray spectroscopy

E_d energy density

EELS electron energy-loss spectroscopy

FFF fused filament fabricaction

HA hydroxyapatite

hcp hexagonal close packed

HIP hot isostatic pressing

ICP-MS inductively coupled plasma mass spectrometry

ICP-OES inductively coupled plasma optical emission spectroscopy

LPSD laser particle size distribution

MIC minimum inhibitory concentration

MOC magnesium oxychloride

MOC-Ag Ag modified magnesium oxychloride

NIR near infra red

OECD Organisation for Economic Co-operation and Development

OP-S oxide polishing solution

P. aeruginosa *Pseudomonas aeruginosa*

PBF powder bed fusion

PBS phosphate buffered saline

PLR powder to liquid ratio

PMAC phenyl-10-methyl-acridinium-9-carboxylate fluorosulphonate

PSD particle size distribution

QC quality control

RBV reduced build volume

ROS reactive oxygen species

SAED selected area electron diffraction

SEM scanning electron microscopy

SLM selective laser melting

STEM scanning transmission electron microscopy

S. aureus *Staphylococcus aureus*

TEM transmission electron microscopy

TGA thermogravimetric analysis

UCS ultimate compressive strength

UK United Kingdom

UTS ultimate tensile strength

μXCT micro X-ray computed tomography

XPS X-ray photoelectron spectroscopy

XRD X-ray diffraction

XRF X-ray fluorescence

CHAPTER 1

INTRODUCTION

ACKNOWLEDGEMENT OF CONTRIBUTING MATERIAL AND AUTHORS

Content within this chapter has been published in the following journal paper(s):

- Morgan Lowther, Sophie Louth, Amy Davey, Azad Hussain, Paola Ginestra, Luke Carter, Neil Eisenstein, Liam Grover, and Sophie Cox. Clinical, industrial and research perspectives on powder bed fusion additively manufactured metal implants. *Additive Manufacturing*, 28:565-584, Aug 2019.

As primary author, M Lowther produced all written work within this thesis chapter. The contributions from publication co-authors to content in this chapter are as follows:

- Dr. P Ginestra, Dr. L N Carter, Dr. N Eisenstein: Editorial guidance.
- Prof. L M Grover, Dr. S C Cox: Editorial and supervisory guidance.

Contributions to publication from co-authors that are not used in this chapter are as follows:

- S E Louth: Collation of FDA approved additively manufactured implants.
- A Davey: Interview forming basis of clinician perspective.
- Dr. A Hussain: Interview forming basis of regulatory perspective.

1.1 Challenges to metallic endoprostheses

Implantation of metal endoprostheses are increasingly frequent surgical procedures, with hip and knee arthroplasty accounting for over 117,000 surgical procedures in the United Kingdom (UK) annually [1]. More broadly, skeletal surgeries are the primary procedure for nearly one tenth of all hospital admissions in England [1–3], and 182 per 100,000 population hip replacements were performed across the Organisation for Economic Co-operation and Development (OECD) in 2017, a 30% increase since 2007 [4]. As populations within OECD nations continue to age [5] and obesity drives a need for implants in increasingly younger cases, demand for implants is projected to continue rising over the coming decades, with estimates exceeding a 27 % increase in total hip replacements by the 2030s [6–8]. Although the complication rate of such procedures is low, there remain significant clinical challenges, which may increase as age and obesity related comorbidities become more prevalent [9, 10]. Risk of infection initiated at implant surfaces, managing osseointegration, and the inherent mechanical incompatibility of most alloys with bone, represent three of the core clinical issues faced. Alongside the initial debilitation of a patient from these complications, implant revision is typically more costly than the primary procedure and further increases the risk of infection or surgical complications [11–13].

All three of these clinical challenges are influenced by the interaction between the implant material, and the native tissue. Currently, the majority of skeletal endoprostheses are produced from titanium (Ti) or cobalt chromium (CoCr) based alloys, which meet the criteria of durability, strength, corrosion resistance and a low immune response [14, 15]. For load bearing implants, maximising osseointegration to minimise risk of aseptic loosening has been a key focus [16], typically through surface modification. However, how best to control or influence cell adhesion to an implant is key not only for managing osseointegration. Doing so whilst minimising bacterial adhesion, remains one of the key challenges in modern orthopaedics [17–19]. Implant associated infections, often referred to as periprosthetic infections, account for around 22 % of revision surgeries in orthopaedics [1], and case series have reported infection in up to 30 % of craniomaxillofacial revisions

[20]. Such infections are particularly difficult to treat due to formation of bacterial biofilms on implant surfaces [21]. A large, co-operative colony of microbes within an extracellular matrix, biofilms are prone to formation on solid inorganic surfaces, particularly the smooth and often hydrophobic surface of implants [22]. Biofilms reduce the efficacy of conventional antibiotic prophylaxis through a range of mechanisms, including the polysaccharide matrix of the film itself, and increased coordination of bacterial populations [23].

The consequences of implant associated infections for both patients and the healthcare system are dire. Duration of patient stay for an implant revision due to infection are 3.4 times longer than other implant failures, and costs 2.6 times higher [12]. In addition to the severe toll taken by the infection itself, increased duration of stay can increase psychological harm to patients, who may be bed bound due to the reduced mobility of an infected joint [24]. Collectively, this increases the long term healthcare burden per patient, reducing resources available and implicitly lowering overall quality of care. Tackling implant associated infection therefore remains a pressing healthcare challenge, and one which is likely to increase in severity as demographies age globally.

1.1.1 Current strategies for implant associated infections

Within the UK, 16.7 % of hip replacement revision procedures in the five years to 2020 were motivated by infection, 24 % of knee revisions, and rates of approximately 25 % for other less common joint endoprostheses [1]. Re-infection risks are high in such cases, with 17.7 % of infection associated hip revisions requiring re-revision, making it the most common indication for secondary revision. The dominant species in these infections are *Enterobacteriaceae*, *Pseudomonas*, and *Staphylococci*, accounting for an estimated 7.3, 8 and 75.5 % of prosthetic joint infections respectively in a 30 month case series [25]. One challenge faced is the frequent delay in onset of symptomatic infection. Though the frequency of revision due to infection generally decreases with time after implantation, over half of all infection associated hip replacement revisions still occur over a year after initial surgery [1].

Current prophylactic measures to prevent infection start with the initial manufacture of implants. A clear chain of custody is required from production to the surgical intervention to ensure sterility, as any contaminants may prevent effective sterilisation prior to implantation. Patients may be provided with an antibiotic prophylaxis to prevent surgical site infection. Previous recommendations encouraged continued antibiotic treatment after surgery, with the intention of preventing delayed infection [26]. However, current analyses of randomised trials do not support this as an effective approach to prevent surgical site infections [26, 27], with current World Health Organisation (WHO) guidelines recommending discontinuation of antibiotics after surgical intervention.

In the event that sterile procedures fail and an implant associated infection occurs, a range of revision approaches are currently used, attempting to balance the risk of re-infection with that of repeated surgeries and time spent immobile [9]. Two-stage revision has historically been considered the gold standard approach, with the implant and any infected tissue removed, and a temporary antibiotic loaded 'spacer' implant inserted in its place. Typically formed from a gentamicin impregnated cement, the spacer implant will elute antibiotic into the implant site and may allow patients a limited degree of load bearing and mobility. Once infection is considered well managed, the second stage of revision is performed, with the spacer removed and a new permanent implant inserted. Concerns have been raised, however, by the long term release of antibiotics by hip spacers. If antibiotic concentration drops below the minimum bactericidal concentration, this may encourage development of resistant strains. The use of antibiotics of last resort in this context, such as carbapenems and vancomycin, is also particularly concerning [28].

Given the increased resources and risk associated with multiple surgeries, single-stage approaches may be favoured, particularly where reduced mobility will lead to increased morbidity. Single-stage revision, wherein the infected implant is replaced with a new permanent sterile implant in the same procedure, allows for more rapid load-bearing than two-stage, though still requires the fixation of a new implant. In contrast, debridement and implant retention aims to retain the original prosthesis, and has been shown to be

effective in follow-up studies when applied appropriately [29]. Debridement typically involves the removal of any infected tissue within the implantation site and thorough irrigation in an effort to remove any adhered biofilm or planktonic bacteria.

Whilst infection management is successful in the majority of cases, the effect upon patients remains severe. The average duration of hospital admission for hip revisions due to infection has been reported as over 30 days, more than quadruple the typical length of stay for the original implantation [12]. On a four-rank scale of severity of illness, 65 % of infected patients ranked as major or extremely severe, with significantly higher readmission rates than patients undergoing revision for other causes [30]. This burden both on individual patients and global healthcare systems is likely to worsen in coming years, with the increasing prevalence of antimicrobial resistant bacteria.

1.2 Antimicrobial resistance

Post surgical infection management is further complicated by species exhibiting antimicrobial resistance (AMR). Due to the large populations, high replication rate, and subsequent high mutation rate of microbial cultures, bacteria are highly adaptable to selection pressures. Subjecting a large bacterial population to a selection pressure - in this case an antibiotic compound - will favour the survival of any isolates with mutations that improve the probability of surviving said pressure. Repeated selection from exposure insufficient to cause eradication may, over time, result in resistance to the antibiotic. At this point, the given strain may have reached a point of complete immunity to a given compound, or sufficient that the required dosage for efficacy cannot be safely applied.

1.2.1 Acquisition of antimicrobial resistance

The acquisition of genes conferring resistance often occurs through mutation during replication in large populations. Such chromosomal resistance has been an established phenomena since the 1940s, after the widespread application of penicillin and streptomycin

for infection management [31]. Resistance can also be acquired by horizontal gene transfer between bacterial cells, for example by plasmids. Such plasmid mediated gene transfer can confer resistance much more rapidly than through more conventional chromosomal selection, and can do so across bacterial species [32]. However, such gene acquisitions often come with an associated fitness cost, and so are unlikely to become prevalent without a selection pressure.

It is increasingly common for resistant pathogens to be encountered within the general population. This is driven in part by the overuse of antibiotics both inside and outside of healthcare settings. Over-prescription of antibiotics in primary care remains a key driver for AMR, particularly given their unnecessary use for common viral respiratory infections [33]. Agricultural usage of antibiotics may also be a major factor, with resistant strains often identified in livestock farms, though further surveillance is needed [34]. In both of these use cases, any antimicrobial may not be delivered exclusively to the infection site, resulting in exposure of a wider range of the microbiome. Every use of an antibiotic contributes to the overall burden in the environment that may select for resistant species. Even non-pathogenic microbes may contribute to resulting healthcare challenges, given their ability to confer resistance via plasmids to established pathogens.

As a result, the primary focus for mitigating AMR must lie in antimicrobial stewardship. Reducing antibiotic usage in agricultural settings and improving prescribing strategies are key cornerstones of this, and have been demonstrated to reduce prevalence of resistance without compromising animal or patient health [35, 36]. However, reducing antibiotic use in broader healthcare settings requires providing alternative antimicrobial strategies to prevent an increase in morbidity.

1.2.2 Biomaterials strategies for mitigation of AMR

In order to provide prophylaxis for implants whilst encouraging antibiotic stewardship, three key goals can be considered;

- First, ensuring any antimicrobial delivery is localised to the implant site to mitigate

exposure of the patient's wider microbiome to the antimicrobial agent.

- Second, avoiding the use of antibiotics to reduce their antimicrobial burden in the community, decreasing selection pressure for resistance to antibiotics as treatments of last resort.
- Third, using antimicrobial agents that have lower prevalence in the environment, reducing likelihood that any implant associated infection will have pre-acquired resistance.

One suggested approach that meets all three criteria is delivery of antimicrobial properties through biomaterial design. By incorporating a non-antibiotic antimicrobial action within the materials comprising an implant, such biomaterials driven strategies could provide prophylaxis whilst reducing usage of compounds in the antibiotic class (Figure 1.1) [37].

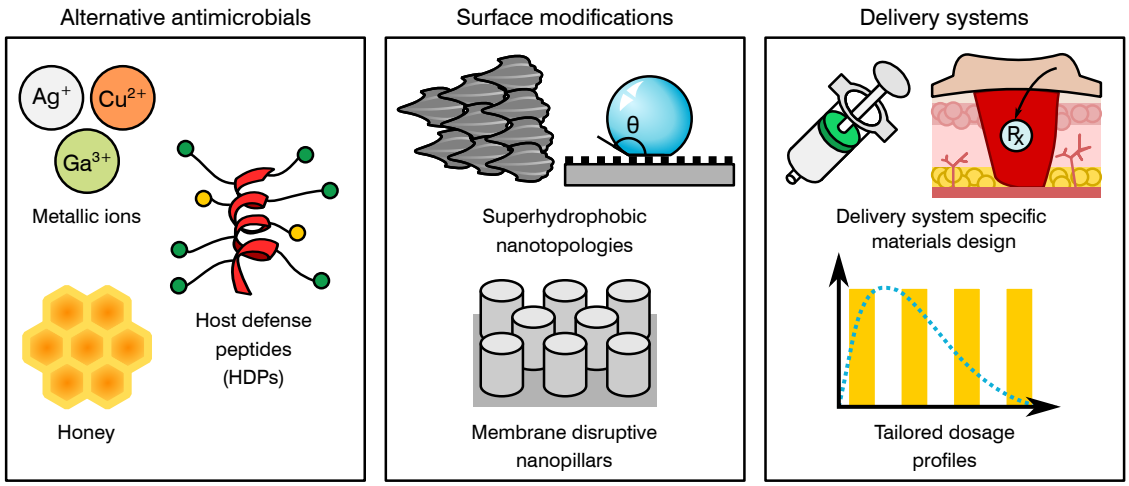


Figure 1.1: Suggested biomaterial driven approaches for reducing antimicrobial resistance; alternative antimicrobials to encourage reduced antibiotic usage, surface texture based antimicrobial strategies, and consideration of delivery systems design. Adapted from figure produced for Hall et al, Biomaterials Science, 2020.

Particularly within an implant regime, localising delivery of antimicrobials at the surgical site has already been explored through the use of coatings. This has primarily been used in cases with identified risk factors for infection, such as immunosuppressed patients or those undergoing a revision for prior infection [38]. Prostheses for reconstruction of resected bone tumours such as osteosarcomas have been a common testing ground for such

surface modification [39]. Whilst gentamicin based coatings have been investigated in vivo, inorganic antimicrobials such as silver and iodine have also shown positive outcomes [40].

Whilst coatings remain a reliable approach for functionalising the surface of implants, they do face limitations. As coatings operate in a comparatively thin layer regime, controlling release of antimicrobials over an extended period can prove challenging, requiring increasingly complex formulations [41]. From a manufacturing perspective, complex geometries can prove challenging to coat uniformly, particularly for line-of-sight approaches such as sputtering [42].

An alternative strategy that tackles both the need for greater diversity in antimicrobials used, and localising delivery in vivo, is use of inherently antimicrobial materials that deliver inorganic antimicrobials. Potentially removing the need for secondary post-processing such as coating, these materials may allow simpler control of release rates due to greater diffusion distances available versus coatings.

1.3 Inorganic antimicrobials

Whilst the vast majority of antimicrobial therapies consist of complex organic compounds such as antibiotics or host defence peptides, a broad range of simpler inorganic antimicrobial molecules and ions have been demonstrated.

A range of metals show antimicrobial behaviour in sufficient concentrations, and can broadly be divided into elements that have a biological role, and those with no biological function. These 'non-essential' metal species are of particular interest as they show efficacy at low concentrations, where those that play a role in the host's biological function may often be deleterious at the high concentrations needed for antimicrobial function [43]. For example, though Cu and Zn exhibit strong antimicrobial behaviour, their complementary functions in angiogenesis and a range of intracellular enzymatic processes respectively limit their safe application as antimicrobials in vivo [44, 45].

A key justification for the use of metals as antimicrobials in an implant context is their effect on biofilms. The susceptibility of cultures to conventional antimicrobials can be dramatically reduced in a biofilm state as compared to planktonic conditions [23]. However, it has been demonstrated that a wide range of metal cations and oxyanions show little or no reduction in efficacy versus biofilms [46]. One crucial factor in selecting which metal species to use is the difference between dosage necessary for effective antimicrobial behaviour, and the concentration at which cytotoxicity or systemic toxicity is observed in surrounding host tissues. A wider therapeutic window makes the safe delivery of species easier. Given the low minimum inhibitory concentration (MIC) of silver in comparison to Zn and Cu (10^{-6} to 10^{-7}; 10^{-4} to 10^{-6}, and 10^{-4} to 10^{-5} M respectively) and low systemic toxicity versus heavy metals, it is frequently used as an inorganic antimicrobial [47].

1.3.1 Silver ions

The antimicrobial behaviour of silver is associated with Ag ions in solution, typically Ag^{+}. The molecular mechanism of silver ion antimicrobial behaviour is not yet fully understood, with evidence that silver disrupts a broad range of bacterial processes such as iron homeostasis, respiratory and metabolic processes, and disulphide bond formation [48]. Two main mechanisms have been suggested based on the uptake of silver ions; binding and disruption of respiratory and transport proteins, or interruption of antioxidant defences producing reactive oxygen species (ROS). The binding of silver ions to transport proteins has been shown to interfere with the proton motive force, causing proton leakage, [49, 50] whilst that to thiol groups in respiratory chain enzymes has been linked to ROS generation, inducing oxidative stress [48, 51]. This correlates with silver's affinity for sulphur, with sulphonation observed both in vitro and in vivo [52]. The interaction across multiple systems is frequently raised as a reason for silver's broad spectrum efficacy.

Careful tailoring of chemistry can allow generation and elution of higher oxidation states. Previous investigations of the antimicrobial efficacy of silver found that Ag^{2+} and Ag^{3+} complexes exhibited greater antibacterial behaviour per-mole than the more stable

Ag^+ [53]. Investigation of higher oxidation states have focussed on the $Ag(Ag_3O_4)_2NO_3$ compound, primarily due to its higher stability and ease of crystallisation in comparison to other silver oxysalts of the $Ag(Ag_3O_4)_2X$ series [54]. In the vast majority of antimicrobial silver preparations, however, it is the Ag^+ ion that is used [55–57].

Silver resistance and toxicity

Due to its broad efficacy, silver has seen common usage as a biocide outside clinical settings, raising the risk of selection pressure for silver resistance [58]. Development of antimicrobial resistance to silver has been observed in both laboratory and clinical settings, with perhaps the most dramatic case being a fatal outbreak of *Salmonella typhimurium* at a burn ward in Massachusetts General Hospital in 1973 [59]. Resistance was found to be associated with plasmid pMG-101, which also increases resistance to several heavy metals and antibiotics [60]. Isolation of a specific gene cluster that encodes for silver resistance (Sil) provides a suggested molecular basis for resistance due to homologs with other heavy metal resistances such as cobalt and copper, the latter of which may be directly linked to silver resistance [60, 61]. Removal of Ag+ from the cell by efflux pumps (SilCBA), in concert with a silver-specific binding protein (SilE), prevents the build-up of silver ions (Figure 1.2) [62].

A series of studies have sought to determine the frequency of these genes in bacterial populations. Screening of 859 clinically isolated species found 31 expressed at least one of these Sil genes. Of these, the majority showed little enhanced resistance to a minimum inhibitory concentration of 200 to 300 micromolar Ag^+; however, two isolates were found to show such elevated resistance that growth was possible in concentrations exceeding 5000 micromolar [63]. These species showed a noticeable darkening in colouration when exposed to silver, the cause of which may be the reduction of silver ions. Acquired resistance has also been demonstrated to occur both endogenously and exogenously in Escherichia coli (*E. coli*) under laboratory conditions, with resistance acquired exogenously through acquisition of the pMG-101 plasmid, though endogenously through the homologous Cus

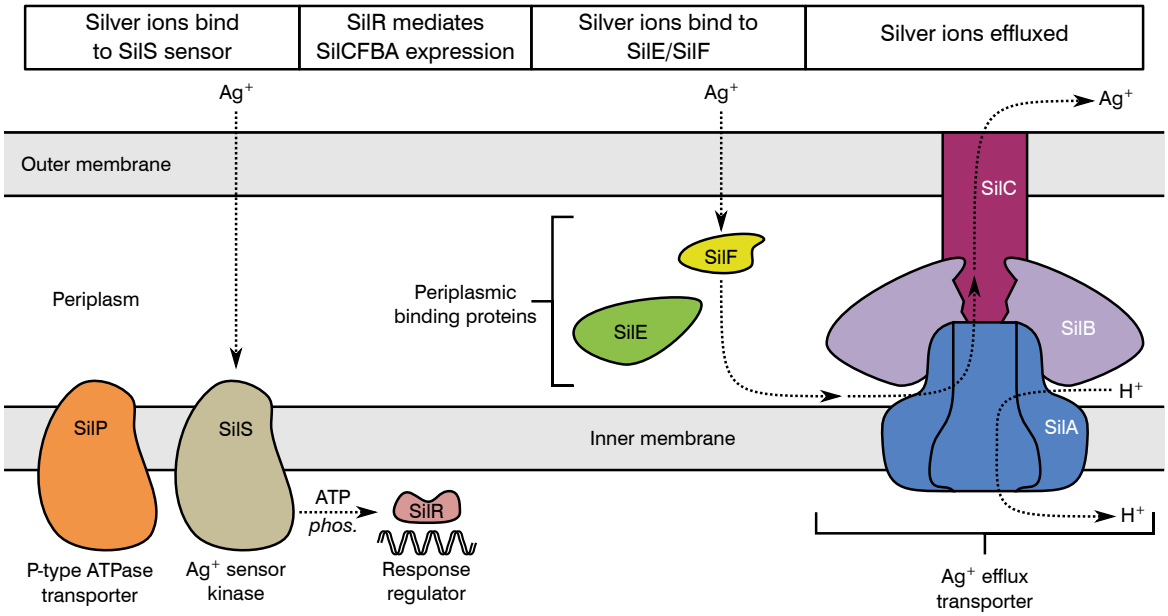


Figure 1.2: Schematic of the Sil system, with proposed functionality of genes. The SilS sensor kinase responds to binding with silver ions, phosphorylating SilR, which in turn regulates expression of SilCFBA. Binding proteins chaperone silver to the SilCBA efflux pump, which removes ions from the cell. Adapted from Randall et al, Journal of Antimicrobial Chemotherapy, 2015.

genes rather than Sil [61]. It is noteworthy that there have as yet been no reports of clinically relevant silver resistance in gram-positive bacterial species, though the SilE gene has been identified in methicillin-resistant *Staphylococcus aureus* (*S. aureus*) isolates [64]. Attempts to produce gram-positive resistant strains have as yet failed, with over 1000 isolates of staphylococci showing no acquired resistance after 42 days exposure to Ag^+ [65].

This is particularly significant in the context of endoprostheses, as up to 75% of species associated with periprosthetic infections are staphylococci [25]. As a result, silver based coatings have typically been used for revision surgeries where initial implant failure has been due to infection. Several clinically approved systems have shown positive results in lowering infection rates or severity, though cohort size remains an issue [39]. Comparing retrospectively gathered control data with that for silver coated titanium tibial megaprostheses, Hardes et al found reduced infection rate, improved 5-year survival and

lower amputation rates [66]. Use of similar tumour-prostheses treated with a proprietary process, Agluna, showed reduced overall infection rate; in those cases where infection did occur, there was a higher likelihood that debridement and antibiotics would be successful prophylaxes [67]. This links to growing evidence that there is a synergistic effect between silver and conventional antibiotic treatment, beyond that which would be anticipated from their efficacy alone [48, 68, 69]. One argument for why silver enhances existing antibiotics in a clinical setting is the ability of silver to penetrate and disrupt biofilms [70–72]. Implant infections are typically biofilm associated, and once colonised, conventional antibiotics show dramatically reduced efficacy [23].

There are concerns regarding long-term silver burden, as excessive exposure has been linked to neurological symptoms, renal failure, hepatic failure, and argyria. Normal blood silver levels have been estimated to reach up to $10\,\mu g\,L^{-1}$ [73], however the threshold for exposure to become symptomatic is not yet well established. Small cohort studies of silver coated implants have reported peak blood concentrations at $20\,\mu g\,L^{-1}$ in the 36 months post-implantation, with no apparent symptoms [74]. However study of a similar implant series found nearly a quarter of patients presented localised argyria, though with no further symptoms [75]. Few extreme cases of silver exposure from medical procedures have been reported, and the direct link with silver is ill-defined; a single case involving use of a 1% silver-impregnated bone cement saw implant loosening, neurological issues and extremely elevated silver serum levels. Though symptoms relieved after subsequent revision, there is no clear evidence of causation between the neuropathy and the presence of silver [76].

1.3.2 Metal compounds

Alongside pure metal species, a range of simple inorganic metal compounds have established antimicrobial efficacy. Often, this activity is due to the dissociation or reaction to release an antimicrobial metal ion in vivo. This is particularly the case for compounds of silver, for example AgO, Ag_3PO_4, and CuO [77, 78]. There is however evidence for direct

contact mechanisms, in which the relevant compound meets the membrane of bacteria, for example in the case of copper oxides [79].

The application of metal oxides has frequently focussed on nanoparticulate delivery methods. A wide range of different metal oxide nanoparticles have been assessed in vitro, ranging from established antimicrobial metals (AgO, CuO) to basic oxides (MgO, CaO) and more esoteric metal species (Sb_2O_3, Bi_2O_3, CdO) [80]. Whilst nanoparticles typically show excellent activity given their high surface area to volume ratio, regulating their behaviour both in vivo and the wider environment remains a serious concern [81]. Migration of nanomaterials throughout the body can be challenging to control and is as yet poorly understood [82].

In order to mitigate the hazard posed by nanomaterials, use of microparticulate or bulk antimicrobial materials may be favourable. Specific metal oxides do still exhibit antimicrobial efficacy even at a bulk scale. Oxides of basic metals such as MgO, and of antimicrobial ions such as AgO, CuO, and ZnO, have all been demonstrated in vitro [83–86].

Inorganic metal compounds are a compelling choice for incorporation into biomaterials. Typically exhibiting good stability and shelf-life, their incorporation into hard biomaterials is well established. Basic oxides are often used as reagents in orthopaedic and dental cements, with both Ca and Mg vital elements in the stable mineralisation of bone tissue [87, 88]. Several biomaterials as delivery vehicles for metal oxides have been identified, and the development of further approaches for integrating inorganic antimicrobials may enable reduced antibiotic usage.

1.4 Additive manufacturing of implants

In order to enable a biomaterial driven approach to incorporating non-conventional antimicrobials, new manufacturing approaches to implants may be advantageous. Typically, metallic implants have been manufactured by formative techniques such as forging or cast-

ing, and subtractive methods for example milling or machining. However, the past decade has seen increasing interest in using additive manufacturing (AM) techniques, and their potential to enable novel implant geometries or properties to tackle the clinical challenges faced. AM technologies produce parts from 3D data, by joining of raw materials in a layer-by-layer process [89]. In the field of metal implant manufacture, the most relevant techniques are based upon powder bed fusion (PBF) methods, the basic principles of which are shown in figure 1.3. In PBF, layers of powder are thermally fused by an energy source, such as selective laser melting (SLM) or electron beam melting (EBM). A subsequent layer of powder is spread across the surface and the next cross section of a part fused with the underlying material, with this process repeated sequentially until completion. Underlying powder layers provide a degree of support to material above, although supporting structures may be required to stabilise parts during manufacture. Other metal AM methods are available, most notably direct energy deposition (DED) techniques, but the clinical exploration of these methods for biomedical manufacture has been more limited, possibly due to the lower resolution of DED (1 mm versus 100 µm for PBF) and more widespread commercialisation of PBF.

Unlike traditional powder metallurgy processes such as sintering, PBF and DED produce geometrically complex parts with densities exceeding 99.5% without additional post-processing [90]. In practice, careful process control is required to avoid remnant porosity or defects. With extremely high localised cooling rates, metal AM processes have unique microstructural characteristics. The melt pool in laser PBF, for example, is typically of the order of 200 µm and cools at a rate of over $10^4\,\mathrm{K\,s^{-1}}$ [91]. This generates very fine microstructures that while stiffer than equivalent cast or wrought materials, have higher yield strength [92]. Whilst this change in material behaviour may require adaptation of surgical techniques - for example the inability of surgeons to deform cranial prostheses in theatre - these challenges may be overcome by the use of custom cutting or mounting guides for implants [93].

The ability to produce patient specific implants and associated surgical guides is a key

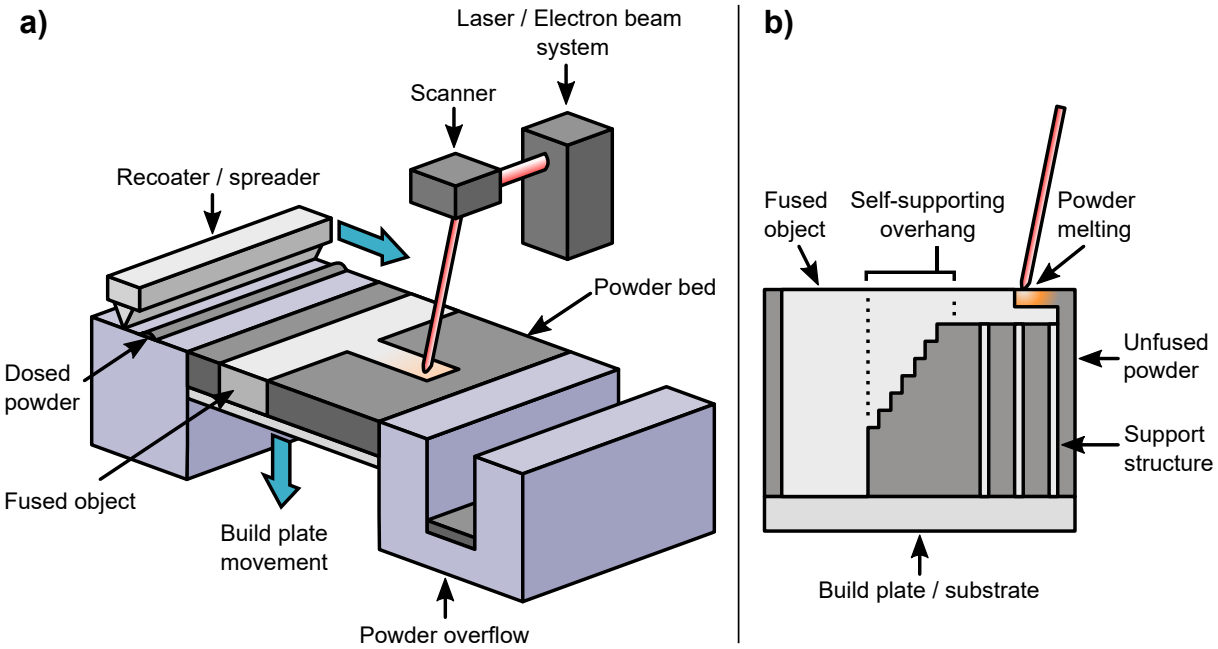


Figure 1.3: Schematic showing the principles of powder bed fusion (PBF) additive manufacturing. a) Typical physical layout of PBF apparatus. Dosed powder is spread across a substrate and a cross section is thermally fused by a directed energy source. The build plate subsequently lowers, another layer of powder is spread, and is fused to the material below. b) Cross section of the build region. Unfused powder provides a degree of support to overhanging material, or support structures can be fused as appropriate.

advantage of the digitised manufacturing approach in AM. The ability to design prostheses directly from patient MRI or CT data not only allows decreased lead-time for custom implants, but also improved surgical management [94]. For complex procedures, this reduces surgical duration [95, 96], a key indicator of improved patient outcome [97, 98]. For uniquely customised implants beyond specific craniomaxillofacial re-constructions, AM implants have seen particular use in treatment of bone tumours, such as giant cell tumours or sarcomas, which severely affect anatomy for which no existing modular implants are available. Patient specific clavicle, scapula, and pelvic implants have all been demonstrated and resulted in patients showing optimal Musculoskeletal Tumor Society 93 (MSTS93) scores over a three year follow-up period [99]. Positive results have also been achieved for anatomical regions where existing implants limit joint function or where large volumes of bone have been resected, affecting stability, such as irregularly shaped massive tibial defects [100]. A series of four proximal tibia blocks demonstrated the advantages

of AM over conventional techniques, allowing use in conjunction with a standard knee prosthesis whilst including a porous surface structure where ligaments can be directly sutured [101]. In such oncological cases, patients are likely to be immunosuppressed, making infection control especially important to consider.

Alongside allowing patient specific implants to be produced more efficiently, use of AM allows for greater flexibility in both implant design and material. Considering the goal of integrating antimicrobial agents to implant materials, two key approaches are worth considering;

- First, use of material flexibility for the direct integration of antimicrobials to the implant alloy.
- Second, using increased design freedom to intercalate an antimicrobial delivery vehicle within an AM implant.

With the ability to rapidly prototype different implant materials by altering feedstock, geometrically complex samples of novel alloys can be produced without the need for specialist casting facilities, and in small quantities. This makes PBF an ideal approach for rapid alloy development.

1.4.1 In-situ alloying

Implanted biomedical alloy choice is restricted, with a narrow range of CoCr and Ti alloys predominant. This limits the possible properties achievable in metallic implants, both mechanical and chemical. Development of new alloy compositions may allow for implants to provide additional functions in vivo. Novel alloys have been explored by a range of methods [102], but development is typically time consuming and requires specialised equipment, with difficulties in creating complex geometries previously limiting the use of more novel materials such as NiTi [103]. Due to the powder feedstock that PBF processes are reliant upon, it is possible to create and validate entirely new alloys either by pre-alloying during atomisation of powders, or simply by blending of feedstocks. A range of compositions can be rapidly assessed at lower expense, by mixing elemental

or alloyed powders such that localised homogenisation of the alloy occurs during the AM process [104].

Using this technique, investigations have been made into alloys that, rather than being effectively inert in vivo, exhibit actively osteogenic or antibacterial properties [105]. Particular focus has been on addition of antimicrobial metal ions, such as silver or copper, but experimental materials with integrated hydroxyapatite (HA) have also been demonstrated (Table 1.1).

Considerable characterisation is needed to find the optimum thermal processing during additive manufacture or heat treatment post-processing, as investigations in non-AM produced antimicrobial alloys have suggested specific metallurgical phases dominate release kinetics [124]. Alongside this, further studies are required to establish the optimum loading of therapeutic materials in alloys. Particularly for those alloys that directly incorporate HA, the effect of incorporating additional elements can significantly alter corrosion behaviour, and may override any benefits from improved antimicrobial behaviour or osseointegration. Given the clear mechanical degradation addition of a ceramic such as HA has on composite alloys, a more subtle microalloying approach may prove more mechanically viable in the long-term. Inclusion of key alloying elements to feedstock, such as zirconium to CoCr alloys, has been explored. Using a rabbit femoral model, Zr additions as low as 0.04 wt% increased the torque required to remove implants after eight weeks by 10 % [125]. Further histological study of implants in rabbit femur sites showed similar mineral crystallinity, apatite to collagen ratio, and osteocyte density to equivalent CoCr implants after eight weeks [126]. For antimicrobial alloying, a very wide range of dopant concentration has been assessed by PBF, indicating significant alloy development is still needed to establish the optimum composition and microstructure for efficacy.

Table 1.1: Examples of additively manufactured bioactive alloys, showing the wide range of base systems and fraction of therapeutic material included.

Active Agent	Base Alloy	Fraction (wt%)	Source	Key Findings
HA	316L steel	5 - 15 vol%	[106, 107]	Across all alloys, observe significant reductions in tensile strength and fracture toughness. Associated with porosity and dissolution of P into base alloys. HA acts as a grain refiner, increasing hardness.
	cp-Ti	2.0 - 5.0	[108]	
		0 - 5.0 gradient	[109]	
	Ti-6Al-7Nb	5.0	[110]	Increases stiffness in Ti. In Mg-3Zn, see reduced corrosion rate due to protective apatite formation - may also be due to grain refinement.
	NiTi	25	[111]	
	Mg-3Zn	2.5 - 10	[112]	
Cu	316L	4.5	[113]	Antimicrobial behaviour increased with ageing of alloy, at the cost of lower corrosion resistance. Cytocompatibility demonstrated.
		2.5 - 3.5	[114]	
	Ti-6Al-4V	1.38	[104, 115]	Efficacy versus *E. coli* and *S. aureus* demonstrated. Observed increase in strength and reduced ductility. Cytocompatibility demonstrated. Addition of Cu encourages differentiation of osteoblasts.
		5.0	[116]	
		2.0 - 6.0	[117, 118]	
	Co-29Cr-9W	3.0	[119–121]	Antimicrobial efficacy demonstrated against*E. coli* and *S. aureus*. Cu increases resistance to corrosion and wear. Cytocompatibility shown.
	Mg ZK60	0.2 - 0.8	[122]	Increased strength, strong antibacterial and cytocompatible.
Ag	Ti-6Al-4V	0.5	[116]	Dramatically increases ductility, but shows minimal antibacterial behaviour at this level.
	Mg ZK30	0.25 - 1	[123]	Increased hardness and compressive strength, reduced degradation rate and increased efficacy against E. Coli versus ZK30 alone.

1.4.2 Two phase implants

Beyond the properties of a metal implant itself, AM can be used as an enabler for other technologies, such as localised delivery of therapeutic agents. Given the established impact of implant associated infections, the ability of an implant to elute antimicrobials or osseointegration-related factors is worth exploring. Coatings are well established as effective for both antimicrobial [40], osseointegrative properties [127, 128], but may be limited in duration of therapeutic efficacy and durability both prior and post implantation.

One example of an alternate AM-enabled approach to the delivery of therapeutic agents is to consider the delivery vehicle as a distinct second phase integral to the implant (Figure 1.4). Intercalation of an eluting phase within a lattice structure may be a way to combine stress matching, therapeutic effects, and improved osseointegration in one implant [129]. This basic proof of concept has been established in cp-Ti with a range of biocompatible fillers [130]. Infiltration of a simvastatin loaded hydrogel into a Ti-6Al-4V scaffold showed significantly greater vascularisation, osseointegration, and bone ingrowth in a rabbit model compared to equivalent structures without a secondary phase [131].

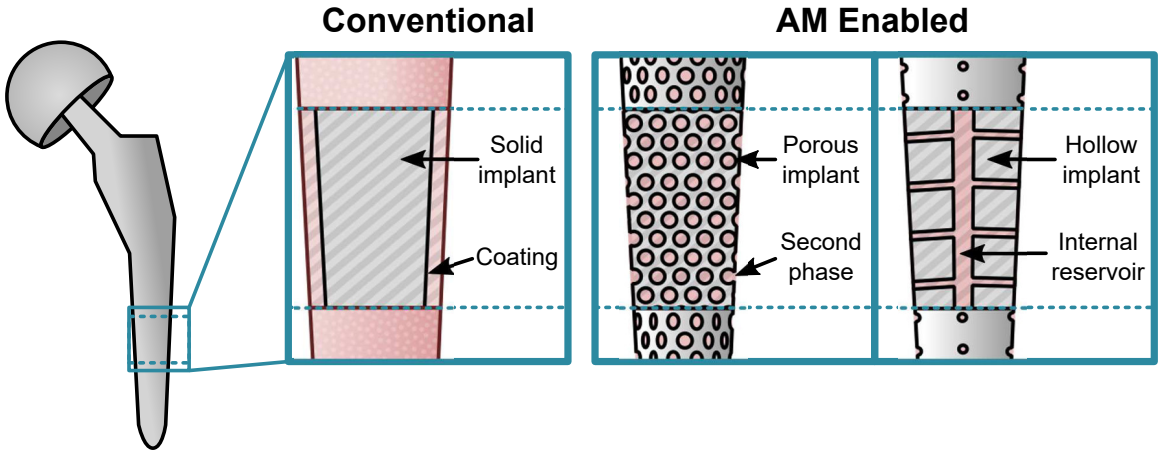


Figure 1.4: Schematic visualising three approaches to adding therapeutic materials to an implant to achieve additional functionality; conventional addition of a coating, intercalation with an AM lattice structure, and inclusion of an internal reservoir through AM

Alternatively, a larger and more controlled volume of material may be delivered by

integrating the second phase inside a physical reservoir, i.e. a hollow implant. In this way, the release characteristics of the therapeutic agents can be tailored both by altering the characteristics of the delivery vehicle, and by modification of the implant pore structures through which elution is achieved [132, 133]. Addition of permeable membranes on the outside of a porous implant could further optimise elution, and simplify loading of the eluting agent prior to implant insertion [134].

Whilst it is crucial that the metallic component of a two-phase implant provides sufficient mechanical stability, it is also key to optimise the delivery phase. For an antimicrobial loaded phase, an appropriate release profile is needed. Whilst burst release may allow a MIC to be reached with a lower total antimicrobial content [37], the established delay in infection onset for prostheses suggests a more continuous profile could be advantageous. It is also important to consider the degradation products of the delivery vehicle [135].

1.5 Aims and content of this research

The continuing need to provide antimicrobial prophylaxis for prosthetic implants whilst simultaneously tackling AMR requires new approaches to implant material design. This work aims to investigate the development of inherently antimicrobial materials, and the viability of using additive manufacturing as an enabling technology for localised delivery of antimicrobials in prosthetic implants. In particular, the use of inorganic antimicrobials - typified by silver - is focussed upon.

First, an antimicrobial magnesium oxychloride cement formulation was assessed. Such a material may provide a useful second-phase for a functional two-phase implant, with higher degradability than conventional calcium phosphate cements. Both silver phosphate doped and undoped oxychloride cement formulations were chemically, physically, and microbiologically characterised, with efficacy against both gram positive *S. aureus* and gram negative *Pseudomonas aeruginosa* (*P. aeruginosa*) assessed, alongside tests for mammalian cell cytotoxicity.

Given the established biocompatibility and widespread clinical use of Ti alloys, development of a silver doped Ti alloy is a key goal. Initial focus has been on the significant manufacturing challenges of dissimilar materials in SLM. A series of Ti-Ag alloys have been produced by in-situ alloying, with the dependence of microstructural characteristics on laser processing parameters investigated. The behaviour of blended powders within the printer powder bed have been considered.

To better understand the optimal microstructure for antimicrobial response from Ti-Ag alloys, a subsequent study of a series of conventionally homogenised and aged alloys has been performed. Drawing on the established Ti-Ag phase diagram, a sequence of heat treatments have been performed to generate different microstructural states with varying phases. Performance in vitro against *S. aureus* was assessed, alongside microstructural investigations.

CHAPTER 2

FORMULATION OF AN ANTIMICROBIAL MAGNESIUM OXYCHLORIDE CEMENT

The growing threat of bacterial resistance to antibiotics is driving an increasing need for new antimicrobial strategies. This work demonstrates the potential of magnesium oxychloride cements (MOC) to be used as inorganic antimicrobial biomaterials for bone augmentation and delivery from two-phase implants.

An injectable formulation was identified at a powder to liquid ratio of $1.4\,\mathrm{g\,mL^{-1}}$, with an initial setting time below 30 min and compressive strength of 35 MPa. Supplementation with Ag_3PO_4 to enhance the antimicrobial efficacy of MOC was considered, and shown via real time X-ray diffraction to retard the formation of hydrated oxychloride phases by up to 30%. The antimicrobial efficacy of MOC was demonstrated in vitro against *Staphylococcus aureus* and *Pseudomonas aeruginosa*, forming zones of inhibition and significantly reducing viability in broth culture. Enhanced efficacy was seen for silver doped formulations, with complete eradication of detectable viable colonies within 3 hours. Investigating the antimicrobial mode of action of these formulations revealed that Mg and Ag release and elevated pH contributed to efficacy, with no clear single mechanism dominating. Interestingly, sustained silver release was demonstrated over 14 days, suggesting the Ag_3PO_4 modified formulation offers two mechanisms of infection treatment, combining the inherent antimicrobial properties of MOC with controlled release of inorganic antimicrobials.

As an initial proof of concept, two phase implant models consisting of porous Ti-6Al-4V cylinders with an internal MOC reservoir were produced. Zones of inhibition were linked to the contact area between cement filled pores and growth media, indicating that the exposed surface area of antimicrobial agent in a two-phase implant will be a key design characteristic.

ACKNOWLEDGEMENT OF CONTRIBUTING MATERIAL AND AUTHORS

Content within this chapter has been published in the following journal paper(s):

- Morgan Lowther, Thomas E Robinson, Victor M Villapun, Christopher Stark, Liam M Grover, Sophie C Cox. Formulation of inherently antimicrobial magnesium oxychloride cement and the effect of supplementation with silver phosphate. *Materials Science and Engineering: C*, Apr 2021.

As primary author, M Lowther produced all written work within this publication and performed all primary experimental work. The contributions of co-authors are as follows:

- Dr. T E Robinson: Guidance in operation of micro X-ray computed tomography (μXCT).
- Dr. V M Villapun: Assistance with mammalian cell culture.
- C Stark: Assistance with the operation of inductively coupled plasma optical emission spectroscopy (ICP-OES).
- Prof. L M Grover, Dr. S C Cox: Editorial and supervisory guidance.

2.1 Introduction

Reconstruction of hard tissues is increasingly challenged by post-operative bone and implant related infections. This clinical need is compounded with a growing incidence of bacterial resistance to various antimicrobials, which has been predicted to become a larger cause of mortality globally than cancer by 2050 [136]. Staphylococci, Enterobacteriaceae and Pseudomonas are frequently established as clinical isolates from device associated orthopaedic infections [25], all of which have established antibiotic resistant strains prevalent in the community [137–139]. Localising the delivery of antimicrobials from biomaterials has been suggested as one approach to improve success in preventing such infections taking hold in the first instance [140–143].

Given the compositional similarity of calcium phosphate cements to the mineral component of bone, there has been a drive towards the development of calcium-based cements as biomaterials that may be delivered in a minimally invasive manner for bone tissue regeneration or augmentation. Whilst these inorganic phases play a significant role in biomineralisation [144], calcium phosphate cements do not exhibit any inherent antimicrobial properties once cured. This has led a number of researchers to explore supplementation of calcium phosphates with broad-spectrum antibiotics to treat infected bone defects [87, 145], however overuse of such compounds is a key driver of antimicrobial resistance [33]. With the need to mitigate usage of conventional antibiotic chemistries, there is an increasing interest in the incorporation of inorganic antimicrobials into various biomaterials [146]. Substitution of silver or copper species into bone cement formulations has been the most well explored [147–149]. The addition of excess alkali oxides or phosphates has also been demonstrated as effective against both gram-positive and gram-negative species in vitro [150]. Based on this concept, inherent antimicrobial behaviour is observed in magnesium phosphate cements, with efficacy ascribed to increased pH and osmolarity in the local environment [151].

Magnesium-based biomaterials more broadly have seen a recent surge in interest due to the significant role of Mg in several biological mechanisms, including stimulation of

cell proliferation and bone tissue development [88]. Otherwise known as Sorel cements, magnesium oxychloride (MOC) cements have predominantly been explored by the construction industry, however its use for these applications is limited by its low resistance to water [152–155]. MOCs are produced from a mix of MgO and $MgCl_2$ brine, with a series of hydrated phases forming in a three step process [156].

Initially, MgO is neutralised by free hydrogen ions in the $MgCl_2$ brine, forming mononuclear magnesium complex ions as described by equations 2.1 and 2.2. This results in a pH increase within the $MgCl_2$ solution as free hydrogen is consumed.

$$MgO + 2\,H^+(aq) + 6\,H_2O \longrightarrow [Mg(H_2O)_6]^{2+}(aq) \tag{2.1}$$

$$MgO + H^+(aq) + 5\,H_2O \longrightarrow [Mg(OH)(H_2O)_5]^{+}(aq) \tag{2.2}$$

As MgO is neutralised, polynuclear complexes form through a hydrolysing-bridging process. Mg^{2+} ions bridge with OH^- or H_2O ligands to form positively charged complexes, which may in turn be hydrolysed to release H^+, further driving neutralisation of MgO. The overall hydrolysing-bridging process, described by equation 2.3, produces a hydrogel, at which point the cement setting begins.

$$xMg^{2+} + (z+y)H_2O \underset{H+}{\overset{OH-}{\rightleftharpoons}} [Mg_x(OH)_y(H_2O)_z]^{2x-y} + yH^+ \tag{2.3}$$

This initial gelation prior to crystallisation is an established feature of several cement systems, having been most rigorously investigated in the calcium silicate hydrate that forms Portland cement [157]. Though behaviour of the gelled state is critical to the final properties of a hardened cement, investigating gel behaviour without disruption of the gelation process is challenging. Non-destructive techniques such as X-ray diffraction (XRD) [158] and differential scanning calorimetry (DSC) methodologies [159] currently provide the best analytical methods for characterising the gelled state in MOC [160].

Lastly, crystallisation into the hydrate phases then occurs with Cl^-, predominantly $3\,Mg(OH)_2 \cdot MgCl_2 \cdot 8\,H_2O$ (phase 3), and $5\,Mg(OH)_2 \cdot MgCl_2 \cdot 8\,H_2O$ (phase 5), with the

overall reactions and standard enthalpy of reaction (ΔH_r°) shown by equations 2.4 and 2.5, respectively [161]. The reaction of MOC pastes is notably less exothermic than that of calcium phosphate or "brushite" cement (-83.0 $\mathrm{kJ\,mol^{-1}}$) assuming total conversion of reagents under standard conditions [162]. Within the typical temperature range of a clinical environment, between room and body temperature, phase 5 is observed to be favoured [163]. Crystallisation occurs over the course of multiple days [164], with the majority of strength seen to develop within the first 2-7 days for MOC based concretes [152, 165].

$$3\,\mathrm{MgO} + \mathrm{MgCl_2} + 11\,\mathrm{H_2O} \longrightarrow 3\,\mathrm{Mg(OH)_2 \cdot MgCl_2 \cdot 8\,H_2O} \tag{2.4}$$

$$\Delta H_r^\circ = -19.82\,\mathrm{kJ\,mol^{-1}}$$

$$5\,\mathrm{MgO} + \mathrm{MgCl_2} + 13\,\mathrm{H_2O} \longrightarrow 5\,\mathrm{Mg(OH)_2 \cdot MgCl_2 \cdot 8\,H_2O} \tag{2.5}$$

$$\Delta H_r^\circ = -5.16\,\mathrm{kJ\,mol^{-1}}$$

Phase 5 provides the greatest strength of the hydrated phases, with excess MgO beyond the stoichiometric requirement added to favour formation versus phase 3 [166]. This may be achieved by altering the powder to liquid ratio (PLR), increasing the mass of MgO in a mix whilst retaining the same concentration of $\mathrm{MgCl_2}$ brine used (Figure 2.1, based upon data from L. Urwongse (1980) [164] and reproduction by J. Stolfi (2018) [167]).

Given the sensitivity of MOC to degradation in water, understanding the leaching behaviour of MOC has been a key focus of research [154]. A wide range of additives to improve stability in aqueous conditions have been explored, including active species that produce new hydration products such as $\mathrm{SiO_2}$ [168] and aluminates [169]. It has been demonstrated that the use of phosphates [170–172] or sulphates [171] can increase water resistance without producing new hydration products, however this is frequently at the cost of reduced mechanical performance [155]. Outside the remit of the construction industry, water sensitivity may not be considered as an inherently deleterious property.

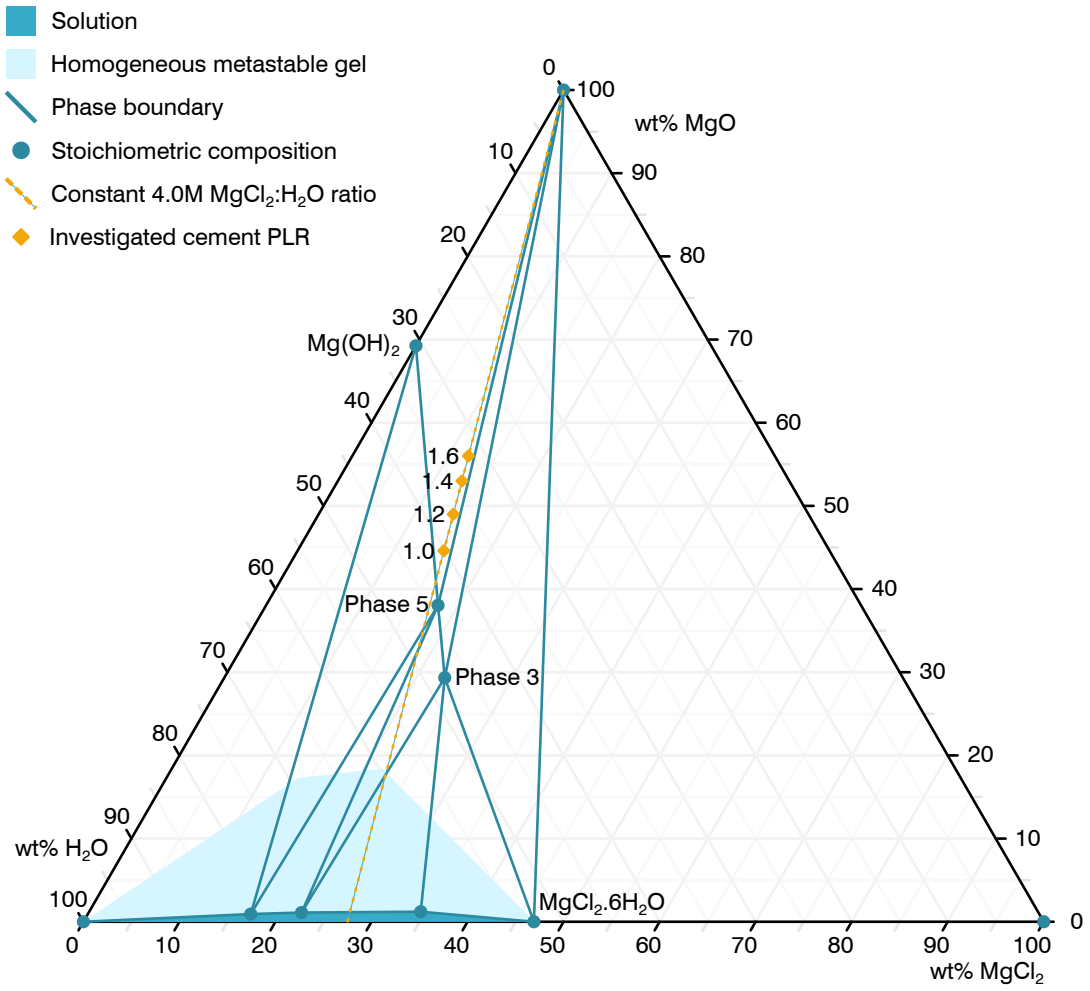


Figure 2.1: Isothermal ternary phase diagram at 23 °C for MgO - $MgCl_2$ - H_2O. A dashed line shows the compositions achievable with a 4.0 M $MgCl_2$ brine, and where the PLR explored in this study lie.

For biomedical usage, it may be advantageous not simply to maximise water resistance, but to tailor resorption rate.

Biomedical investigations of MOC have been limited to tailoring resorption and in vitro cytocompatibility, both with and without the addition of hydroxyapatite [173, 174]. The established antibacterial and antifungal properties of MgO both at a micro- and nano-scale make MOC a prime candidate for an antimicrobial biomaterial [83, 175]. Alongside any possible antimicrobial efficacy inherent to MOC, modification of the cement as a carrier of an antimicrobial agent may prove valuable. As the addition of phosphates has been established to improve the water stability of MOC [155, 170, 171, 176], use of an

antimicrobial phosphate may confer additional benefits beyond improving efficacy. The antimicrobial and biofilm disrupting behaviour of silver and its compounds has been well established [65, 71] including its synergistic behaviour in combination with conventional antibiotic prophylaxis [48]. Hence, Ag_3PO_4 is an ideal antimicrobial compound to explore for modifying MOC. This is further demonstrated by the low prevalence of silver resistance, with no reports of clinically relevant silver resistance in gram-positive bacterial species and extensive testing of over 1000 isolates of staphylococci showing no acquired resistance to Ag^+ [65].

This work seeks to establish whether MOC demonstrates inherent antimicrobial efficacy, and how supplementation with silver phosphate may modulate this behaviour. In order to assess the effect of doping MOC with Ag_3PO_4, detailed XRD investigations were performed, emphasising the effect of this modification on curing behaviour. A series of formulations with different MgO to $MgCl_2$ brine ratios were considered, with physical characterisation focussed on practical considerations for clinical usage of a cement formulation, including setting time and injectability. Promising candidate formulations were then assessed for cytotoxicity and antimicrobial efficacy in vitro, with the inherent efficacy of MOC and the alteration of this by Ag_3PO_4 explored. As 75% of prosthetic joint infections are associated with staphylococci [25], *S. aureus* was chosen as a clinically relevant species, alongside *P. aeruginosa* to assess efficacy against gram negative bacteria. To elucidate a possible mechanism for efficacy, extracts from a 14-day release study were investigated for changes in pH, reactive oxygen species generation, and metal ion elution. Finally, preliminary assessments of release characteristics when incorporated into two phase AM models were made, alongside bacteriological assays.

2.2 Materials and methods

2.2.1 Cement production and characterisation

Cement manufacture

MOC were manufactured by combining a 4.0 M magnesium chloride brine, produced from $MgCl_2 \cdot 6\,H_2O$ (Scientific Laboratory Systems, UK) and deionised water (Milli-Q, UK), with MgO powder (Scientific Laboratory Systems, UK). PLR of 1 to 1.6 $g\,mL^{-1}$ were produced. For silver doped formulations (Ag modified magnesium oxychloride (MOC-Ag)), Ag_3PO_4 (Alfa Aesar, UK) was added to the MgO powder at a ratio of 0.2 $g\,mL^{-1}$ of brine.

For density analysis, compressive strength testing and the release studies, cylindrical samples were produced by extruding cement pastes into polyethylene split moulds of 6 mm diameter and 12 mm height, which were then cured for 48 hours at room temperature without immersion. To account for the possible photosensitivity of Ag compounds, MOC-Ag were stored in foil wrapped containers during curing to minimise illumination.

As control samples, citrate modified dicalcium phosphate dihydrate (brushite, DCPD) cements were manufactured with a PLR of 3 $g\,mL^{-1}$, with addition of 0.1 $g\,mL^{-1}$ gentamicin sulphate to act as a positive antimicrobial control (DCPD-Ge). Briefly, monocalcium phosphate monohydrate (MCPM, Sigma, UK) and β-tricalcium phosphate (β-TCP, Sigma, UK) powders were mixed in a ratio of 1:1.23, with 0.5 M citric acid [177]. Calcium sulphate (CS) cements, that are known to have no inherent antimicrobial efficacy, were also produced from $CaSO_4 \cdot 0.5\,H_2O$ powder (Sigma, UK) and deionised water at a powder to liquid ratio of 1.67 $g\,mL^{-1}$ as a negative control [178].

Cement composition

In order to establish the phases present in the cured formulations, ground cements were subjected to XRD analysis using a Bruker D8 diffractometer with a Cu-Kα anode. Diffraction patterns were collected between $2\theta = 10°$ to 50°, using a step size of 0.02° and acquisition time per step of 0.3 s. Bruker Diffrac.EVA software (version 4.2.2) was used to

analyse collected patterns, with background automatically removed and peaks indexed against references from the International Centre for Diffraction Data. The relative portions of each phase present were calculated using the semi-quantitative function in EVA software. To account for the high intensity of AgCl diffraction peaks in MOC-Ag samples, the ratio of Mg and Ag containing phases was then normalised based on the proportion of reagents used.

Monitoring cement setting reaction

The formation rate of different phases was monitored by XRD to study the effect of Ag_3PO_4 on cement curing. Cement pastes were placed into a custom 3D-printed polylactic acid cup with an internal diameter of 25 mm, and depth of 4 mm. The same scan settings were used as described above, with the scan repeated immediately after each sweep of 10° to 50° was completed for 400 min. Equilibrium measurements of the same samples were taken after two weeks storage at room temperature. The area of peaks that have the least interference with adjacent peaks was measured for each timepoint using the Bruker Diffrac.EVA software (Table 2.1). Considering the scan step size and acquisition time per step, the nominal time of measurement for peaks was interpolated based on the central point of the peak.

Table 2.1: Reference spectra used for indexing and quantification of phases in XRD, including parameters used for calculation of diffraction peak area in the Diffrac.EVA software for calculation of ξ

Phase	Reference pattern	Measured peak (°)	Relative intensity (%)	Peak 2θ range measured (°)
Phase 5	00-007-0420	21.499	75	20.0 - 22.5
MgO	00-045-0946	42.917	100	40.5 - 45.0
AgCl	00-031-1238	32.224	100	31.5-33.7
Ag_3PO_4	00-006-0505	33.293	100	32.7- 33.7
$Mg(OH)_2$	01-071-5972	-	-	-
Phase 3	00-007-0412	-	-	-

Considering the initial and final equilibrium area of a given peak, A_0 and A_f respectively, taking the area at a given time point A_t allows calculation of the fractional extent of the reaction, ξ.

$$\xi = \frac{A_t - A_0}{A_f - A_t} \tag{2.6}$$

The value of ξ was calculated both for the products phase 5 and AgCl, and the reactants MgO and Ag_3PO_4. Any lag in the value of ξ between reactants and products may indicate the formation of intermediate species [158].

Curing, flow, and extrusion behaviour

The flow, setting and extrusion characteristics of cements are important to determine the period in which the material remains workable and whether formulations can be delivered precisely in a clinical context. To visualise the flow behaviour of cements, 1 mL of each formulation was placed into a cuvette and inverted and images collected after 60 s. Initial and final setting time of MOC and MOC-Ag samples were measured using a modification of the Gilmore needles method [179], with samples constrained in 1 cm deep wells to restrict spreading during curing. The maximum pressure required for extrusion from 1 mL syringes with 2 mm diameter orifice (Plastipak, BD) without needles was also assessed as a measure of injection ease using a mechanical tester (Z030, Zwick/Roell) at a load rate of $1\,\mathrm{mm\,s^{-1}}$ with a pre-load of 0.25 N, with tests commenced five minutes after cements were mixed (N = 3) [180].

In order to assess the washout sensitivity of cements, MOC and MOC-Ag with PLR of $1.4\,\mathrm{g\,mL^{-1}}$ were selected. Pats of 1 mL were extruded and immersed in water after 5, 45 and 90 min of curing. Cements were visually inspected and photographed immediately after immersion, and after a further 48 h.

Density measurements

As cement strength and degradation behaviour can be highly dependent on total porosity, the relative density of samples was established. The dimensions of cylindrical cement

samples were measured using callipers and mass recorded to the nearest mg, and the dry density calculated (N = 3). Samples of each cement type were also ground manually with a marble pestle and mortar, and the strut density measured by He pycnometry (AccuPyc II 1340, Micrometrics, USA). Five sequential measurements of each sample were made, with five gas purges at 19 MPa per measurement (N = 3). The relative densities of cements were taken as the ratio of dry to strut density.

Mechanical behaviour

To establish the mechanical properties of cements, compressive strength testing of cured MOC, MOC-Ag, DCPD, and DCPD-Ge was performed on cylindrical samples at cross-head speed of $1\,\mathrm{mm\,min^{-1}}$ (N = 3, 3) (Z030, Zwick/Roell). The ultimate compressive strength (UCS) was calculated from the maximum force experienced by each sample, and the cross sectional area as calculated from the measured diameter of each specific sample. Young's modulus was calculated by linear regression across the linear stress/strain region prior to failure. The strain energy density of samples was also established by integrating the area between the curve and the pre-load stress. Processing of data was performed in R (v 4.0, R Foundation).

Weibull analysis

Variation in strength due to the random distribution of flaw sizes within samples can be described by the Weibull modulus. By modelling a brittle material as a chain of linked segments, all of which must not break for the sample to survive a given stress, the likelihood of failure can be mapped to a Weibull distribution. For a given series of samples tested to failure, the probability of failure P_f at a given stress σ can be described by equation 2.7,

$$P_f = 1 - exp\left[-\left(\frac{\sigma - \sigma_u}{\sigma_\theta}\right)^m\right] \tag{2.7}$$

where σ_θ is the characteristic strength determined by specimen geometry, and m is Weibull modulus, which describes the width of the critical flaw distribution. The threshold stress parameter, σ_u, is the stress below which no test specimen will break. Typically this parameter is neglected, unless proof-testing of the sample set has been performed or there is a clear limit to the maximum flaw size and therefore the minimum possible strength [181]. Reduced to the two-parameter Weibull distribution, it is possible to determine the Weibull modulus m and characteristic strength σ_θ from a linear relationship as described in equation 2.8.

$$\begin{aligned} P_f &= 1 - exp\left[-\left(\frac{\sigma}{\sigma_\theta}\right)^m\right] \\ \implies \ln(1 - P_f) &= -\left(\frac{\sigma}{\sigma_\theta}\right)^m \\ \implies \ln\left[\ln\left(\frac{1}{1 - P_f}\right)\right] &= m\ln\sigma - m\ln\sigma_\theta \end{aligned} \tag{2.8}$$

In order to assign the probability of failure to each sample, results were ranked according to UCS. For a given result with rank i, the failure probability is given by

$$P_f(\sigma_i) = \frac{i - 0.5}{N} \tag{2.9}$$

where N is the total number of test specimens investigated.

Cement microstructure

Microstructural assessment of MOC samples were made using μXCT and scanning electron microscopy (SEM) in order to understand any possible influence on mechanical behaviour. Cylindrical samples of MOC and MOC-Ag cured for 48 hours were mounted vertically and scanned with a XCT (Skyscan 1172, Bruker) at 80 kV, 100 µA and an effective pixel size of 7.85 µm. A 0.5 mm Al filter was used to attenuate the source, with an exposure time of 400 ms, rotation step of 0.4° and averaging of four frames. Recon-

struction was performed with a fixed beam hardening correction of 45% and ring artefact correction factor of 10 (NRecon, Bruker). The pore size distribution was calculated for the reconstructed μXCT data (CTAn, Bruker) and used to estimate the toughness of samples. A simple model of the relationship between UCS and pore size assuming brittle fracture, based on the Griffith criterion for crack propagation, determines an inverse-square relationship between strength and mean pore size [182]:

$$\sigma = K_1 \frac{(1-p)}{\sqrt{r_m}} \tag{2.10}$$

where σ is compressive strength, K_1 is the empirical fracture toughness, p is porosity, and r_m is the mean pore radius. Based on this equation, the fracture toughness K_1 may be estimated, but is highly dependent upon the choice of mean pore size used.

SEM imaging was performed on fracture surfaces of cement cylinders affixed to carbon tabs on Al stubs, and sputtered with Au at a current of 15 mA for 20 s. Images were obtained to compare microstructure and porosity at 15 kV (TM3000, Hitachi). energy-dispersive X-ray spectroscopy (EDS) (Oxford Instruments) maps were also taken to assess distribution of Ag, Mg, Cl, and P.

2.2.2 Cytotoxicity assessment

Culture conditions

The possible cytotoxicity of MOC and MOC-Ag cements was considered using the mouse osteoblastic precursor cell line (MC3T3-E1, P13), with DCPD cement used as a positive biomaterial control. 50000 cells were initially seeded in a 24 well plate and incubated in 1 mL of Dulbecco's Modified Eagle Medium (10% Fetal bovine serum, 12% L-Glutamine and 1% penicillin/streptomycin; Sigma Aldrich) for 24 h at 37 °C and 5% CO_2. Cements samples of 5 mm diameter and 2 mm height were sterilised by immersion in 70% ethanol and washed with phosphate buffered saline (PBS) before drying under laminar air flow. Cements were introduced to cultures in transwell inserts, and old media exchanged with

1.5 mL of fresh modified DMEM. Two sets of samples (N = 3) were prepared and incubated for 24 h and 7 days with media exchange performed every two days for the latter.

Viability assessment

To analyse proliferation and viability of cells, Alamar Blue assay (Fisher Scientific) and fluorescence microscopy were performed. Transwell inserts were removed and 10% of the media volume of Alamar Blue was added to wells, before incubation for 4 h at 37 °C. 100 µL was transferred to a 96 well plate and fluorescence read at 570 nm excitation and 590 nm reading wavelengths (SPARK, Tecan).

For live/dead fluorescence imaging, samples were washed gently three times with 10 mM PBS, stained with a solution of 200 µL of 5 mM calcein-AM (VWR International) and 1.5 mM propidium iodide (Thermo Fisher Scientific) and incubated for 30 min. Stained cells were imaged using a fluorescence microscope (M5000, EVOS). The number of live and dead cells were analysed using ImageJ (NIH) at 5x objective magnification, with the live cell density estimated from 40x magnification images when cells were sufficiently confluent to prevent reliable automated separation of individual cells.

2.2.3 Microbiological characterisation

Culture conditions

To assess the possible antimicrobial function of MOC and MOC-Ag cements compared to DCPD and DCPD-Ge, efficacy was assessed against *S. aureus*, a model bacteria associated with a large number of implant related infections [25], and *P. aeruginosa*, a model gram negative species.

Unless otherwise stated, all bacterial cultures used unsupplemented LB broth (Lennox, Sigma) or LB agar (Lennox, Sigma) plates, and were under aerobic conditions at 37 °C. Calibration of colony forming units per mL (CFU mL^{-1}) to optical density at 600 nm (OD_{600}) was performed using a spectrophotometer (Evolution 300, Thermo Scientific), with an OD_{600} of 0.2 approximately equal to 10^8 CFU mL^{-1}. For all tests, overnight

cultures in LB broth were grown to 10^{10} CFU mL^{-1} at 37 °C and 150 rpm.

Agar diffusion test

Zones of inhibition for both cured cements and uncured pastes were assessed on LB agar plates, inoculated with 100 µL of overnight culture. A sterile 12 mm diameter stainless steel bore was used to create three equidistant cylindrical wells in each plate. Cement mixes were extruded into wells from 5 mL syringes, whilst cements crushed after curing were placed into wells and compacted with a spatula to ensure good contact with the agar without distorting the surface, with the volume of cement delivered sufficient to form a level surface with the agar plates in all cases. Plates were then incubated at 37 °C for 24 hours. Measurements were made with a ruler at 1 mm increments across the diameter of the zone, and corrected by subtraction of the well diameter and halving. Zones were assessed with three biological repeats, each performed in triplicate (N = 3, 3).

Planktonic bacteria

Direct antimicrobial action against planktonic bacteria in broth was demonstrated using LB broth culture at 10^7 CFU mL^{-1}. Cement cylinders were placed into 1 mL of culture in lidded non-adherent 24 well plates, and wrapped in foil to minimise illumination. Well plates were incubated at 37 °C and 150 rpm on a shaking incubator for 24 hours, before media was sampled and serially diluted for viable colony forming units (CFU) by the Miles-Misra method [183]. MOC and MOC-Ag cements aged in LB broth for 72 hours at 37 °C in dark conditions were subjected to the same analysis (N = 3, 2).

Bactericidal efficacy of cement extracts were also considered to establish possible elution of antimicrobial species. MOC and MOC-Ag cylinders were aged in sterile LB broth at a cement to broth ratio of 0.5 g mL^{-1}. Media was withdrawn after 72 hours of aging, and an inoculation of 20 µL of *S. aureus* at 10^8 CFU mL^{-1} added to 980 µL of aged media to produce a culture of 10^7 CFU mL^{-1}. Samples of 75 µL were taken at 3, 6, and 24 hours, and serially diluted before plating to assess viable CFU mL^{-1} (N = 3).

This protocol was also used to study the efficacy of cement extracts at a cement to broth ratio of $0.14\,\mathrm{g\,mL^{-1}}$. Sample volumes were reduced for use in a 96 well plate, with extracts from a sterile release study inoculated and sampled for viable $\mathrm{CFU\,mL^{-1}}$ after 24 hours of culture (N = 3).

2.2.4 Release studies

Release study conditions

In order to assess possible bactericidal mechanisms, the release of Ag and Mg ions, ROS, and pH changes of media were studied daily over a 14 d period. Two cylindrical samples were placed in either 10 mL of PBS (Oxoid) or LB broth, equivalent to a cement to broth ratio of $0.14\,\mathrm{g\,mL^{-1}}$ (N = 3). Samples were incubated at 37 °C, with the full media volume changed on a daily basis. Measurements of pH were made on 2 mL aliquots using a pH probe (FiveEasy, Mettler Toledo).

Reactive oxygen species generation

Production of ROS was investigated by a chemiluminescence assay using phenyl-10-methyl-acridinium-9-carboxylate fluorosulphonate (PMAC) (Cayman Chemical) [184]. A stock solution of $50\,\mathrm{\mu g\,mL^{-1}}$ of PMAC in dimethyl sulphoxide was diluted 100 fold in 0.1 M KCl prior to use in the assay. A 50 µl aliquot of this working solution was pipetted into 100 µl of the extract under investigation in a black 96 well plate to minimise cross-well illumination. Samples were then immediately measured for luminescence in repeated sequence over the course of 20 minutes using a plate reader (SPARK, Tecan, Switzerland), with an integration time of 1000 ms per measurement point.

Elemental analysis

The concentration of Mg and Ag present in extracts were measured with inductively coupled plasma optical emission spectroscopy (ICP-OES, Perkin-Elmer 8000 Optima). Due

to the very low solubility of Ag in solutions containing Cl ions [185], extracts were acidified with 10% hydrochloric acid before filtration through 0.22 µm PES filters. Whilst in low concentrations of chloride, AgCl may precipitate prior to filtration, the use of high concentrations produces the soluble $AgCl_x^{1-x}$ anionic complex. Matrix-matched calibration standards of 2.5 to 900 ppm Mg and 0.1 to 50 ppm Ag were used, whilst In and Sc internal standards were used to correct the intensities of Ag and Mg respectively due to their similar atomic weights.

2.2.5 Two-phase implant model

As an initial proof of concept for the performance of MOC in a two-phase implant, cylindrical implants with an internal MOC reservoir and a porous surface were designed (Figure 2.2). Digital models were produced using the Inventor 2020 software package (Autodesk, US). All models were exported to .stl format before generation of slice files for manufacture.

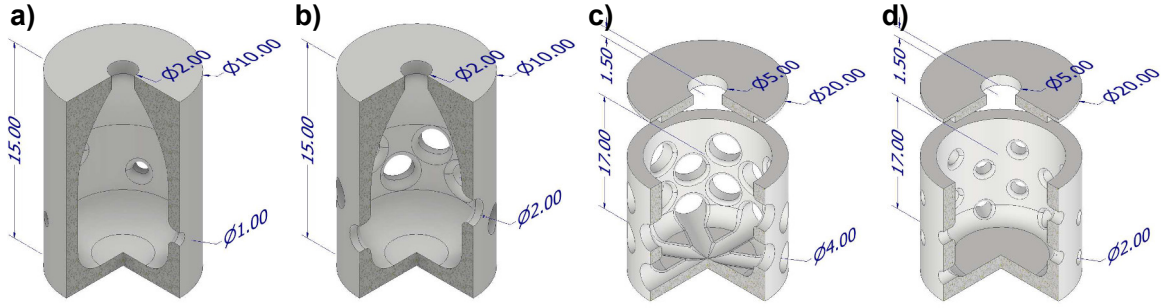


Figure 2.2: Two phase implant models used for proof of concept. CAD models of Ti−6Al−4V cylinders with (a) 1 mm and (b) 2 mm diameter pores; PET cylinders with (c) 2 mm and (d) 4 mm diameter pores.

Antimicrobial efficacy

To assess antimicrobial behaviour of two-phase implant models, porous Ti-6Al-4V implants were used (Figure 2.2a and b). Hollow cylinders of 10 mm diameter, 2 mm wall thickness, with either three pores of 1 mm, or twelve pores of 2 mm, diameter, were produced by SLM (RenAM 500M, Renishaw, UK). Cement pastes with PLR of 1.4 g mL^{-1}

were extruded into implants from a syringe, with a PET sheath used to prevent escape of the formulation during extrusion. Once filled, cylinders were placed into cylindrical holes within an agar plate inoculated with *S. aureus*, following the experimental protocol described for zone of inhibition tests of cements.

Elution of bromothymol blue

To investigate the release characteristics of two-phase models, MOC with a PLR of $1.4\,\mathrm{g\,mL^{-1}}$ was modified by addition of $0.02\,\mathrm{g\,mL^{-1}}$ bromothymol blue (BTB) (Alfa Aesar, UK). Larger scale cylindrical implant models with 20 mm diameter were produced by fused filament fabricaction (FFF) with a 0.4 mm print nozzle diameter (CR-20 Pro, Creality 3D, China) using PET (Filamentative, UK) (Figure 2.2c and d). Hole spacing, frequency, and radius were defined parametrically to enable consistent changes in geometry as these properties are altered. The diameter of pores was altered from 2 to 4 mm, with 18 holes radially distributed in 3 rows.

Supports and any surface adhered loose filament were removed manually, and the internal faces sanded with 120 grit paper. Cements were loaded into cylindrical implants from a 10 mL syringe and cured for 48 hours, with an external sheath containing implants used to minimise spreading of cements beyond the implant shell. Once cured, devices were immersed in 10 mL of PBS and stored at 37 °C. After 24 h, media was withdrawn and replaced with fresh PBS. Eluent was measured for absorbance at 427 nm and 602 nm with 10 flashes at a settle time of 50 ms (SPARK, Tecan, Switzerland). This process was repeated over a seven day period.

2.2.6 Statistical methodology

Prior to any assessment of the statistical significance of results, samples were assessed for equal variance using Levenes test ($\alpha = 0.05$). Where equal variances were confirmed, one-way Fisher ANOVA was used to determine if any difference in means was observed. For statistically significant differences in mean, the Tukey-Kramer post-hoc test was used for comparison and on an individual formulation basis, with PLR and formulation type (MOC/MOC-Ag) treated as a single variable ($\alpha = 0.05$). For results with non-equal variance, Welchs ANOVA and the Games-Howell post-hoc test were instead applied ($\alpha = 0.05$).

In order to assess the significance of formulation type (MOC/MOC-Ag) and PLR on behaviour, results were also subject to two-way ANOVA ($\alpha = 0.05$). The results of fitting the general linear model are listed in table 2.3.

For clarity, figures are labelled only with grouping according to the respective Tukey-Kramer or Games-Howell tests applied, with those means that do not share letters significantly different from one another.

2.3 Results

2.3.1 Cement production and chemical characterisation

Compared to a base formulation of 1 g MgO to 1 mL of 4 M $MgCl_2$ brine, increasing the MgO PLR to 1.6 g mL^{-1} produced additional remnant $Mg(OH)_2$, with phase 5 remaining the predominant component of the cured cements (Figure 2.3a). The addition of Ag_3PO_4 was found to alter the phases present, reducing phase 5 formation and increasing remnant MgO, and the formation of AgCl indicated by sharp diffraction peaks at 27.8° and 32.2° (Figure 2.3b). This transformation of Ag_3PO_4 to AgCl is further evidenced by the change in colour of formulations from yellow to white during curing (Figure 2.3c), followed by a change to grey if left exposed to light likely due to the photoreduction of AgCl to Ag.

Across the PLR tested for unmodified MOC (1 to 1.6 g mL^{-1}), the mass fraction of hydrated phases formed decreases from 80% (PLR 1 g mL^{-1}) to 60% (PLR 1.6 g mL^{-1}) (Figure 2.3a). Ag doped formulations with equivalent PLR values exhibited lower relative mass of hydrated phases compared with unmodified MOC samples, with a more rapid reduction from PLR 1 to 1.6 g mL^{-1} of 60 to 28%, alongside a significant lack of MgO neutralisation. The ratio of phase 3 to phase 5 is notably increased to 1:1.6 and 1:1 at PLRs of 1.4 and 1.6 g mL^{-1} respectively, compared to 1:5 and 1:4 for MOC at the same PLR. The crystallinity of cements also decreased with increasing PLR, with lower crystallinity for all MOC-Ag samples than MOC, with the most notable difference at PLR 1.6 g mL^{-1} of 64 and 78%, respectively (Figure 2.3a).

In order to explore the mechanisms driving compositional variations, real time XRD was performed over the course of six hours for MOC and MOC-Ag at a PLR of 1.4 g mL^{-1}. Calculating ξ (Equation 2.6) shows that crystallisation of the hydrate phase 5 occurs after an initial lag of 60 minutes (Figure 2.3d). However, for MOC-Ag, conversion of Ag_3PO_4 to AgCl begins immediately upon formulation mixing. This reaction approaches completion after an hour, which is prior to the starting time for crystallisation of hydrate phases in MOC. Notably, no measurable formation of hydrate phases was observed during the 6

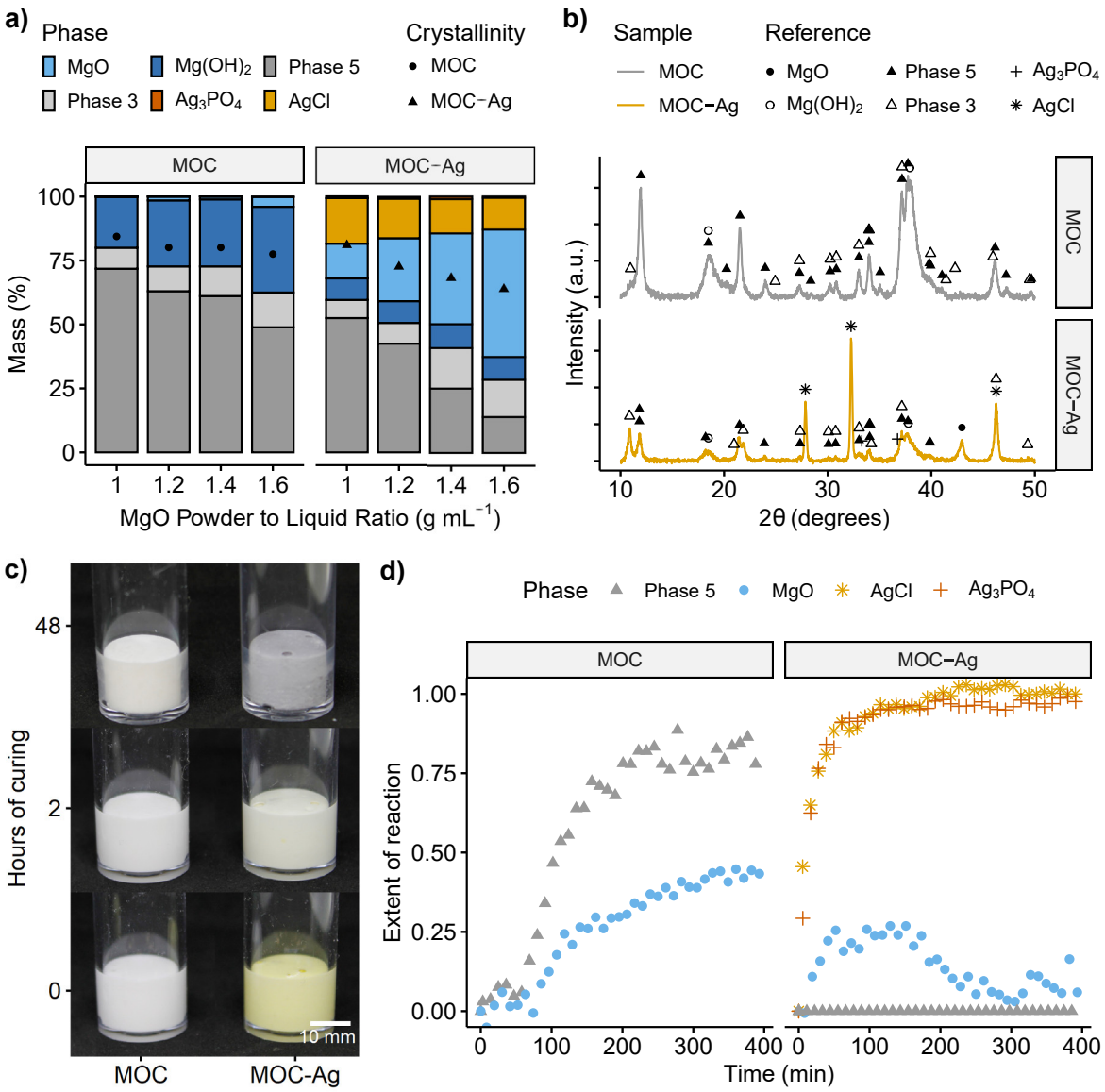


Figure 2.3: Effect of formulation chemistry upon cement phases formed; a) composition of cements based on the semi-quantitative method provided by Bruker Diffrac.Eva software. Reported crystallinity by mass according to software also shown; b) representative XRD patterns for 1.4 MgO powder to liquid ratios, with indexing of cement phases; c) colour change of 1.4 MgO to liquid ratio formulations after mixing, 2 hours of curing, and 48 hours exposure to light; d) real time quantification of extent of reaction.

hours for the MOC-Ag formulation.

2.3.2 Physical characterisation of cements

The initial and final setting time of MOC formulations decreased linearly with increasing MgO content (R^2 = 0.9 and 0.8), with the interval between initial and final setting remaining constant (Figure 2.4a). The addition of Ag_3PO_4 significantly retards the onset of setting, with initial setting times greater than double those for unmodified MOC at all PLR.

The handling properties of the formulations showed an increase in shape retention as PLR increases, with both MOC and MOC-Ag cements at PLR 1.6 g mL^{-1} exhibiting no flow when inverted (Figure 2.4b). Furthermore, at the highest MgO content investigated, pastes were sufficiently stiff as to be inextrudable, requiring manual loading into moulds with a spatula. Attempts to extrude at PLR 1.6 g mL^{-1} showed a low fraction of mass extruded (>70%) (Figure 2.4c), and sufficiently large forces (>40 N) that syringes failed prior to completion of injectability testing (Figure 2.4d). In contrast, formulations with a PLR of 1.4 g mL^{-1} or below exhibited a high degree of injectability with >90% of mass extruded (Figure 2.4c) and <14 N required to extrude through a 1 mL syringe (Figure 2.4d). The washout sensitivity of 1.4 g mL^{-1} PLR cements is increased by the addition of Ag_3PO_4, with a greater volume of debris visible upon immersion and after a further 48 h under water (Figure 2.5).

Within the MOC and MOC-Ag type cement formulations, no statistically significant variations in compressive strength are observed between MgO ratios (Figure 2.6b), with an average maximum of 30 to 21 MPa, respectively. MOC-Ag cements do show reduced strength compared to the unmodified MOC, with the 1.4 g mL^{-1} PLR MOC formulation exhibiting significantly ($p < 0.05$) higher strength than the MOC-Ag formulations from PLR 1 to 1.4 g mL^{-1}. Calculation of the Young's modulus of MOC and MOC-Ag showed a significant reduction in stiffness for silver doped cements (Figure 2.6c). Despite the reduced strength of MOC-Ag, a higher strain energy density at failure is observed (Fig-

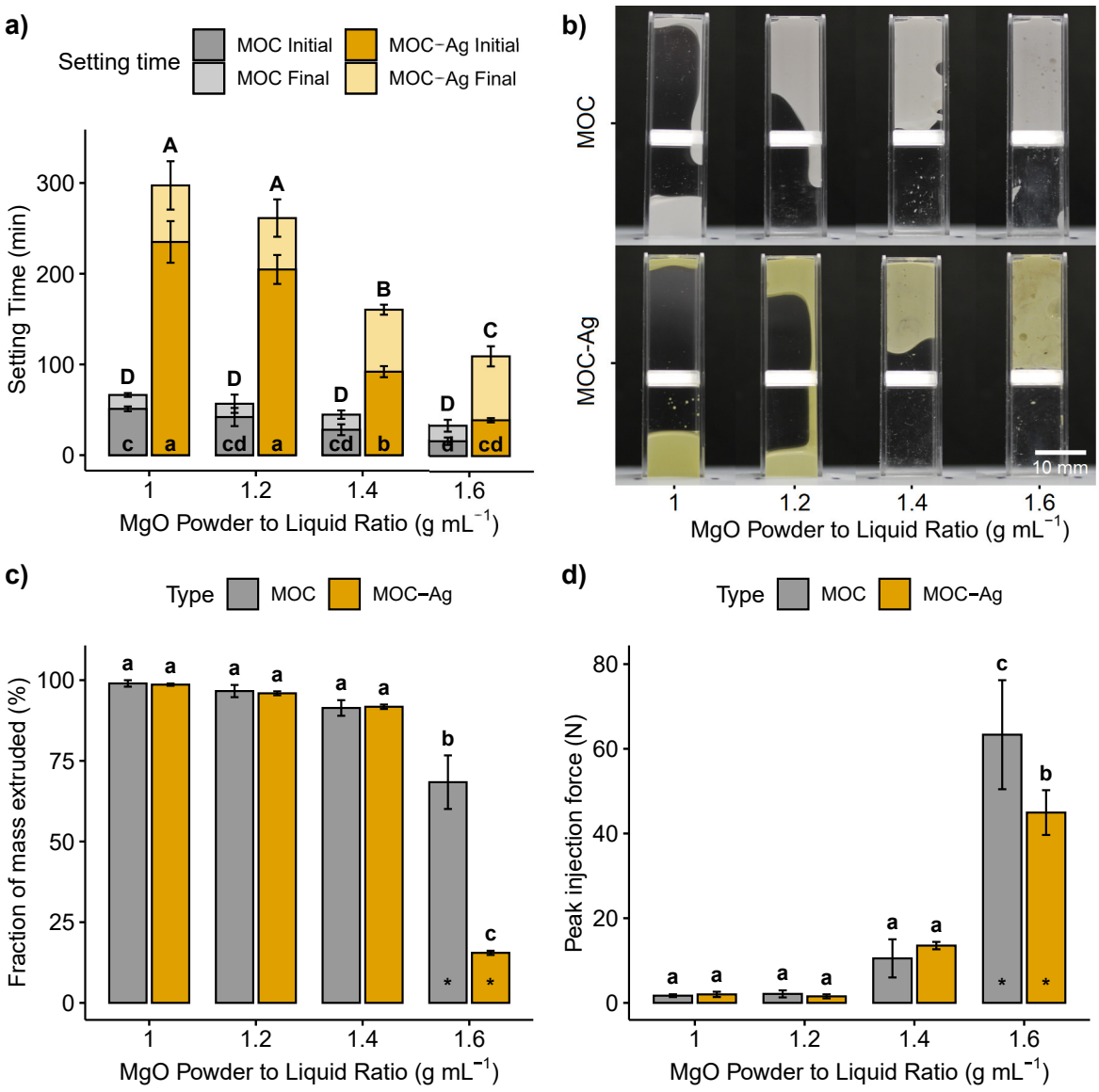


Figure 2.4: Setting time (a) according to Gilmore needles method, with statistical comparisons made separately within initial and final setting time groups; visualisation of formulation flow (b) after 1 minute inversion in 1 mL cuvette; fraction of cement mass extruded (c) and peak extrusion force (d) from 1 mL syringes, where formulations marked with * exhibited syringe buckling prior to complete extrusion. Means that do not share letters are significantly different from one another.

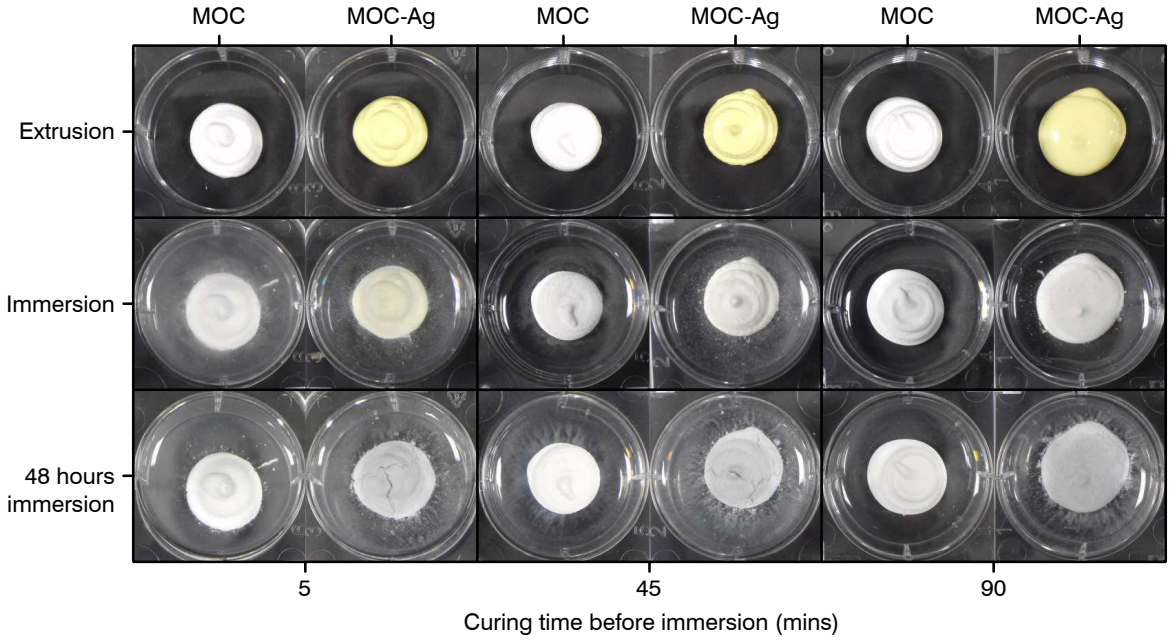


Figure 2.5: Washout behaviour of 1.4 g mL^{-1} formulations when immersed in water. Samples of MOC and MOC-Ag are shown after extrusion; immediately after immersion following 5, 45, or 90 minutes curing; and after 48 h of immersion.

ure 2.6d). As PLR was not a significant factor in determining UCS (Table 2.3), Weibull analysis of the MOC and MOC-Ag groups was performed (Figure 2.6c). The results of Weibull analysis confirm the reduced mechanical performance of MOC-Ag, with slightly lower characteristic strength σ_θ, however with a higher Weibull modulus of 4.21 compared to 3.68, indicating a narrower distribution of strengths (Figure 2.6e). Note that these results exclude the extreme outlier specimen for MOC-Ag at PLR of 1.2 g mL^{-1}. Assessment of relative density by He pycnometry and dimensional measurements found minor variations, however all MOC and MOC-Ag cements exhibited relative densities over 80% (Figure 2.6f).

As a significant difference in compressive strength is seen at the 1.4 g mL^{-1} ratio between MOC and MOC-Ag, these formulations were investigated by μXCT. Assessing the pore distribution, the largest defects for both MOC and MOC-Ag have radii of approximately 400 μm (Figure 2.7a and b). A volume-weighted average particle size of 117 to 140 μm for MOC and MOC-Ag was used to calculate fracture toughness using equation 2.10, resulting in values of 0.40 and 0.23 MPa m$^{-1/2}$, respectively (Table 2.2).

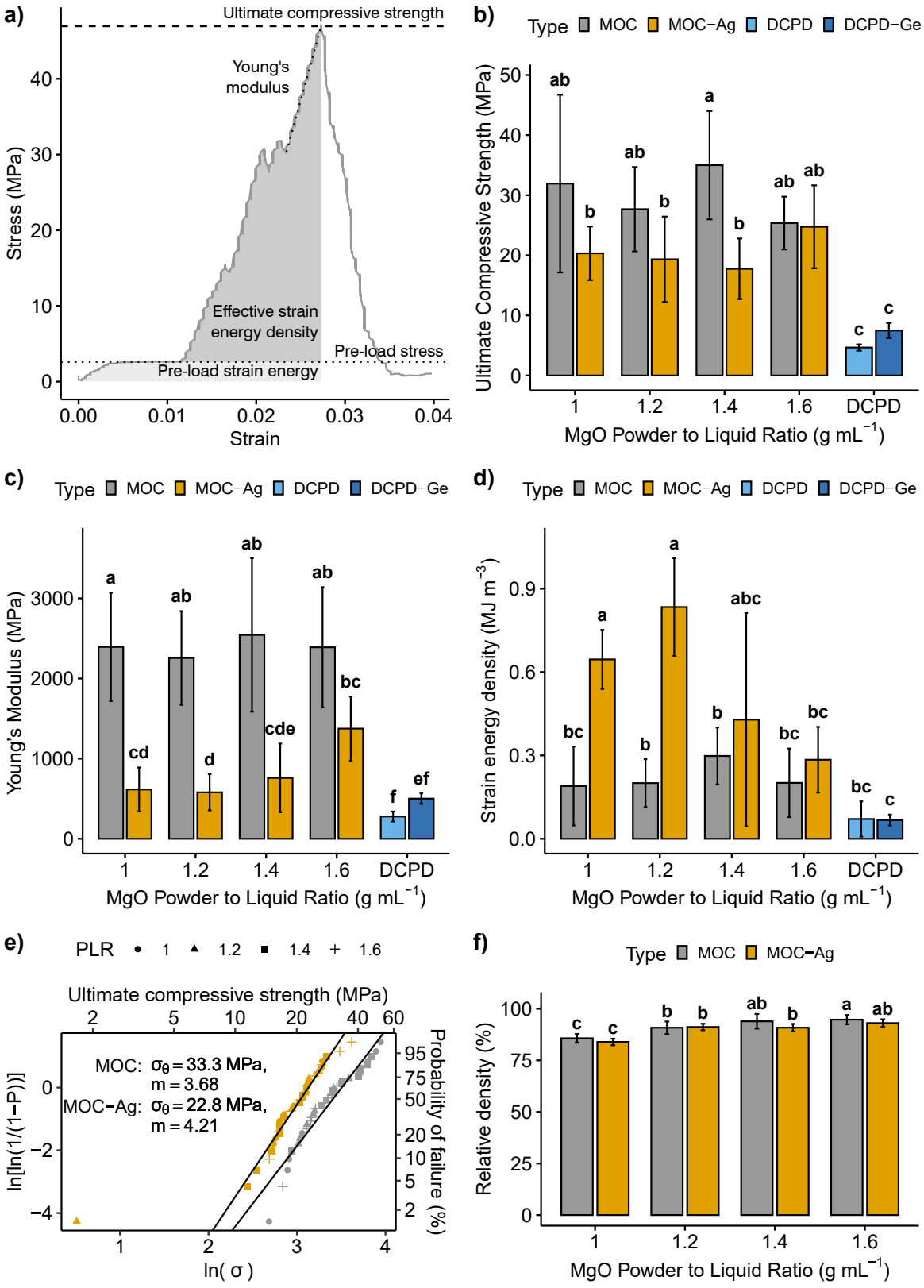


Figure 2.6: Mechanical properties of cements cured for 48 hours at room temperature; (a) Typical compressive stress profile with key parameters labelled; (b) Ultimate compressive strength of cements; (c) Young's moduli; (d) strain energy density at failure; (e) Weibull plots for MOC and MOC-Ag, with best fit lines excluding outlier; (f) relative density of cements.

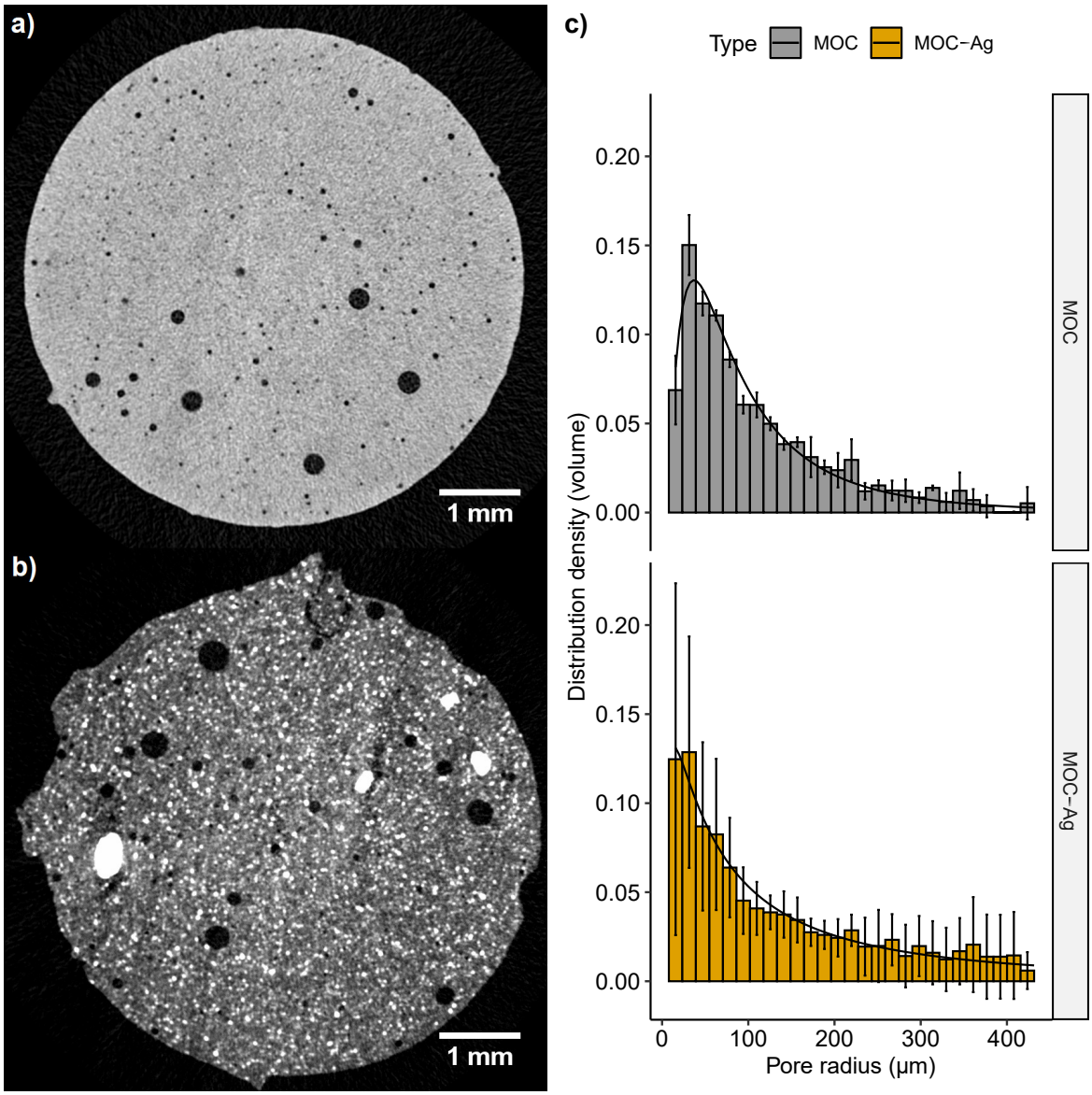


Figure 2.7: Example 2D XCT cross section of (a) MOC and (b) MOC-Ag at $1.4\,\mathrm{g\,mL^{-1}}$ PLR; (c) Volume distribution of pore radii in MOC at $1.4\,\mathrm{g\,mL^{-1}}$ PLR according to µXCT analysis, with log-normal fit.

Table 2.2: Estimated values of fracture toughness (K_1) for samples based on volume weighted mean pore radius.

Formulation	MOC	MOC-Ag
Powder to liquid ratio ($g\,mL^{-1}$)	1.4	1.4
Ultimate compressive strength (MPa)	35 ± 9	18 ± 5
Apparent density by pycnometry (%)	94 ± 4	90 ± 2
Volume weighted mean pore radius (µm)	117	140
Volume mean fracture toughness ($MPa\,m^{-1/2}$)	0.40 ± 0.10	0.23 ± 0.07

The volume of pores measurable by µXCT provides an apparent density of 98.1 ± 0.1 and $98.8 \pm 0.4\%$ for MOC and MOC-Ag respectively. Comparing this to porosity calculated from relative density (Figure 2.6f), this indicates that 4.1 and 8.8% of cement volume consists of micropores below the resolution of µXCT scans performed (8 µm pixel size).

Investigating the structure of defects at fracture surfaces with SEM revealed spherical pores present in all samples (Figure 2.8). The presence of cracks perpendicular to the surface of pores is characteristic of their involvement in crack nucleation (Figure 2.8a/b). Additional pores of approximately 10 µm diameter were observed in MOC-Ag samples surrounded by silver rich phases, particularly AgCl (Figure 2.8e). This second population of pores do not show cracks perpendicular to their surface, instead fault lines tended to divert along the interface between the silver phases and the magnesium hydrate matrix (Figure 2.8c/d). These silver rich regions are of a similar size to the agglomerations of particles observed in the Ag_3PO_4 powder (Figure 2.8f), suggesting that these clusters do not entirely dissociate during mixing of the formulations. Assessment of the Ag_3PO_4 feedstock with He pycnometry indicates a density of 99.3%, confirming pore formation occurs within the formulation itself, and is not due to inherent porosity with the smaller sub-particles.

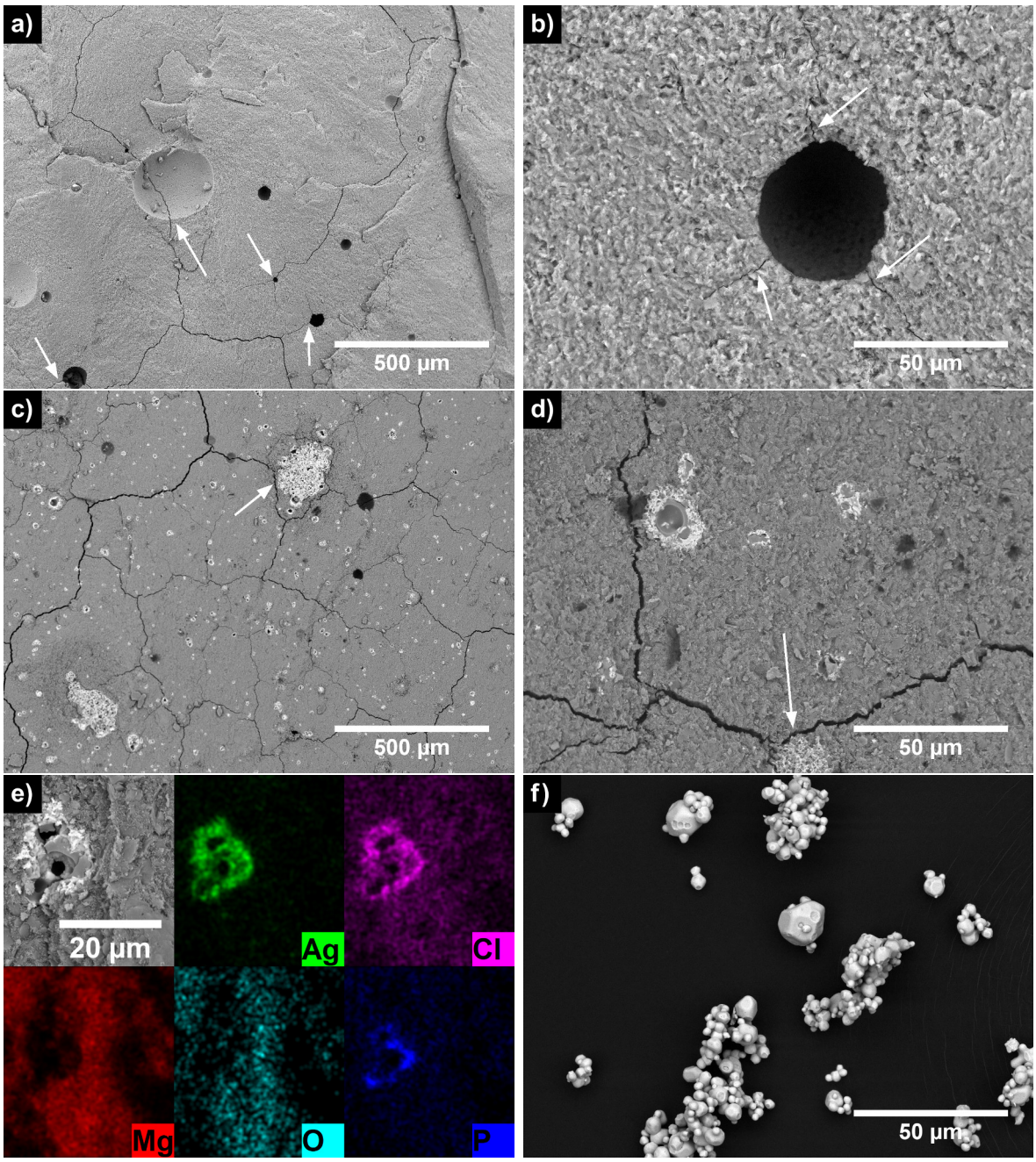


Figure 2.8: Scanning electron micrographs of pores present in a) and b) MOC, with arrows indicating radial cracks from pores; c) and d) MOC-Ag cements, with arrows indicating crack diversion at the interface of Ag rich regions; e) EDS mapping of elements present around Ag rich regions in Ag_3PO_4 cement; f) SEM micrograph of Ag_3PO_4 reagent powder.

2.3.3 Cytotoxicity assessment of cements

After 24 h, MOC showed a statistically significant reduction in the fraction of live cells compared to both DCPD cements and empty control transwell inserts, but with 96% of cells remaining live. Promisingly, no significant difference in viability was observed after seven days of culture, with over 98% of cells alive in all groups. Compared with cell only control samples, Alamar blue assays indicated no significant difference in metabolic activity after exposure to MOC, MOC-Ag or DCPD positive control cements.

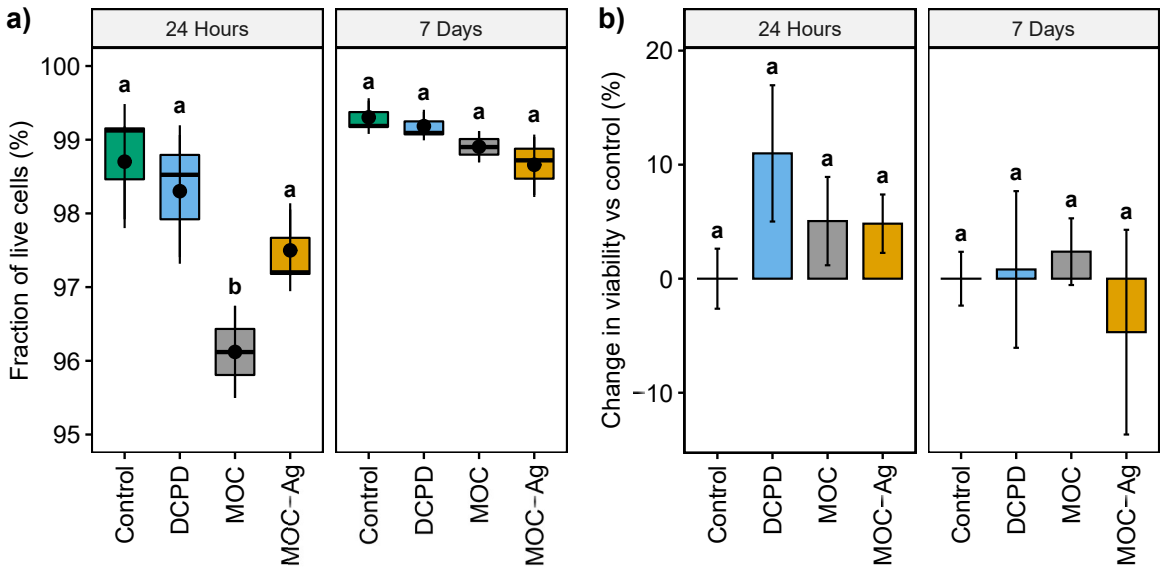


Figure 2.9: Cytotoxicity and viability assessment of MC3T3 cell cultures when exposed to cements for 24 h and 7 d; a) fraction of cells alive according to fluorescence microscopy; b) viability of cultures compared to control according to Alamar Blue assay.

2.3.4 Antimicrobial efficacy of cements

Both the MOC and MOC-Ag samples caused zones of inhibition in the agar diffusion assay after 24 hours culture for both *S. aureus* and *P. aeruginosa*, indicating an antimicrobial effect (Figure 2.10a). Efficacy was observed when the cements were cured in-situ, and applied as a crushed powder after setting. In contrast, DCPD and CS cements showed no inhibition of growth in the cured state. Notably, zone size is increased when curing in-situ versus cured cements for all formulations except the negative CS control. Efficacy is

seen for DCPD when cured in-situ, possibly due to the acidity of the freshly mixed paste [186], and the susceptibility of *P. aeruginosa* to organic acids [187], such as the citric acid present in the DCPD. These initial results provide strong evidence for an inherent antimicrobial efficacy of MOC cements, with additional efficacy against *P. aeruginosa* from the inclusion of Ag_3PO_4.

The retention of efficacy beyond the initial curing period is further demonstrated when cured cements are in direct contact with planktonic bacterial cultures, with efficacy approaching the minimum detectable limit (MDL) of surviving bacteria for the test performed (Figure 2.10b). This high efficacy is retained for MOC-Ag after 72 hours aging at cement to broth ratio of $0.5\,\mathrm{g\,mL^{-1}}$, though the efficacy of MOC is slightly reduced with a 6.8log reduction in viable $\mathrm{CFU\,mL^{-1}}$ versus 8.7log for aged MOC-Ag.

Cement extracts from this 72-hour aging were also demonstrated to be highly bactericidal, leading to a total reduction in viable *S. aureus* CFU after just 3 hours for MOC-Ag (Figure 2.10c). Again, in this case, the efficacy of MOC-Ag is higher than that of MOC with complete eradication of viable CFU after 3 hours, though both show strong antimicrobial response after 24 hours culture of 8.4log and 7.6log reduction compared to control cultures. Broth extracts from a release study at a low cement to broth ratio of $0.14\,\mathrm{g\,mL^{-1}}$ were also investigated, with day 1 samples for both MOC and MOC-Ag demonstrating bactericidal properties (Figure 2.10d). At day 2, the efficacy of the unmodified formulation is reduced with MOC only showing bacteriostatic behaviour, with no increase in viable $\mathrm{CFU\,mL^{-1}}$. MOC-Ag maintained strong bactericidal behaviour over both day 1 and 2.

2.3.5 Release characteristics

Over the course of 14 days, the pH of LB broth cement extracts were elevated for both the MOC and MOC-Ag formulations (Figure 2.11a), remaining at approximately pH 8.50 from day 2 onwards. This strong increase in pH compared to the starting value of below 7.0 may link to the lack of buffering capacity present in LB. When immersed in PBS, the

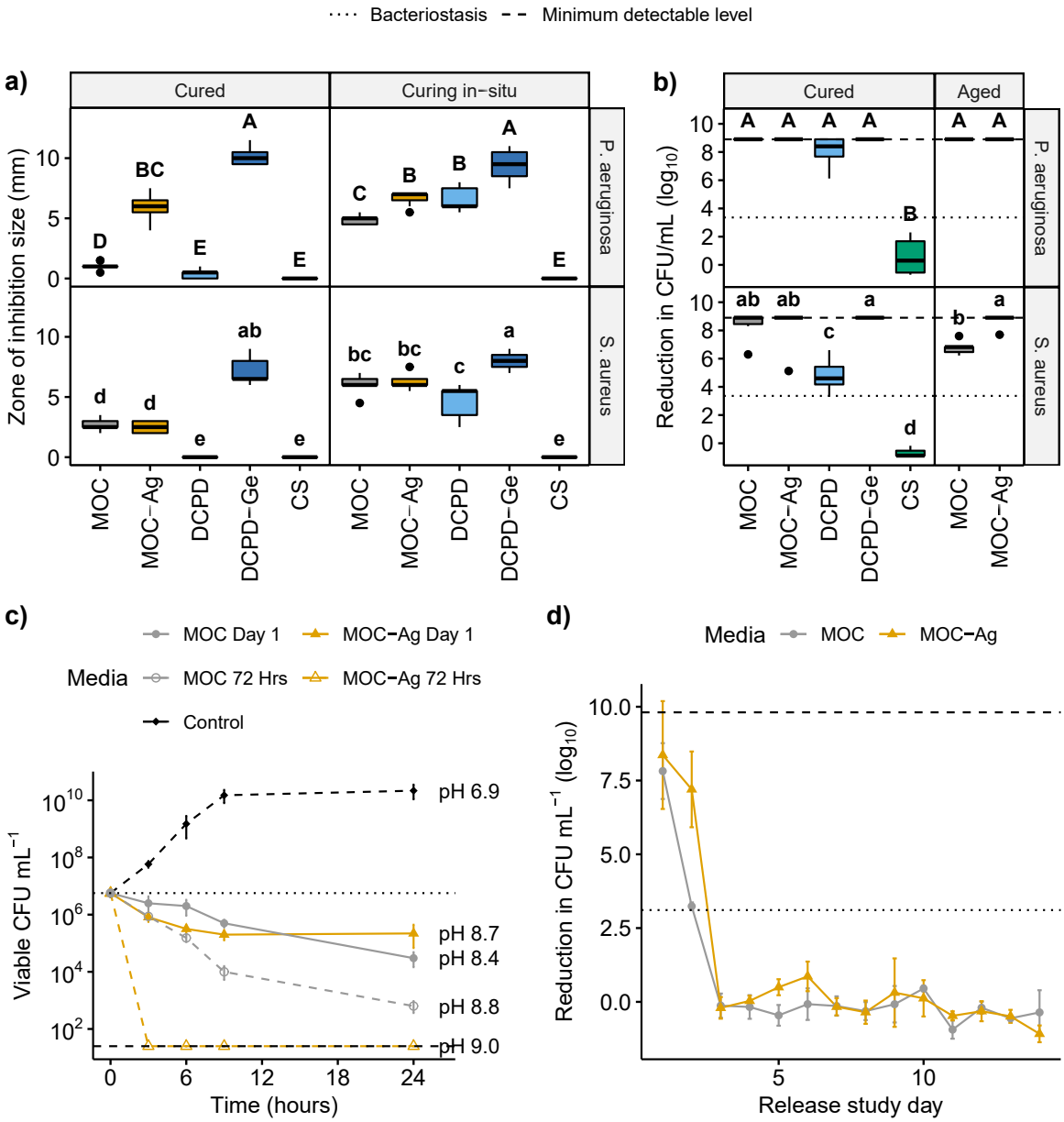


Figure 2.10: Microbial assessment of cement formulations with *S. aureus* and *P. aeruginosa*; a) Zones of inhibition for both crushed and curing cements; b) response of LB broth cultures to incubation with cements, including MOC and MOC-Ag aged for 72 hours; c) 24 hour *S. aureus* growth curves in extracts from 72 hours aging at cement to broth ratio of $0.5\,\mathrm{g\,mL^{-1}}$ cement, and from 24 hours aging at a ratio of $0.14\,\mathrm{g\,mL^{-1}}$; d) 24 hour survival of *S. aureus* cultures in extracts from $0.14\,\mathrm{g\,mL^{-1}}$ cement to broth ratio release study. For planktonic cultures, dotted and dashed lines represent bacteriostasis and the minimum detectable level of viable bacteria, respectively.

MOC formulation still shows an increase to pH 8.5 at day 2 and a positive correlation over the course of the 14 days. In contrast, the pH of the MOC-Ag PBS eluent only varied between 7.09 to 7.26 over the two week period. Visual inspection of the cements showed that the MOC cements in PBS had physically degraded, with fracture across the plane of the cylindrical samples in several cases and a greater amount of fine particulate matter in suspension. MOC-Ag cements showed variable discolouration, with cements in PBS showing a grey colouration similar to that seen after extended exposure to light. Those stored under LB media darkened further, with a blackened surface.

A low level of ROS generation is observed in MOC-Ag eluant by the PMAC chemiluminescence assay, with an average of 36 and 51 count s^{-1} for PBS and LB respectively (Figure 2.11b). No excess ROS generation above the 12 count s-1 background is observed in MOC LB media, or for the first eight days in PBS. From day 9 to 14, a rise to 372 ± 207 count s^{-1} is present. Examining the release characteristics of Mg (Figure 2.11c), the MOC shows a burst-release behaviour, with 82% and 54% of all magnesium released in the first 24 hour elution period for PBS and LB media, respectively. This decreases from 4000 ppm to a consistent release of 25 (PBS) and 250 ppm (LB) daily after the second day. For the MOC-Ag, a more sustained release is observed over the 14 day period, with only 27% and 18% of Mg released during day 1. Initial concentrations of 1100 and 750 ppm Mg for PBS and LB fall to the same baseline level as the MOC after 8 and 14 days, respectively. This results in the concentration of Mg in elution media overtaking the MOC after the second day. Ag release is also sustained, and shows no burst-release characteristics, with 6% of Ag released in the first day for LB media (Figure 2.11d). An order of magnitude more Ag is released in LB media, with an average of 5.9 ppm over the 14 days compared to only background levels of 0.2 ppm in PBS, as seen for the MOC formulations.

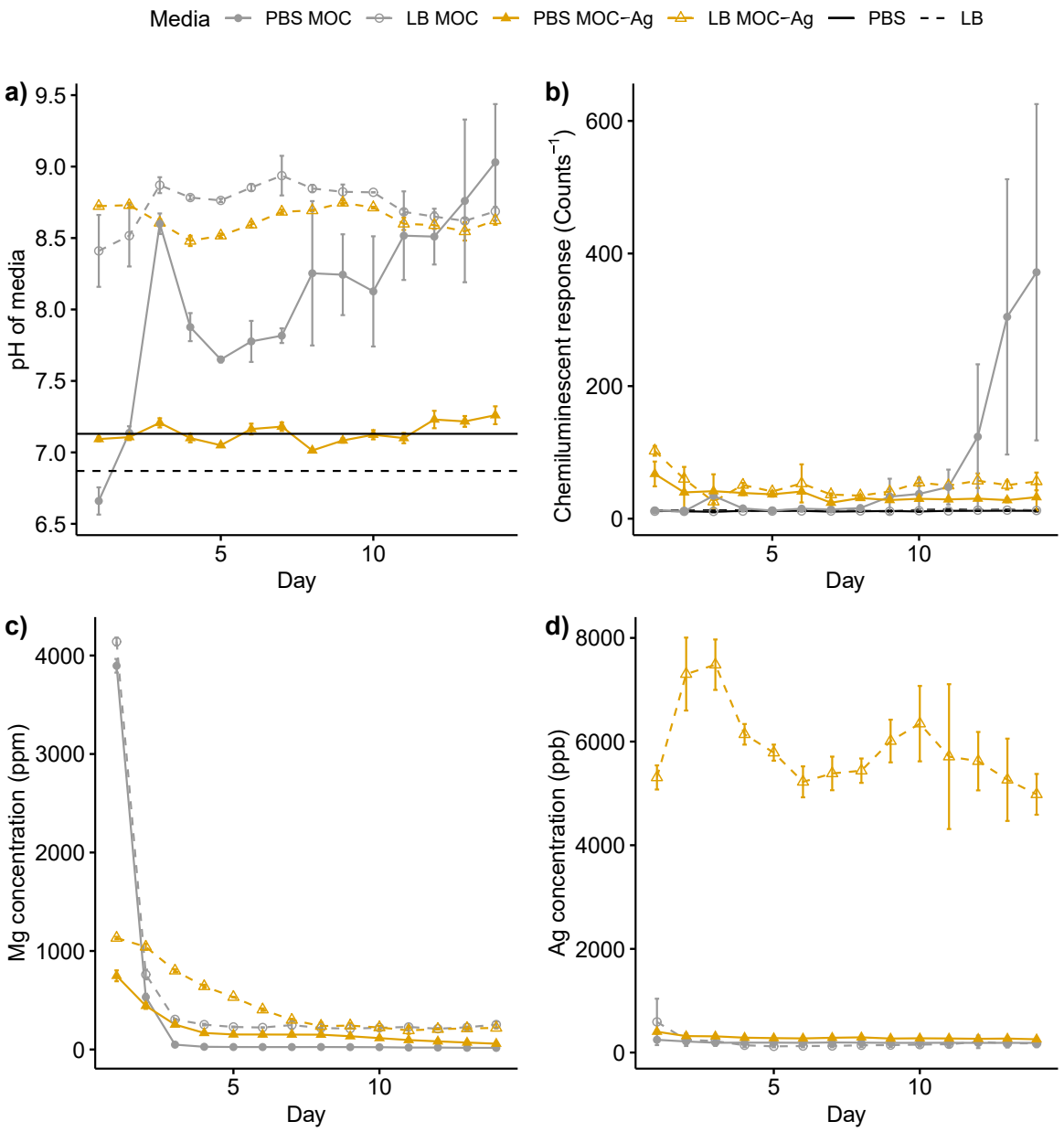


Figure 2.11: Characteristics of release study media; a) pH, b) reactive oxygen species chemiluminescence assay, and background corrected concentrations of c) Mg, and d) Ag. The pH and chemiluminescence of control LB and PBS media are shown. For ICP data, LB and PBS blanks are substracted from sample measurements as part of the calibration process and as such are not displayed.

2.3.6 Statistical analyses

In order to better assess the influence of PLR and the formulation type upon performance, results were subject to 2-way ANOVA. The addition of Ag_3PO_4 was found to influence all characteristics assessed except for the peak injection force during extrusion. PLR significantly altered responses except for the UCS.

Table 2.3: Statistical parameters for 2-way ANOVA of data, with the formulation type (MOC/MOC-Ag), PLR, and the interaction of these two variables considered.

	Type		PLR		Type*PLR	
Variable	F-value	P-value	F-value	P-value	F-value	P-value
Initial setting time	575	0.000	141	0.000	73.1	0.000
Final setting time	811	0.000	84.6	0.000	43.8	0.000
Mass extruded	107	0.000	432.06	0.000	103	0.000
Injection force	3.40	0.084	137.89	0.000	5.30	0.010
UCS	25.1	0.000	0.48	0.969	3.39	0.023
Relative density	6.47	0.022	34.9	0.000	1.88	0.173

2.3.7 Two phase implant model

Zones of inhibition were observed around two-phase implant models containing MOC, with no inhibitive effect for Ti−6Al−4V cylinders alone (Figure 2.12a). For models with highly reduced orifice diameter of 1 mm, a distinct radial inhibition zone was visible around each pore of 1 mm, with zones insufficiently large to meet.

Elution of BTB showed a clear dependency on orifice area and the resulting exposure of MOC to the immersion media, with the same mass of indicator eluted per total pore area (Figure 2.12b).

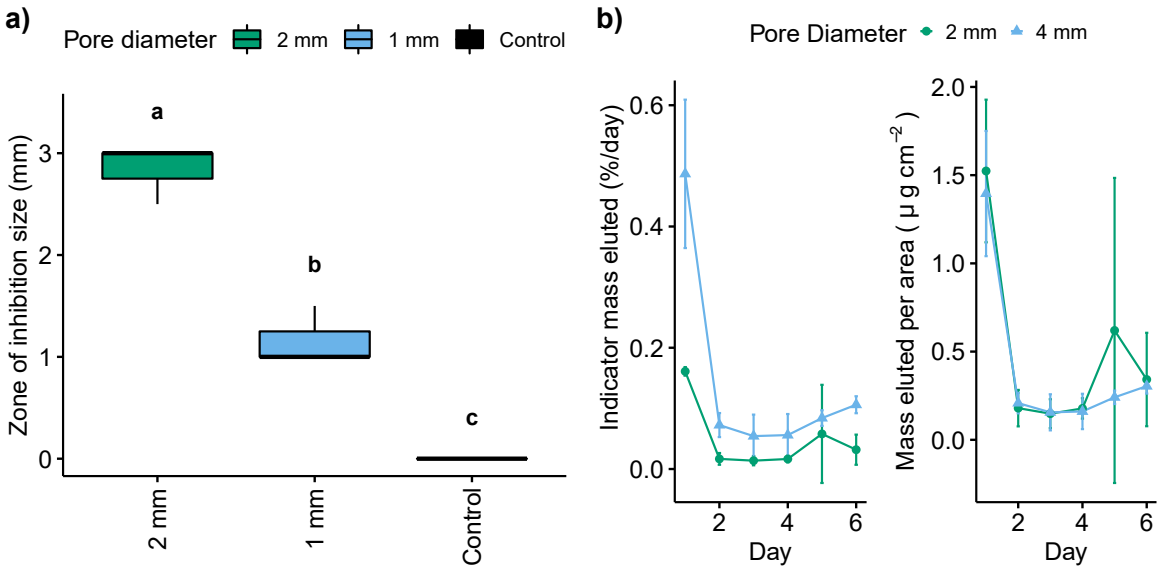


Figure 2.12: a) Zone of inhibition sizes measured around MOC-Ti two phase implants; b) concentration of bromothymol blue eluted from polymer two-phase implants.

2.4 Discussion

There remains a continuing need to develop antimicrobial biomaterials for the prevention of infection. In particular, developing approaches that utilise a broader range of antimicrobials, such as inorganic species, may help to reduce the burden of antibiotic usage [70, 146]. Doping of existing biomaterials to generate antimicrobial efficacy has been heavily investigated, with silver showing promise in a range of hard and soft biomaterials [55]. Less attention has been paid to the prospect of generating inherently antimicrobial hard materials, with focus instead on antimicrobial polymers [188]. The combination of these two approaches - doping of an inherently antimicrobial matrix with a known antimicrobial, such as Ag - may improve efficacy while also providing the possibility to control activity via both mechanisms. It is crucial, however, to consider how addition of such a dopant will alter the physical properties of the MOC scaffold.

The behaviour of MOC formulations can be understood within the existing framework posited by Dehua et al [156], with addition of sufficient MgO resulting in neutralisation of the excess, as demonstrated by the greater presence of $Mg(OH)_2$ as PLR increases (Figure 2.3a). However, the addition of Ag_3PO_4 has a deleterious effect on curing behaviour that is more complex than excess MgO. The formation of AgCl at an early stage, prior to the formation of phase 5 in undoped MOC at 60 min (Figure 2.3d), may play a disruptive role at all three stages within the curing process. First, the exchange of Cl^- for PO_4^{3-} will deplete free H^+ in solution, due to the significantly higher pK_a of orthophosphoric acid (2.16, 7.21, 12.32) [189] in comparison to HCl (-5.9) [190]. This limits the neutralisation of MgO, a step required for curing to begin. Despite an initial consumption of MgO in the MOC-Ag formulation, the mass of MgO present returns to the original level, signified by the decrease in ξ from a peak of 0.25 after 100 minutes of curing to 0 at 300 minutes (Figure 2.3d). This suggests that MgO initially neutralised and dissolved may reprecipitate, possibly due to the pH change as phosphate ions deprotonate the formulation. In turn this may limit the conversion of excess MgO to $Mg(OH)_2$. If the outer surface of MgO particles is not neutralised but is hydrated, MgO will not be solubilised, limiting the surface area

accessible for further reaction as $Mg(OH)_2$ does not react to form the hydrated phases. This may explain both the lower total amount of hydrated phases formed in MOC-Ag, ranging from 28 to 60 % compared to 63 to 80 % for MOC (Figure 2.4b), and the greater ratio of phase 3 to phase 5 present, which rises to 1:1 due to the lower amount of neutralised MgO per mole required.

Second, the hydrolysing-bridging process of mononuclear Mg species requires both solvated Mg^{2+} ions in parallel with the decreased pH caused by neutralisation of MgO. Alongside deprotonation of the formulation, PO_4^{3-} ions may cause precipitation of Mg phosphates, depleting Mg in solution. No additional such phases are observed by XRD however.

Finally, as Cl^- is required for the crystallisation of the hydrogel phases, a lower fraction of phase 3 and phase 5 will crystallise from the polynuclear complexes. This lack of crystallisation is evidenced by the greater remnant amorphous material observed for MOC-Ag, with lower crystallinity across all tested PLR (1 to 1.6 $g\,mL^{-1}$) (Figure 2.3a). Such a mechanism would, however, run counter to the greater fraction of phase 3 present in the MOC-Ag, which contains a larger number of chloride atoms per mole of MgO.

As a result of these changes in chemistry, the MOC-Ag formulations take from 3 to 5 times longer to set (Figure 2.4a). The significantly slower curing rate of MOC-Ag correlates with real-time XRD results that showed no measurable formation of phases 3 or 5 within the first six hours of curing (Figure 2.4a). In comparison, the final setting of the 1.4 $g\,mL^{-1}$ PLR MOC occurs after 45 min (Figure 2.4a), prior to the onset of phase 5 formation after 60 min (Figure 2.3d), confirming that the set cement is the amorphous hydrogel phase and not the crystallised hydrate phases. Reducing the setting time would be crucial to developing a practical formulation in future for conventional clinical use. Note however that for delivery of cements from additively manufactured implants, pre setting of cements within the implant would be feasible prior to commencement of surgery, reducing the need for this setting acceleration. Given that setting occurs prior to crystallisation for the MOC formulation, it is the initial mechanism of H^+ depletion

that should be tackled first. Though the depletion of free hydrogen may be resolved by use of an alternative silver dopant instead of a phosphate, the consumption of chloride ions by AgCl is likely to occur for the majority of silver compounds given the very high affinity of Ag^+ for Cl^- [191]. Use of AgCl as a dopant may be the most viable alternative, though the higher photosensitivity of the compound may prove a challenge to creating a shelf-stable formulation. Acidification of the $MgCl_2$ brine to increase the concentration of H^+ may also assist in this.

In comparison to the phase diagram of the MgO-$MgCl_2$-H_2O system, a lower mass of remnant MgO than would be expected at equilibrium, and excess $Mg(OH)_2$ and Phase 3, are observed by XRD (Table 2.4). The lack of MgO and increased $Mg(OH)_2$ can be most easily explained through the presence of excess moisture, for example from the MgO and $MgCl_2 \cdot 6\,H_2O$ feedstock. Both materials are hygroscopic under ambient conditions. XRD of the MgO powder shows a clear presence of $Mg(OH)_2$, calculated as 20% by mass. No useful information can be obtained on the moisture content of $MgCl_2$ via XRD as the higher co-ordination hydrate phases $MgCl_2 \cdot 8\,H_2O$ and $MgCl_2 \cdot 12\,H_2O$ are both unstable at room temperature [192], and so any adsorbed water will not induce a clear crystallographic transformation. A portion of the absent MgO may also be due to the amorphous fraction observed, ranging from 16 to 23%. The justification for formation of phase 3 is more complex. Stoichiometrically, a larger ratio of H_2O:MgO and $MgCl_2$:MgO is required for formation of phase 3 than phase 5. Provided excess moisture is introduced via the MgO feedstock, thereby reducing the actual mass of MgO delivered, the effective $MgCl_2$:MgO ratio will be increased, driving formation of phase 3 (Figure 2.1). If, however, excess moisture were introduced via $MgCl_2 \cdot 6\,H_2O$ feedstock, the driving force for formation of phase 3 would instead be reduced.

Alongside setting, the ability to deliver any potential biomaterial is key to consider. Injectable formulations are increasingly favoured to minimise invasiveness of any clinical intervention [193]. Though direct correlation between extrusion force and real-world use is challenging, recent studies have shown that extrusion forces in excess of 38 N are imprac-

Table 2.4: Comparison of the phases measured in unmodified MOC by XRD, with anticipated composition from stoichiometry.

	Stoichiometric composition			Measured composition			
PLR	5-Phase	$Mg(OH)_2$	MgO	5-Phase	3-Phase	$Mg(OH)_2$	MgO
1	85.1	8.3	6.5	71.8	8.2	19.9	0.1
1.2	78.1	7.7	14.2	63.0	9.7	25.8	1.5
1.4	72.2	7.1	20.7	61.1	11.6	26.2	1.1
1.6	67.1	6.6	26.3	48.9	13.6	33.5	3.9

tical for use in 5 mL syringes [194], and whilst use of a smaller 1 mL syringe cross-section may reduce the force requirements, there is greater risk of syringe failure. Considering these results, the 1.4 g mL^{-1} mixes of MOC and MOC-Ag showed an ideal combination of shape retention (Figure 2.4b) and shorter setting times in comparison to other studied formulations of 45 and 160 min (Figure 2.4a), whilst retaining extrudability with peak extrusion forces of 11 and 14 N (Figure 2.4d).

It is also key to balance these handling properties with appropriate mechanical behaviour. As cements crack in a brittle fashion under compression, structural defects such as pores play a crucial role in determining UCS [182]. In all cases, MOC and MOC-Ag cements exhibited a larger UCS than the DCPD and DCPD-Ge cements used in this study and values reported in literature for off-the-shelf reagents (8 to 20 MPa) [147, 195] though strengths of 100 MPa have been achieved with more complex processing of calcium phosphates [196]. The relatively low porosity of both MOC formulations (<17% MOC and <15% MOC-Ag) (Figure 2.6b) compared with DCPD (typical range 40 to 60 %) [195] likely effects the significantly higher average strength (18 to 35 MPa). Though a significant difference between individual formulations is only observed for MOC-Ag at a PLR of 1.4 g mL^{-1} (Figure 2.6a), the formulation type (MOC/MOC-Ag) is a significant factor in 2-way ANOVA (Table 2.3). The stiffness of MOC (2.3 to 2.5 GPa) is approximately double that of MOC-Ag (0.6 to 1.4 GPa), and within the typical reported range of Ca phosphate cements (0.4 to 0.8 GPa) [197]. More remarkable is the increased strain energy

density of MOC-Ag at failure, particularly at low PLR. Investigating the stress against strain curves, small reductions in stress can be observed whilst strain continues to increase (Figure 2.6a). These fluctuations can be attributed to small subcritical fractures within samples, followed by densification as the applied strain increases. These small deviations increase the effective strain energy density and the strain to failure, and are more frequent within the low PLR MOC-Ag formulations.

Investigating the Weibull distribution of MOC and MOC-Ag formulations independent of PLR, MOC exhibits a greater characteristic strength of 33.3 MPa versus 22.8 MPa. The Weibull moduli of both materials (3.7 MOC, 4.2 MOC-Ag) are comparable to calcium phosphate cements [198]. Mechanical reliability remains a challenge for ceramic bone cements [199], but it is positive that MOC is comparable to established cements. The specimens examined in this study also exhibit high strain to failure, resulting in large strain energy density at failure (Figure 2.6d). For understanding the underlying mechanism for differences in mechanical behaviour, assessing both the chemical and physical differences between MOC and MOC-Ag, with a focus on the $1.4\,\mathrm{g\,mL^{-1}}$ PLR, is informative.

Considering the physical properties, the relative density of over 90% (Figure 2.6b) and similarity of pore distributions observed for both MOC and MOC-Ag formulations at PLR $1.4\,\mathrm{g\,mL^{-1}}$, are unlikely to be dominant features in reducing strength. Two-thirds of pores measured by XCT smaller than 120 µm (Figure 2.7c) in both cases, with similar mean pore sizes of 117 and 140 µm. Estimating toughness further indicates that the reduced strength is not dominated by macroporosity. Using the volume weighted mean pore size derived from log-normal best fit distributions results in toughness of 0.40 and $0.23\,\mathrm{MPa\,m^{-1/2}}$ for MOC and MOC-Ag (Table 2.2) similar to other cement materials, which lie in a range of 0.2 to $1.2\,\mathrm{MPa\,m^{-1/2}}$ [200–202]. More accurate determination of the local fracture toughness may be achieved by indentation testing, but may be difficult to extrapolate to the bulk performance of material where microstructures are inhomogeneous [203].

Inspection of microstructure by SEM shows that the addition of Ag_3PO_4 has not

altered the morphology of larger pores present in MOC, however as observed in μXCT (Figure 2.7b), silver is not uniformly distributed throughout the cement matrix (Figure 2.8c). Small pores are observed at the centre of these Ag rich regions. The formation of these fine pores will not be caused directly by the reaction of Ag_3PO_4 to form AgCl as, per mole of Ag, silver chloride exhibits a lower density. One hypothesis is that the cluster-like particles (Figure 2.8f) trap air or water when mixed. This entrapment results in a pore when the reaction to form AgCl occurs, during which time the silver phase precipitates at the boundaries of this pore, leaving a phosphate rich core. These agglomerations of silver rich phase significantly weaken the MOC-Ag formulation at PLR $1.4\,g\,mL^{-1}$. However, cracks are not seen to nucleate within this second phase, instead appearing to propagate along the interface of the phase and cement matrix (Figure 2.8c and d). Given that crack deflection typically increases the toughness of materials [204], the slightly reduced toughness of the MOC-Ag could suggest a weak interface with the magnesium oxychloride, or an overall reduction in strength of the matrix. The significant effect of Ag on phase composition across all PLR (>60% hydrate phases MOC and <60% MOC-Ag) (Figure 2.3b) may be a driving factor in this strength reduction. Phase 5 is widely reported as the primary strengthening phase in MOC, and the lower mass fraction observed is likely a key aspect of reduced strength, along with the increased degree of microporosity in MOC-Ag. Based on the difference between relative density and the total pore volume measured by μXCT, 4.1 and 8.8% of MOC and MOC-Ag volume is microporosity, compared to 1.9 and 1.2% for macropores.

Both MOC and MOC-Ag formulations show antimicrobial efficacy in agar diffusion (Figure 2.10a), in direct contact with planktonic bacteria (Figure 2.10b), and in the generation of an antimicrobial eluent (Figure 2.10c/5d). Lower efficacy is seen than the positive control DCPD-Ge, but is expected when assessing inorganic antimicrobials against strains that do not exhibit resistance to antibiotics, which remain the most effective antimicrobial agents in such cases [205]. Inclusion of positive biomaterial controls is infrequent in studies of antimicrobial cements, making direct comparison challenging. Efficacy is

observed both for gram positive *S. aureus* and gram negative P. aeruginosa. The larger zones of inhibition observed for *S. aureus* may relate to membrane specific activity of Mg^{2+} against staphylococci, though activity of Ca^{2+} ions is also reported [206].

Remarkably, efficacy against *S. aureus* is even seen for extracts at a cement to broth ratio of $0.14\,g\,mL^{-1}$, significantly below the $0.8\,g\,mL^{-1}$ ratio used in similar studies [151]. No antimicrobial efficacy was expected for the cement extracts taken from this study, given the system is much closer to sink conditions. This behaviour and the variation in response to MOC versus MOC-Ag cannot be explained by pH alone, with only small differences between the pH of the media observed, and *S. aureus* growth demonstrated up to pH 10 [207]. Previously demonstrated antimicrobial extracts from Mg cements have exhibited high osmolarity [151], and the decreasing efficacy of MOC eluent over time (Figure 2.10d) could link to the rapid decrease in Mg release, which was found to be only 760 ppm after 48 hours in LB media versus over 4000 ppm in the first 24 hours (Figure 2.11c).

Addition of Ag_3PO_4 does mitigate this decrease in efficacy, with extracts from day 2 and 3 showing bactericidal and bacteriostatic behaviour respectively (Figure 2.10d). Considering that the average silver concentration of 6 ppm is below the minimum inhibitory concentration (MIC) for this strain indicates neither Mg nor Ag release alone is the determining factor in efficacy. The exact MIC of silver ions is difficult to determine in practice due to its strong affinity for thiol groups, which may be present in culture media proteins [65], with this level of silver above the reported MIC of some laboratory *S. aureus* and *E. coli* strains of 1 ppm [47], but below typical ranges of 8 to 128 ppm [65]. Crucially, the observed release of silver is sustained between 7.5 and 5.0 ppm over 14 days in LB media, crucial for encouraging long-term antimicrobial function. Peak concentrations of 0.4 ppm Ag in PBS reinforce the importance of media used in release studies, which can drastically alter kinetics and degradation behaviour [208]. Neither the MOC nor MOC-Ag formulations altered mammalian cell viability or metabolic activity within a 7 day period, demonstrating that the addition of Ag_3PO_4 enhances antimicrobial

efficacy without negatively impacting the established cytocompatibility of MOC in these conditions [173, 174].

The more rapid elution of Mg from MOC compared to MOC-Ag may explain the higher pH observed by the end of the study, sufficient to overcome the buffering capacity of PBS (Figure 2.11a). This behaviour is contrary to the higher microporosity of MOC-Ag, which typically increases release of active species from cements [209]. As has been previously demonstrated, addition of soluble phosphates can have a protective effect against aqueous degradation of MOC [170, 176]. Conversely, silver phosphate exhibits very low solubility in aqueous conditions, with a molar solubility product pK_{sp} of 16.05, and the gradual colour change of formulations (Figure 2.3d) suggests it does not dissolve in MOC. In this case, it is instead the retardation of hydrated phase formation by AgCl that limits degradation and Mg release, due to the lower solubility of MgO compared to the hydrate phases [210]. Future investigation of the morphology of microporosity, for example the tortuosity of pores, may provide a better understanding of how physical and chemical properties have contributed to release characteristics.

Due to the implication of ROS generation in the antimicrobial efficacy of MgO suspensions, the possible production of ROS was investigated as a contributing factor (Figure 2.11b) [83, 184]. Whilst a low background chemiluminescent response is observed for all conditions from day 1 to day 10, the MOC PBS extracts showed a significant increase toward the end of the 14-day study, albeit with high variability in measurements. As no antimicrobial behaviour was observed for extracts after the first three days, it is unlikely that ROS played a significant part in the efficacy of formulations. The increase in chemiluminescent response correlated with visual observations of greater particulate matter in suspension in the final days of the study for PBS MOC extracts. Given the short lifespan of ROS, this indicates that outside of the local environment of the cement surface, there is no consistent ROS generation.

Though the underlying mechanism of antimicrobial action remains unclear, the successful demonstration of inherent antimicrobial function of MOC is promising. As the

observed pH is established as insufficient to inactivate *S. aureus*, and no significant ROS generation is observed at the peak of antimicrobial efficacy, it is posited that the release of Mg^{2+} directly contributes to the efficacy of the cements. Establishing the exact mechanism of action for inherently antimicrobial Mg cements should be a priority of future work. Mg^{2+} ions have demonstrated membrane disruptive activity against *S. aureus* [206], but this does not explain the demonstrated efficacy against *P. aeruginosa* and the established efficacy of Mg phosphates against gram negative strains. Appropriate control studies comparing the confounding variables of Mg concentration, osmolarity, and pH, will be necessary to unpick this mechanism.

Tailoring antimicrobial behaviour by doping with Ag to control Mg release rate may prove advantageous, and the sustained release of silver from the modified formulation over 14 days suggests that MOC may prove a useful carrier for other inorganic antimicrobials. Future work should therefore be focused on making minor modifications to improve setting rate to within a 10 to 30 min window [151, 158] and to tailor silver dosage to achieve elution within the typical MIC range of 8 to 128 ppm [65]. These modifications will alter the other physical properties of the cements, and should be assessed in parallel to other key performance indicators, such as the cohesivity of cement pastes once injected [195]. A range of hydrophilic colloids to improve cohesivity such as carboxymethylcellulose salts have been previously identified as compatible with MOC, and may prove promising candidates for future optimisation of washout resistance [211].

Whilst MOC shows promise as an inherently antimicrobial cement alone, it is worth also considering its behaviour as a component of two-phase implant model. The reduction in zone of inhibition size (3 versus 6 cm for cement alone) is likely due to the reduced surface area of cement in direct contact with the agar, and the resulting limit on diffusion.

Using BTB as an easily measurable molecule provides a basic model of the release behaviour in a two-phase model. Given the significantly larger molecular size of BTB than the ionic species eluted from unmodified MOC and MOC-Ag, these results cannot be directly correlated with Mg or Ag release. However, conventional antibiotics such as

gentamicin exhibit similar molecular mass and so release characteristics can be considered comparable, and may provide an understanding of degradation. As observed for Mg concentration in the 14 day release study (Figure 2.11c), an initial burst release of BTB in the first 24 hours quickly subsides to a gradual background release. When normalised for the surface area of cement exposed by the pores, release characteristics appear independent of pore diameter. Given that the internal reservoir size and pore number is identical across samples, this indicates that elution is dominated primarily by contact area, as observed in the zones of inhibition. This indicates that in assessing two-phase implant models for clinical use, careful design of surface pore area will be crucial in tailoring antimicrobial release kinetics.

2.5 Conclusion

This work demonstrates that an inherently antimicrobial magnesium oxychloride cement can be produced. Crucially, this formulation has good practical characteristics with initial setting time below 30 mins, ease of injection with peak extrusion force of 10.5 N, and significantly higher strength of 35 MPa compared to 8 to 20 MPa for typical calcium phosphate based cements. Modification of the cement to release a constant silver dosage over a 14 day period has also been shown, further enabling use as an alternative to conventional antibiotic doped formulations. The increased antimicrobial efficacy of silver doped formulations against planktonic cultures in broth is encouraging, with complete eradication of *S. aureus* after 3 hours exposure to broth extracts, and no observed cytotoxicity within 7 days. Based upon the suggested mechanism for Ag_3PO_4 to disrupt curing behaviour, it should be feasible to modify the formulation to better retain the advantageous curing behaviour of undoped oxychloride by using an alternate silver dopant or acidification of the formulation.

CHAPTER 3

IN-SITU ALLOYING OF TITANIUM AND SILVER BY LASER POWDER BED FUSION

Using blended elemental or pre-alloyed powders as feedstocks for selective laser melting (SLM), new alloy compositions can be assessed by alloying in-situ. This process is typically challenged by the need to generate homogeneity of composition, relying either upon large melt pool volume during printing or post-processing thermal treatments. However, for materials where mechanical properties are not the primary goal, greater flexibility in microstructure utilising deliberate segregation of alloy components in SLM may be advantageous.

The Ti-Ag system provides a challenging manufacturing regime to investigate this behaviour, given the severely different optical and thermal properties of Ti and Ag. Manufacturing parameters for pure Ti, Ag, and Ti-xAg blends were compared. The feasibility of producing well consolidated Ti-3Ag, Ti-10Ag and Ti-25Ag alloys was demonstrated, with observed pore volumes below 0.1 % achieved for all three blends. By tailoring laser parameters, microstructures ranging from homogeneous to highly segregated were demonstrated, with significant microstructural segregation observed at incident energy densities below $300\,\mathrm{J\,m^{-1}}$. A model for this microstructure formation is suggested, with results of track melting experiments informing understanding of layer densification. To assess the performance of blended powders, samples were assessed based upon their location within the build bed, demonstrating that spread induced de-mixing of the Ti-Ag blend was occurring.

ACKNOWLEDGEMENT OF CONTRIBUTING MATERIAL AND AUTHORS

As primary author, M Lowther produced all written work within this chapter and performed all primary experimental work. The contributions of co-workers are as follows:

- Dr. V M Villapun: Acquisition of Alicona surface topography data.
- Prof. L M Grover, Dr. S C Cox: Editorial and supervisory guidance.

3.1 Introduction

As an approach for delivering inorganic antimicrobials from additively manufactured implants, use of an inherently antimicrobial alloy offers a conceptually simple approach. However, in order to do so, development of appropriate alloy compositions and microstructures must be performed rapidly. Manufacture of blended alloys by PBF is one possible approach to this, mitigating the need for pre-alloyed powders. As discussed in §1.4.1, use of blended feedstocks allows for more rapid assessment of a wide compositional range than production of pre-alloyed feedstocks. This may also allow for a wider range of microstructural features than conventional alloying approaches. However, whilst there has been some investigation of how blended powders may alter microstructural development in SLM, this has often focussed on achieving a homogeneous resulting alloy akin to that achieved with pre-alloyed feedstock [212–214].

Previous efforts to deliberately generate non-homogeneous alloys via SLM have often used nanoscale additives with low solubility in the bulk matrix, for example inclusion of wear resistant ceramics to improve the mechanical properties of the end microstructure [215, 216]. In a biomedical context, hydroxyapatite and Ag nanoparticles have been assessed in a range of base alloys (see Table 1.1, §1.4.1). Whilst it may be possible to generate an alloy feedstock by blending conventional 15 to 45 µm SLM powders with Ag nanoparticles, the challenges of regulating nanoparticle behaviour in vivo [217, 218] and the additional safety measures required for handling of nano-scale materials [219, 220] pose barriers to industrialisation of such an approach. The tendency of biomodal particle distributions to segregate or "de-mix" into component powders, adds to the challenge [221, 222]. It may instead be favourable to use a blended powder with a monomodal distribution. This in turn would enable a more aggressive pursuit of microstructural segregation, given the greater diffusion distance required to achieve homogeneity versus nanoscale feedstocks.

In order to explore the potential of bulk microstructural segregation in SLM - i.e. at the 15 to 45 µm scale of individual powder particles - several key characteristics are

desirable in a candidate alloy system:

- Binary alloy to reduce complexity at the proof of concept stage
- Alloy components with differences in optical or thermal properties that may encourage segregation
- Individual alloy components with an established feasibility of manufacture by SLM
- An alloy system where microstructural segregation may provide functional benefits that offset potential mechanical disadvantages
- System that may be amenable to microstructural development on heat treatment that cannot be achieved from a homogeneous feedstock

Considering these criteria, the Ti-Ag binary alloy system provides an optimal starting point. Ti and Ag have widely divergent thermal and optical properties, with silver exhibiting the highest thermal conductivity of any pure metal. Both Ti and Ag alloys have been widely manufactured by SLM, including high purity Ag and cp-Ti [223, 224]. The in-situ alloying of Ti-Ag alloys has only been briefly assessed, with a blend of 15 to 45 µm Ti-6Al-4V, and Ag particles of below 5 µm, shown to homogenise in process [116]. There is however, reasonable evidence for a higher likelihood of microstructural segregation in a monomodal blend. Melt spinning of Ti-Ag-Cu alloys has demonstrated a miscibility gap for Ti and Ag at cooling rates of $10^5\,\mathrm{K\,s^{-1}}$, which may be achieved during SLM given established values of over $10^6\,\mathrm{K\,s^{-1}}$ in Ti alloys [91, 225, 226]. Ti-Ag has seen development for dental applications, with a combination of good corrosion and wear behaviour, and evidence of antimicrobial response [227, 228]. Intermetallics have been implicated in the antimicrobial response of Ti-Ag alloys, though the exact mechanism remains unclear [124, 229]. In particular, Ti_2Ag has been suggested as the dominant contribution to this behaviour. Provided this is the case, by generating localised concentration of Ag, precipitation of intermetallics such as Ti_2Ag during ageing at lower bulk silver concentrations may be possible (Figure 3.1, phase diagram modified from [280])).

In order to optimise SLM of new materials, it is common to perform a screening of laser parameters. Laser scanning speed and power are frequently selected as the vari-

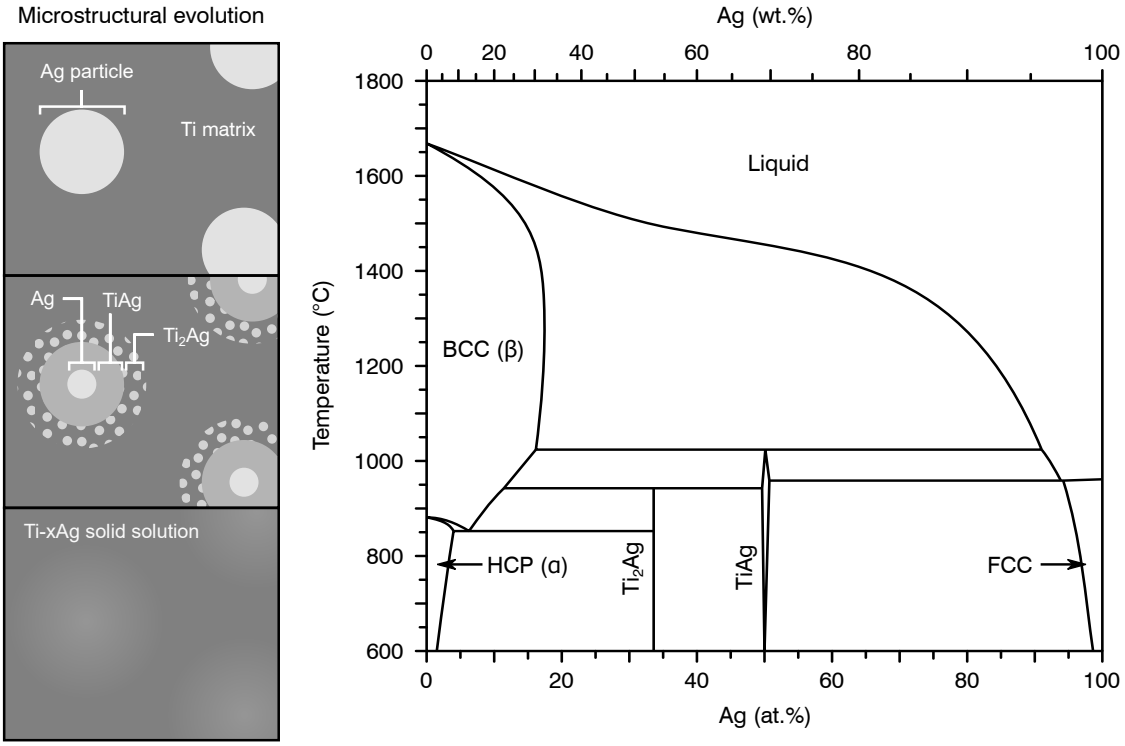


Figure 3.1: Schematic showing the proposed model for generating non-equilibrium microstructures by in-situ alloying. Initially highly segregated microstructures are generated by SLM, and act as spherical diffusion couples. The possible microstructural evolution with heat treatment is shown schematically, with intermetallic formation and subsequent homogenisation. The current established Ti-Ag phase diagram is shown at right to contextualise the equilibrium phases. Phase diagram adapted from Dezellus et al, 2011.

ables, providing a two-dimensional parameter space to explore. These parameters can be combined to provide a single parameter - an applied energy density - which is in principle representative of the thermal energy a point will experience.

Simple models for linear, area, and volumetric energy density E_d can all be calculated:

$$\text{Linear energy density} = \frac{\text{Laser power}}{\text{Scan speed}} = E_d^L \tag{3.1}$$

$$\text{Area energy density} = \frac{\text{Linear energy density}}{\text{Scan spacing} \times \text{Focus diameter}} = E_d^A \tag{3.2}$$

$$\text{Volumetric energy density} = \frac{\text{Area energy density}}{\text{Layer thickness}} = E_d^V \tag{3.3}$$

In practise, several of the parameters included above are fixed based on the physical nature of the SLM apparatus used and practical manufacturing considerations. Increasing focus diameter will reduce resolution, and the necessary scan spacing required to achieve overlap of scanning paths and adequate densification will be dependent on this factor. Altering of layer thickness may have greater practical relevance to either increase vertical resolution or conversely maximise build rate, but again is typically selected for a specific value. If layer thickness is too large, powder layers may not melt to full depth, resulting in delamination [230]; excessively thin layers reduce manufacturing speed and increase risk of uneven layer spreading [231]. Given this, the use of simple linear energy density is assumed in future discussions, as both area and volumetric E_d will be directly proportional due to these factors being fixed. Simplistic energy density models do suffer from significant assumptions and oversimplifications, only assessing the theoretical energy applied by the laser, and take no consideration of optical effects such as the reflectivity, or thermal behaviours including heat diffusion and melt pool behaviour [232]. For a mixed powder these factors are particularly challenging to take account of. As such it is key to perform screening builds to understand in-situ behaviour, as current models of PBF processes struggle to account for these complexities in untested materials [233].

Existing parameter spreads explored for the manufacture of cp-Ti and Ag show wide divergence in the optimal laser parameters used, as expected given their divergent thermal and optical properties (Table 3.1). The majority of prior research has used continuous mode lasers, where each scan line vector is a single exposure. For a pulsed laser, scan speed is not directly fixed. Instead, scan vectors consist of a series of individual point exposures with a set spacing and duration of exposure. As such, the effective scan speed is given by the ratio of exposure spacing to exposure duration. Behaviour does not necessarily convert directly between continuous scan speed and effective pulsed scan speed, but provides some guidance for a likely manufacturing window, and as such the effective scan speed is used to make comparison across these processes.

Alongside manufacturing of bulk samples, single track melting experiments may be

Table 3.1: Laser parameter spaces previously explored for manufacture of c=cp-Ti and pure Ag by SLM. Scan speeds and powers for cp-Ti are notably lower than those used to manufacture other Ti alloys, with recommended values provided by Renishaw of 200 W and 1500 mm s^{-1} for Ti-6Al-4V.

Material	Power W	Scan speed mm s^{-1}	Spot size µm	Layer thickness µm	Source
cp-Ti (Gd 1)	30 - 75	20 - 30	2000-3000	45	[234]
	50 - 250	-	-	30	[235]
	122 - 166	400	64	30	[236]
	150 - 200	100 - 180	80	100	[237]
	100 - 200	50 - 200	100	50	[238]
Ag (99.9%)	350 - 370	400 - 1000	100	30 - 60	[223]

performed as a model to understand the interaction of laser and powders in-situ. Typically these consist of a single layer of powder spread across a substrate, onto which individual scan paths are exposed. Whilst this may not be reflective of the bulk behaviour of material, formation of a continuous single track is often correlated with good performance of melting parameters [239]. In reality, several limitations of the single track model can be noted and are rarely discussed. Neglecting the remelting and densification that may occur both from adjacent scan paths and the subsequent layer are reasonable concessions, but perhaps most notably the thermal effect of the interaction between tracks and substrate is also neglected. For a single powder layer, the contiguous material provided by the underlying substrate may significantly alter laser absorptivity, thermal diffusion, and wettability [240]. Practical experience of SLM also raises the often atypical behaviour of spread powders in the first few layers of manufacture, due both to the difference in friction across a solid substrate versus powder layers, and any tilt of the baseplate.

In this work, a series of Ti-Ag alloys with varying microstructure have been produced by SLM of blended elemental Ti and Ag powders. To assess the effects of laser parameters and composition on microstructural development, imaging by SEM and extensive image analysis have been performed. Density, porosity, composition, microstructural segrega-

tion and microhardness have been quantified. Statistical analyses of variation in these characteristics with sample location were made to establish any de-mixing of powder components during manufacture. Based on these results, a probable route for the formation of microstructures observed is posited. To further characterise densification behaviour, single track melting experiments were performed on plinths produced in-situ.

3.2 Materials and methods

3.2.1 Sample preparation

Feedstock preparation

Argon atomised commercially pure grade 1 titanium (cp-Ti) (LPW Ltd) and high purity nitrogen atomised Ag-999 (CooksonGold Ltd) powders of 15 to 45 µm size distribution were blended in ratios of 3, 10 and 25 wt% Ag under Ar atmosphere with O_2 below 40 ppm and H_2O content of below 3 ppm. The subsequent Ti-Ag blends were homogenised by roller blending for 10 h. For manufacture of pure Ag and cp-Ti, powders were used as supplied with no additional conditioning.

Powder bed fusion

All samples were manufactured by PBF with a continuous wave 500 W 1070 nm Ytterbium fibre laser (RenAM 500M, Renishaw Plc). Energy is delivered to the powder bed as a series of modulated exposures with a given spacing and exposure duration. This was performed within an Ar atmosphere, with O_2 below 1000 ppm during lasing. Printing of cp-Ti, Ag-999, and Ti-3Ag powders, utilised a manufacturer provided reduced build volume (RBV). To further minimise required powder volumes for Ti-10Ag and Ti-25Ag, apparatus was modified with an in-house ancillary, described as the U-RBV (Appendix B). Samples were manufactured onto Ti-6Al-4V substrates.

In order to optimise laser parameters for each material, a parameter spread was generated with variable laser exposure time and power. Layer thickness, scan spacing pa-

rameters, and exposure point distance were maintained across all builds from existing optimised Ti-6Al-4V build parameters (Table 3.2).

Table 3.2: Additional parameters that must be defined for manufacturing via selective laser melting, and the fixed values chosen for all experiments in this work.

Parameter	**Value**	**Description**
Exposure point distance	90 µm	Distance between each point in a line vector of exposures
Hatch distance	90 µm	Spacing between each hatch line vector
Slice thickness	30 µm	Thickness of each layer
Layer angle	67°	Orientation of line vectors in each layer, relative to the previous layer
Focus offset	−4 mm	Vertical offset to account for elevation of RBV apparatus in chamber.
Spot diameter	75 µm	Nominal diameter of laser in focal plane

Samples of cp-Ti, Ag, and Ti-3Ag were produced as a grid of vertical cylinders with 12.5 mm diameter and 5 mm spacing between each cylinder. Due to the restricted build volume of the U-RBV, samples of Ti-10Ag and Ti-25Ag were produced as 5 mm cubes with 1.5 mm spacing. Given the possibility of in-process de-mixing of blended powders, additional quality control samples were manufactured for all Ti-Ag builds. These extra parts were built using duplicate laser parameters at different points along the length of build substrates, in order to assess any de-mixing of the powder blend during processing. Manufactured samples were removed from substrates by wire electrical discharge machining (EDM) (CUT 20 P, GF AgieCharmilles).

Track melting

To assess the formation of melt tracks during processing, a series of Ti-3Ag samples were prepared. Plinths of 2 mm height and 10 mm side length were produced during printing, upon which individual laser tracks could be formed during the subsequent layer of powder spreading and laser exposure. Five tracks were exposed along each sample, parallel to the

spreading direction to minimise the risk of damage by subsequent motions of the recoater blade. Orientation of layers was generated such that the line vectors of these layers lay at approximately 67° to the previous layer, as is standard in the bulk processing of materials (Table 3.2). A second set of samples featured four consecutive layers of laser track, with each layer of track offset by 45 µm to reduce repeated re-exposure of the same exact position along the track.

3.2.2 Characterisation

Powder feedstock validation

Powder feedstock was characterised for size, composition, and morphology. Particle size was assessed by laser particle size distribution (LPSD) with water as the dispersant media (Mastersizer M2000, Malvern). Droplets of Polysorbate 80 detergent were used to minimise agglomeration where necessary. Multi-element panels of ICP-OES, inert gas fusion for oxygen and nitrogen, and combustion measurement of carbon and sulphur interstitials were used to confirm composition (AMG Superalloys, UK).

To assess particle morphology, backscattered electron (BSE) SEM analysis of as received powder and of blended feedstocks was performed (TM3000, Hitachi). A sample of powder was directly added to an adhesive carbon tab, tapped to remove loose particles, and imaged.

Due to observed poor flow performance of Ag-999 powder, assessment of moisture content was performed by thermogravimetric analysis (TGA), with nitrogen purge gas (TGA 209 F1, Netzsch). A powder sample was placed in an Al_2O_3 crucible and heated at $10\,\mathrm{K\,min^{-1}}$ to 300 °C, before dwelling for a further 30 min. Mass readings were taken at 15 s intervals.

Microstructure and compositional analysis

Sample cross sections were cut parallel to the build substrate with abrasive SiC cut-off wheels, and hot mounted in conductive Bakelite (Presidon-ML-C, Aptex Ltd). Samples

were ground and polished according to the recommended protocol for cp-Ti (Table 3.3) using an automated rotary preparation machine (Tegramin-25, Struers) according to the protocol described in table 3.3. For final polishing of samples, activated oxide polishing solution (OP-S) was prepared using colloidal silica suspension (Struers) and 10 vol% H_2O_2 (Sigma).

Table 3.3: Sequence of polishing procedures used to prepare metallographic specimens with the Struers Tegramin-25 automated rotary preparation machine.

Step	**Surface**	**Dosing**	**Force**	**Duration**	**Rotation**	**Co-rotation**
1	MD-Piano 220	Water	25 N	Until plane	300 rpm	150 rpm
2	MD-Largo	DiaPro	15 N	4:00 min	150 rpm	150 rpm
3	MD-Chem	OP-S	10 N	25:00 min	150 rpm	150 rpm

Imaging of microstructures was performed by BSE SEM due to the strong compositional contrast between Ti and Ag ($Z = 22, 47$). Images were taken towards the centre of samples, avoiding the external contour region which is subject to additional remelting and less representative of the bulk microstructure.

Compositional analysis was performed on mounted and polished cross sections by X-ray fluorescence (XRF) (M4 Tornado, Bruker). Maps were taken with a point spacing of 25 µm, 15 ms acquisition time per point at 50 kV voltage and 500 µA tube current. A Rh anode with no filters was used, and a vacuum of below 20 mbar maintained. Peaks for Ti, Ag, and Rh were separated, and a series of Ti-Ag samples with known composition used to calibrate measurements.

Density

For cp-Ti and Ti-3Ag samples, apparent density was assessed by Archimedes measurement (Adventurer Precision AX223, Ohaus) in pure ethanol. The liquid temperature was allowed to equilibrate for one hour prior to measurement of samples, and measurements recorded after one minute of immersion. One sample of cp-Ti exhibited sufficient open porosity that entrapped gas was observed escaping the sample with a resulting drift in

measurement over the course of immersion. This outlying sample was dried, and measurement instead taken immediately upon immersion.

Due to the smaller volume of Ti-10Ag and Ti-25Ag samples, density was instead assessed by He pycnometry (AccuPyc II 1340, Micrometrics, USA). Three sequential measurements of each sample were made, with five gas purges at 19 MPa per measurement.

Surface topography

Topographical measurements of track melting samples were made using an optical non-contact profilometer (Infinite Focus G5 Optimax, Bruker Alicona Austria). Scans were taken at x20 magnification, with light intensity and contrast selected to minimise scanning artefacts. A 1.5 mm wide strip was imaged perpendicular to the track melting direction. Data was levelled by mean plane subtraction, and the surface roughness of regions between tracks measured (Gwyddion 2.57).

3.2.3 Image analysis

General procedures

Image analyses were performed using the Fiji distribution of ImageJ [241, 242]. Initial processing of images involved the removal of any non-uniform background, for example caused by sample tilt, by fitting and subtraction of a cubic polynomial. Any analysis of thresholded images was preceded by use of automated despeckle function.

Estimating microstructural segregation

Due to the varying degrees of porosity, silver segregation, and limitations of the Hitachi TM3000 SEM, imaging with a fixed brightness and contrast across all samples was not feasible without loss of detail or overexposure. As a result, it is not possible to quantitatively analyse images without further processing.

Given the variable degree of mixing and resulting diffuse boundaries of silver agglomerates with the matrix, automated methods for both local and global thresholding such as

those available in Fiji face challenges, particularly when seeking a consistent methodology that is reproducible for both highly segregated and homogeneous samples. To avoid resorting to subjective manual thresholding, a criterion for selecting a consistent greyscale threshold was sought.

The greyscale histogram of each image was extracted. The distribution of brightness values can be considered as an overlap of four distributions, visualised in Figure 3.2:

1. A Gaussian distribution of values for the primarily Ti matrix
2. A Gaussian distribution with higher mean brightness for the regions where Ti and Ag have mixed
3. A distribution of values for highly segregated silver, truncated to a delta function for greyscale values above 255
4. A distribution of values for porosity, truncated to a delta function for greyscale values below 0

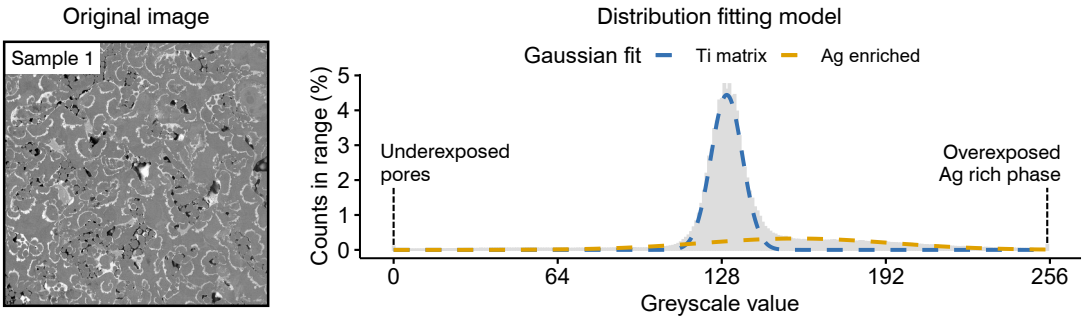


Figure 3.2: Example of a typical greyscale distribution from a backscatter SEM micrograph of a Ti-25Ag alloy sample. Increased electron yield from Ag due to its higher atomic number than Ti results in strong elemental contrast. Fitted Gaussian distributions for the bulk Ti matrix and Ag enriched phase are shown, with fully saturated and de-saturated values representing Ag and pore regions.

A model of two overlapping Gaussian distributions was fit to each histogram (R 4.0.2), neglecting the extreme saturated values of each distribution due to pores and segregated silver (greyscale values of 0 and 255 respectively). Where attempts to fit two Gaussian distributions resulted in a singular convergence - indicative that fitting does not support the number of parameters utilised - a single Gaussian distribution was used instead. As the degree of mixing will be variable between samples, histograms are matched based upon

fit for the primary Ti matrix Gaussian. Translating distributions such that the mean for Ti matrix Gaussians overlap, and scaling the range of each histogram such that the same standard deviation is achieved, results in an approximation for all samples returning the same distribution (Figure 3.3).

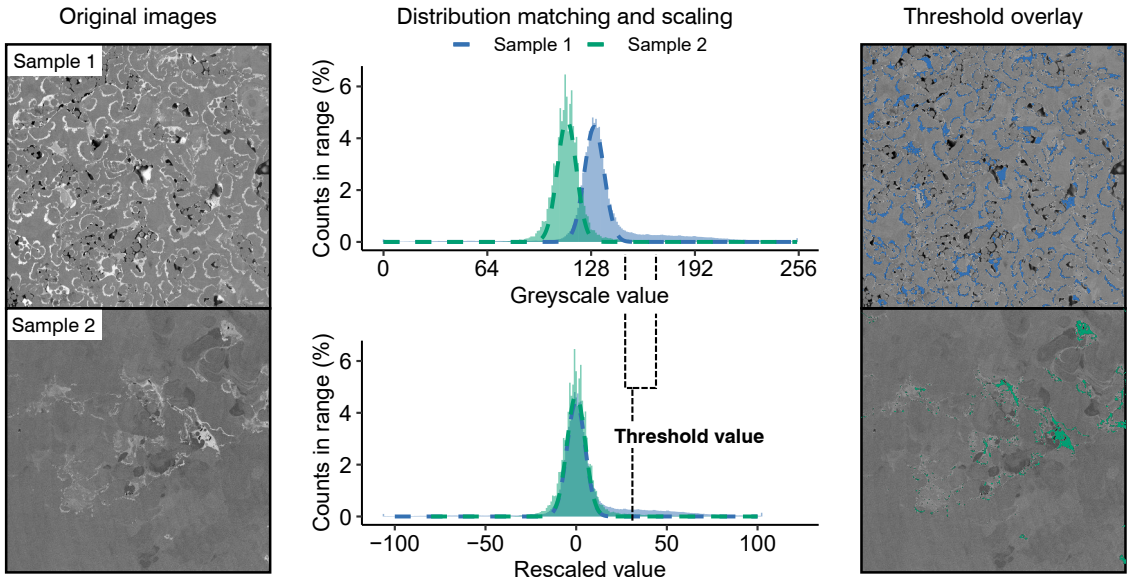


Figure 3.3: Diagram of the basic procedure for matching greyscale distributions for microstructures with different degrees of segregation and potentially variable imaging conditions. Once fitting of Gaussian distributions for each histogram has been performed, they are normalised to the same mean and standard deviation for the Ti matrix phase. This allows for a uniform threshold value to be applied to these scaled distributions.

From this, any threshold chosen will be consistent across all images, allowing a single selected greyscale value to reliably be used for microstructural analyses. Though still reliant upon the subjective manual selection of a threshold value, this step is only required once for all samples, allowing quantification of the microstructural differences present.

3.2.4 Statistical analysis

To assess dependency of physical characteristics on plate position, a statistical framework is needed for considering the quality control (QC) samples included in Ti-Ag builds (Figure 3.4). Whilst comparison of response within a specific set of QC samples - with identical laser parameters and composition - can simply be done through regression, the statistical

power is highly limited by the number of samples, and verifying if the same dependency applies across other sample sets is necessary.

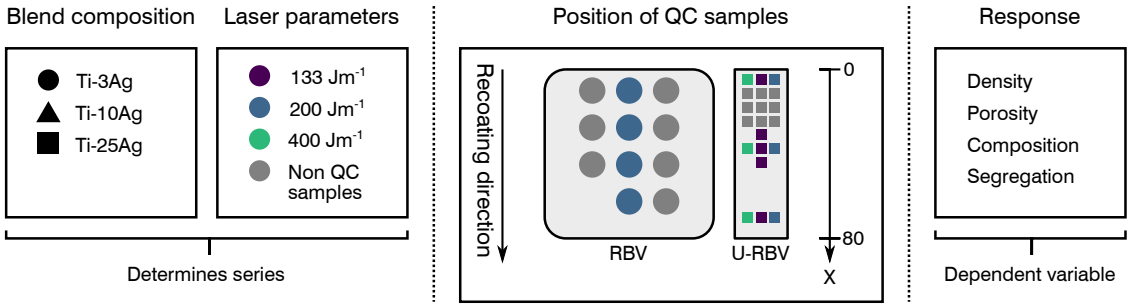


Figure 3.4: Schematic describing the variables involved in analysing positional dependency of manufacturing. Each individual alloy composition and laser parameter defines a series of samples, which have specified positions on the printing substrate. Sample position, X, is defined relative to the substrate edge over which powder is first spread. A statistical model is required to assess the relative significance of the sample series, and the position, on each of the measured responses.

To achieve this, regression can be performed across the entire group of QC samples, but with the inclusion of dummy variables for which specific series an individual datum relates to. In the simplified example model below, we wish to establish whether the response is dependent upon position, and if this dependency is consistent between the different series. As such, a linear model can be generated as follows:

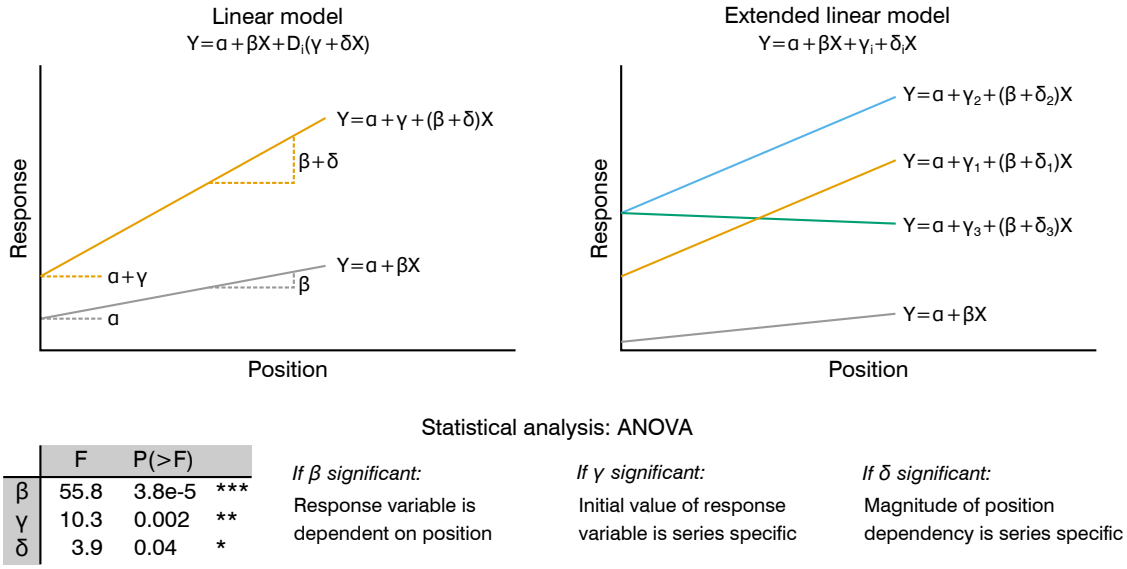
$$Y_i = \alpha + \beta X_i + \gamma D_i + \delta(X_i D_i) \tag{3.4}$$

where α is the initial intercept, and β the gradient. In this model, γ represents the change in intercept between the two series, and δ the difference in gradient. Crucially, the indicator variable D_i has a value dependent upon the series, such that

$$D_i = \begin{cases} 0 & \text{for series 1} \\ 1 & \text{for series 2} \end{cases} \tag{3.5}$$

As a result, the model effectively fits an initial gradient to series 1, and includes the

modifiers γ and δ in fitting series 2 (Figure 3.5). Subsequent statistical analysis by analysis of variance (ANOVA) can be used to assess the significance of model parameters, determining whether a trend is observed and how this is modified between series.



	F	P(>F)	
β	55.8	3.8e-5	***
γ	10.3	0.002	**
δ	3.9	0.04	*

Figure 3.5: Schematic describing the parameters used in the linear fitting model for assessing quality control samples. Assuming a linear dependency of the response variable upon the position, an initial gradient and intercept of best fit are assigned to a series. Subsequent series may be compared by including parameters for the change in intercept, γ, and difference in gradient, δ. The implications of statistical significance for each parameter is described.

Considering the physical situation assessed in this model, the resulting parameters α, β, γ, and δ can be described as follows. The baseline value of the response at the plate edge - e.g. the anticipated density of a sample produced at $x = 0$ - may be given by α. Regarding positional dependency, this value can in effect be neglected, and is fixed across series. If the gradient parameter β is statistically significant, this means all of the series assessed show a common trend in response with position - e.g. density increases for parts manufactured farther from the plate edge. Similarly to α, the series specific intercept γ describes the anticipated response at the plate edge for a specific manufacturing parameter, and allows the model to account for variations between materials and laser parameters, that may otherwise mask overall trends. Finally, δ acts to establish if

positional dependency of responses is series specific, i.e. whether any trend in behaviour is shared across all builds. If the inclusion of δ is not significant, this suggests any behaviour is a shared characteristic of the manufacturing process, independent of the specific alloy blend or laser parameters used.

Where there are more than two series, this approach can be extended such that each series is modelled as

$$Y_i = \alpha + \beta X_i + \gamma_i + \delta_i X_i \tag{3.6}$$

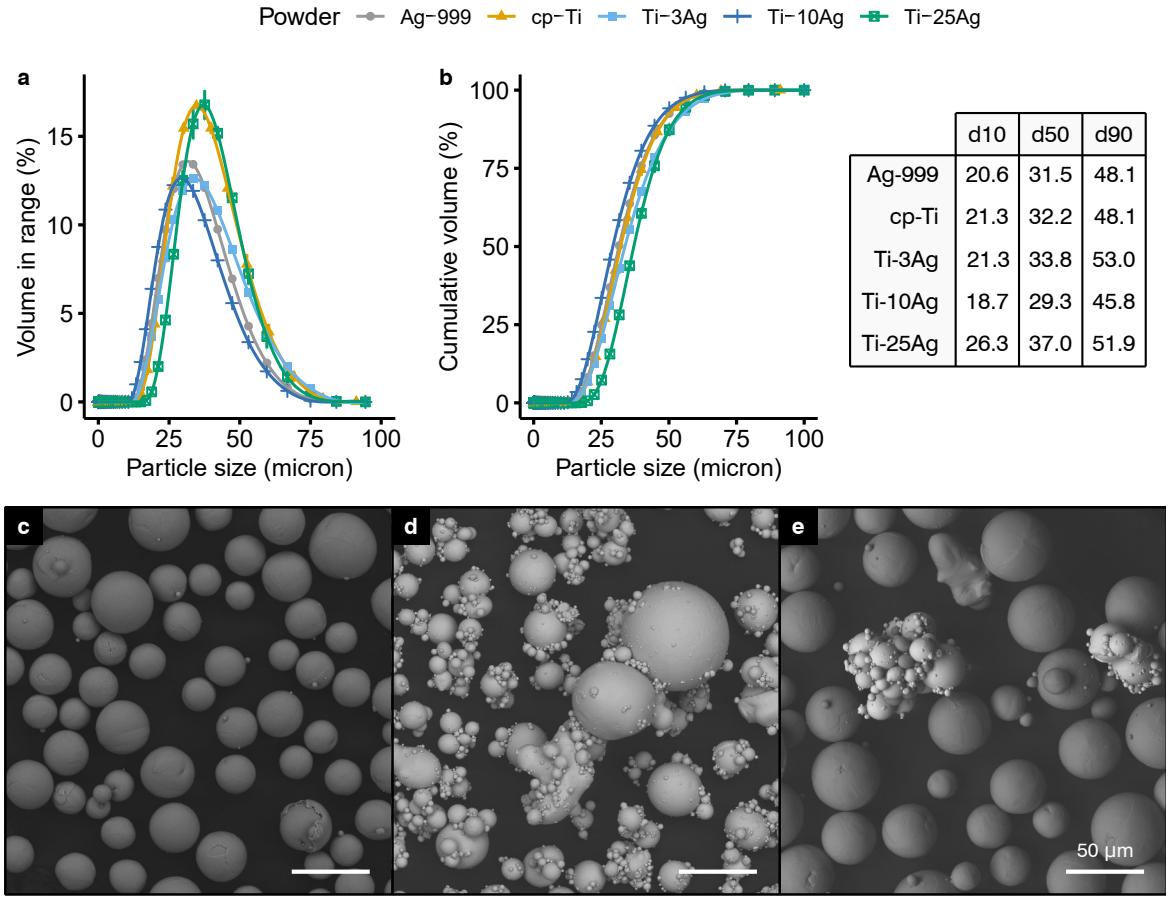
with differing values of γ and δ per series. ANOVA can again be applied to the parameter set. This will determine if the overall inclusion of β, γ and δ are statistically significant across the entire data set, as opposed to assessing quality of fit only on a per-series basis. Note that use of the ANOVA framework ensures no dependency upon which series is used to fit initial model parameters of α and β. This statistical framework was used to assess the physical properties of Ti-Ag builds (R 4.0.2). Results for each build were normalised to assign each result a Z-score prior to analysis, enabling comparison of characteristics across different materials.

3.3 Results

3.3.1 Powder characterisation

The particle size distribution (PSD) of as-received feedstock and powder blends show agreement with the nominal 15 to 45 µm size range required for SLM (Figure 3.6a). Blended powders do not show bimodal distributions, with d_{50} ranging from to 29 to 37 µm. Inspection by SEM shows high sphericity in cp-Ti, but significant agglomeration and satelliting of Ag-999 powder (Figure 3.6a and b). Individual Ag agglomerates consist of larger 15 to 45 µm particles and very fine <5 µm satellite particles. Agglomerates within blended powders form primarily from Ag-999, with Ti particles of around 5 µm adhered. Visual inspection of Ag-999 showed poor flow behaviour. Investigating the moisture con-

tent by TGA indicated no mass loss after 30 min dwell time at 300 °C, indicating the high cohesivity of Ag was not caused by entrapped moisture [243].



	d10	d50	d90
Ag-999	20.6	31.5	48.1
cp-Ti	21.3	32.2	48.1
Ti-3Ag	21.3	33.8	53.0
Ti-10Ag	18.7	29.3	45.8
Ti-25Ag	26.3	37.0	51.9

Figure 3.6: Powder analyses of feedstocks, with a) range and b) cumulative particle size distributions of each powder with d10, d50, and d90 given; and SEM micrographs of c) Ti, d) Ag, and e) Ti-3Ag powders. The satellited and agglomerated nature of Ag is apparent, and the accumulation of fine Ti particles into Ag agglomerates is visible in e).

All powders met specifications for composition. cp-Ti powder showed oxygen and nitrogen content of 0.12 wt% and 0.03 wt% respectively. In comparison, Ag-999 had significantly lower interstitial content of 0.006 wt% O_2 and < 0.001 wt% N_2.

3.3.2 As manufactured microstructure

During manufacture of pure Ag, geometric deviation was observed on the leading edge of cylinders, with the gradual formation of a melted lip disrupting powder spreading. Manufacture of these parts were suppressed for subsequent layers to minimise interference

with other samples on the build plate. Very little densification was observed during processing across the full range of linear energy densities, ranging from 133 to 1833 J m^{-1}, with cylinders after manufacture appearing visually similar to the unmelted powder in colouration and texture. Large, open pores along layers indicative of delamination were visible in several samples (Figure 3.7).

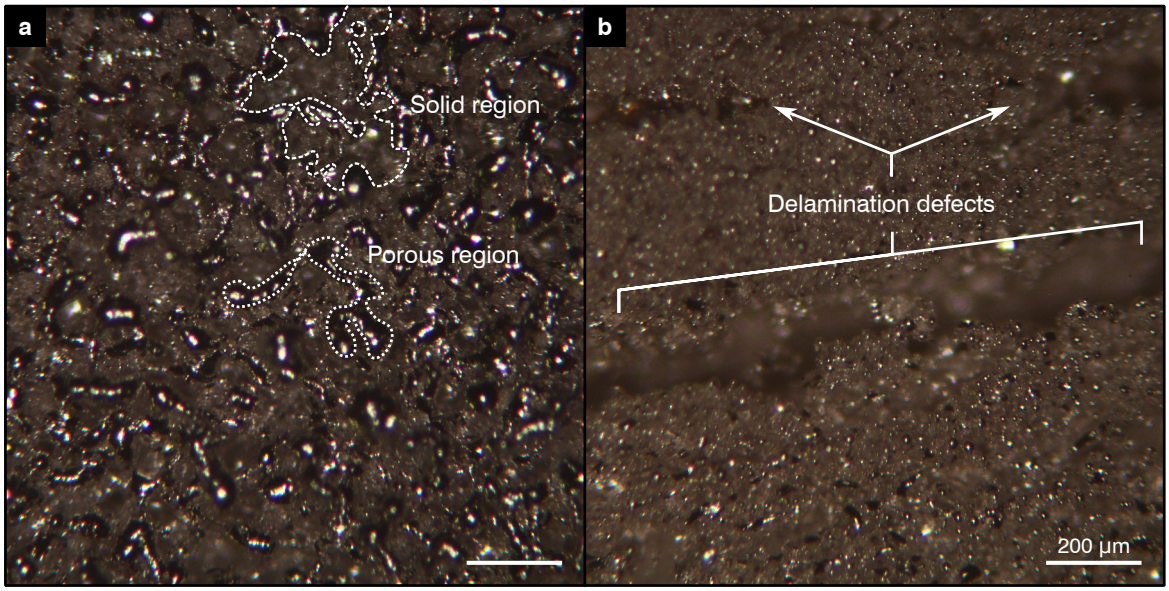


Figure 3.7: Optical micrographs of the a) top and b) side surface of additively manufactured Ag, showing highly porous and unmelted texture with large delamination perpendicular to the build direction.

Removal of material from the build plate by EDM caused fragmentation and delamination in some cases, with cylinders falling away prior to the completion of cuts. Samples exhibited sufficient open porosity to make measurement of density by Archimedes method infeasible. Geometry measurements were instead taken, with density estimated from this and mass measurements. No significant difference between samples was found, with an average density of $6.8 \pm 0.4\,\mathrm{g\,cm^{-3}}$, equivalent to a nominal $65 \pm 4\%$ of fully dense silver. This indicates that any melting was insufficient to cause densification, effectively fusing particles together in an open pore network.

In comparison, cp-Ti showed good melting from 67 to 1333 J m^{-1}. Significant porosity is present below a linear energy density (E_d^L) of 200 J m^{-1} (Figure 3.8). All samples manufactured at scan speed of 150 mm s^{-1} show near complete densification. However,

significant sparking and generation of condensate was observed for these samples during manufacture, indicative of excess energy input, though there is no clear indication of keyhole pore formation. The presence of unmelted particles within pores indicate porosity was primarily caused by lack of fusion, however the $> 100\,\mu m$ size of pores may indicate discontinuities in the powder bed. This remained the case at 200 W and $1500\,mm\,s^{-1}$, the existing optimised parameters used for manufacturing Ti-6Al-4V.

Ti-3Ag samples showed similar trends of behaviour to cp-Ti, with increasing energy density within the range of 133 to $667\,J\,m^{-1}$ reducing observed porosity (Figure 3.9). Regions of high Ag were present, typically 30 to 100 µm with elongated and rough shape. The extent of silver segregation similarly reduces with E_d^L. The addition of 3 wt% Ag appears to increase densification when assessing samples of the same scan speed and laser power, most significantly at low energy densities (see Figure 3.8 and 3.9 at $133\,J\,m^{-1}$).

Ti-10Ag and Ti-25Ag exhibit similar microstructures, with segregation decreasing as energy density increases (Figure 3.10 and 3.11). Notable is the lower porosity observed by SEM for Ti-10Ag. Within larger 200 µm agglomerations of silver, 15 to 45 µm spherical pockets of Ti rich phase are observed. Retained silver rich phase does not exhibit the same geometry as Ag agglomerations observed in the unmelted powder, indicating these are not lack of fusion defects.

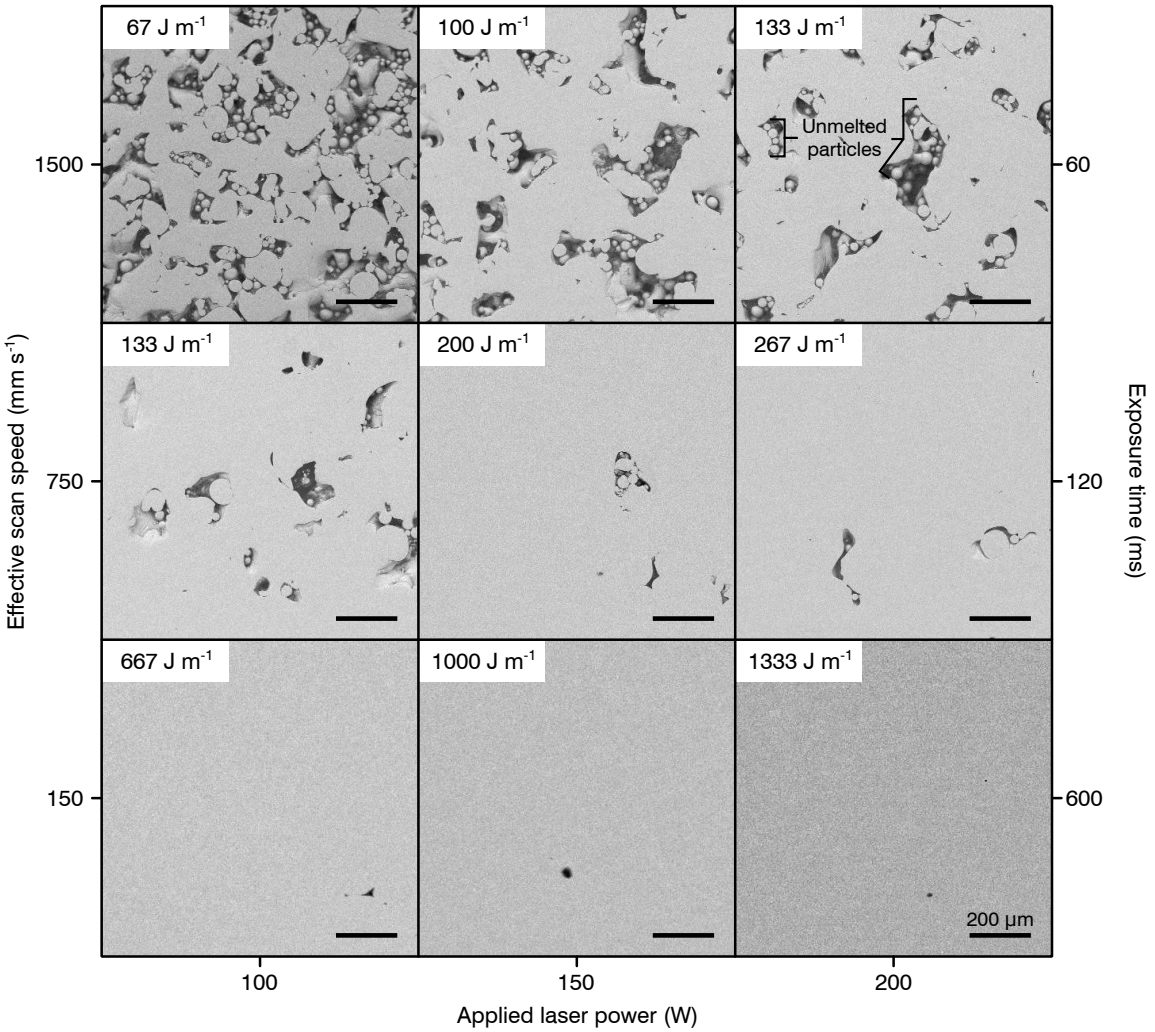


Figure 3.8: Backscatter SEM micrographs of additively manufactured cp-Ti. Each sample is labelled with linear energy density (E_d^L) values. Lack of fusion defects are visible, identifiable as pores with unmelted powder particles. As energy density increases, the apparent porosity of samples decreases.

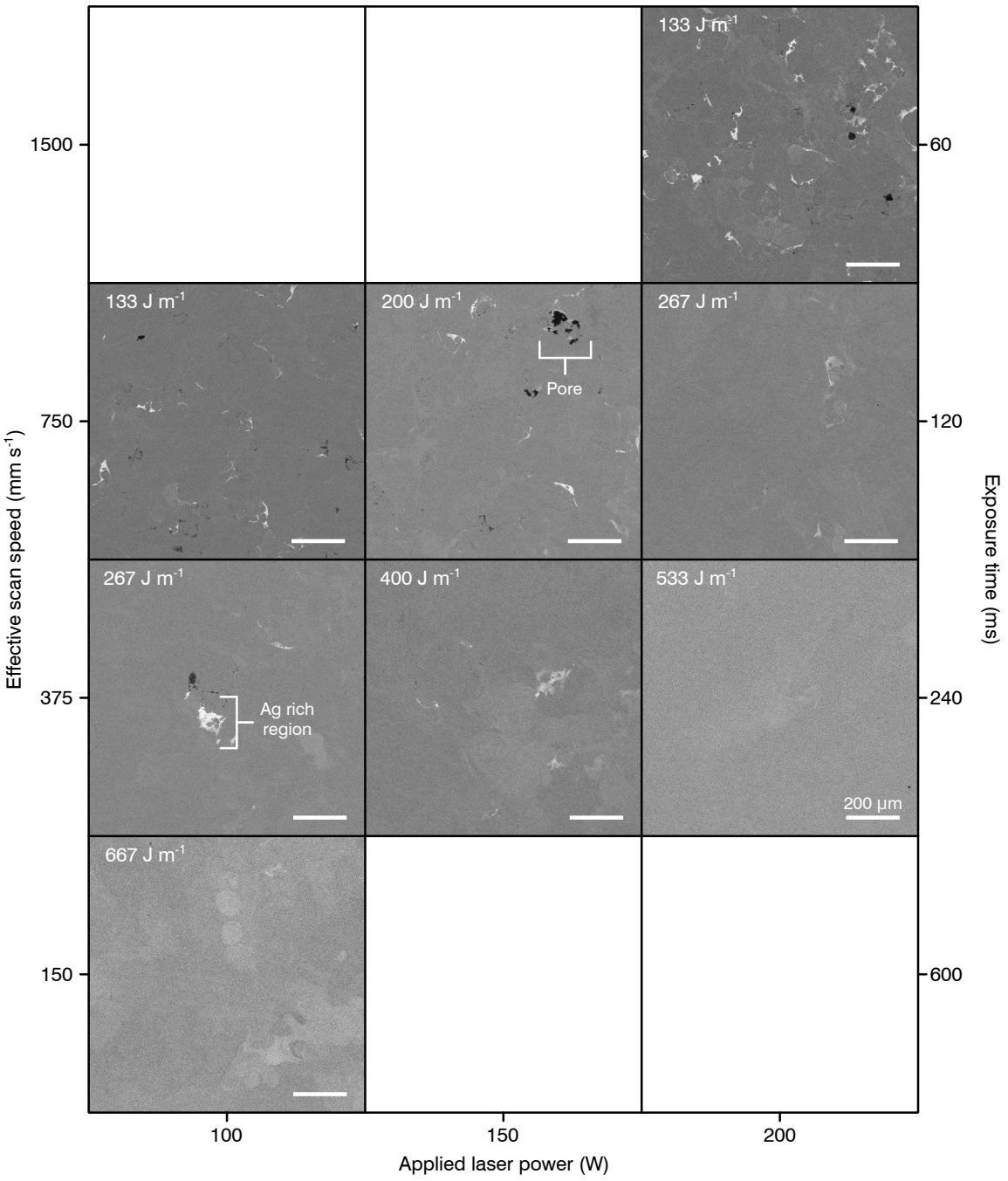


Figure 3.9: Backscatter SEM micrographs of additively manufactured Ti-3Ag. Each sample is labelled with linear energy density (E_d^L) values. Small regions of high silver content are identifiable by higher brightness. Increasing energy density results in increased microstructural homogeneity, as indicated by fewer bright regions and greater uniformity of greyscale.

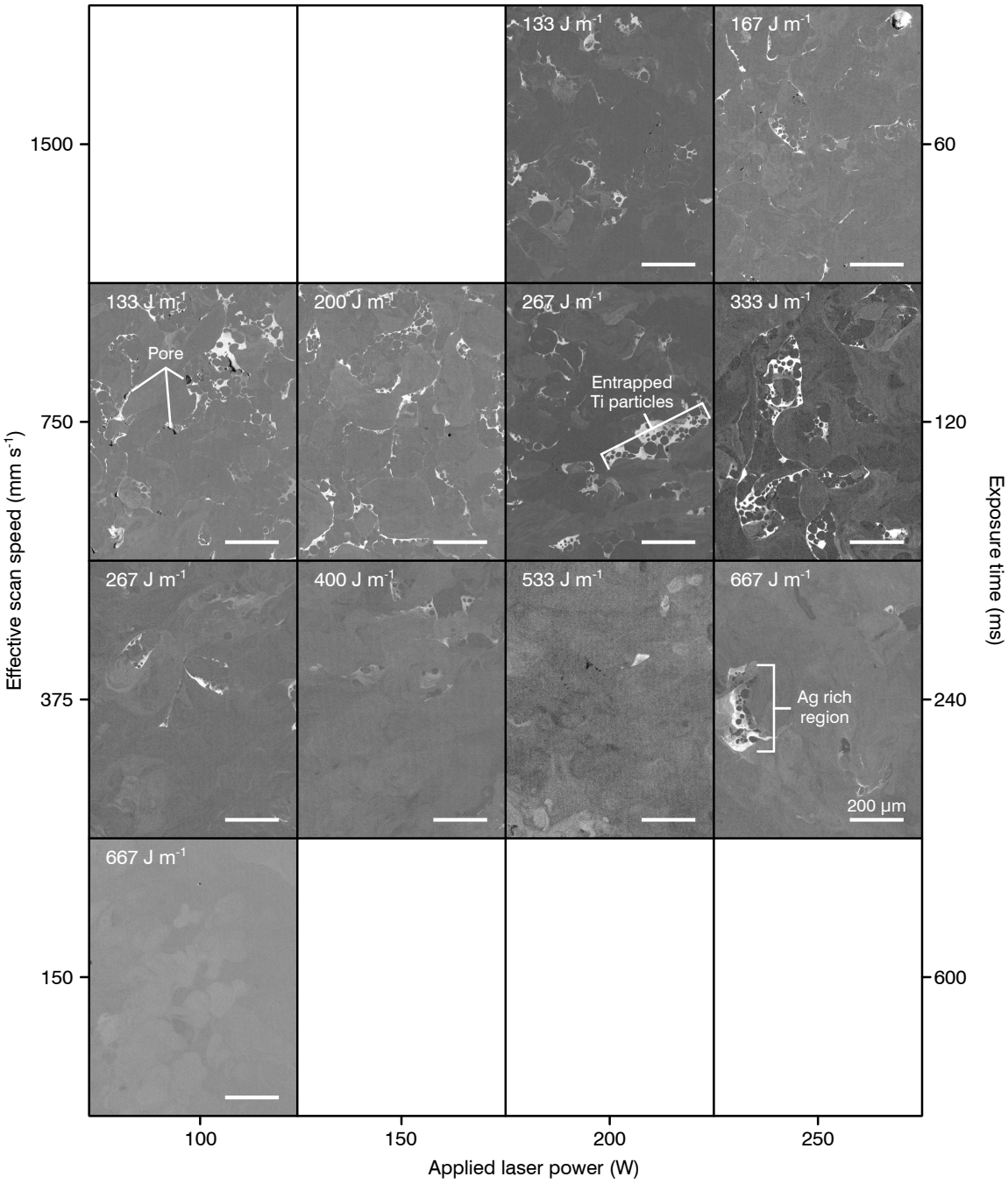


Figure 3.10: Backscatter SEM micrographs of additively manufactured Ti-10Ag. Each sample is labelled with linear energy density (E_d^L) values. Regions of high silver content are identifiable by higher brightness, with larger 200 µm silver regions present than the 30 µm particles in Ti-3Ag. Increasing energy density results in increased microstructural homogeneity, as indicated by fewer bright regions and greater uniformity of greyscale. Spherical Ti particles are visible entrapped within Ag rich regions, as marked.

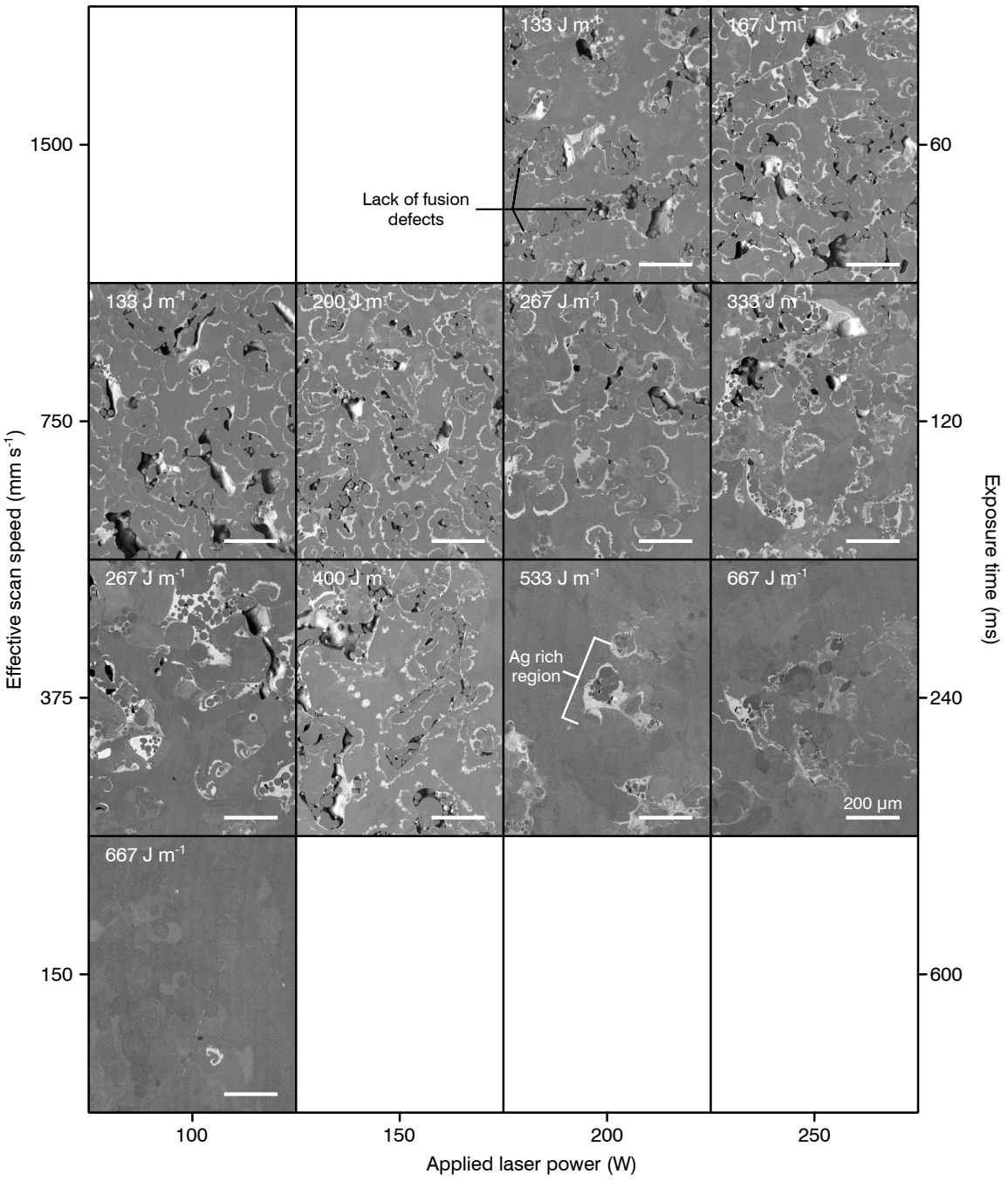


Figure 3.11: Backscatter SEM micrographs of additively manufactured Ti-25Ag. Each sample is labelled with linear energy density (E_d^L) values. Lack of fusion defects are present at lower energy density, alongside regions of silver rich phase identifiable by higher brightness. At higher E_d^L, segregation and porosity decrease, indicated by more homogeneous brightness.

3.3.3 Physical characteristics

Both cp-Ti and Ti-3Ag show trends in density that correlate with increasing energy density, with consolidation improving rapidly up to a plateau around $400\,\mathrm{J\,m^{-1}}$ (Figure 3.12). Measurement of envelope density according to the Archimedes balance method showed densities ranging from 89 to 100 % density compared to the theoretical $4.506\,\mathrm{g\,cm^{-3}}$, though it should be noted that cp-Ti samples at 100 and $67\,\mathrm{J\,m^{-1}}$ exhibited sufficient open porosity that the suspending liquid infiltrated samples, possibly artificially inflating the apparent density. This trend is not apparent for Ti-10Ag or Ti-25Ag, with a random scatter of values showing no clear correlation. Broadly for all materials, a converse trend in porosity is observed with a plateau towards zero porosity above $400\,\mathrm{J\,m^{-1}}$. Both cp-Ti and Ti-25Ag show significantly higher pore volumes at energy density below $200\,\mathrm{J\,m^{-1}}$.

Assessing the silver content measured by XRF, no significant trend in behaviour is present as E_d increases, suggesting that evaporation or sublimation of Ag during processing does not vary between parameter sets (Figure 3.13). The wide variability in apparent Ag content may correlate with inhomogeneity of the powder bed between different layers, providing an indication of the total variability in Ag content within a build. Lower scan speed does appear to reduce Ag content at high energy densities as observed for Ti-10Ag and Ti-25Ag at $667\,\mathrm{J\,m^{-1}}$. Microstructural segregation shows a clearer trend in behaviour as observed in SEM micrographs. Increasing energy density results in increased homogeneity, with all three Ti-Ag blends showing minimal segregated Ag at $667\,\mathrm{J\,m^{-1}}$.

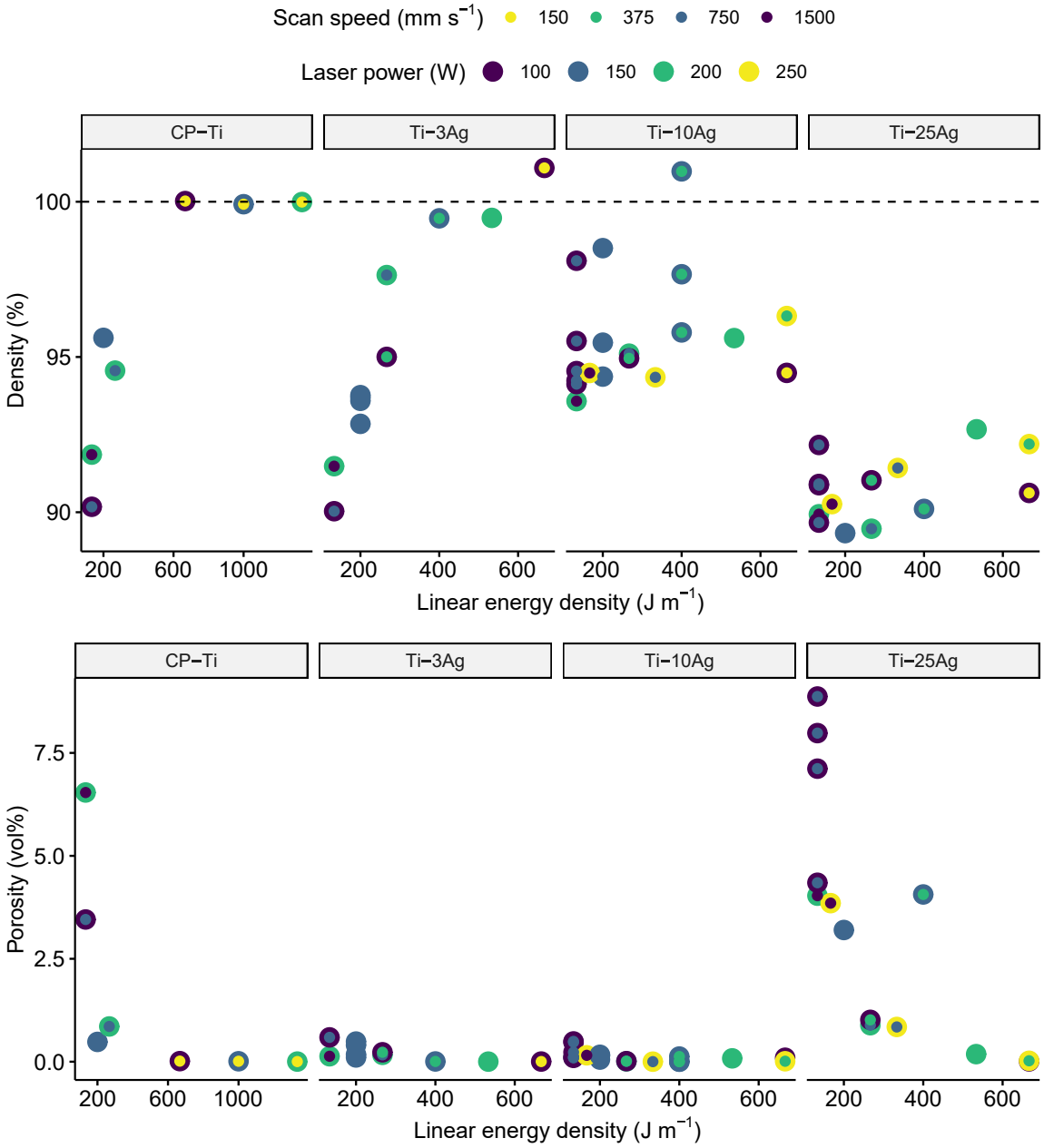


Figure 3.12: Relative density of samples compared to theoretical value of a binary mix of Ti and Ag, and porosity of samples based on SEM image analysis, versus linear energy density. Colour scales representing applied laser power and effective scanning speed are shown, to differentiate between scan parameters with the same linear energy density.

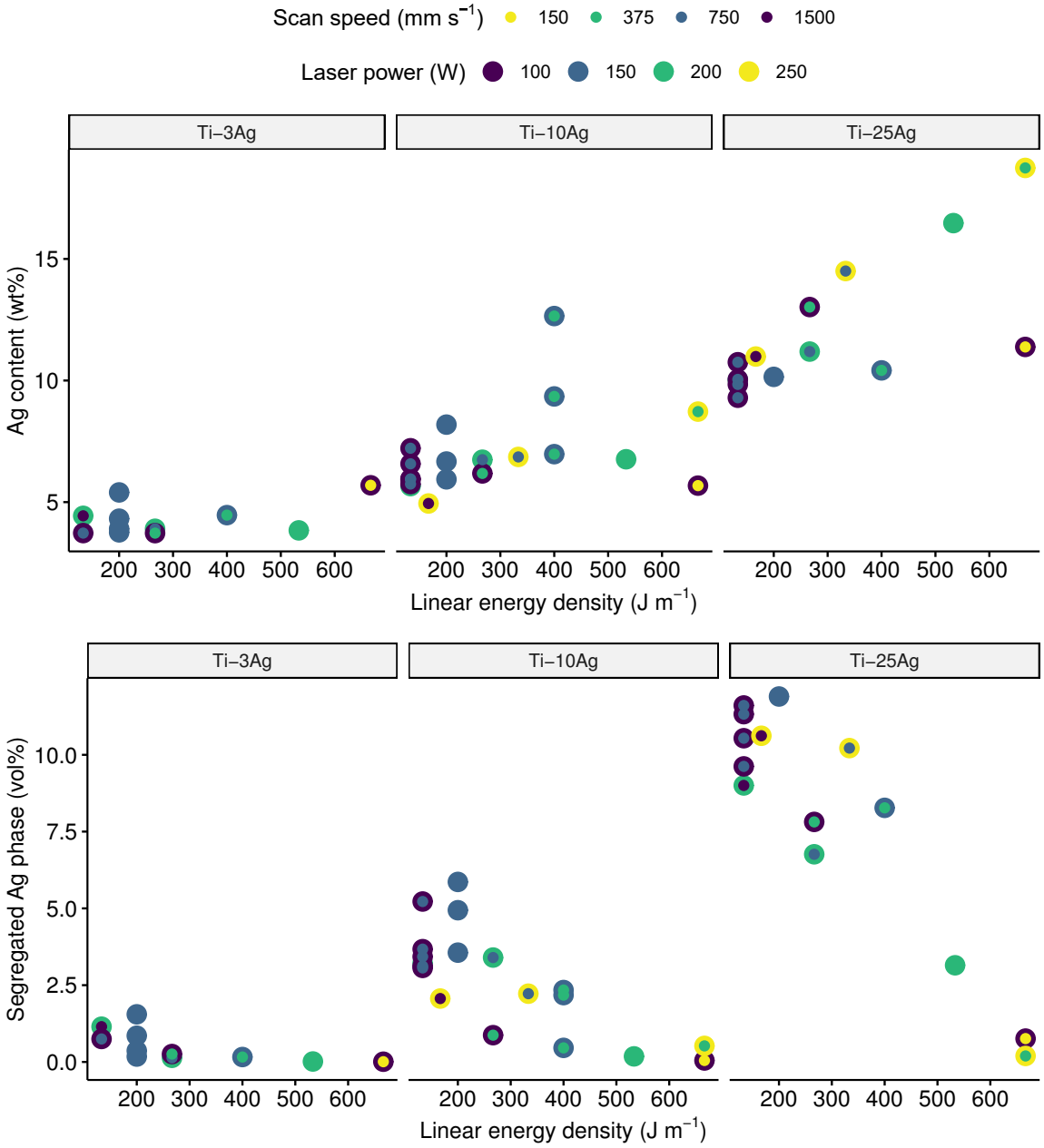


Figure 3.13: Composition of samples according to XRF, and microstructural segregation based on image analysis, versus linear energy density. Colour scales representing applied laser power and effective scanning speed are shown, to differentiate between scan parameters with the same linear energy density.

3.3.4 Variation with build plate position

Investigating location dependent behaviour of Ti-Ag blends, a general trend is observed in the density and Ag content of samples (Figure 3.14). As plate position relative to the recoating direction increases, the density and Ag content increases. No apparent trend is present for porosity.

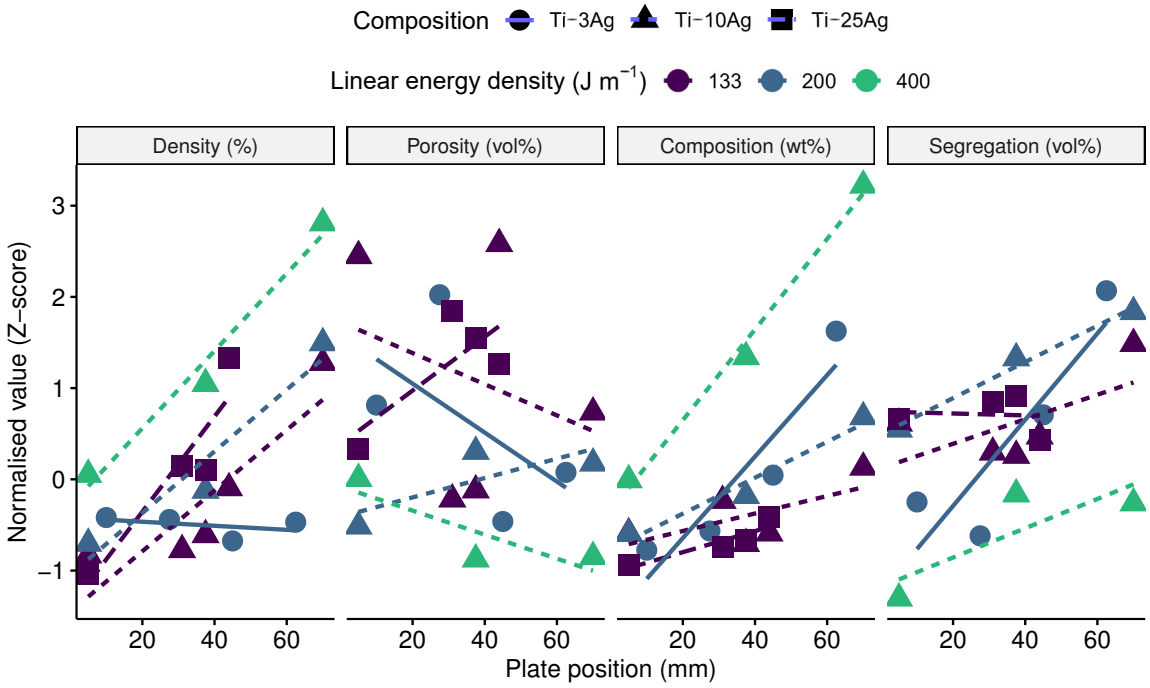


Figure 3.14: Variation of density, porosity, composition and microstructural segregation of Ti-Ag QC samples, versus location on build substrate in the direction of spreading. Values have been normalised relative to the distribution of each build. Linear regression lines of best fit are shown for each series, providing an indication of any trend in behaviour along the build plate. Statistical analysis of these linear fits can indicate whether trends are shared across series, indicating a behaviour that is inherent to the manufacturing process.

Assessing the statistical significance of parameters by applying ANOVA to the model described in equation 3.6, density, composition, and microstructural segregation all show statistically significant dependence on the position of samples on the substrate (Table 3.4). A weakly significant dependence on the interaction of position and the series variable for density and composition can primarily be attributed to the Ti-3Ag 200 J m^{-1} series, which shows outlying behaviour in both cases ($P = 0.031, 0.002$ respectively).

Table 3.4: ANOVA statistical comparison of density, porosity, composition and microstructural segregation relative to position within the build bed, the specific series (i.e. laser parameters and composition), and the interaction of position with series. These variables are labelled β, γ, and δ as per the model described in equation 3.6. Significance is labelled such that $0 < *** < 0.001 < ** < 0.01 < * < 0.05 < . < 0.1 < < 1$. Parameters have been rounded to two significant figures for ease of display.

	Density			**Porosity**		**Composition**			**Segregation**		
	F	P		F	P	F	P		F	P	
Position (β)	56	3.8e-05	***	0.64	0.44	84	7.6e-05	***	15	0.0036	**
Series (γ)	10	0.0021	**	1.8	0.22	22	0.00011	***	6.7	0.0088	**
Pos*Ser (δ)	3.9	0.043	*	0.62	0.66	6.7	0.0089	**	2.0	0.19	

3.3.5 Single track melting

Single and quad track melting tests of Ti-3Ag showed marked variations in layer quality and track continuity. Imaging with SEM shows higher roughness in the plinth surface at lower energy density (Figure 3.15). At $133\,\mathrm{J\,m^{-1}}$, single layer tracks do not appear to stand proud of the underlying surface variation, though four layer tracks are more apparent. Small regions of silver rich phase in the plinth surface and the tracks do not appear to interrupt the continuity beyond general variability seen. The outer contour region of the plinths is also apparent, with a notable difference in surface texture to that of the core (outer 0.3 mm of plinths in Figure 3.15).

Visualising the sample surface by optical 3D measurement, surface properties indicated by SEM are apparent. At $133\,\mathrm{J\,m^{-1}}$, the plinth layer is heavily textured, with areal roughness S_a of $42 \pm 4\,\mu\mathrm{m}$ between tracks (Figure 3.16). This compares to roughnesses of 13 ± 2 and $17 \pm 3\,\mu\mathrm{m}$ at 167 and $267\,\mathrm{J\,m^{-1}}$. As observed by SEM, single layer tracks at lowest energy density are difficult to distinguish from plinth surface variations.

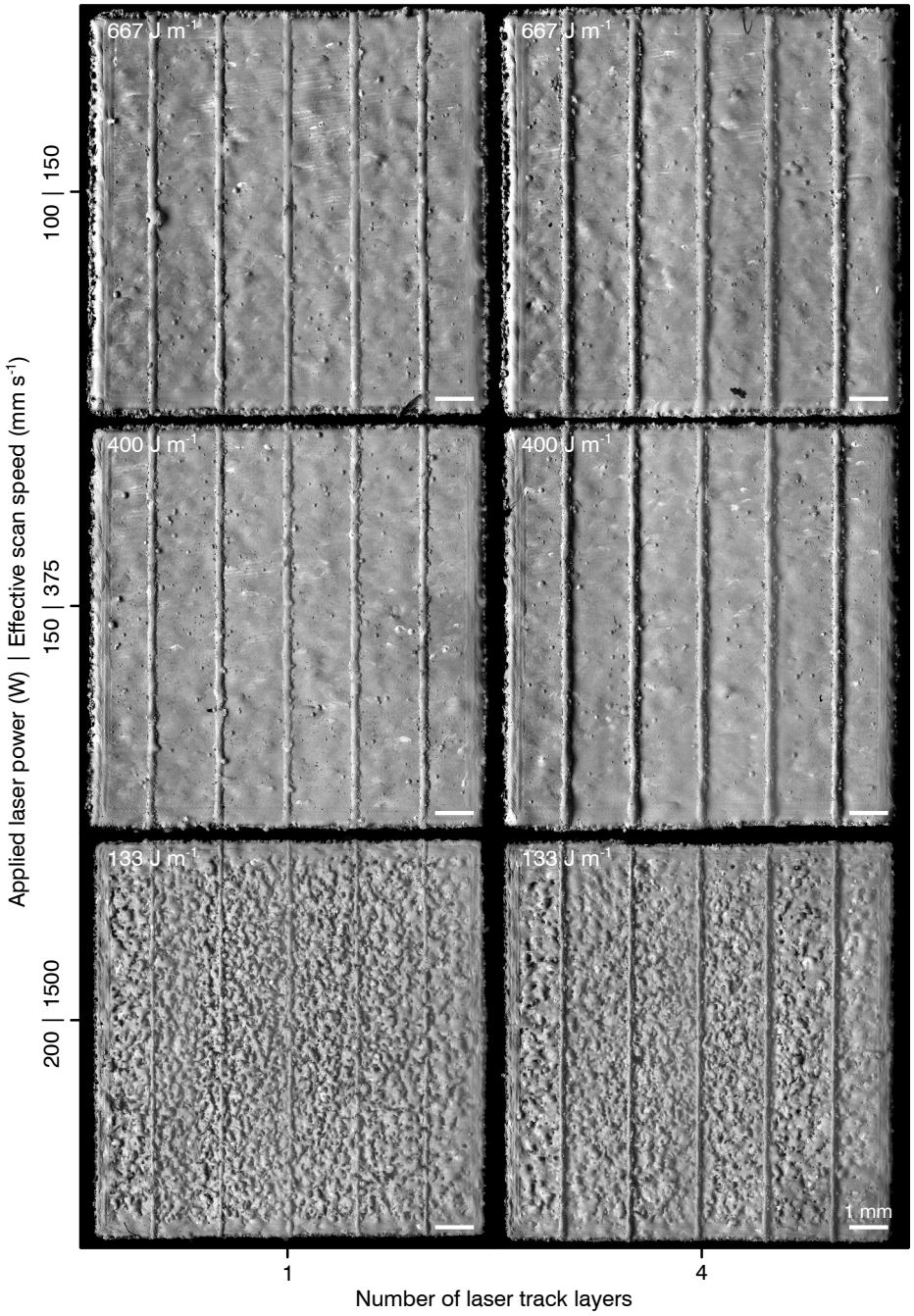


Figure 3.15: Stitched SEM micrographs of Ti-3Ag single and quad laser track melting tests, labelled with linear energy density. At $133\,\mathrm{J\,m^{-1}}$, the surface texture of the plinth is notably pronounced, with single layer tracks difficult to distinguish from the underlying roughness. Contour regions show different surface texture to the plinth, visible as the outer 0.3 mm.

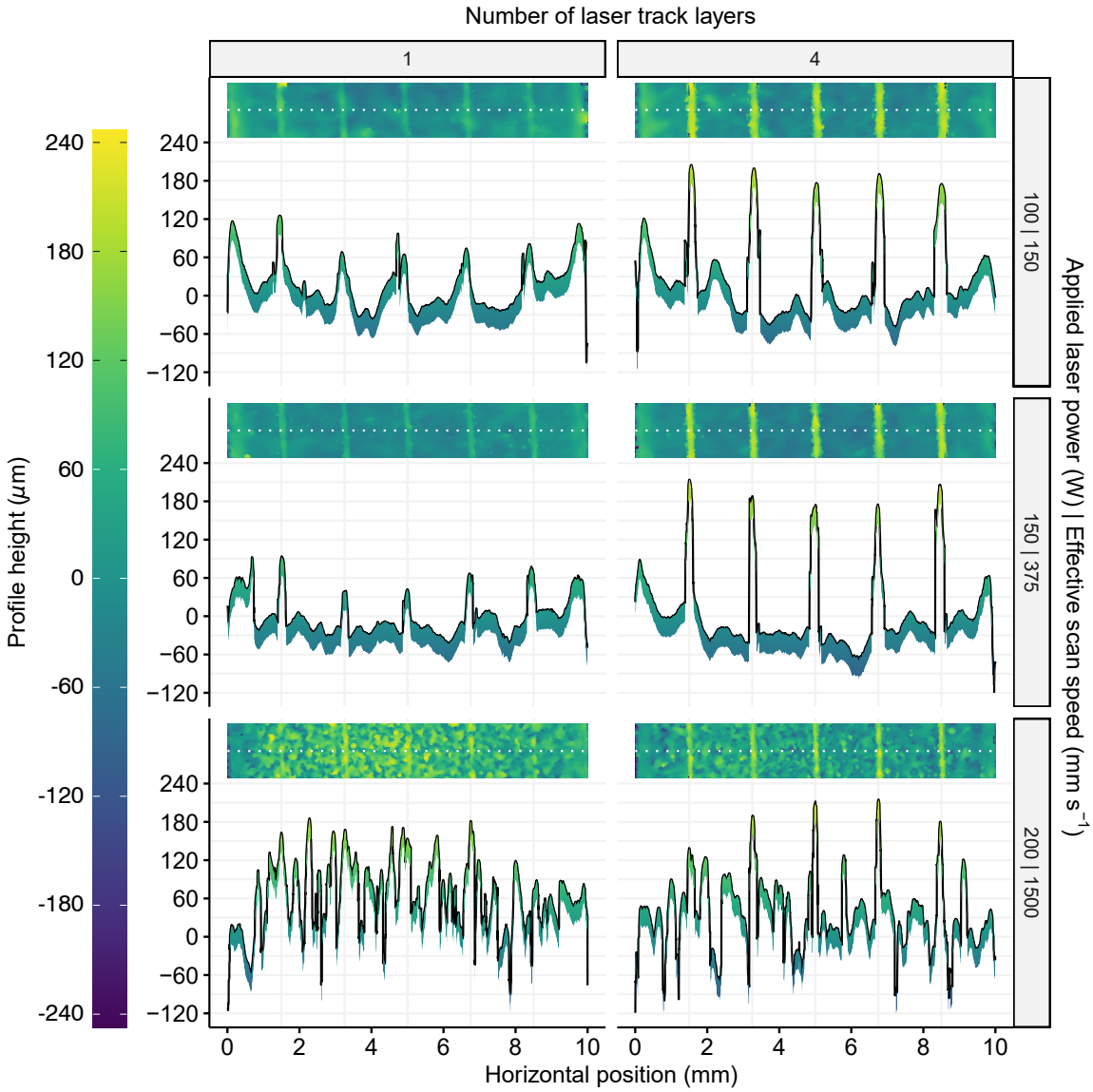


Figure 3.16: Surface profile measurements across Ti-3Ag single and quad laser track melting tests. A 2 mm wide height map across the centre of each sample is shown with a pseudocolour, with a line profile - shown by a dashed white line - represented below. Surface tracks are more easily distinguished from the underlying plinth roughness at higher energy density.

3.4 Discussion

Comparing the manufacturing performance of Ti-Ag to cp-Ti, it is apparent that Ag significantly alters behaviour during SLM. Remarkably, the addition of silver at 3 and 10 wt% improves consolidation, with samples manufactured using the same parameters exhibiting improved density and less visible porosity than cp-Ti. This is particularly clear for samples at $133\,\mathrm{J\,m^{-1}}$ (see Figure 3.8, 3.9, 3.10, and 3.11). This may be unexpected given that silver has a reflectivity of over 85% compared to below 40% for Ti at the 1070 nm wavelength used by the RenAM 500M (Table 3.5), suggesting an increased energy input would be required. There remains some disagreement in the optical constants of Ag, particularly in the near infra red (NIR) region. Tabulated data from Johnson and Christy is frequently quoted, however has a particularly large error margin in the NIR region ($n = 0.04 \pm 0.03$ and $k = 7.15 \pm 0.07$ at 1080 nm) [244]. Experimental determination of behaviour is further complicated by the variation in techniques used, and particularly the extent to which thin metallic films are exposed to atmosphere. Recent attempts to avoid oxidation produce values in good agreement with modelling and a resulting reflectance of 0.54 [245], though whether this accurately represents the realistic optical properties of material not prepared in high purity vacuum is difficult to determine. Though the Ag-999 shows low interstitial content, being N_2 atomised it is unlikely to exhibit the same properties as the high purity films.

Table 3.5: Optical constants of Ti and Ag at 1070 nm, and the implied reflectance and penetration depth for normally incident radiation from vacuum. Calculations assume Fresnel regime reflectivity and Beer-Lambert regime attenuation (see Appendix §A.2).

Material	Refractive index n	Extinction coefficient k	Reflectance R	Penetration depth δ_p, nm	Source
Ti	3.47	4.01	0.31	21.2	[246]
	4.14	4.34	0.37	19.6	[247]
Ag	0.04	7.65	0.85	11.1	[244]
	0.15	7.27	0.54	11.7	[245]

Whilst Ag shows a shorter penetration depth than Ti due to the higher extinction coefficient, reflectance at the initial vacuum/metal interface is significantly higher, both for experimentally derived and modelled optical coefficients [244, 245]. Given the standard specification of SLM powders is typically within the range of 15 to 45 µm, the very short penetration depth ensures any radiation initially transmitted into a particle will be absorbed within the outer 10 to 100 nm skin-layer. As such, the effective power transmitted is dominated by the reflectance of a material. In practise, the absorption of radiation within a powder bed system is significantly more complex than that of a planar solid. Ray-tracing models of powder bed absorption show that where the beam radius is significantly larger than the size of particles, the effective absorptivity of Ag increases by a factor of 7.2 compared to a planar solid. Given the nominal laser spot size of 80 µm and powder size of 15 to 45 µm, more realistic modelling of a Gaussian particle size distribution with similar laser spot size suggests a factor of 4.5 increase in absorbance for Ag [248]. This still, however, places the absorptivity of a silver particle bed at 0.081, below even conservative estimates of the absorptivity of a single Ti sphere of 0.40. In effect, whilst the inclusion of scattering effects within the powder bed is likely to bring the effective absorptivity of Ag closer to that of Ti, it is unlikely to surpass it.

Whilst the relative absorptivity of phases will heavily influence the effective energy input from laser exposures, subsequent thermal and thermodynamic properties will then play a significant role in how this energy is distributed and the effect on melting and subsequent microstructure. Based upon literature values for heat capacity and enthalpies of fusion, the estimated enthalpy to raise Ti and Ag to 2000 K from 298 K, beyond the melting point of Ti at 1941 K, is 70.7 kJ mol^{-1} and 63.3 kJ mol^{-1} respectively [249, 250]. Whilst to melt Ag requires just 38.8 kJ mol^{-1}, as the anticipated energy input to a particle of Ag is estimated to be just a fifth of that to Ti at 1070 nm, achieving full melting across a blended powder bed is still likely to require significantly higher energy input than Ti alone. This estimate neglects the effect of heat diffusion from the melt pool to the surrounding material during the lasing process, effectively modelling the melting of powder as an

instantaneous process. The anisotropy in thermal behaviour across the powder bed can be further demonstrated by considering the difference in thermal diffusivity for Ag and Ti. Effectively acting as a quantification of the thermal inertia of a system, diffusivity provides a indication of how quickly variations in temperature return to equilibrium for a given material.

Thermal diffusivity, α, is given by

$$\alpha = \frac{\kappa}{\rho c_p} \tag{3.7}$$

where κ is thermal conductivity, ρ density, and c_p specific heat capacity at constant pressure. Assessing estimates for α based upon measured or calculated values for κ, ρ and c_p, it is immediately apparent that in both liquid and solid state, Ag particles will rapidly equilibrate temperature variations (Table 3.6). Given the established significance of heat flow down through already solidified material in underlying layers and the low thermal conduction through powder [251], any heat absorbed by Ag - either from direct laser exposure or adjacent melting of Ti - will be more rapidly conducted across the entire particle to surrounding and underlying material.

Table 3.6: Reported thermal conductivity κ, specific heat capacity c_p and density ρ for species in the Ti-Ag binary system at respective melting points, and estimated thermal diffusivity α. Note that estimates of thermal diffusivity in liquid neglect any considerations of convection. *Data for thermal conductivity of liquid Ag taken at 1373 K.

Temp K	Species	κ $\mathrm{W\,m^{-1}\,K^{-1}}$	c_p $\mathrm{J\,mol^{-1}\,K^{-1}}$	ρ $\mathrm{g\,cm^{-3}}$	α $\mathrm{mm^2\,s^{-1}}$	Source
1235	Ag (s)	360	31.4	9.665	130	[250, 252, 253]
	Ag (l)	180*	33.4	9.346	62	[250, 253, 254]
	Ti (s)	15.0	30.2	4.371	5.4	[249, 255, 256]
1943	Ag (l)	180*	33.4	8.703	67	[250, 253, 254]
	Ti (s)	15.0	47.9	4.321	3.5	[249, 255, 257]
	Ti (l)	34.0	48.9	4.195	7.9	[258, 259]

Previous experimental measurements of melt pool behaviour in Ti-6Al-4V have shown peak melt pool temperatures of over 4000 K and cooling rates in excess of $10^7\,\mathrm{K\,s^{-1}}$ [226]. As a crude model to visualise cooling behaviour in Ti and Ag melt pools, consider a 30 µm deep melt pool with a homogeneous initial temperature and ideal interface with a substrate at fixed temperature. Neglecting the slower conduction of heat to surrounding powder particles, the resulting evolution in thermal gradient demonstrates the significantly faster cooling of an Ag melt pool (Figure 3.17) [260]. Crucially, for initial temperatures well in excess of the melting point of Ti, the solidification front transits significantly faster in Ag.

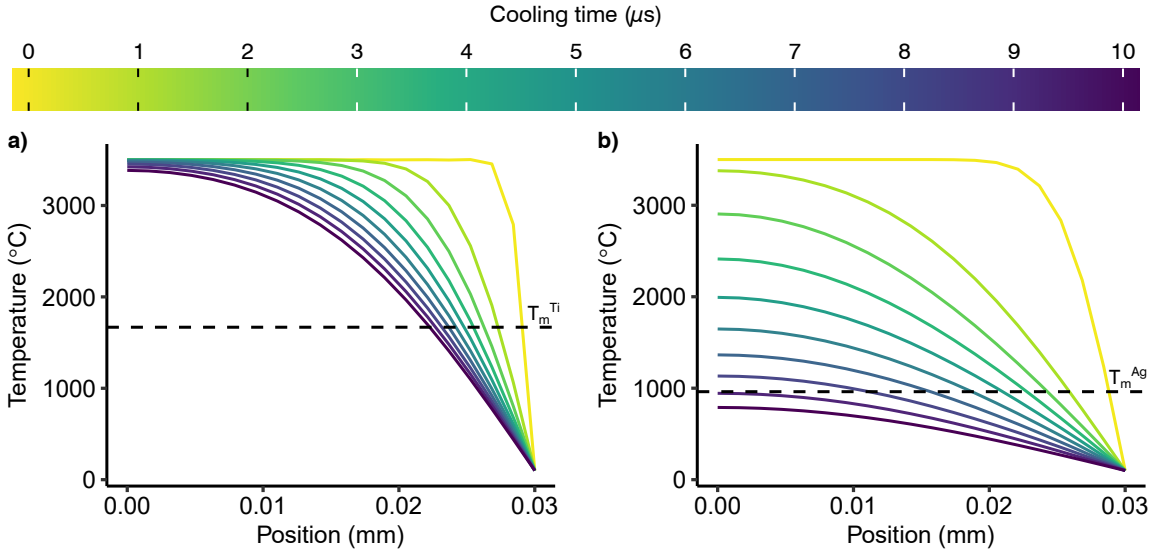


Figure 3.17: Model of thermal evolution in a homogeneous melt pool with an ideal interface to a fixed temperature substrate, for a pure a) Ti and b) Ag melts. Respective melting points are shown to indicate transit of solidification front as cooling time progresses.

To estimate how microstructural evolution is likely to be limited once solidification has occurred, consider a simple case of an infinite source of Ag diffusing into β-Ti in one-dimension. The diffusion length, $2\sqrt{Dt}$, provides a convenient measure of how far solute has propagated after a duration of time, t. The diffusivity, D, can be readily calculated given that Ti and Ag observe Arrhenius diffusion behaviour (Table 3.7). Even at the melting point of the Ti matrix itself, the diffusion length after a second is just 1 µm. Given an ambient chamber temperature of approximately 35 °C, the build bed will cool sufficiently quickly that - beyond remelting due to subsequent layer exposures - once

initial solidification occurs, bulk microstructural evolution can be neglected. In effect, for in-situ alloying, the melt pool lifetime, which can be directly controlled through laser parameters, will be the determining factor in microstructure formation.

Table 3.7: Arrhenius type diffusion coefficients for species in the Ti-Ag binary system. The maximal diffusion coefficient D_0, and activation energy Q, are provided for each of the relevant matrices.

Solute	Matrix	D_0, $m^2 s^{-1}$	Q, $kJ mol^{-1}$	Source
Ag	α-Ti	$(1.00 \pm 0.75) \times 10^{-4}$	279 ± 6	[261]
	β-Ti	$(1.08 \pm 1.25) \times 10^{-3}$	358 ± 18	[262]
Ti	Ag FCC	$(1.33 \pm 0.49) \times 10^{-4}$	198 ± 3	[263]

Given the high anticipated cooling rates, and likely local variations in absorptivity, microstructural evolution of Ti-Ag may therefore be anticipated to follow one of two paths:

1. Homogenisation: by formation of sufficiently large melt pools to form a Ti-Ag melt, with possible further homogenisation in remelting from subsequent layers

2. Segregation: by incomplete melting, or rapid quenching inducing melt segregation through miscibility gap

Considering the microstructures observed in Ti-10Ag and Ti-25Ag, even in segregated microstructures, melting of Ag must be occurring. Unlike classical lack of fusion where the boundaries of particles can be distinguished, the structure of Ag rich regions do not show boundaries consistent with original Ag agglomerations (see Ag particles in figure 3.6c versus 3.10). However, spherical pockets of Ti rich phase are observed within the Ag rich regions, consistent instead with retention of Ti particles. These Ti pockets are frequent across all segregated microstructures, giving the appearance of Ag bubbles forming the surface of Ti cores. A suggested mechanism for this is shown in figure 3.18, with the reduction in energy due to reflection and the rapid conduction of heat in liquid Ag (Table 3.6) meaning that Ti particles captured in Ag melt pools are not melted. This results

in the well defined boundaries between phases. As observed in SEM of Ti-Ag powder blends, agglomerations of Ag particles have a tendency to capture approximately 5 µm Ti fines (Figure 3.6), but the size of these particles does not correlate with the 15 to 45 µm Ti pockets observed in solidified microstructures.

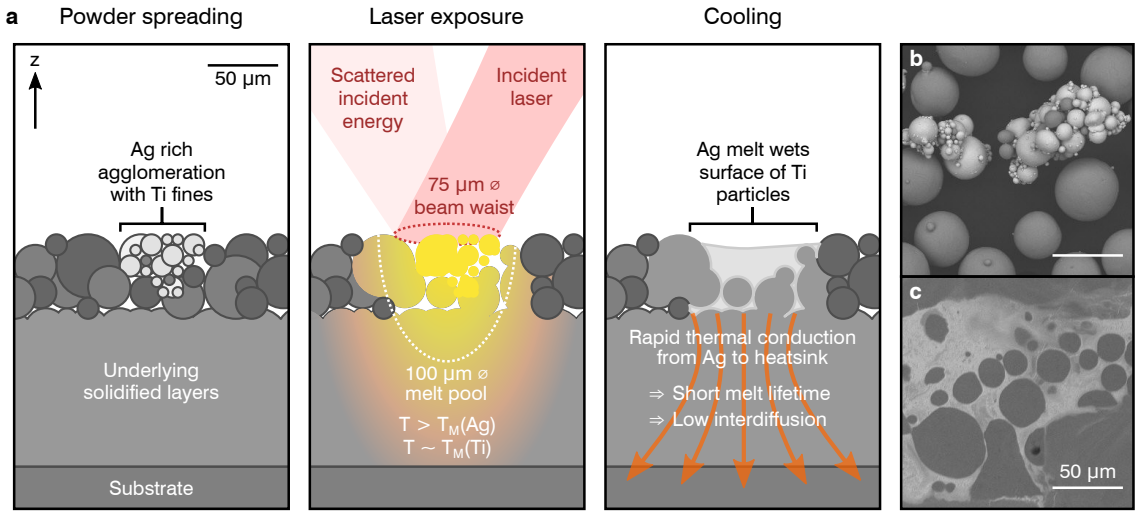


Figure 3.18: a) Schematic of suggested formation mechanism of segregated microstructures observed in Ti-Ag blends. Silver rich agglomerations are packed within the predominantly Ti powder layer. Upon laser exposure, the low absorptivity of Ag results in temperatures that far exceed the melting point of Ag, but are similar to or below that of Ti. Combined with the rapid cooling observed in SLM, Ti particles solidify before homogenisation occurs, followed by solidification of the surrounding silver rich melt. b) Example powder particles, and c) resulting microstructure. Note the discrepancy in size of 5 µm Ti fines within the Ag rich agglomeration, versus the 15 to 45 µm Ti pockets in solidified microstructure.

The unexpected improvement in consolidation at 3 and 10 wt% Ag could be attributed to the reduction in liquidus temperature of Ti. Whilst on a bulk scale the addition of 10 wt% Ag will only reduce the liquidus and solidus temperatures from 1668 °C to 1625 and 1638 °C respectively, at the boundary between Ag and Ti particles the local concentration will be significantly higher once melting begins. Above 32 wt% or equivalently 17 at%, the gap between solidus and liquidus widens dramatically, with the solidus fixed at the melting point of TiAg at 1025 °C (Figure 3.1). In effect, this means that provided a degree of mixing occurs at the Ti-Ag particle boundary during melting, the solidification temperature of the Ti melt pool will decrease. This in turn will likely increase the

melt pool lifetime, allowing more time for a Ti melt to fill surrounding interstices before solidification is induced by diffusion of heat to the surrounding material.

Given that porosity increases again for Ti-25Ag, particularly pores associated with adjacent silver particles, it is apparent that several competing effects are likely in evidence. As Ag content increases and the effective absorptivity of the powder bed decreases, the local absorption will eventually reduce to the extent that heating of Ti is insufficient to melt adjacent Ag particles, thereby reducing the role of the solidus effect. This in turn correlates with the extremely poor consolidation observed for pure Ag even at significantly higher energy densities (up to $1833\,\mathrm{J\,m^{-1}}$).

The differences in consolidation behaviour as energy density increases is shown clearly through the single track melting experiments performed in Ti-3Ag, especially regarding the differences between final track layers and the underlying top surface of the Ti-3Ag plinths. The surface of 400 and $667\,\mathrm{J\,m^{-1}}$ show minimal roughness, with only small spatter particles adhered between tracks (Figure 3.15). In contrast, at $133\,\mathrm{J\,m^{-1}}$ agglomerated molten splashes are clearly visible, and the approximate geometry of some individual powder particles remain present.

Considering the extreme surface roughness of the low energy density plinth surface ($133\,\mathrm{J\,m^{-1}}$), it is surprising that porosity of less than 0.2 % is apparent under SEM (Figures 3.9 and 3.12). The clear distinction of the plinth contour from the core of the samples provides an indication of how this may occur, with a smoother texture apparent. The additional re-melting of contour regions that occurs before subsequent spreading of powder results in improved apparent consolidation. The re-melting of underlying material is inherent to the adequate bonding of layers in PBF processes, and whilst the powder layer attenuates this compared to the contouring process, it will still be sufficient to allow the densification that must be occurring in these low energy density samples. As silver content increases up to Ti-25Ag, the net absorptivity of the layer decreases, and given the poor flow dynamics of Ag-999 particles, we may expect rougher powder layers. This may contribute to a lack of infill in the underlying roughness of low energy density samples,

and the dramatic increase in porosity from a maximum of 0.6 % in Ti-3Ag to 8.9 % for Ti-25Ag (Figure 3.12).

Whilst the feasibility of producing a range of microstructures has been demonstrated, a key consideration for manufacturing with blended powders is the concern of spread induced de-mixing during processing. As has been demonstrated, a higher silver content is measured towards the end of spreading each layer (Figure 3.14), suggesting that silver particles are preferentially deposited towards the end of the spreading motion. This correlates with visual observations of higher Ag particle frequency in the excess powder slop at the end of each sweep. The elevated silver content partly explains the increased density and greater microstructural segregation seen in these samples. It is interesting that the fraction of porosity observed does not show a significant trend based on bed position, indicating that spontaneous variability within this small sample size masks any effect that Ag particles may have on pore formation. This is despite an apparent association of silver at the surface of pores in Ti-25Ag, though this apparent correlation does not indicate any causal link.

De-mixing may be induced by large variations in particle size within a given powder. The deposition of larger particles at the end of recoating sweeps has been demonstrated both in computational modelling and physical experiments [264–266]. Whilst the powder blends are monomodal, agglomeration of Ag-999 is observed under SEM (Figure 3.6), and this may be a contributing factor. The response to spreading conditions may also be contingent upon the differing density or flow behaviour of Ag. The high cohesivity of Ag-999 and tendency to agglomerate both in pure feedstock and Ti-Ag blends may link to the nobility of Ag. Whilst Ti powders form a passive oxide surface film even in low oxygen atmospheres, Ag and other precious metals show much lower tendency to oxidise. The presence of oxide films may play a significant role in reducing the cohesive surface energy of metal powders [267]. As shown by inert gas fusion measurements, the oxygen content of the Ag powder is 0.006 %. Concurrent to this, the surface area of particles is also an established factor in powder cohesion, with finer particles showing a greater tendency

towards agglomeration [268]. Though the PSD of cp-Ti and Ag powders are similar and monomodal, as observed by SEM the Ag consists of agglomerated and satellited particles of far smaller individual size, simultaneously increasing the surface area and the risk of particle inter-locking causing disrupted flow [266].

Changing the physical characteristics of the Ag powder will be crucial to establishing which factors dominate the spread induced de-mixing behaviour. Improving feedstock sphericity and altering surface chemistry could provide indications to whether de-mixing can be avoided, or is a natural consequence of the significant differences in density of Ti and Ag.

3.5 Conclusion

The feasibility of manufacturing high density Ti-Ag alloys from blended powder feedstocks was demonstrated by selective laser melting. Significantly, the ability to produce distinct microstructures whilst retaining high densities was proven by altering scanning parameters. Use of energy densities below $300\,\mathrm{J\,m^{-1}}$ was shown to cause significant microstructural segregation, with silver rich agglomerations within a Ti matrix. Densification and microstructural homogeneity increased with applied energy density, with samples manufactured below $200\,\mathrm{J\,m^{-1}}$ at significantly higher risk of porosity. Statistical analyses of sample behaviour dependent on position indicated de-mixing of powder components during spreading, with reduced Ag deposition towards the start of each spread. This has significant implications for future manufacture of blended powder alloys.

CHAPTER 4

INVESTIGATION OF BINARY TITANIUM SILVER ALLOY BEHAVIOUR

In order to provide localised antimicrobial prophylaxis for metallic implants, formulation of an inherently antimicrobial alloy would be advantageous. This work investigates previous claims of efficacy for Ti-Ag alloys.

In order to elucidate the relationships between composition, microstructure, and antimicrobial efficacy of Ti-Ag, a series of alloys ranging from 6 to 25 wt% Ag with different thermal histories have been considered. In-depth microstructural characterisation with SEM and TEM confirmed the formation of Ti_2Ag precipitates after ageing for up to 555 h. Both nanoscale and bulk lamallae of intermetallics correlated well with the established phase diagram for the binary system, with the ability to suppress precipitation during quenching from β-Ti solid solution to supersaturated α-Ti also confirmed. Bulk characterisation confirmed a predominantly TiO_2 oxide layer, with no significant changes in oxidation state between supersaturated solid solution alloys, and equilibrium intermetallic precipitated samples. Across the range of microstructures and compositions assessed, no antimicrobial efficacy against *S. aureus* was observed under the study conditions used. The absence of antimicrobial response is likely linked to the lack of Ag release from alloys, due to the low corrosion potential of silver in the metallic state.

This calls into question previously asserted elution-free mechanisms for efficacy in Ti-Ag, with the presence of either nanoscale or bulk Ti_2Ag insufficient. Based upon these results, it should be feasible to further narrow the possible routes of antimicrobial efficacy for future biomedical alloys.

ACKNOWLEDGEMENT OF CONTRIBUTING MATERIAL AND AUTHORS

As primary author, M Lowther produced all written work within this chapter and performed all primary experimental work. The contributions of co-workers are as follows:

- Dr. M D Wadge: Performance of XPS measurements and assistance with analysis.
- Dr. M Wang: Assistance with twin jet electropolishing of TEM samples.
- Dr. J Nutter: Performance of TEM imaging.
- C Stark: Assistance with the operation of ICP-OES.
- Prof. L M Grover, Dr. S C Cox: Editorial and supervisory guidance.

4.1 Introduction

With increasing frequency of antimicrobial resistant nosocomial and implant associated infections, increasing emphasis is placed on alternative modes of antimicrobial delivery, and the use of a wider variety of antimicrobials [37]. Inorganic antimicrobials, such as metal ions and oxides, are of particular interest given their lower tendency for resistance development versus antibiotics [269], and the possibility of easier integration into existing biomaterials.

In concert with this, formulation of antimicrobial alloys has been a field of interest for some time. Whilst Cu alloys have long been favoured for self-sterilising behaviour in healthcare settings, such as brass contact points [270–272], the cytotoxicity of Cu has limited its use in biomedical alloys [273–275]. Conversely, though use of silver doped alloys has been less extensive in healthcare settings, it has frequently been used as an alternative inorganic antimicrobial in vivo, with an extensive history of Ag coatings and surface treatments for orthopaedic implants [276]. The implantation of silver alloys has predominantly been limited to dental regimes, given its historic use as an alloying component of up to 70 wt% in dental amalgams and casting alloys [277]. However, antimicrobial efficacy has not been a focus of these materials, and their use may not be appropriate in other implantation sites.

As Ti and Co-Cr alloys remain the predominant implanted metals for hard tissue repair, both Ag doped Co-Cr and Ti alloys have been explored in laboratory settings [228, 278]. Given the biocompatibility of Ti alloys, owing to the stable Ti oxide and its osseoconductive nature, more extensive research has been performed on the development of binary Ti alloys for biomedical applications [279]. The Ti-Ag binary system is characterised by high solubility of Ag in the body-centred cubic β-Ti phase, with Ag acting as a weak β-stabiliser (Figure 4.1, modified from [280]). Two intermetallic phases - body-centred tetragonal γ-Ti_2Ag and primitive tetragonal η-TiAg - are present. Whilst Ti_2Ag shows a stoichiometric composition, investigations have shown a widening of the TiAg phase field at higher temperatures. The most rigorous explorations of the Ti-Ag alloy

system has been due to interest in the Ti-Ag-Cu ternary, commonly used as a diffusion barrier layer when joining Ti alloys to dissimilar materials [280, 281].

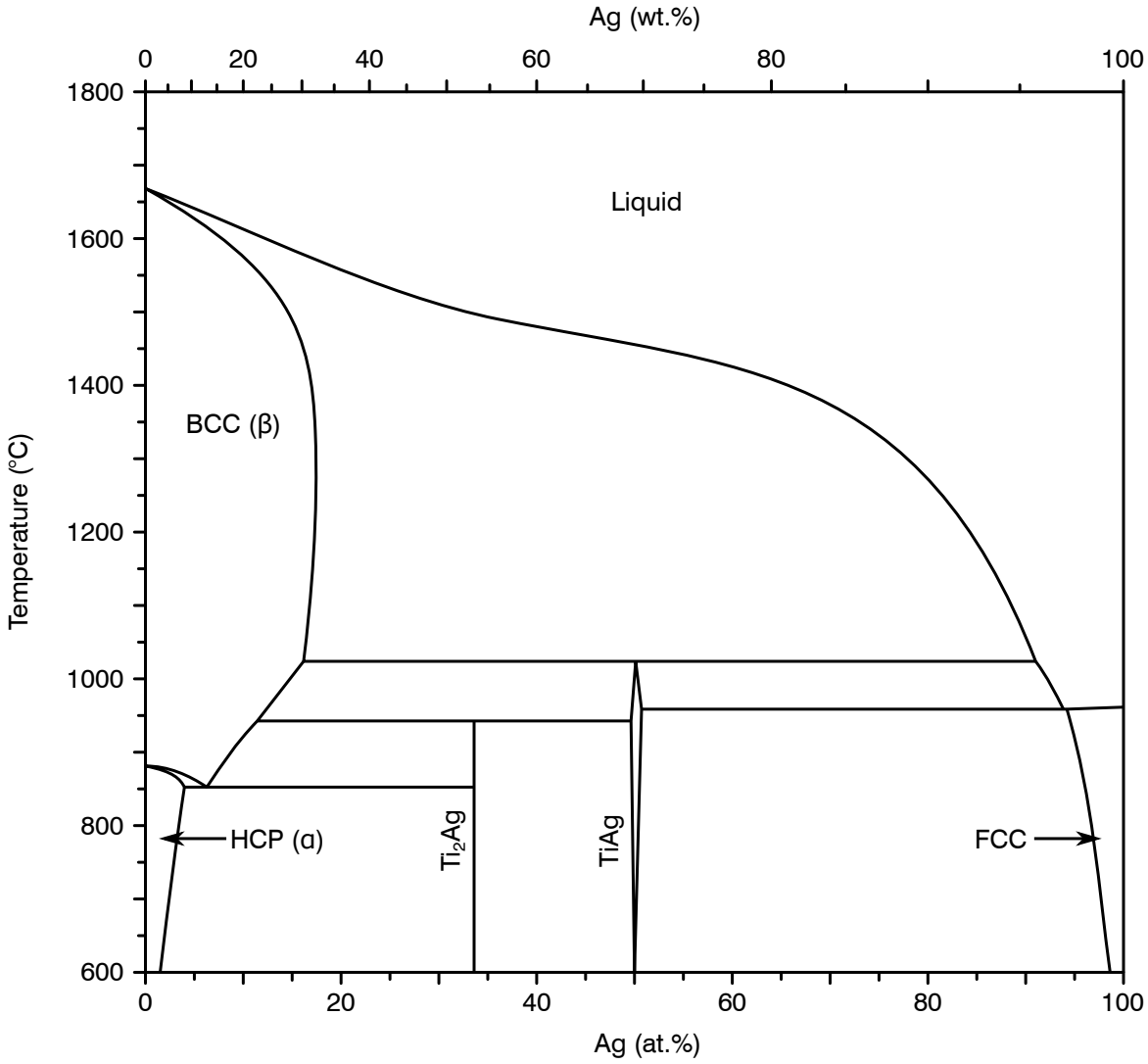


Figure 4.1: Binary phase diagram for the Ti-Ag system. Adapted from Dezellus et al, 2011.

Brazing applications tend to focus on high Ag and Cu content, with additions of below 10 wt% used to allow the Ag-Cu eutectic to wet Ti alloys [282]. For biomedical applications, it is desirable for Ti to form the majority of the alloy, with sufficient Ag content to achieve the desired antimicrobial properties. Alongside ensuring sufficient efficacy against infection, it is important to minimise long-term exposure to any physiologically active compounds where possible. Whilst most patients show good tolerance of silver compounds, the risk of atypical responses should be considered. Case series for silver

coatings of megaprostheses have reported localised argyria in 23 % of implantees, despite no neurological symptoms and no elevated blood silver levels versus non-presenting patients [75]. More frequent reports of negative reactions to silver in burn patients have been reported, though this is likely due to the high prevalence of silver coated dressing use for burn treatment, typically delivered as nanocrystalline Ag bonded to a polymer mesh [283–285].

For biomedical use, the primary focus of Ti-Ag alloys has been for dental usage. The need for durable, biocompatible materials able to cope with a corrosive environment makes Ti-Ag alloys a natural fit. Thanks to the high nobility of Ag, corrosion resistance in artificial saliva solution is improved compared to pure Ti alone at Ag concentrations up to 15 wt% [124, 228, 286–288]. As is the case for conventional Ti alloys, fluoride ions - commonly used in topical dental applications - have been shown to disrupt the passive TiO_2 film, but to a reduced extent compared to cp-Ti [287, 288].

Mechanically, reports into the binary alloy indicate reduced ductility on the addition of Ag. Materials with up to 25 wt% Ag showed increased ultimate tensile strength (UTS) and yield strength than pure Ti, at the expense of reduced elongation [227]. Microhardness assessments of cast alloys show increasing hardness with Ag content, as acicular $\alpha - \beta$ Ti or lamellar Ti-Ti_2Ag microstructures form [227, 228], with sintered materials also showing significantly higher hardness than cp-Ti [286, 289].

Previous efforts to produce Ti-Ag alloys have used a variety of approaches, ranging from powder metallurgy routes of sintering to conventional ingot casting. It is important to consider that the manufacturing route will influence the possible complexity of implant structure that can be achieved. For large scale production, investment casting is likely to reach a near final implant geometry more efficiently. Production of antimicrobial alloys has been explored primarily by casting, with mass fractions of up to 15 wt% considered. There is however, no direct relationship between alloy composition and efficacy, further complicated by variations in definition of antimicrobial efficacy. Ti alloys with as low as 0.7 wt% Ag have demonstrated over 98 % kill rate against both *S. aureus* and *E. coli*

[290], whilst alloys with a greater silver content show negligible antimicrobial behaviour [116, 124, 286]. As yet, explanations of this have focussed on linking efficacy to specific intermetallic phases, rather than silver in solid solution or metallic form [124].

Ternary and thin-film Ti-Ag alloys further complicate the relationship between microstructure and efficacy. Antimicrobial response has been observed from an Ag rich phase in Ti-Nb-Ag alloy which does not show the tetragonal Ti_2Ag structure [290], whilst Ti-Ag thin films and surface modifications have also shown efficacy that is independent of Ti_2Ag, with metallic silver or Ti_3Ag attributed [291]. The efficacy of alloys has been notably variable, with the minimum concentration within alloys needed ranging from 1 to 15 % (Figure 4.2) [124, 286, 290, 292].

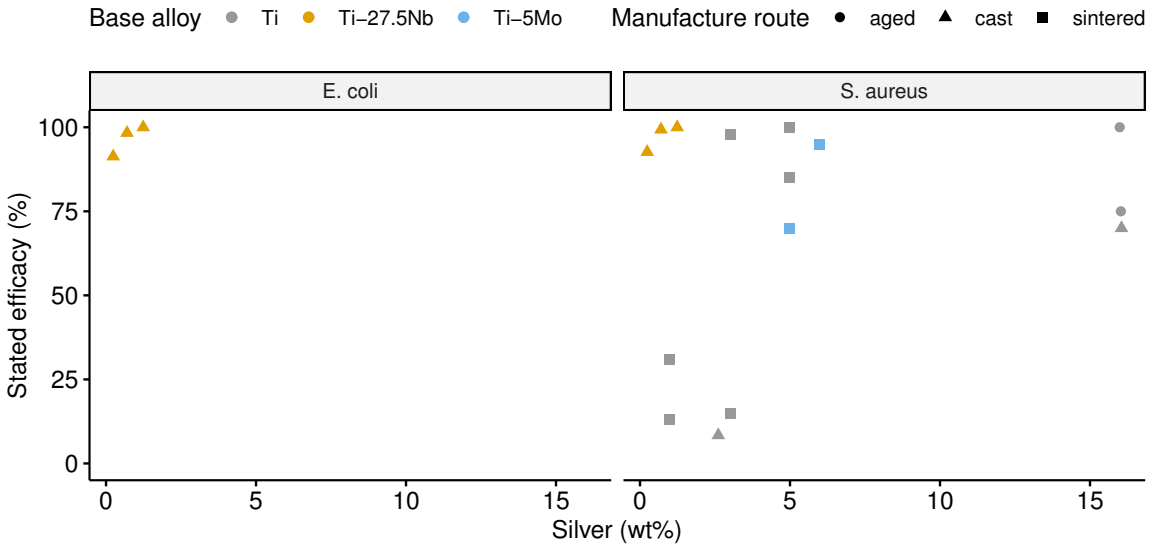


Figure 4.2: Summary of previously demonstrated antimicrobial Ti-Ag alloys, with the stated efficacy against *E. coli* and *S. aureus* shown.

The range of preparation methods, lack of detailed reporting of subsequent microstructures, and microbial testing methodologies used (Table 4.1) complicates discussion of the specific mode of action of Ti-Ag, with suggestions ranging from ionic release of silver to surface contact with nanoscale intermetallic precipitates [124, 293]. No positive controls are presented in any of these studies, making claims regarding their relative efficacy difficult to assess.

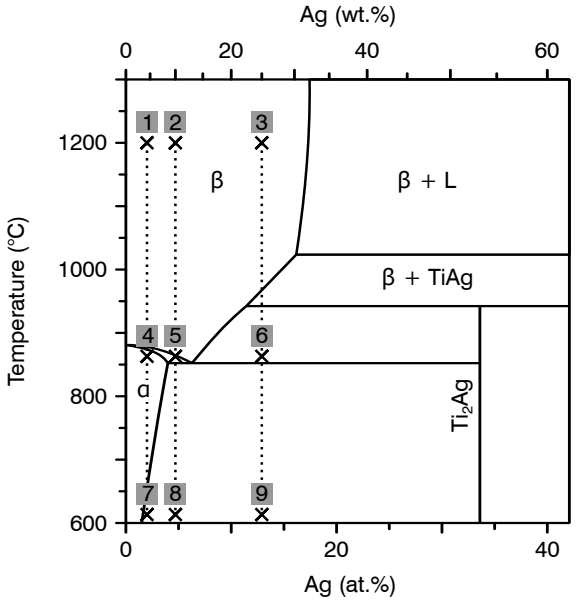
Table 4.1: Parameters used in previous bacteriological assessments of antimicrobial Ti-Ag alloys.

Species	Media	CFU mL^{-1}	Duration (h)	Media to sample ratio ($mL\,cm^{-2}$)	Source
S. aureus	Nutrient broth	10^5	24	0.04	[286]
S. aureus	Nutrient broth	10^5	24	Not stated	[124]
S. aureus; *E. coli*	Nutrient broth	4×10^5	24	0.5	[290]
S. aureus	PBS	10^6	24	0.25	[292]

In brief, the key requirements for antimicrobial efficacy in Ti-Ag alloys have not been established, with alloy composition, phases present, and microstructural features frequently confounded within the literature. To attempt to separate these factors, a fundamental study of the Ti-Ag system is needed. Starting from well homogenised feedstocks, heat treatments in different phase fields allows precipitation and ageing of precipitates to generate variable microstructures.

Considering the phase diagram (Figure 4.1), several key compositional regimes can be considered in the low silver content region. Given the intention to start from homogenised stock with nominally identical microstructure independent of composition, homogenisation must occur in the body centred cubic (bcc) β-Ti state. This establishes a maximum Ag content of 25 wt% at which this can reliably be achieved. If it is possible for alloys in the solid-solution state to exhibit antimicrobial behaviour, feedstocks of different composition within this phase field should determine any dependence on Ag concentration (Figure 4.3).

As the presence of Ti_2Ag precipitates has been posited as the key cause of efficacy, subsequent controlled precipitation by ageing will enable comparison of how phases present alter antimicrobial response, independent of bulk composition. Considering the hexagonal close packed (hcp) α-Ti phase field, a minimum of 6 wt% Ag is necessary to precipitate Ti_2Ag at 600 °C. Any further reduction in silver content is likely to require prohibitively



1	
2	Homogenisation in β phase field
3	
4	Ageing in α phase field
5	Ageing in α-β hypoeutectoid field
6	Precipitation in β-Ti_2Ag field
7	Precipitation in α-Ti_2Ag field
8	
9	Ageing of precipitates in α-Ti_2Ag field

Figure 4.3: Annotated section of Ti-Ag binary phase diagram, indicating the composition and heat treatments used to generate samples in this work. A brief description of each point is provided.

low temperatures for ageing, such that kinetic barriers for nucleation and diffusion may not be overcome.

With the sequence of key equilibrium phase fields established, consideration must be given to the manufacture of an initial feedstock which may be homogenised in the β-Ti field. Whilst ingot casting has been frequently investigated for Ti-Ag alloys, reliable melting of Ti without contamination with interstitial elements such as O and N can be challenging and requires specialised inert furnaces. The dissimilar melting temperatures and miscibility gap of Ti and Ag may also prove challenging [294]. Conventional sintering can be performed at lower temperatures, but requires significant time to achieve good densification. Instead, hot isostatic pressing (HIP) of blended Ti-Ag powder feedstock allows rapid densification in an inert atmosphere, whilst avoiding the melting of alloy components. The resulting feedstock is likely to be locally inhomogeneous, providing another microstructural state to be assessed for antimicrobial efficacy.

Based upon this need for a targeted study, this work aims to establish what compositional and microstructural characteristics control the antimicrobial efficacy of Ti-Ag

alloys. In order to assess the effect of Ag content and microstructure independently, Ti-xAg with 6, 10 and 25 wt% Ag were produced and subjected to a series of heat treatments. Specific phase fields within the established Ti-Ag binary were targeted. Thorough microstructural assessment was performed, with a focus on confirming the specific phases present and validating the existing phase diagram. A combination of SEM, XRD, and compositional measurement by EDS were used to characterise the alloys produced. Specific alloys of interest were investigated by transmission electron microscopy (TEM) and X-ray photoelectron spectroscopy (XPS). Alloys were then characterised for antimicrobial response. Given the importance of *S. aureus* in nosocomial infections and the established literature regarding its response to Ti-Ag, it was chosen as a clinically relevant species. Finally, to elucidate mechanisms for any observed variations in efficacy between alloys, their response to culture conditions was assessed, with extracts from a release study investigated for metal ion elution.

4.2 Materials and methods

4.2.1 Alloy production and sample preparation

Feedstock preparation

Commercially pure grade 1 titanium (cp-Ti) (LPW Ltd) and high purity Ag-999 (CooksonGold Ltd) powders of 15 to 45 µm size distribution were blended in ratios of 6.0, 10 and 25 wt% Ag. Powder blends were homogenised by roller blending for 10 h under Ar atmosphere with O_2 below 40 ppm and H_2O content of below 3 ppm. Homogeneity was assessed by SEM (TM3000, Hitachi) and LPSD (Mastersizer 2000, Malvern). Particle size analysis was performed at two wavelengths, with red 633 nm and blue 433 nm lasers. Tween 80 detergent was used as required, with distilled water as the dispersant fluid. A Mie scattering hard sphere model of particles is assumed. For cp-Ti and blended Ti-Ag powders, refractive indices of pure titanium were used [246], as both numerically and

by volume the Ti alloy particles dominates the blend. For analysis of Ag-999, refractive indices for pure silver were used [244].

Hot isostatic pressing

Welded mild steel cans of 2.5 cm diameter and 15 cm height, degreased with anhydrous acetone, were filled with use of vibration table to ensure compaction. Cans were evacuated overnight before crimping to seal. Powders were densified by HIP at 850 °C with a dwell time of 4 h, with applied isostatic pressure of 150 MPa and heating and cooling rates of 5 °C min^{-1}. Post HIP, cans were sectioned lengthways into quarters by EDM (CUT 20 P, GF AgieCharmilles). Cylindrical cores of 12.5 mm diameter were removed from the centre of each segment to minimise interdiffused contamination from the canning steel. After EDM, the passivated oxide surface of each sample was removed by manual grinding with 240 grit SiC paper (MetPrep Ltd). Samples were then assessed for density using an Archimedes balance (Adventurer Precision AX223, Ohaus) in anhydrous ethanol.

Heat treatment

Subsequent heat treatments were performed in a box furnace, with temperature monitored by K-type thermocouple (Table 4.2). To minimise oxidation, samples were wrapped in 0.1 mm thick Mo foils (Sigma-Aldrich) to act as a getter, and encapsulated in 99.999% quartz (Multi-Lab Ltd), evacuated and backfilled with Ar. Fresh Mo foil and quartz encapsulation was used for each subsequent heat treatment, with oxide films removed by grinding with 240 grit SiC paper before re-encapsulation.

Table 4.2: Parameters of heat treatments used for samples

Heat treatment	Label	Temperature (°C)	Cooling	Duration (h)
Hot isostatic pressing	HIP	850	Furnace cooled	4
Homogenisation	HOM	1200	Water quench	120
Primary ageing	A1	865	Water quench	435
Secondary ageing	A2	600	Furnace cooled	120

TEM sample preparation

EDM was used to cut 500 µm thick discs of materials. Both faces of sections were sequentially ground using SiC papers to a thickness of below 120 µm. A hole-punch was used to cut 3 mm diameter discs from the thinned sections. Discs were twin-jet electropolished (Struers Tenupol-3) with 5 % perchloric acid / methanol solution cooled to below −10 °C with liquid nitrogen, at an applied potential of 10 V.

Microbiological sample preparation

Samples were sectioned and manually polished to 2400 grit according to procedures described in Table 4.3. Control samples of Cu (99.99%, Alfa Aesar) and Ag (99.9%, Alfa Aesar) were cut from 1.0 mm thick foils. Squares of length 11 mm were cut such to maintain surface area equivalent to Ti-Ag discs. In order to produce cp-Ti controls, the same powder used for blending of alloys was manufactured into solid cylinders of 12.5 mm diameter by SLM using the machine default parameters for Ti-6Al-4V (RenAM 500M, Renishaw).

Table 4.3: Sequence of polishing procedures used to prepare samples for bacteriological testing.

Step	Surface	Dosing	Duration (min)	Rotation (rpm)
1	400 grit SiC	Water	1:00	150
2	1200 grit SiC	Water	3:00	250
3	2400 grit SiC	Water	3:00	250

Sterilisation was performed by immersion in 75% ethanol and drying in a sterile flow cabinet.

4.2.2 Physical and chemical characterisation

Electron microscopy

SEM images were taken of mounted and polished samples (TM3000, Hitachi) equipped with an EDS module (Oxford Instruments). Images were taken in BSE mode to provide elemental contrast with the high atomic number of silver. Contrast and brightness adjustments were made using the Fiji distribution of ImageJ [241, 242]. Point EDS spectra were taken of key microstructural features, with large area scans taken at x500 magnification for 100 s to assess bulk composition. Measurements were taken at five locations on each sample. EDS measurements were taken at the recommended focal distance of approximately 7.5 mm, with standard background correction for spectra used in the Bruker QuantAX software package during quantification.

TEM analysis was performed on select samples (JEM-F200, JEOL). TEM, scanning transmission electron microscopy (STEM), EDS and electron energy-loss spectroscopy (EELS) measurements were made of features of interest. Key microstructural features were also used to generate selected area electron diffraction (SAED) patterns, which were indexed against reference files (Table 4.4) using the CrystalMaker SingleCrystal software package (version 4.0.3).

Table 4.4: Reference files used for indexing of TEM SAED patterns.

Phase	Reference	Crystal structure	Source
α-Ti	90008517	Hexagonal close packed (6/mmm)	[295, 296]
Ti_2Ag	mp-979115	Tetragonal (4/mmm)	[297]

Quantitative STEM-EDS mapping data was analysed taking the ratio of Ti and Ag at each point (R 4.0.2), with the net ratios converted to a point raster image. Regions within each image were analysed for the average composition of the respective area (ImageJ 1.52g).

X-ray diffraction

In order to establish the bulk phases present, 1 mm thick discs were subjected to XRD analysis using a Bruker D8 diffractometer with a Cu-Kα anode. Diffraction patterns were collected between $2\theta = 25°$ to 85°, using a step size of 0.02° and acquisition time per step of 0.3 s. Bruker Diffrac.EVA software (version 4.2.2) was used to analyse collected patterns, with background automatically removed and peaks indexed against references from the International Centre for Diffraction Data (Table 4.5).

Table 4.5: Reference patterns used for identification and indexing of alloy phases in XRD.

Phase	Reference pattern	Quality mark	Crystal structure
α-Ti	00-044-1294	Star	Hexagonal close packed (6/mmm)
β-Ti	00-044-1288	Calculated	Body centred cubic
TiAg	00-006-0560	Blank	Tetragonal (4/mmm)
Ti_2Ag	01-078-9899	Prototyping	Tetragonal (4/mmm)

X-ray spectroscopy

For assessment of surface oxidation state, 1 mm thick discs were used for XPS with a VG ESCALab Mk II photoelectron spectrometer, combined with an Al-Kα anode. An incident angle of 30° was maintained for all substrates, with calibration conducted using the C 1s spectra peak, charge corrected to 284.8 eV. Survey and high-resolution scans were conducted over a binding energy range of 0 to 1200 eV, with step sizes of 1 and 0.2 eV and acquisition times of 0.2 and 0.4 s per step respectively. Five scans were taken in each case, with resulting spectra analysed in CasaXPS. Full Width at Half Maximum was constrained to the same value for all deconvoluted spectral peaks for the same element. In addition, all j-j coupling/spin orbit splitting peaks, most notably Ti 2p peaks, were constrained to an area ratio of 2:1 for 3/2:1/2 peaks, respectively.

Hardness testing

Vickers microhardness testing of mounted and polished samples was performed at 50x optical magnification and 100 g indentation force (Buehler Wilson VH1202). Five indentations were made per sample, with additional tests made to distinguish between the Ti matrix and large intermetallic particles in the as-HIPed state. Measurement of indents was performed automatically, with manual adjustments made when software failed to accurately locate indent corners (DiaMet, Buehler).

4.2.3 Microbiological characterisation

Bacterial cultures used unsupplemented LB broth (Lennox, Sigma) or LB agar (Lennox, Sigma) plates, and were under aerobic conditions at 37 °C. Calibration of colony forming units per mL (CFU mL^{-1}) to optical density at 600 nm (OD_{600}) was performed using a spectrophotometer (Evolution 300, Thermo Scientific), with an OD_{600} of 0.2 approximately equal to 10^8 CFU mL^{-1}. For all tests, overnight cultures in LB broth were initially grown to 10^{10} CFU mL^{-1} at 37 °C and 150 rpm. This overnight culture was then diluted 100-fold in fresh LB broth, re-incubated for 2 h before dilution to an OD_{600} of 0.020, equivalent to approximately 10^7 CFU mL^{-1}. A 20 µL droplet of culture was pipetted onto sterile alloy discs, and incubated for 4 h at 37 °C, in order to assess the initial colonisation period.

Samples were then transferred to 2 mL of aqueous 0.024 m M Tween 80 detergent, equivalent to twice the critical micelle concentration, and vortexed for 10 s. The resulting suspension was sampled and serially diluted for viable CFU by the Miles-Misra method [183]. Selected additional samples were also cultured for a 24 h period under the same protocol.

4.2.4 Release study

Three sample discs of each material were suspended in 3 ml of sterile LB broth culture media to achieve alloy to media ratio of 0.4 $mL\,cm^{-2}$, and incubated for 15 d at 35 °C in dark conditions. Resulting media was acidified with 10 % hydrochloric acid before filtration through 0.22 µm PES filters. Acidified samples were subjected to ICP-OES (Perkin-Elmer 8000 Optima), with matrix-matched Ag and Ti standards used for calibration. In and Sc internal standards were used to correct the intensities of Ag and Ti respectively due to their similar atomic weights.

4.2.5 Statistical methodology

Prior to any assessment of the statistical significance of results, samples were assessed for equal variance using Levenes test ($\alpha = 0.05$). Where equal variances were confirmed, one-way Fisher ANOVA was used to determine if any difference in means was observed. For statistically significant differences in mean, the Tukey-Kramer post-hoc test was used for comparison and on an individual alloy basis, with nominal composition (6, 10 and 25 wt%) and alloy state (HIP, HOM, A1, A2) treated as a single variable ($\alpha = 0.05$). For results with non-equal variance, Welchs ANOVA and the Games-Howell post-hoc test were instead applied ($\alpha = 0.05$).

In order to assess the significance of nominal composition and alloy state on behaviour, results were also subject to two-way ANOVA ($\alpha = 0.05$). The results of fitting the general linear model are listed in table 4.8.

4.3 Results

4.3.1 Alloy production

All three powder blends exhibited a distribution of Ag particles throughout, visible both by visual inspection and SEM (Figure 4.4). Ag-999 showed a tendency to agglomerate, with cp-Ti fines of below 5 µm frequently captured in the agglomerations. All particle size distributions show good agreement with a nominal 15 to 45 µm size range, with d_{10} ranging from 19 to 26 µm and d_{90} 48 to 53 µm. Ti-25Ag shows the highest d_{10} and d_{50}, which may indicate a greater agglomeration of fine particles, though no bi-modality of the distribution is apparent.

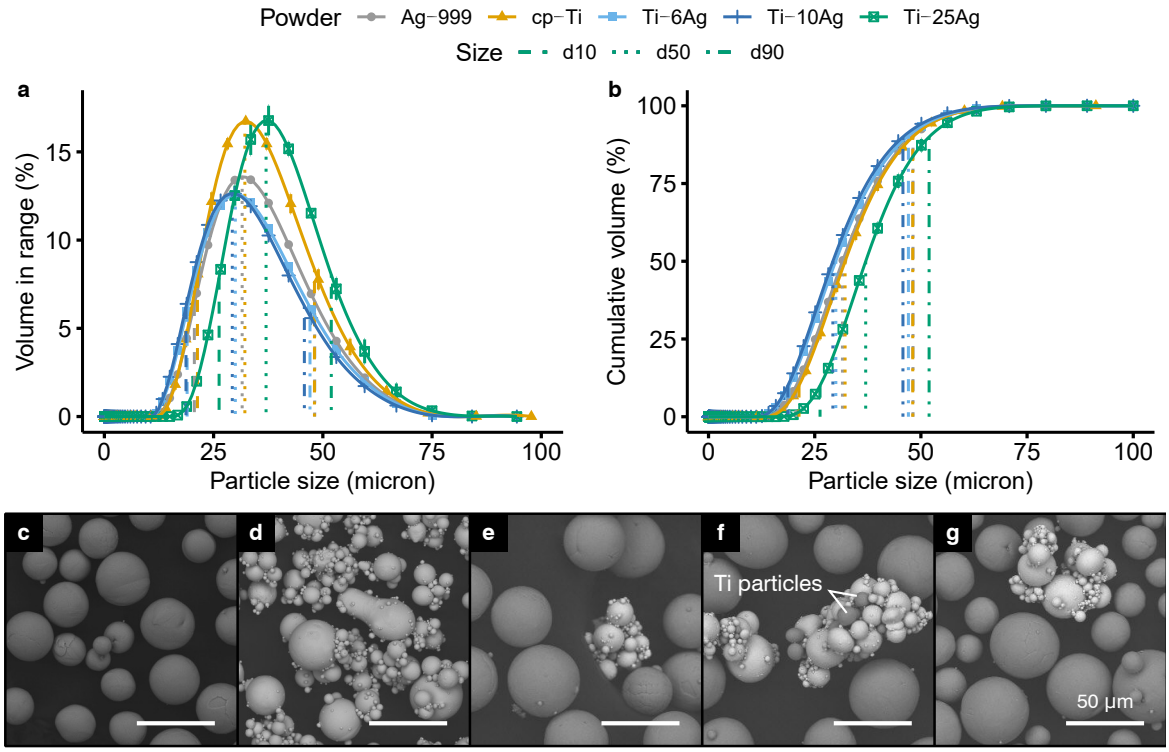


Figure 4.4: Particle size analysis of feedstocks, with a) range and b) cumulative size distributions; and SEM micrographs of c) cp-Ti, d) Ag-999, e) Ti-6Ag, f) Ti-10Ag, and g) Ti-25Ag powders. Accumulation of fine Ti particles onto Ag agglomerates is marked in d).

After HIP each alloy ingot was sectioned into four segments. The uniform densification and distribution of Ag between segments was confirmed by Archimedes balance assessment, with densities of 4.69 ± 0.01, 4.77 ± 0.02 and $5.30 \pm 0.06\,\mathrm{g\,cm^{-3}}$ for Ti-6Ag, Ti-10Ag and Ti-25Ag respectively. Predicted densities for a binary mix of Ti and Ag would be 4.579, 4.691 and $5.168\,\mathrm{g\,cm^{-3}}$ respectively.

Analysing the oxygen content of alloys post heat treatment, all samples exhibited oxygen content below 0.5 wt% (Figure 4.5a). Broadly, oxidation over the course of heat treatment is lower for higher Ag content. The composition of alloys is consistent between heat treatment states, though a reduced apparent Ag content of 3.0, 5.4 and 18.1 wt% is observed by EDS in the as-HIPed state (Figure 4.5b). The presence of trace Si, particularly in Ti-10Ag samples after primary ageing, may indicate de-vitrification of the quartz encapsulation.

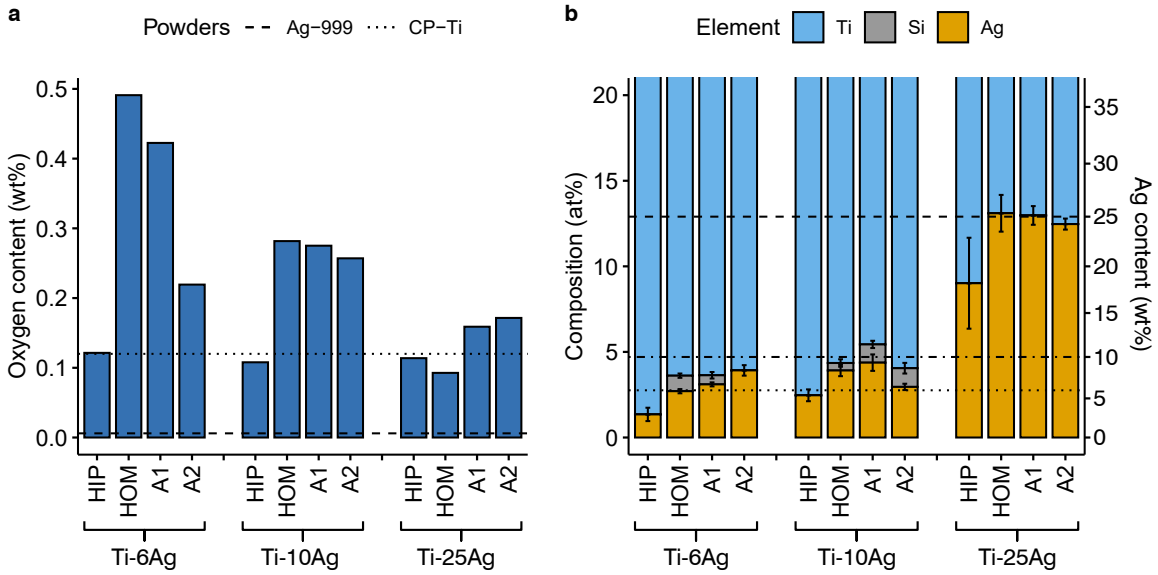


Figure 4.5: a) Oxygen content by inert gas fusion of alloys with base alloy powders shown, and b) composition of Ti-Ag alloys according to SEM-EDS with nominal target composition of 6, 10 and 25 wt% shown. A scale for the wt% of Ag is provided; note that this does not accurately represent the wt% of Si present.

4.3.2 Microstructural characterisation

Scanning electron micrographs taken under BSE imaging conditions provide a visual indication of silver distribution within samples, due to the increased electron yield of Ag. After HIP, high Ag content particles are constrained within the Ti matrix, with a second silver rich phase at the boundary (Figure 4.6). Samples showed good consolidation, with only small amounts of residual porosity visible in Ti-10Ag.

Following homogenisation, no clear microstructural variation or compositional segregation is present in any samples, indicating quenching was sufficient to suppress precipitation. An increased degree of porosity is observed, particularly for Ti-10Ag, suggesting that Ar entrapment may have occurred during HIP, with heat treatment leading to condensation into larger pores. An apparent string-like texture visible in several samples was established as a surface artefact of the polishing procedure, and not a microstructural feature.

Primary ageing results in precipitation of Ti_2Ag in the Ti-25Ag samples, with a lamellar microstructure interspersed with larger intermetallic precipitates. Both Ti-6Ag and Ti-10Ag remain homogeneous in structure. Following secondary ageing, fine grain boundary precipitates are found in Ti-6Ag (Figure 4.7 a and b). No significant change in microstructure is observed for Ti-25Ag A2, indicating that the primary ageing process was sufficient to achieve an equilibrium microstructure. No high-contrast phases are present in the aged Ti-10Ag samples, indicating a lack of silver rich phases. Dark, irregularly shaped precipitates do appear in Ti-10Ag A2.

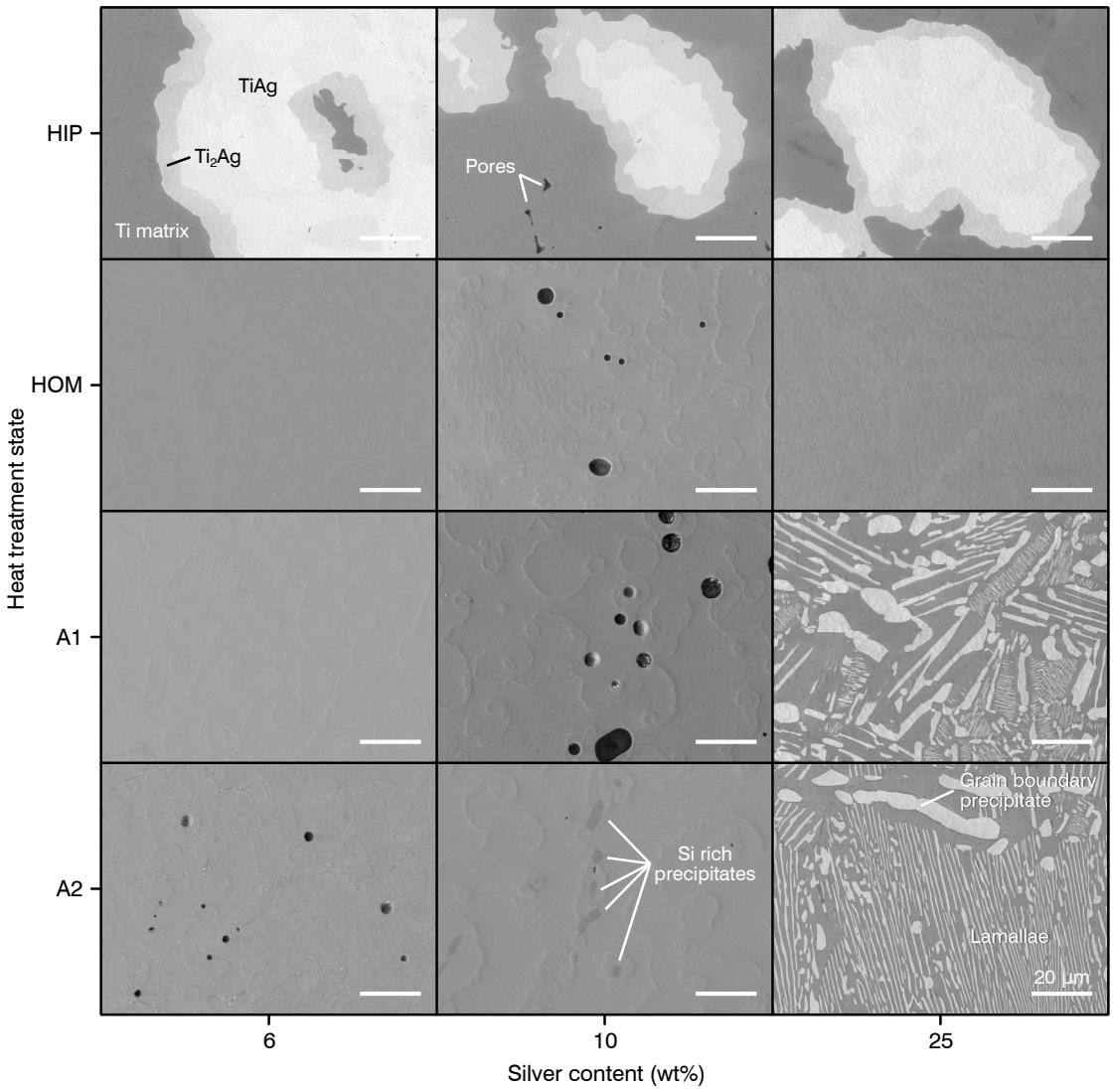


Figure 4.6: SEM micrographs of Ti-6Ag, Ti-10Ag, and Ti-25Ag after at each stage of the heat treatment process. Scale bars are 20 µm. HIP samples comprise 100 µm Ag rich particles within a Ti matrix. Porosity is observed in Ti-10Ag, and dark precipitates are present in Ti-10Ag A2.

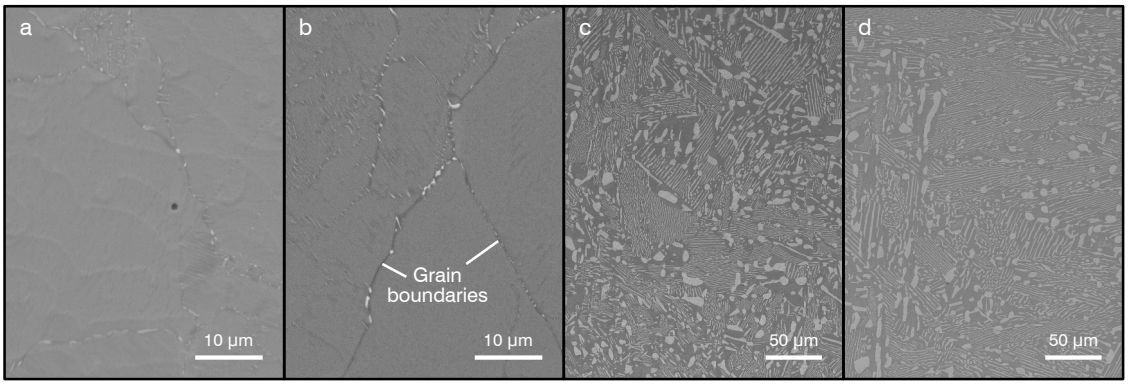


Figure 4.7: SEM micrographs of specific microstructural features of interest; a) and b) grain boundary precipitates in Ti-6Ag A2 indicating precipitation of Ti_2Ag as predicted by phase diagram; and low magnification comparison of Ti-25Ag c) A1 and d) A2, demonstrating that no major changes in microstructural features occurred on secondary ageing.

Provided the microstructures imaged are representative - i.e. assuming samples are approximately isotropic - the area fraction of phases can be directly correlated with volume fraction. The proportion of intermetallic phase in both Ti-25Ag A1 and A2 correlates with the current binary phase diagram (Table 4.6). Due to the small scale of precipitates present in Ti-6Ag, measurements of phase distribution from SEM micrographs were not feasible.

Table 4.6: Ratio of phases present in Ti-6Ag A2, Ti-10Ag A2, and Ti-25Ag A1 and A2. The expected proportion according to phase diagram is present for nominal and measured composition, alongside the imaged phase ratio by SEM.

	Calculated from phase diagram		*Measured*
Sample	Nominal Ti_2Ag (vol%)	EDS Ti_2Ag (vol%)	SEM Ti_2Ag (area%)
Ti-6Ag A2	3	7	N/A
Ti-10Ag A2	5	5	N/A
Ti-25Ag A1	20	20	34
Ti-25Ag A2	35	34	33

Based upon EDS measurements, as HIPed microstructures consist of a TiAg core with a Ti_2Ag boundary layer (Figure 4.8). However, deviation from the expected stoichiometry is observed (Figure 4.8). In the HIP state, both Ti-10Ag and Ti-25Ag show silver deficiencies of approximately 5 at% in the TiAg phase, whilst Ti_2Ag intermetallics in Ti-25Ag A1 and A2 exhibit measured silver contents of 29 ± 1 at%. This may suggest microstructural inhomogeneity below measured length scales, but there is no clear indication of multiple phases present within these regions. No Ti-Ag intermetallics are noted in aged Ti-10Ag samples, with precipitates previously noted instead Si rich particles. Their darker colouration is therefore due to reduced backscatter yield from Si.

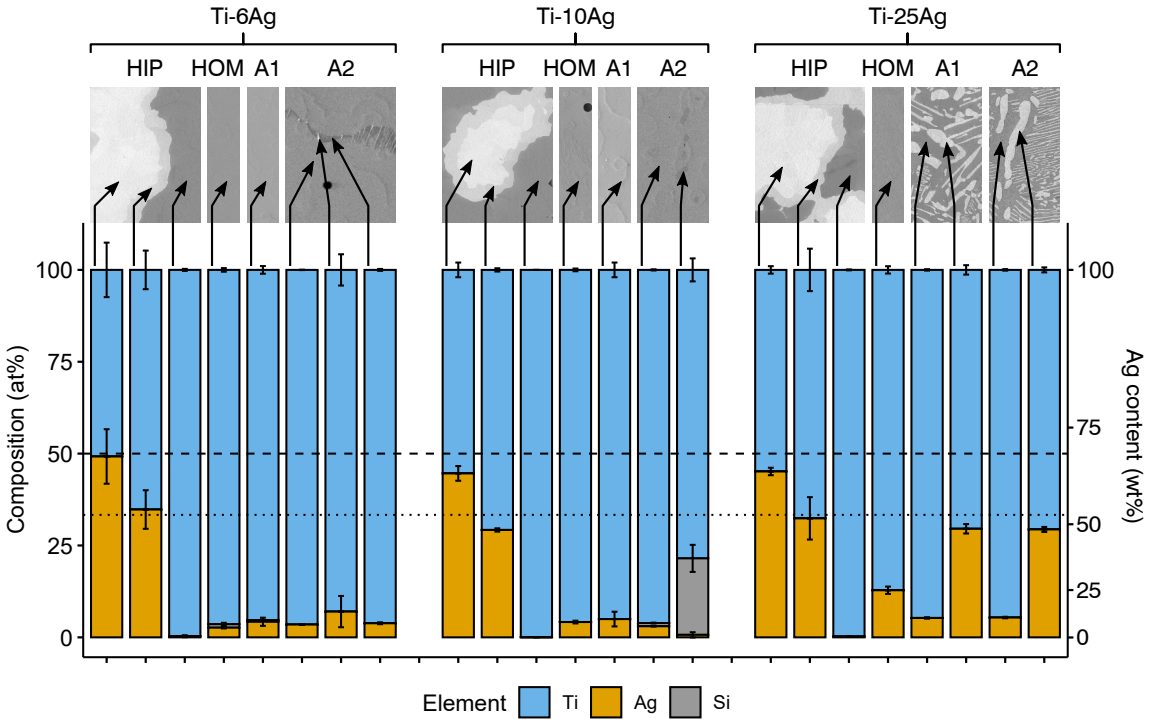


Figure 4.8: Composition of individual microstructural features according to SEM-EDS. A scale for the wt% of Ag is provided; note that this does not accurately represent the wt% of Si present.

To investigate the microstructure of intermetallic precipitates in the secondary aged state, Ti-6Ag A2 and Ti-25Ag A2 were subjected to TEM. Bright and dark field images indicate grain boundary precipitates present in Ti-6Ag (Figure 4.9), as was observed in SEM. An apparent depletion zone is present either side of grain boundaries, with very fine 30 nm precipitates distributed in a band outside of the depleted region (Figure 4.9c). Dislocation pile-ups are frequently observed around precipitates, indicating they may provide pinning locations (Figure 4.9d).

In Ti-25Ag A2, the lamellar nature of precipitates is apparent, with 0.5 µm wide lamellae visible (Figure 4.10 a and b). Lamellae appear wedge-shaped, though this is likely an artefact of increasing sample thickness away from the thinned hole edge, visible also in the decreasing contrast at the top left of micrographs. As in Ti-6Ag, dislocations are visible. Clusters of dislocations bridge perpendicular between individual Ti_2Ag lamellae (Figure 4.10 c and d).

Identification of phases from SAED patterns confirmed that microstructures consisted of hcp α-Ti and tetragonal (I4/mmm) Ti_2Ag precipitates for both Ti-6Ag and Ti-25Ag A2 (Figure 4.11) [297]. This correlates with predicted phases from the current Ti-Ag phase diagram (Figure 4.1).

Attempts to generate EELS spectra to investigate local oxidation state were unsuccessful due to excessive thickness of samples, indicating the need for further optimisation of electropolishing. Efforts to thin samples by Ar ion milling (Precision Ion Polisher System, Gatan) resulted in sample damage, negating any reduction in thickness.

Quantitative compositional maps of microstructures indicate a higher proportion of Ag present in the core of precipitates than the 33 at% expected for Ti_2Ag stoichiometry, and diffuse boundaries below stoichiometry. Selecting the boundaries of precipitates manually, the composition of the precipitate measured in Ti-6Ag is 33 ± 8 at%. The surrounding Ti matrix contains 11 ± 5 at%, with denuded zones adjacent to precipitates in Ti-6Ag ranging from 4 ± 2 at%. Lamallae in Ti-25Ag were measured as 36 ± 6 at%, with surrounding Ti matrix containing 11 ± 2 at%. Whilst results for precipitates correlate well with both

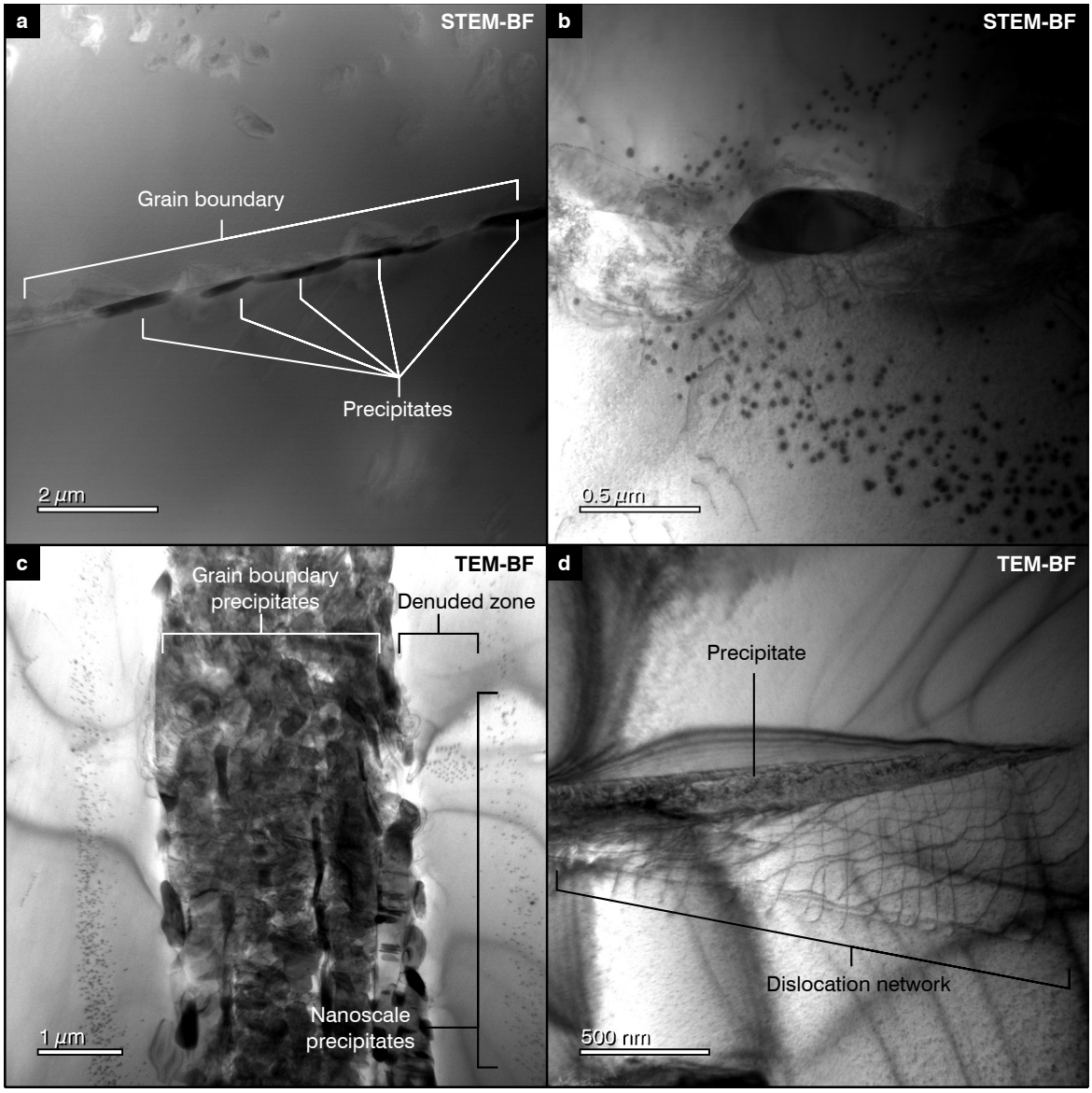


Figure 4.9: Bright field STEM and TEM micrographs of grain boundary precipitates in Ti-6Ag A2. a) The presence of elongate precipitates along the length of boundaries are apparent. Both for b) individual 0.5 µm precipitates and c) 2.5 µm wide agglomerations of precipitates, clusters of smaller 30 nm precipitates are visible either side of the grain boundary. A precipitate-free denuded zone is present between the larger grain boundary particles and the nanoparticles. In d), a 2 µm long precipitate is shown to have an adjacent network of dislocations in the Ti matrix.

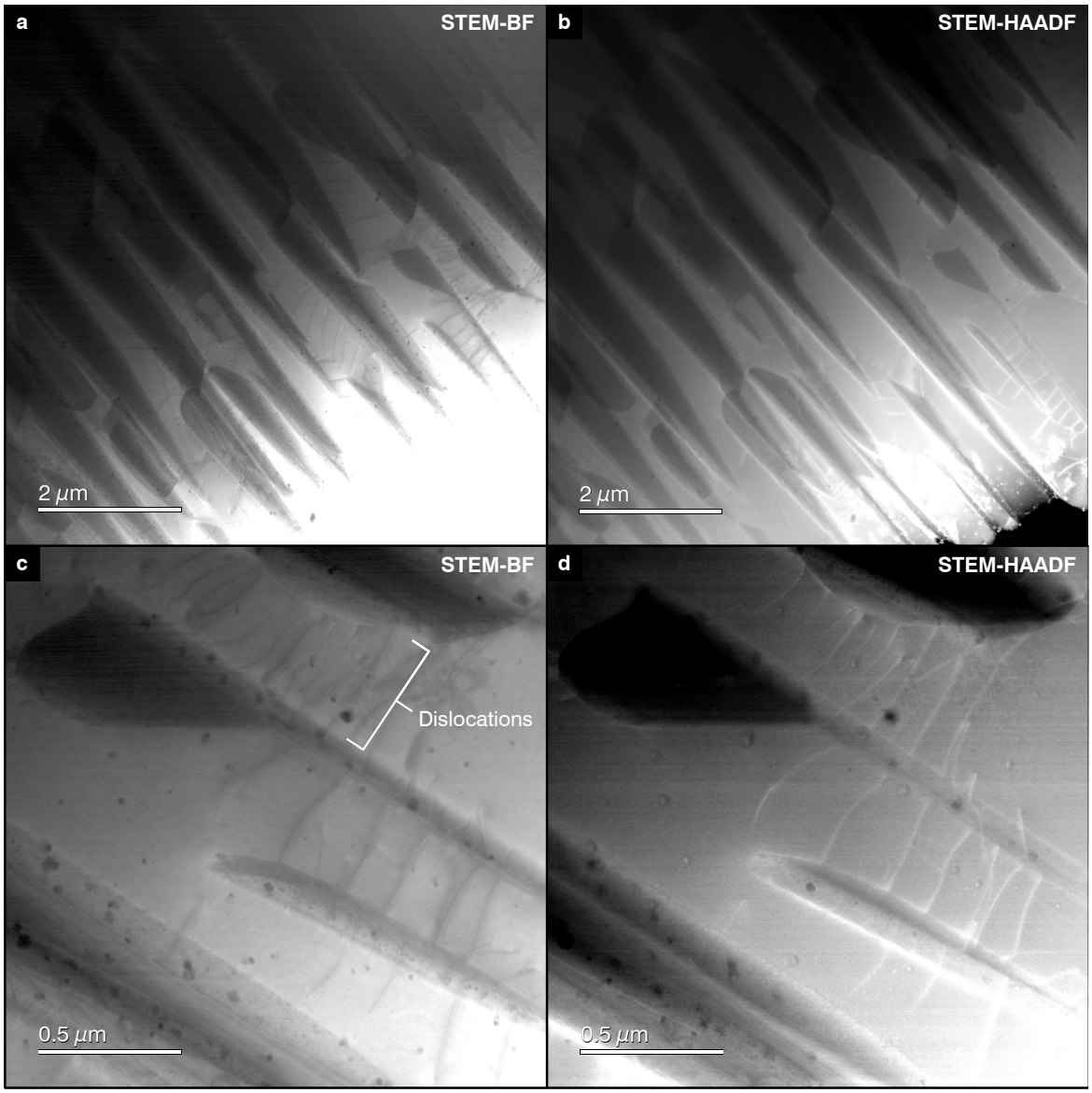


Figure 4.10: Bright field and HAADF STEM micrographs of Ti-25Ag A2. a) and b) Parallel lamellae of intermetallic precipitates are clearly distinguishable, with a network of dislocations spanning between adjacent lamallae. These dislocations are shown at higher magnification in c) and d)

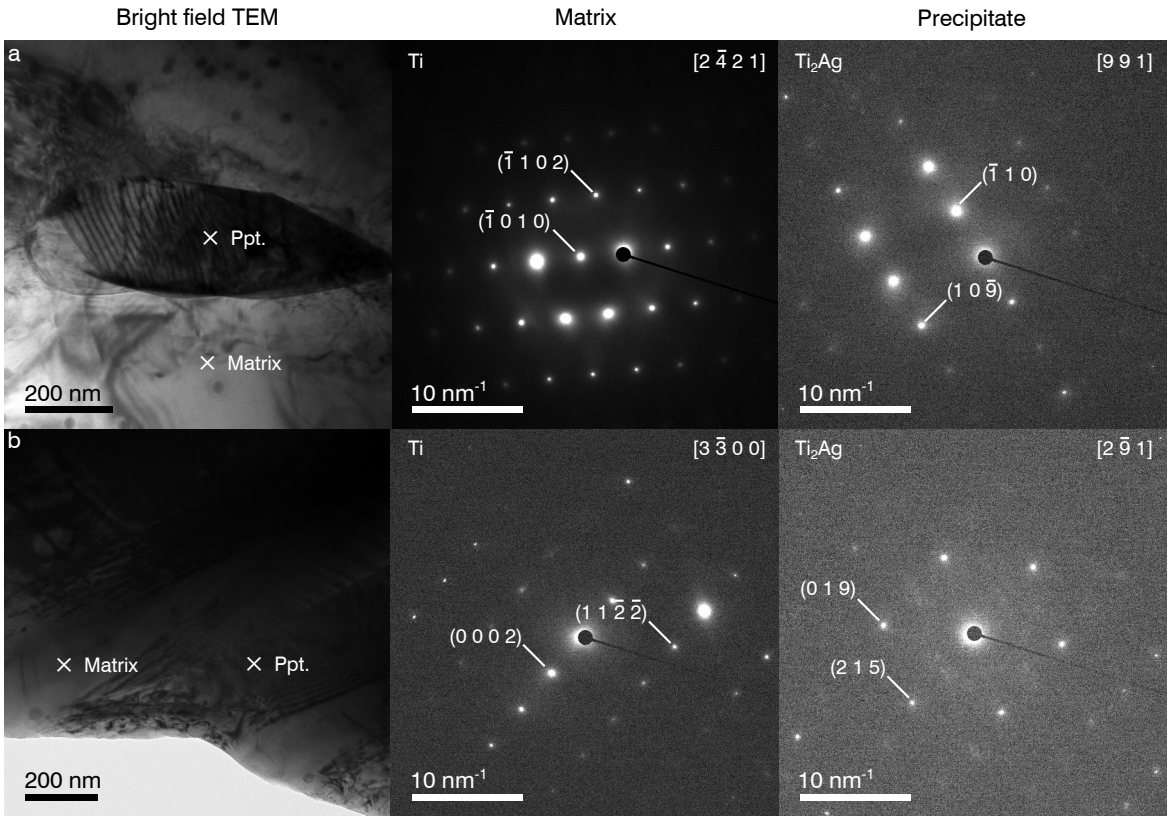


Figure 4.11: Indexed SAED patterns for a) Ti-6Ag A2 and b) Ti-25Ag A2, with best fitting phase considering spot locations and systematic absences. Two reciprocal lattice vectors are labelled to clarify orientation.

phase diagram and SEM-EDS measurements, matrix compositions indicate excess Ag has been measured compared to the equilibrium phase diagram. This may indicate poor measurement quality due to excess sample thickness.

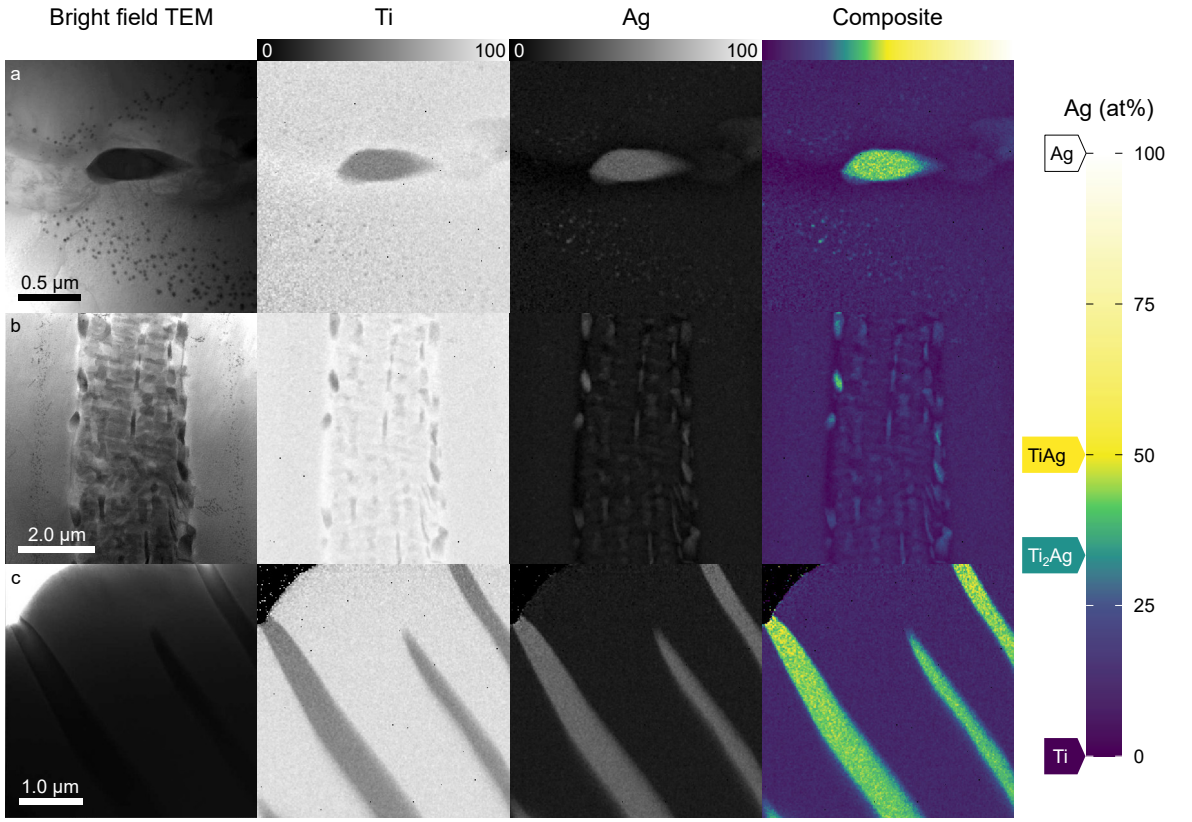


Figure 4.12: Quantitative maps of TEM-EDS analysis for a) and b) Ti-6Ag A2, and c) Ti-25Ag A2. Composite map colour scale has been chosen to visually differentiate between TiAg and Ti_2Ag intermetallics.

4.3.3 Bulk characterisation of alloys

In the as HIP state, TiAg particles exhibit a hardness of approximately 135HV0.1, though this value is likely an overestimate given their constraint within the stiffer Ti matrix and similar length scale to the indentation at 100 g force. For heat treated samples, increased silver content decreases hardness, with Ti-25Ag samples broadly showing the lowest hardness for each heat treatment state (Table 4.7).

In homogenised, supersaturated state, higher Ag content is associated with decreasing hardness, with Ti-6Ag HOM and A1 showing the highest hardness of 354HV0.1 and 334HV0.1 respectively. However, the statistical significance of variations between samples is low, with various groups overlapping.

In order to better assess the influence of nominal composition and the alloy state upon hardness, results were subject to 2-way ANOVA (Table 4.8). Nominal composition was

Table 4.7: Vickers hardness of polished samples at loading of 100 g force. Due to inhomogeneity at the length scale of indentations for samples in the HIP state, separate indentations were made for intermetallic particles and the Ti matrix phase. Groupings are presented based on Tukey statistical comparison, with samples that do not share letters significantly different from one another.

Ag wt%	Heat treatment	Microstructural feature	HV0.1	Grouping
6	HIP	Intermetallic particles	144 ± 14	E
	HIP	Matrix	178 ± 11	D E
	HOM		354 ± 38	A
	A1		334 ± 49	B C D
	A2		248 ± 28	A B
10	HIP	Intermetallic particles	148 ± 7	E
	HIP	Matrix	166 ± 15	E
	HOM		274 ± 24	A B C
	A1		199 ± 30	A B
	A2		329 ± 26	C D E
25	HIP	Intermetallic particles	127 ± 8	E
	HIP	Matrix	173 ± 24	D E
	HOM		273 ± 17	A B C
	A1		225 ± 8	A B C
	A2		255 ± 11	B C D

found to be a significant factor in determining hardness, as well as the alloy state. This remains the case when the high softness of samples in the HIP state is removed from statistical analyses.

Assessing the bulk crystallographic phases present in samples was performed by XRD. Analysis of XRD patterns correlates with the phases predicted by phase diagram, and those indicated by compositional analyses and SAED patterns. In the as HIP state, there is no clear indication of additional Ag rich phases beyond TiAg and Ti_2Ag present in patterns (Figure 4.13). Suppression of precipitation in the homogenised state is confirmed, with only α-Ti peaks present.

Table 4.8: Statistical parameters for 2-way ANOVA of hardness data, with the alloy composition and heat treatment state considered. Results are presented both for all samples, and excluding samples in the HIP state due to the significant inhomogeneity at the length scale of indentations.

	Composition		State	
Variable	F-value	P-value	F-value	P-value
Hardness (All)	6.94	0.002	45.76	0.000
Hardness (-HIP)	6.41	0.004	3.68	0.034

In the aged states, A1 and A2, the large proportion of Ti_2Ag present in Ti-25Ag is clear. Overlap of the Ti_2Ag {103} and α-Ti {002} peaks at 38.0° and 38.4° makes identification of intermetallic in Ti-6Ag and Ti-10Ag challenging, suggesting any volume fraction present is below the threshold of noise in the data.

In order to understand how the oxidation state of Ti and Ag may change in intermetallics compared to in solid solution, XPS was performed on pure Ti, Ti-25Ag HOM, and Ti-25Ag A2 samples. No significant change in the oxidation state of Ti was observed between samples, with only a slight shift in the position of peaks (Figure 4.14). In both the homogenised and aged state, Ag was found in a mixture of $Ag^{(0)}$ and Ag_2O oxidation states. Ag_2O was the dominant state in both cases, indicating that precipitation of the Ti_2Ag intermetallic does not significantly alter the passive oxide film. No Si content was observed for the three materials assessed.

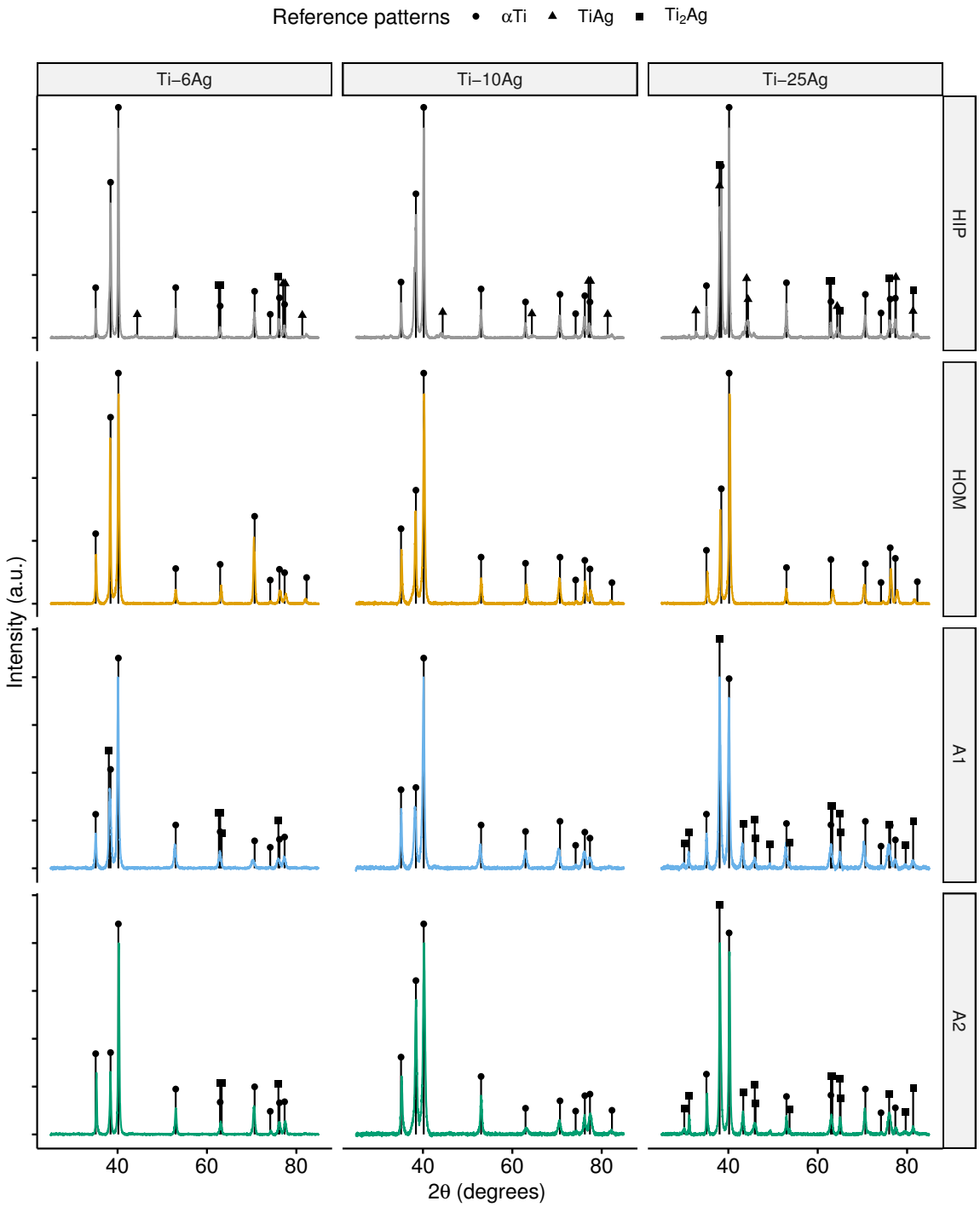


Figure 4.13: Indexed XRD patterns of materials. Markers for reference patterns are shown at the expected 2θ values, allowing the assignment of phases to relevant peaks. Peaks correlating with Ti, TiAg, and Ti_2Ag are observed in all HIP samples, with intermetallic peaks subsequently missing in the HOM state, confirming that samples are in solid solution. Ti_2Ag diffraction peaks are clearly present in the Ti-25Ag A1 and A2 states, however are not distinguishable in Ti-6Ag and Ti-10Ag.

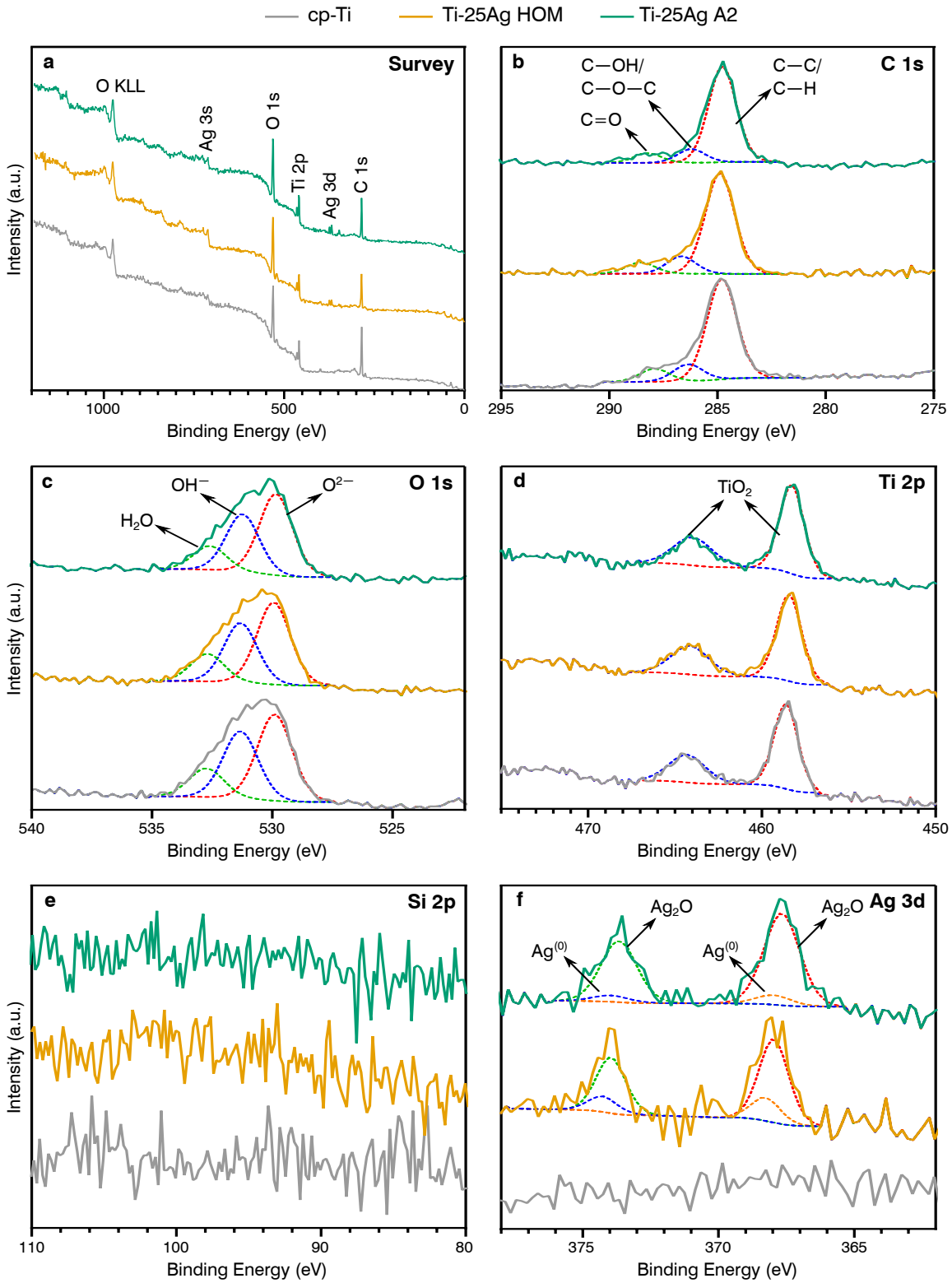


Figure 4.14: Measured XPS spectra of cp-Ti, and Ti-25Ag HOM and A2. Survey data a) indicates similar behaviour across all three materials, with the presence of Ag 3d and 3s the most notable change. Peaks for b) C 1s, c) O 1s and d) Ti 2p show only minor variations. Si spectra e) indicated no contamination. Slight shifts in the oxidation states of f) Ag are observed, but with Ag_2O remaining the dominant oxidation state for both HOM and A2 states.

4.3.4 Antimicrobial efficacy of alloys

Assessing the response of *S. aureus* to alloys within the initial four hour culture period, there was no significant antimicrobial effect for any Ti-Ag alloys compared to cp-Ti (Figure 4.15a). Whilst complete eradication of all cultures is observed for Cu, neither pure Ag nor Ti-Ag in any heat treatment state exhibited any antimicrobial response. A distinctive region of corrosion where culture media contacted the sample surface is observed for Cu samples, whilst no visible change in the surface is observed for other materials, including Ag. Investigating behaviour after a full 24 h culture again showed no significant difference in response for the selected alloys (Figure 4.15b).

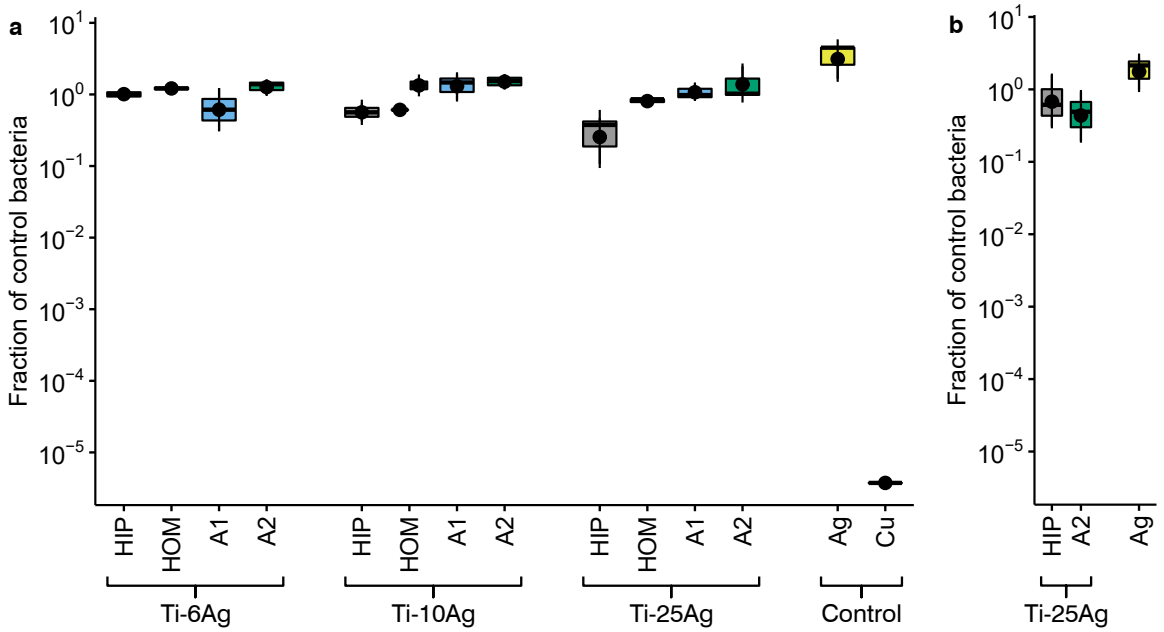


Figure 4.15: Response of *S. aureus* cultures to the surface of alloys after a) 4 h culture, compared to cp-Ti, and b) after 24 h culture for select samples.

After incubation in LB broth at 35 °C for 15 days, negligible release of Ag is observed for all alloys investigated, with less than 1 ppm detected (Figure 4.16). Only the as-HIPed Ti-25Ag shows release above the background level observed for cp-Ti and blank LB controls. Samples of Ti-10Ag in the as-HIPed and homogenised state were not assessed due to microbial contamination in the eluent. All samples show significantly less Ag release than the high-purity Ag plate controls, which even at the high surface area to

eluent volume ratio of $0.4\,\mathrm{mL\,cm^{-2}}$ produced a concentration of only $4.7 \pm 0.3\,\mathrm{ppm}$.

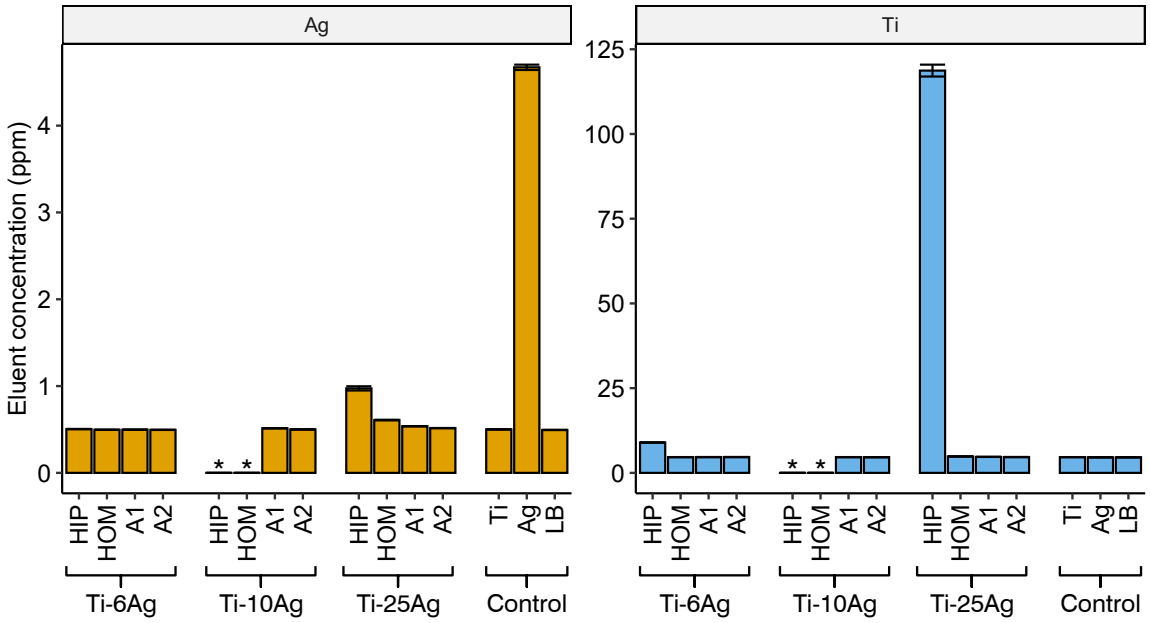


Figure 4.16: Concentration of Ti and Ag in LB broth eluent after ageing alloy samples for 15 d at 35 °C. Eluent of Ti-10Ag in the as-HIPed and homogenised state were not assessed due to microbial contamination. Control samples of cp-Ti, Ag, and an LB blank are included for comparison. Samples marked * were excluded due to microbial contamination.

4.4 Discussion

Considering the physical properties of the Ti-25Ag alloys produced in this study, there is broad agreement with previously manufactured Ti-Ag binary alloys. The absence of precipitates after initial homogenisation and quenching, internally consistent composition, and α-hcp phase of all three alloys, correlates with the massive transformation of homogenised β-bcc, as has previously been demonstrated for a range of both hyper and hypo-eutectoid Ti-Ag alloys [298]. Etching of polished sections to generate grain boundary contrast under polarised optical microscopy may allow the identification of martensite laths to confirm this transformation [299].

The ratio of phases present in Ti-25Ag A2 matches well with the existing phase diagram (Table 4.6). The increased proportion of Ti_2Ag present in the A1 condition suggests

that quenching was insufficient to prevent further intermetallic precipitation as β-Ti transformed to supersaturated α-Ti. Given that no precipitation was observed after quenching in the homogenised state - which exhibits a significantly greater supersaturation of Ag - it is likely that existing Ti_2Ag precipitates continued to grow, rather than additional nucleation occurring as undercooling increased.

A possible deficiency in Ti_2Ag for Ti-6Ag and Ti-10Ag raises some questions. As precipitates are only observed on the grain boundary in Ti-6Ag, the ratio of grain to precipitate size makes measurement of phase ratio by SEM infeasible. Previous studies have indicated a lower proportion of Ti_2Ag than anticipated, with ingot cast materials at 15 wt% where only 0.7% nanoscale Ti_2Ag was observed [124]. The cause of a lack of Ti_2Ag precipitation in Ti-10Ag A2 is more difficult to ascertain. It may be that the Si contamination detected by EDS and observed as darkened precipitates in SEM (Figure 4.6) suppresses intermetallic nucleation or growth. The presence of high Si content precipitates in Ti-10Ag may correlate with previously observed precipitation of coarse silicides in Ti alloys [300]. Long ageing periods, as used in this study, may contribute to the size of these precipitates, as coarsening of silicides is an established behaviour in long-term high temperature service. Whilst this Si contamination prevents conclusions being drawn on the behaviour of aged Ti-10Ag A2, both the HOM and A1 states can be considered when drawing trends across samples.

Considering the position of Ti-6Ag A2 samples on the phase diagram (Figure 4.3), the alloy is in the hypo-eutectoid state. Previous assessments of hypo-eutectoid Ti-X alloys have typically exhibited bainitic microstructures, however Ti-Cu - a binary system with significant similarities to Ti-Ag - does favour lamellar microstructures as undercooling increases [301]. The lines of precipitates observed under TEM in Ti-6Ag (Figure 4.9) are more representative of the bainitic structures observed in hypo-eutectoid Ti-X alloys, which may indicate the trend in Ti-X behaviour holds true for Ti-Ag.

In contrast, Ti-25Ag has a strongly hyper-eutectoid composition. The lamellar morphology of Ti_2Ag precipitates has been observed in cast alloys of 22.5 to 30 wt% [227]

and sintered 20 wt% Ag alloy [289]. As large volumes of intermetallics are typically considered mechanically unfavourable, the hyper-eutectoid regime in Ti-X binary alloys has been less well explored. The formation of a lamellar structure - analogous in appearance to the well characterised pearlitic ferrite-cementite microstructure in the Fe-C binary - has previously been observed in Ti-X binaries near the eutectoid composition [302]. This microstructure is likely formed through the same co-operative growth mechanism leads to in both Ti-Ag and pearlitic steels. Co-operative growth significantly reduces the required diffusion distance to reach an equilibrium phase distribution, compared to formation of equiaxed precipitates.

Both Ti-25Ag A1 and A2 exhibit the same microstructural features, with lamellar colonies of Ti_2Ag and larger grain boundary precipitates (Figure 4.7 c and d). This indicates that, even after combined ageing duration of 555 h, consolidation of lamellae into larger equiaxed precipitates is not favourable. Considering evolution of the analogous Fe-Fe_3C system, ageing of pearlitic microstructures below the eutectoid temperature results in spheroidisation of the Fe_3C phase. Spheroidisation of overaged pearlite is demonstrated to be clearly distinguishable after 10 h and to reach visible completion after 100 h [303, 304] Given that the co-operative growth of lamellae is functionally the same for Ti-Ag and Fe-C, it might be anticipated that the same subsequent microstructural evolution would be observed when aged further.

However, the process of spheroidisation will be highly constrained by diffusion rate. The difference in diffusivity at typical ageing temperatures between Ti-Ag and Fe-C is several orders of magnitude (Ag in α-Ti: $4.0 \times 10^{-20}\,m^2\,s^{-1}$ at 865 °C; C in α-Fe: $4.9 \times 10^{-17}\,m^2\,s^{-1}$ at 700 °C respectively) [307]. An approximate diffusion length can be estimated as $2\sqrt{Dt}$ for a given duration, t. Despite the significant total ageing dwell time of 555 h, the estimated diffusion distance for Ag is an order of magnitude less than that expected for C after just 10 h, making any significant microstructural change unlikely (1.74×10^{-7} and 2.66×10^{-6} m) [261, 262, 307]. Even if the boundary between Ti_2Ag and α-Ti is sufficiently disordered as to enable fast grain-boundary type diffusion, distances

remain short (7.2×10^{-6} m) [308], though this is on a similar scale to the interlamellar spacing. In summary, after the initial rapid co-operative growth of lamallae, the slow rate of substitutional diffusion makes further microstructural evolution unlikely without extreme ageing times.

To understand possible thermodynamic factors for microstructural evolution, it is also informative to consider how precipitation of Ti_2Ag alters local strain in the alpha Ti matrix. Assessing the HOM state, the lack of precipitation present in Ti-25Ag after homogenisation may be surprising, given the significant supersaturation of the lattice with Ag solute. However, despite their difference in electronic structure and atomic mass, the radii of Ti and Ag are remarkably similar. The Seitz radii - calculated from the atomic volume - of Ti and Ag are 1.6153 and 1.5969 Å [305, 306]. Whilst the presence of solute atoms does alter the effective radii of the surrounding matrix, volumetric strain can be crudely approximated based on a rule of mixtures, such that

$$\frac{\Delta V}{V} = \frac{(x{R_{Ag}}^3 + (1-x){R_{Ti}}^3) - {R_{Ti}}^3}{{R_{Ti}}^3} = \frac{x({R_{Ag}}^3 - {R_{Ti}}^3)}{{R_{Ti}}^3} \tag{4.1}$$

where ΔV is the effective volume change caused by solutes, and R_{Ag} and R_{Ti} are the Seitz radii of Ti and Ag respectively. For 25 wt% Ag in solution, this results in a -0.44 % strain (i.e. for a cp-Ti cube of unit volume, the volume of a Ti-25Ag cube with the same number of lattice points is 0.9956). This low strain is clearly sufficiently low that it can be accommodated by the α-Ti matrix on quenching, and does not provide the required driving force for any form of rapid precipitation as a form of strain relief.

Similarly, the effective volumetric change on precipitation of Ti_2Ag can be estimated. Considering the respective crystallographic unit cell volumes of α-Ti and Ti_2Ag, the effective volumes per atom of 17.658 Å^3 and 17.421 Å^3 indicates a volume difference of -0.47 % between pure α-Ti and precipitation of Ti_2Ag [297]. For 25 wt% Ag, the volume of Ti_2Ag present is expected to be 35 %.

The estimated volume change of aged Ti-25Ag compared to cp-Ti is -0.50 %, indicating an additional -0.06 % volume reduction after precipitation. Assuming zero strain in

Ti_2Ag, the remaining volumetric strain in the surrounding α-Ti matrix is just $-0.05\,\%$. As expected, the overall lattice strain is likely to therefore be reduced as Ti_2Ag precipitates in Ti-25Ag. It may be possible to confirm this through higher resolution XRD analyses, comparing the location of α-Ti peaks in patterns. However, the overlap of Ti_2Ag peaks in spectra for the aged Ti25Ag samples may require Rietveld analysis of a sample series to accurately assess lattice strain.

The composition of microstructural features broadly agrees with that predicted by the Ti-Ag phase diagram. SEM-EDS indicates a slight Ag deficiency of intermetallic phases in the as-HIPed and aged states. This effect could be caused by measurement errors, wherein adjacent Ti matrix is included in the sampled volume. This is unlikely to be the case for TiAg intermetallics in the HIP state, given the penetration depth of EDS is typically below $5\,\mu m$ [309]. It is possible that the difference in backscatter coefficient between Ti and Ag has resulted in inaccurate quantification, though this effect is considered automatically by the software used. Given that no additional phases are present in XRD patterns for the as-HIPed state, this suggests that any deviations in the measured Ag content of phases are either within measurement error, or the TiAg intermetallics are slightly deviating from stoichiometry. As has previously been demonstrated, TiAg does not exhibit perfect stoichiometry, with the phase field widened at elevated temperatures (Figure 4.1). Given the nature of HIP as a powder metallurgy process, alloys are likely to have a high vacancy concentration, allowing for more defective structures, able to support atypical compositions.

As the largest precipitates in the A1 and A2 samples are below $10\,\mu m$ in width, the small but consistent deficiency in Ag content in SEM-EDS can be ascribed to overlap of the measurement volume with surrounding α-Ti matrix. This is confirmed by measurements of Ti_2Ag in STEM-EDS, where the mean composition of precipitates agrees well with the expected 33 at% composition (Figure 4.12). Variability across individual precipitates may be an artefact of excess sample thickness, such that the cross section of non-equiaxed precipitates changes throughout the sample volume. Efforts to thin samples further by Ar

ion milling resulted in pockmarking of samples, possibly due to the wide difference in the sputtering rates of Ti and Ag [310]. Further refinement of electropolishing parameters for Ti-Ag binary alloys will be necessary to improve resolution in TEM. This may also allow for EELS spectra to be successfully measured, providing data on the relative oxidation state of specific microstructural features. This may also allow SAED patterns to be collected from the nanoscale precipitates observed either side of the denuded zone in Ti-6Ag A2 (Figure 4.9).

In summary, despite some minor variations and the contamination of Ti-10Ag A2 with Si, the physical characteristics of alloys agree well with existing literature. This includes hardness measurements. The lack of a statistically significant difference between Ti-25Ag in the A1 and A2 states compared to Ti-6Ag A2 may be surprising, given the dramatically different intermetallic contents (Table 4.7). Other binary Ti intermetallics typically exhibit hardnesses significantly above that of a surrounding α matrix [311]. However, previous investigations of Ti-Ag intermetallics suggest only a small trend in increasing hardness as Ag content rises, from 130Hv to 264Hv at 30 wt% [227]. In this work, both the alloy state (HIP, HOM, A1, A2) and the composition (6, 10 and 25 wt%) were statistically significant factors in the hardness of alloys (Table 4.8) Whilst coarse grain size due to long ageing durations can contribute to a low hardness, the interlamellar spacing of below 1 µm within grains should limit ductility, and both alloys in the A2 state have undergone the same thermal history. Any residual porosity due to Ar entrapment would also contribute to reduced hardness, though these results remain surprising given the absence of porosity observed in SEM for Ti-25Ag.

Given that these alloys can be considered well characterised, with the presence of Ti_2Ag intermetallic confirmed, previous literature suggests bactericidal behaviour should be observed. However, despite the broad compositional range and variety of microstructural states assessed, no significant antimicrobial efficacy was observed for these alloys (Figure 4.15). For comparison, pure Cu control material showed complete elimination of bacterial cultures. Given the distinct lack of any antimicrobial response from these alloys

under the conditions assessed, two key hypotheses for this can be presented. First, that the bulk or surface chemistry of alloys is such that they are inactive or inactivated by the culture medium; and second, that if ionic release does occur, silver ions are complexed by other agents within the culture medium (Figure 4.17).

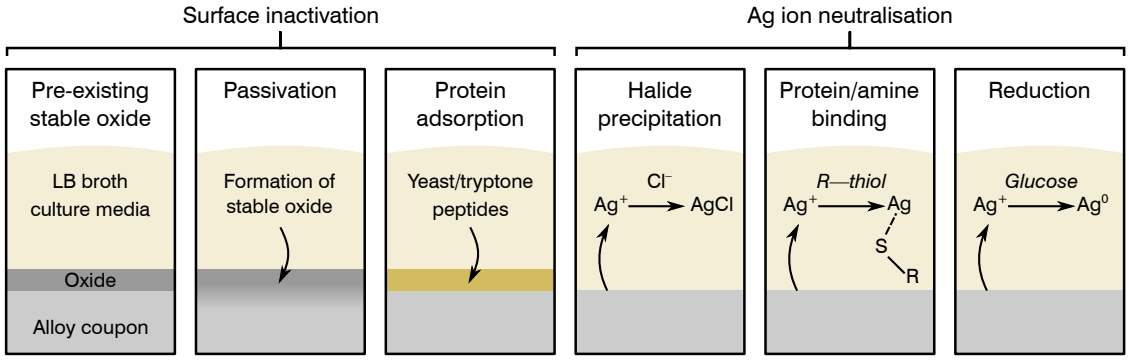


Figure 4.17: Schematic of possible mechanisms for inactivation of antimicrobial behaviour in Ti-Ag alloys.

Consider first the possibility of total surface inactivation or passivation. It is the passive surface oxide that will first encounter any biological system, and plays a crucial role both in any release mediated behaviour, and any contact associated bactericidal mechanism. For Ti alloys, XPS can provide information regarding the oxide film present as a surface sensitive technique [312] The lack of significant change in oxide state either for Ti or Ag between the homogenised and secondary aged state of Ti-25Ag may correlate with the continued absence of antimicrobial response observed, despite significant microstructural change (Figure 4.14). Subsequent research into Ti-Ag alloys has demonstrated that selective etching - effectively exposing Ti_2Ag particles within the Ti matrix - does increase efficacy, albeit fractionally [229]. There has been demonstrated antimicrobial action for Ag doped TiO_2 films, which may further confirm the need for Ag to be either present in the oxide film or otherwise exposed [313–315]. Within this work, surface preparation of bacteriological samples was limited to grinding with SiC grit papers, and subsequent degreasing. Previous studies have followed similar protocols, occasionally including an additional 1.5 µm diamond particle polishing step [124]. Whilst this is likely to reduce

surface roughness, it is unlikely to alter the passive oxide film, suggesting this difference in procedure does not account for the lack of antimicrobial action in this work.

Regarding the adhesion of proteins and other long chain amino acids, there is an established behaviour for absorption of proteins such as albumin and fibrinogen to Ti alloys in vitro [316–319]. In an in vivo setting, recent studies have assessed the specific proteins adsorbed to the surface of titanium implants after an initial two minutes of insertion. The resulting implant proteome consists primarily of intracellular proteins, with haemoglobin subunit β and serum albumin dominating [320]. Approximately $7\,\mu g\,cm^{-2}$ of adsorbed protein was recovered from implants. For comparison, assuming that surface adsorption is limited by surface availability, rather than protein availability, for the release study samples at a ratio of $0.4\,mL\,cm^{-2}$, this would indicate $17.5\,\mu g\,mL^{-1}$ of protein would need to be deposited to reach the same coverage. In comparison to biological sera encountered in vivo, LB broth contains significantly less long chain protein by mass. Considering the components of tryptone and yeast extract respectively, both contain a wide range of short chain amino acids, but have undergone sufficient enzymatic processes to contain minimal long chain proteins [321]. Whilst this does not preclude the adhesion of these short chain compounds to the passive TiO_2 surface, the fundamental response of both bacteria and the TiO_2 to short chain peptides versus proteins may differ [322]. Empirical studies disagree on the fundamental effect of proteins on ionic release, with both accelerated and decelerated corrosion demonstrated under similar conditions [323, 324]. Whilst measurement of any protein adsorption observed on Ti-Ag alloys may be informative, the relative tendency for adsorption will fundamentally be driven by the nature of the oxide film, and as such this can be argued to be the primary factor.

Regarding the possibility of oxide growth leading to further passivation, whilst the corrosion potential of alloys was not directly assessed, previous investigations of Ti-Ag have found the addition of Ag does not have a significant deleterious effect on corrosion resistance [286, 325]. Given the sensitivity of Ti to F, the presence of fluoride ions in an oral environment has been a frequent consideration, with additions of Ag up to 3.5 wt%

mitigating the effect on open circuit potential of F^- concentration [228]. However no significant F^- concentration is anticipated in LB media.

If, as has been previously suggested, α-Ti and Ti_2Ag were to act as galvanic couples in corrosion conditions, the microstructural state will play a significant role. It has previously been established that lamellar Ti intermetallic microstructures can show anomalously high corrosion resistance [326]. This was ascribed to the low projected area of individual lamellae resulting in a contiguous "envelope" of corrosion protection from the adjacent phase. This would correlate with the lack of change in oxidation state between the HOM and A2 states for Ti-25Ag (Figure 4.14), which indicates a contiguous oxide film across samples.

Assessing the second possible route of alloy inactivation - the formation of silver compounds or complexes by the culture media used - release study results provide perspective on the significance of this effect. The peak concentration of Ag detected is below 1 ppm for all alloys, significantly below the 4 ppm of pure Ag controls and within the baseline noise level of negative cp-Ti and LB controls (Figure 4.16). It is likely that the silver measured was bound as an insoluble precipitate. Past attempts to prepare ICP calibration standards with LB media made clear that conventional acidification with HNO_3 alone is insufficient to maintain Ag^+ in solution. Subsequent filtering at 0.22 µm removed Ag compound precipitates, resulting in inconsistent standards. As has been used in the protocol for this study, acidification with sufficient HCl does solvate Ag, converting AgCl precipitate into the soluble $AgCl_x^{1-x}$ anionic complex. Together, this indicates that precipitation of Ag^+ ions in LB media is likely dominated by halide precipitation, rather than binding of thiol groups or glucose mediated reduction. Thiol groups may dissociate with relative ease, but the anticipated thiolate bond strength with Ag^+ will be significantly less than that for free Cl^-. Neglecting solvation effects, the bond dissociation energy (BDE) of Ag_2S is less than that of AgCl (ΔH_f AgCl 341 kJ mol, Ag_2S 213 kJ mol) and will be further attenuated given that the thiolate RS^- will exhibit lower polarity than free S^{2-} [327, 328]. This behaviour is unlikely to change in vivo, as previous studies have demonstrated that ionic

silver rapidly reacts to form colloidal AgCl nanoparticles in biological media including glucose, PBS, and LB media [185]. The nanoparticles are stabilised by a protein corona, and it is through surface interaction or uptake by cells that antimicrobial effect is likely to occur.

Whilst the electrochemical behaviour of Ti_2Ag is not well established, pure silver controls were included to provide a negative control that still contained silver. As has previously been observed, pure Ag shows negligible antimicrobial activity in various media due to a lack of corrosion [329]. Pourbaix diagrams can be constructed for the conditions observed in LB media, with an approximate chloride concentration of 0.05 M (Figure 4.18) [330]. A metal concentration of 5×10^{-5} M is shown, equivalent to the 5 ppm release measured for pure Ag samples in LB media (Figure 4.16).

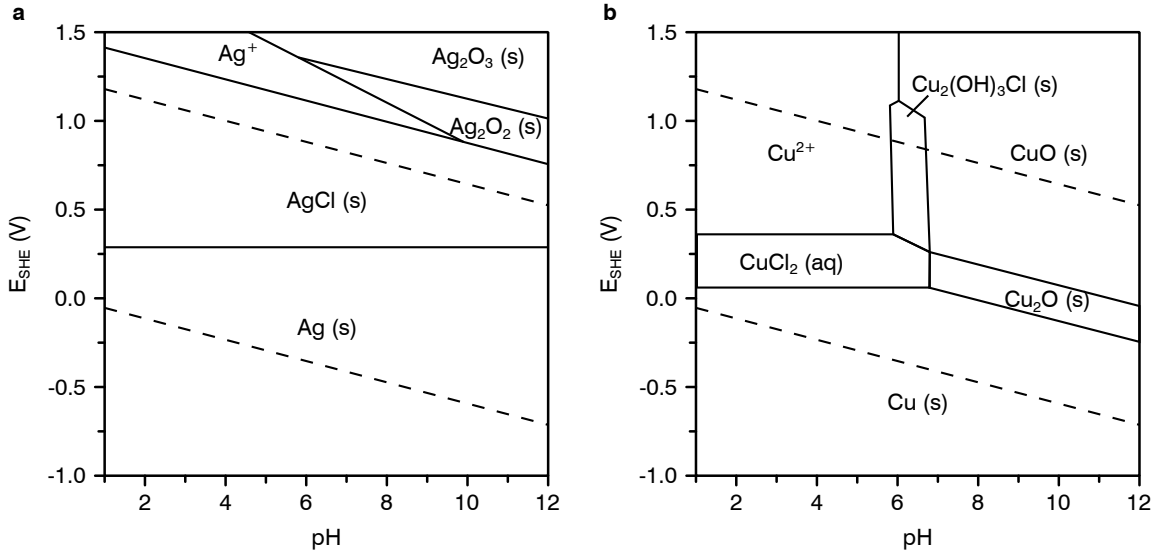


Figure 4.18: Pourbaix diagrams for a) Ag and b) Cu at 35 °C in aqueous conditions, with a Cl^- concentration of 0.06 M. Metal concentration was set at 5×10^{-5} M. Dashed lines represent the region of stability for water.

It is further apparent that generation of Ag^+ ions is improbable, and that any corrosion of pure silver that occurs will only generate insoluble AgCl. For comparison, the positive control material used, Cu, showed significant corrosion over the study duration. Both soluble $CuCl_2$ and $Cu_2{}^+$ are stable within the region of stability for water, and only a small cathodic potential is required for active corrosion to take place. The stability of

Ag further drives the point that, in a metallic state, silver is unlikely to generate any aqueous species, without a significant cathodic potential. The presence of Ti is only likely to further enhance the stability of Ag, given the highly stable oxide of Ti cannot provide an appropriate anode.

It has, instead, been suggested that a contact mode-of-action is the predominant mechanism for antimicrobial activity of Ti-Ag alloys [124, 229]. The true mechanism behind this contact sterilisation has still not been established, with investigations to demonstrate the physiological basis for this still needed. Currently established modes of action for silver indicate two key pathways of antimicrobial efficacy:

- Membrane specific activity resulting in rapid loss of integrity [65]
- Generation of ROS and interference with oxidative stress response [331]

Both of these mechanisms will require the release of Ag in some respect. Given how frequently efficacy has been demonstrated with negligible elution of Ag^{+}, it may be that the metabolism of bacteria adsorbed or otherwise adhered to the surface encourages micro corrosion. Whilst microbe-induced corrosion is a well established phenomenon in ferrous alloys and has been briefly observed in titanium [332], this is a process that occurs due to sulphate reduction at a bulk scale. Studies of how microbial adhesion alters the immediate surface chemistry of materials are comparatively scarce [333]. As has been done in this work, assessing ionic release is predominantly performed in sterile conditions, not with active bacterial or cell cultures present, and often in different media to that used for culture experiments [118, 124, 229, 286, 292, 334].

However, this still fails to adequately explain the antimicrobial action observed in previous studies. In comparison, the bacterial results within this work show increased variation. Variability in experimental technique may therefore be masking statistically significant variations in efficacy. However, it is also important to consider the practical significance of results. Previous studies have typically presented antimicrobial efficacy as a percentile value, with no positive antimicrobial controls included. This can have the effect of implying greater practical significance of results than may be merited. An

apparent 99 % kill rate is equivalent only to a $2log_{10}$ reduction in viable colonies. For comparison, the positive control used in this work - samples of high purity copper - exhibited a $5log_{10}$ reduction versus control samples. Improved bacteriological technique may reveal statistically significant differences in efficacy that have been masked, but the likely practical significance of any such results must be considered. The lack of significance for actual clinical practise in current surface testing protocols has been noted in the past, and it may be appropriate to consider a new standardised approach to testing beyond the existing ISO 22196 and ASTM E2149 standards [335, 336].

Given the dearth of conclusive evidence for the antimicrobial mode of action of Ti-Ag alloys, significant further research is needed. First, conclusive evidence de-coupling the posited surface-mediated response and a more likely elution-mediated efficacy is crucial. In the first instance, recovery of cultures for analysis with inductively coupled plasma mass spectrometry (ICP-MS) may provide sufficient resolution to confirm if Ag is being eluted under the culture conditions used to demonstrate efficacy. Use of combined flow-cytometry ICP could allow direct correlation between the silver content of bacteria exposed to the surface of such alloys and the degree of stress they are under [337], further distinguishing between bacteria damaged by Ag uptake and any that have been killed by surface interaction.

Second, confirming what specific aspect of microstructure and composition cause any efficacy is still required. Whilst previous research has indicated Ti_2Ag as the dominant phase, this work has clearly demonstrated that even in high quantities, that alone is not sufficient for efficacy. It is possible that targeting high Ag content alloys with the exact stoichiometry of Ti-Ag intermetallics could allow clearer distinction of whether the intermetallic phase alone can be responsible for any antimicrobial effect, and establishing corrosion behaviour of the intermetallic phase alone.

4.5 Conclusion

This work demonstrates the correlation of highly aged Ti-Ag alloys with the established phase diagram for the binary system. The suppression of precipitation during quenching from β-Ti solid solution to supersaturated α-Ti was observed. Subsequent ageing allows for the formation of hypereutectoid lamellar microstructures in Ti-25Ag, and fine grain boundary precipitates in Ti-6Ag. Nanoscale precipitates either side of denuded zones adjacent to grain boundaries were also observed. Crucially, despite the range of microstructures and compositions assessed, no antimicrobial behaviour was observed under the study conditions used. The absence of antimicrobial response is likely linked to the lack of Ag release from alloys, due to the low corrosion potential of silver in the metallic state. This calls into question previously asserted elution-free mechanisms for efficacy in Ti-Ag, with the presence of either nanoscale or bulk Ti_2Ag insufficient. Based upon these results, it should be feasible to further narrow the possible routes of antimicrobial efficacy for future biomedical alloys.

CHAPTER 5

CONCLUSIONS AND FUTURE WORK

5.1 Antimicrobial magnesium oxychloride cements

The inherent antimicrobial efficacy of magnesium oxychloride cements was demonstrated in Chapter 2. Generation of such inorganic antimicrobial materials with established biocompatibility will be a key strategy for the biomaterials community in tackling antimicrobial resistance in the coming decades. Translating bench-top research to clinical settings will require significant further investigation, both to understand the biological mechanisms of inherently antimicrobial materials, and the practical limitations of such an approach.

Establishing the mechanism of antimicrobial efficacy for MOC will be challenging given the numerous confounding factors that may contribute. Improving the PMAC based reactive oxygen luminescence assay may prove helpful. In the experiments performed in this work, PMAC was added to cements ex-situ before measurements were taken. Using a plate reader equipped with an in-situ dosing mechanism would allow for immediate readings, which may be important if reactive oxygen is present in high quantities and neutralises PMAC rapidly before reliable measurements may be taken.

Beyond understanding how formulations interact with bacteria, practical improvements to the formulation are required prior to clinical translation. In particular, the sensitivity of uncured cement to water will need to be tackled. This is particularly relevant for any uses where cements will be delivered in vivo as uncured pastes, such as root

end fillings. It may also be clinically relevant to accelerate the curing reaction, provided it does not become sufficiently exothermic as to cause localised tissue damage. Use of phosphoric acid dopant in the magnesium chloride brine has shown some promise in this area, but further work will be required to confirm this does not have a deleterious effect on efficacy.

Development of composite additively manufactured and cement filled structures, with appropriate load bearing properties, should also remain an area of active research. Whilst the feasibility of permanent implants with these behaviours remains out of scope in current clinical settings, use for short term implants such as hip spacers in two-stage revision may be viable. Only limited load bearing is permitted on current hip spacers. With the addition of an additively manufactured titanium core or intercalating lattice, it may be possible to greatly improve patient mobility between surgeries, whilst effectively tackling any infections in surrounding tissues. Modelling of the release behaviour from MOC in such a setting will be necessary, alongside significant mechanical assessments to ensure appropriate strength for the intended duration of implantation.

5.2 Binary Ti-Ag alloys

Both Chapter 3 and 4 focus upon the Ti-Ag binary alloy system. Whilst the challenges of additive manufacture of Ti-Ag and development of antimicrobial microstructures were assessed in parallel, it will be crucial in future to unify these two avenues of research. Based on the investigation of antimicrobial response to Ti-Ag, it is not anticipated that the as-manufactured additively manufactured alloys will be effective. Provided a specific antimicrobial microstructure can be identified through conventional alloying means, a key next step will be investigation of microstructural development of additively manufactured Ti-Ag alloys. This will allow heat treatments to be targeted at microstructures that will provide optimum functionality of the final alloy.

5.2.1 Additive manufacture of Ti-Ag alloys

The work presented in Chapter 3 has demonstrated clearly the ability to generate strongly segregated binary Ti-Ag microstructures by SLM. Using in-situ alloying, with appropriate selection of laser parameters results in samples that exhibit low porosity, whilst having controlled degrees of homogeneity. Several key challenges remain to be assessed for any future experimental work in the Ti-Ag system.

First, from a manufacturability perspective, solving the issue of spread-induced Ag demixing presents a critical challenge both for this alloy and for any future multi-component powder bed systems. Given the observed difference in flow behaviour and tendency of Ag-999 powder to agglomerate, homogenising the flow properties of the two component powders may help in this. Second, homogenising the optical properties of Ti and Ag, though counter-intuitive to the efforts to induce microstructural segregation, may provide advantages for improving densification. If, as posited, the microstructural features observed are primarily determined by the rapid cooling of Ag as opposed to reduced local absorptivity, improving homogeneity of optical response could ensure that surrounding Ti particles are not optically shielded by adjacent Ag.

One as yet untested approach to homogenising the optical response of blended powders is to alter the absorptivity of one component in the blend. Previous efforts to tailor reflectivity of powders have been effected by producing a core-shell microstructure within particles through a heat treatment induced chemical gradient [338]. Whilst this approach as demonstrated for Cu-Cr may be extended to other alloy systems, it relies upon initial production of alloyed feedstock. An approach to altering surface absorptivity with a desired chemistry is required, as has been demonstrated by immersion coating of powders and fluidised bed chemical vapour deposition [339, 340]. Coating of Ag powder with a surface layer of Ti would allow improved homogeneity of optical response, whilst maintaining alloy chemistry for Ti-Ag blends. Further to this, as the cohesive nature of powders is dominated by surface energy, such an approach may simultaneously improve flow characteristics and reduce the tendency for further agglomeration during blending. Preliminary work in this area shows promise, but has yet to be rigorously demonstrated in-blend.

Beyond the general use of Ti-Ag as a proof of concept system for in-situ segregation, assessing the microstructural development of segregated feedstocks is a crucial next step. Whilst a probable microstructural development has been posited in line with bulk diffusion couples, it has not been demonstrated that intermetallic phases may be reliably precipitated in alloys deficient in Ag at the bulk scale. Ti_2Ag intermetallic precipitation has been observed in Ti-3Ag alloys by sintering nanoparticulate Ag with Ti, but this may only be feasible due to increased diffusivity at grain boundaries [124].

5.2.2 Antimicrobial response of Ti-Ag alloys

As discussed in Chapter 4, a reliable understanding of the relationship between microstructure and antimicrobial efficacy in Ti-Ag alloys has yet to be established. Despite previous assertions that Ti_2Ag phase was the primary cause, alloys with up to 35 % intermetallic content showed no significant efficacy. The absence of positive controls in previous studies may have resulted in statistically significant, but practically insignificant differences in efficacy being reported. Two primary research challenges need to be met before further

consideration of these binary alloys can be made for translation to medical applications.

First, repeatable generation of demonstrably antimicrobial alloys will be required. Direct replication of previous studies that have demonstrated apparent efficacy may elucidate what specific microstructural characteristics are required and, by extension, must be absent from the alloys produced in this study. Whilst previous research has indicated Ti_2Ag as the dominant phase, this work has clearly demonstrated that even in high quantities, that alone is not sufficient for practical efficacy. It is possible that targeting high Ag content alloys with the exact stoichiometry of Ti-Ag intermetallics could allow clearer distinction of whether the intermetallic phase alone can be responsible for any antimicrobial effect.

Second, provided efficacy observed in previous studies can be confirmed, the antimicrobial mode of action requires examination. Understanding the relationship between silver ion release and efficacy in vitro will be a crucial first step. Assessing elution under bacterial culture conditions as used to test efficacy would allow for any direct relationship to be demonstrated. Recovery of cultures for analysis with ICP-MS may provide sufficient resolution to confirm if Ag is being eluted, whilst use of combined flow-cytometry ICP could allow direct correlation between the silver content of bacteria exposed to the surface of such alloys and the degree of stress they are under [337], further distinguishing between bacteria damaged by Ag uptake and any that have been killed by a surface interaction.

5.3 Overall conclusions

The formulation of antimicrobial biomaterials, suitable for delivery in additively manufactured implants, shows promise as an approach for implant associated infection management.

First, an antimicrobial cement formulation was investigated. An injectable magnesium oxychloride cement (MOC) was formulated, and the effect of doping with Ag_3PO_4 as an antimicrobial agent considered. Whilst silver doped MOC showed sustained Ag release over 14 days and enhanced efficacy in vitro, undoped MOC also showed significant inherent antimicrobial behaviour.

Second, novel Ti-Ag alloy microstructures were produced through laser powder bed fusion (L-PBF) additive manufacturing. Blended elemental feedstocks were manufactured with a range of laser parameters, with resulting microstructures ranging from highly segregated to homogenised. Statistical analysis demonstrated in-situ spread induced demixing of the powder blend, with varying Ag content across the build bed.

Finally, the possible mode of action of antimicrobial Ti-Ag alloys was assessed. Despite previous assertions that specific intermetallic phases dominate efficacy, high Ti_2Ag content alloys showed no statistically significant change in antimicrobial action versus control samples. This study further indicates the poorly understood nature of antimicrobial alloys, and the need for more in depth mechanistic investigations.

Together, this work contributes to the growing need for biomaterials driven approaches to infection prevention in hard tissue reconstruction.

LIST OF REFERENCES

[1] Peter Howard, Robin Brittain, Sandra Lawrence, Jeffrey Stonadge, Mark Wilkinson, and Timothy Wilton. National Joint Registry — 17th Annual Report. *National Joint Registry*, pages 130–147, 2020. URL www.njrcentre.org.uk.

[2] Scottish Arthroplasty Project. Scottish Arthroplasty Project Annual Report 2017. Technical report, 2017. URL https://www.arthro.scot.nhs.uk/docs/2017/2017-08-08-SAP-Publication-Report.pdf.

[3] Health and Social Care Information Centre. Hospital Admitted Patient Care Activity. Technical Report November, National Health Service, 2018. URL https://digital.nhs.uk/data-and-information/publications/statistical/hospital-admitted-patient-care-activity/2016-17http://content.digital.nhs.uk/catalogue/PUB22378/hosp-epis-stat-admi-summ-rep-2015-16-rep.pdfhttps://digital.nhs.uk/data-and-information/.

[4] OECD. Hip and knee replacement. In *Health at a Glance 2019*, Health at a Glance. OECD, Paris, nov 2019. ISBN 9789264807662. doi: 10.1787/4dd50c09-en. URL https://www.oecd-ilibrary.org/social-issues-migration-health/health-at-a-glance-2019{_}2fc83b9a-en.

[5] OECD. OECD Labour Force Statistics. Technical report, OECD, feb 2018. URL https://www.oecd-ilibrary.org/employment/oecd-labour-force-statistics-2017{_}oecd{_}lfs-2017-enhttp://www.oecd-ilibrary.org/employment/oecd-labour-force-statistics-2017{_}oecd{_}lfs-2017-en.

[6] Steven Kurtz, Kevin Ong, Edmund Lau, Fionna Mowat, and Michael Halpern. Projections of Primary and Revision Hip and Knee Arthroplasty in the United States from 2005 to 2030. *The Journal of Bone and Joint Surgery (American)*, 89(4):780, apr 2007. ISSN 0021-9355. doi: 10.2106/JBJS.

F.00222. URL http://www.ncbi.nlm.nih.gov/pubmed/17403800http://jbjs.org/cgi/doi/10.2106/JBJS.F.00222.

[7] Veronika Pilz, Tim Hanstein, and Ralf Skripitz. Projections of primary hip arthroplasty in Germany until 2040. *Acta Orthopaedica*, 89(3):308–313, may 2018. ISSN 1745-3674. doi: 10.1080/17453674.2018.1446463. URL https://www.tandfonline.com/doi/full/10.1080/17453674.2018.1446463.

[8] D. Culliford, J. Maskell, A. Judge, C. Cooper, D. Prieto-Alhambra, and N.K. Arden. Future projections of total hip and knee arthroplasty in the UK: results from the UK Clinical Practice Research Datalink. *Osteoarthritis and Cartilage*, 23(4):594–600, apr 2015. ISSN 1063-4584. doi: 10.1016/J.JOCA.2014.12.022. URL https://www.sciencedirect.com/science/article/pii/S106345841401396X.

[9] W. Zimmerli and P.E. Ochsner. Management of Infection Associated with Prosthetic Joints. *Infection*, 31(2):99–108, mar 2003. ISSN 0300-8126. doi: 10.1007/s15010-002-3079-9. URL http://link.springer.com/10.1007/s15010-002-3079-9.

[10] Hirotaka Chikuda, Hideo Yasunaga, Hiromasa Horiguchi, Katsushi Takeshita, Shurei Sugita, Shuji Taketomi, Kiyohide Fushimi, and Sakae Tanaka. Impact of age and comorbidity burden on mortality and major complications in older adults undergoing orthopaedic surgery: an analysis using the Japanese diagnosis procedure combination database. *BMC Musculoskeletal Disorders*, 14(1):173, dec 2013. ISSN 1471-2474. doi: 10.1186/1471-2474-14-173. URL http://bmcmusculoskeletdisord.biomedcentral.com/articles/10.1186/1471-2474-14-173.

[11] NG Farrar, M Alaker, and SP Duckett. A cost analysis of elective hip revision arthroplasty versus periprosthetic hip fracture management in a district general hospital. *The Bulletin of the Royal College of Surgeons of England*, 97(5):E26–E29, may 2015. ISSN 1473-6357. doi: 10.1308/147363515X14134529302506. URL http://publishing.rcseng.ac.uk/doi/10.1308/147363515X14134529302506.

[12] S. Klouche, E. Sariali, and P. Mamoudy. Total hip arthroplasty revision due to infection: A cost analysis approach. *Orthopaedics & Traumatology: Surgery & Research*, 96(2):124–132, apr 2010. ISSN 1877-0568. doi: 10.1016/J.OTSR.2009.11.004. URL https://www.sciencedirect.com/science/article/pii/S1877056810000095.

[13] Emine Alp, Fatma Cevahir, Safiye Ersoy, and Ahmet Guney. Incidence and economic burden of prosthetic joint infections in a university hospital: A report from a middle-income country. *Journal of Infection and Public Health*, 9(4):494–498, jul 2016. ISSN

1876-0341. doi: 10.1016/J.JIPH.2015.12.014. URL https://www.sciencedirect.com/science/article/pii/S1876034116000058.

[14] H.J. Rack and J.I. Qazi. Titanium alloys for biomedical applications. *Materials Science and Engineering: C*, 26(8):1269–1277, sep 2006. ISSN 0928-4931. doi: 10.1016/J.MSEC.2005.08.032. URL https://www.sciencedirect.com/science/article/pii/S0928493105002237.

[15] Ingrid Milošev. *Biomedical Applications*, volume 55 of *Modern Aspects of Electrochemistry*. Springer US, Boston, MA, 2012. ISBN 978-1-4614-3124-4. doi: 10.1007/978-1-4614-3125-1. URL http://link.springer.com/10.1007/978-1-4614-3125-1{_}1http://link.springer.com/10.1007/978-1-4614-3125-1.

[16] Vitali Goriainov, Richard Cook, Jeremy M. Latham, Douglas G. Dunlop, and Richard O.C. Oreffo. Bone and metal: An orthopaedic perspective on osseointegration of metals. *Acta Biomaterialia*, 10(10):4043–4057, oct 2014. ISSN 17427061. doi: 10.1016/j.actbio.2014.06.004. URL http://linkinghub.elsevier.com/retrieve/pii/S1742706114002517.

[17] Yong Wu, Joseph P. Zitelli, Kevor S. TenHuisen, Xiaojun Yu, and Matthew R. Libera. Differential response of Staphylococci and osteoblasts to varying titanium surface roughness. *Biomaterials*, 32(4):951–960, feb 2011. ISSN 01429612. doi: 10.1016/j.biomaterials.2010.10.001. URL http://www.sciencedirect.com/science/article/pii/S0142961210012792http://linkinghub.elsevier.com/retrieve/pii/S0142961210012792.

[18] Laurent Le Guehennec, Marco-Antonio Lopez-Heredia, Benedicte Enkel, Pierre Weiss, Yves Amouriq, and Pierre Layrolle. Osteoblastic cell behaviour on different titanium implant surfaces. *Acta Biomaterialia*, 4(3):535–543, may 2008. ISSN 17427061. doi: 10.1016/j.actbio.2007.12.002. URL http://www.sciencedirect.com/science/article/pii/S1742706107002000{\#}fig6http://linkinghub.elsevier.com/retrieve/pii/S1742706107002000.

[19] J Lincks, BD Boyan, CR Blanchard, CH Lohmann, Y Liu, DL Cochran, DD Dean, and Z Schwartz. Response of MG63 osteoblast-like cells to titanium and titanium alloy is dependent on surface roughness and composition. *Biomaterials*, 19:2219–2232, 1998. URL https://ac.els-cdn.com/S0142961298001446/1-s2.0-S0142961298001446-main.pdf?{_}tid=0cc9afb8-1252-11e8-893f-00000aab0f26{\&}acdnat=1518700605{_}67d9f3156b5afcd781690fd4a4ed1ddb.

[20] L.R. Williams, K.F. Fan, and R.P. Bentley. Custom-made titanium cranioplasty: early and late complications of 151 cranioplasties and review of the literature. *International Journal of Oral and Maxillofacial Surgery*, 44(5):599–608, may 2015. ISSN 09015027. doi: 10.1016/j.ijom.2014.09.006. URL http://linkinghub.elsevier.com/retrieve/pii/S0901502714003397.

[21] Carla Renata Arciola, Davide Campoccia, and Lucio Montanaro. Implant infections: adhesion, biofilm formation and immune evasion. *Nature Reviews Microbiology*, 16 (7):397–409, jul 2018. ISSN 1740-1526. doi: 10.1038/s41579-018-0019-y. URL http://www.nature.com/articles/s41579-018-0019-y.

[22] Nuno Cerca, Gerald B. Pier, Manuel Vilanova, Rosário Oliveira, and Joana Azeredo. Quantitative analysis of adhesion and biofilm formation on hydrophilic and hydrophobic surfaces of clinical isolates of Staphylococcus epidermidis. *Research in Microbiology*, 156(4):506–514, may 2005. ISSN 0923-2508. doi: 10.1016/J.RESMIC.2005.01.007.

[23] Philip S Stewart and J William Costerton. Antibiotic resistance of bacteria in biofilms. *The Lancet*, 358(9276):135–138, jul 2001. ISSN 0140-6736. doi: 10.1016/S0140-6736(01)05321-1. URL https://www.sciencedirect.com/science/article/pii/S0140673601053211.

[24] Naif Alzahrani. The effect of hospitalization on patients' emotional and psychological well-being among adult patients: An integrative review. *Applied Nursing Research*, 61:151488, oct 2021. ISSN 0897-1897. doi: 10.1016/J.APNR.2021.151488.

[25] C.R. Arciola, Y.H. An, D. Campoccia, M.E. Donati, and L. Montanaro. Etiology of Implant Orthopedic Infections: A Survey on 1027 Clinical Isolates. *The International Journal of Artificial Organs*, 28(11):1091–1100, nov 2005. ISSN 0391-3988. doi: 10.1177/039139880502801106. URL http://journals.sagepub.com/doi/10.1177/039139880502801106.

[26] Patrick Thornley, Nathan Evaniew, Michael Riediger, Mitchell Winemaker, Mohit Bhandari, and Michelle Ghert. Postoperative antibiotic prophylaxis in total hip and knee arthroplasty: a systematic review and meta-analysis of randomized controlled trials. *CMAJ Open*, 3(3):E338, sep 2015. doi: 10.9778/CMAJO.20150012. URL /pmc/articles/PMC4596117//pmc/articles/PMC4596117/?report=abstracthttps://www.ncbi.nlm.nih.gov/pmc/articles/PMC4596117/.

[27] de Jonge SW, Boldingh QJJ, Solomkin JS, Dellinger EP, Egger M, Salanti G, Allegranzi B, and Boermeester MA. Effect of postoperative continuation of antibiotic

prophylaxis on the incidence of surgical site infection: a systematic review and meta-analysis. *The Lancet. Infectious diseases*, 20(10):1182–1192, oct 2020. ISSN 1474-4457. doi: 10.1016/S1473-3099(20)30084-0. URL https://pubmed.ncbi.nlm.nih.gov/32470329/.

[28] Surendra Senthi, Jacob T. Munro, and Rocco P. Pitto. Infection in total hip replacement: meta-analysis. *International Orthopaedics 2010 35:2*, 35(2):253–260, nov 2010. ISSN 1432-5195. doi: 10.1007/S00264-010-1144-Z. URL https://link.springer.com/article/10.1007/s00264-010-1144-z.

[29] P Sendi, P. O. Lötscher, B. Kessler, P. Graber, W. Zimmerli, and M. Clauss. Debridement and implant retention in the management of hip periprosthetic joint infection. *https://doi.org/10.1302/0301-620X.99B3.BJJ-2016-0609.R1*, 99B(3):330–336, mar 2017. doi: 10.1302/0301-620X.99B3.BJJ-2016-0609.R1. URL https://online.boneandjoint.org.uk/doi/abs/10.1302/0301-620X.99B3.BJJ-2016-0609.R1.

[30] Atul F. Kamath, Kevin L. Ong, Edmund Lau, Vanessa Chan, Thomas P. Vail, Harry E. Rubash, Daniel J. Berry, and Kevin J. Bozic. Quantifying the Burden of Revision Total Joint Arthroplasty for Periprosthetic Infection. *The Journal of Arthroplasty*, 30(9):1492–1497, sep 2015. ISSN 0883-5403. doi: 10.1016/J.ARTH.2015.03.035.

[31] M Demerec. PATTERNS OF BACTERIAL RESISTANCE TO PENICILLIN, AUREOMYCIN, AND STREPTOMYCIN. *The Journal of clinical investigation*, 28 (5):891–893, 1949. ISSN 00219738. doi: 10.1172/jci102173.

[32] Fabian Svara and Daniel J Rankin. The evolution of plasmid-carried antibiotic resistance. *BMC Evolutionary Biology 2011 11:1*, 11(1):1–10, may 2011. ISSN 1471-2148. doi: 10.1186/1471-2148-11-130. URL https://bmcecolevol.biomedcentral.com/articles/10.1186/1471-2148-11-130.

[33] Carl Llor and Lars Bjerrum. Antimicrobial resistance: risk associated with antibiotic overuse and initiatives to reduce the problem. *Therapeutic advances in drug safety*, 5(6):229–41, dec 2014. ISSN 2042-0986. doi: 10.1177/2042098614554919. URL http://www.ncbi.nlm.nih.gov/pubmed/25436105http://www.pubmedcentral.nih.gov/articlerender.fcgi?artid=PMC4232501.

[34] Sophie Thanner, David Drissner, and Fiona Walsh. Antimicrobial resistance in agriculture. *mBio*, 7(2), apr 2016. doi: 10.1128/MBIO.02227-15. URL https://journals.asm.org/journal/mbio.

[35] Frederick J. Angulo, Nicole L. Baker, Sonja J. Olsen, Alicia Anderson, and Timothy J. Barrett. Antimicrobial use in agriculture: controlling the transfer of antimicrobial resistance to humans. *Seminars in Pediatric Infectious Diseases*, 15(2): 78–85, apr 2004. ISSN 1045-1870. doi: 10.1053/J.SPID.2004.01.010.

[36] Christin Löffler, Attila Altiner, Annette Diener, Reinhard Berner, Gregor Feldmeier, Christian Helbig, Winfried V. Kern, Anna Köchling, Michaela Schmid, Gerhard Schön, Helmut Schröder, Karl Wegscheider, and Anja Wollny. Hospitalization for Acute Respiratory Tract Infection in a Low-Antibiotic-Prescribing Setting: Cross-Sectional Data from General Practice. *Antibiotics 2020, Vol. 9, Page 653*, 9(10): 653, sep 2020. doi: 10.3390/ANTIBIOTICS9100653. URL https://www.mdpi.com/2079-6382/9/10/653/htmhttps://www.mdpi.com/2079-6382/9/10/653.

[37] Thomas J. Hall, Victor M. Villapún, Owen Addison, Mark A. Webber, Morgan Lowther, Sophie E. T. Louth, Sophie E. Mountcastle, Mathieu Y. Brunet, and Sophie C. Cox. A call for action to the biomaterial community to tackle antimicrobial resistance. *Biomaterials Science*, 8(18): 4951–4974, sep 2020. ISSN 2047-4830. doi: 10.1039/D0BM01160F. URL https://pubs.rsc.org/en/content/articlehtml/2020/bm/d0bm01160fhttps://pubs.rsc.org/en/content/articlelanding/2020/bm/d0bm01160fhttp://xlink.rsc.org/?DOI=D0BM01160F.

[38] Michele Fiore, Andrea Sambri, Riccardo Zucchini, Claudio Giannini, Davide Maria Donati, and Massimiliano De Paolis. Silver-coated megaprosthesis in prevention and treatment of peri-prosthetic infections: a systematic review and meta-analysis about efficacy and toxicity in primary and revision surgery. *European Journal of Orthopaedic Surgery and Traumatology*, (3):1–20, sep 2020. ISSN 14321068. doi: 10.1007/s00590-020-02779-z. URL https://doi.org/10.1007/s00590-020-02779-z.

[39] Tom Schmidt-Braekling, Arne Streitbuerger, Georg Gosheger, Friedrich Boettner, Markus Nottrott, Helmut Ahrens, Ralf Dieckmann, Wiebke Guder, Dimosthenis Andreou, Gregor Hauschild, Burkhard Moellenbeck, Wenzel Waldstein, and Jendrik Hardes. Silver-coated megaprostheses: review of the literature. *European Journal of Orthopaedic Surgery & Traumatology*, 27(4):483–489, may 2017. ISSN 1633-8065. doi: 10.1007/s00590-017-1933-9. URL http://link.springer.com/10.1007/s00590-017-1933-9.

[40] Volker Alt. Antimicrobial coated implants in trauma and orthopaedicsA clinical review and risk-benefit analysis. *Injury*, 48(3):599–607, mar 2017. ISSN 00201383. doi:

10.1016/j.injury.2016.12.011. URL http://linkinghub.elsevier.com/retrieve/pii/S0020138316308178.

[41] Erika L Cyphert and Horst A von Recum. Emerging technologies for long-term antimicrobial device coatings: advantages and limitations:. *https://doi.org/10.1177/1535370216688572*, 242(8):788–798, jan 2017. doi: 10.1177/1535370216688572. URL https://journals.sagepub.com/doi/full/10.1177/1535370216688572?casa{_}token=fxfR{_}IAwCjAAAAAA{\%}3AUDhPqAqxd8vrBjqeNzurFQpb7A2Z-ODX2OOO{_}cMgpTf{_}MQnf7V91XbWn{_}clzcSLvNC4YKO3U9CtyrQ.

[42] Ruggero Bosco, Jeroen Van Den Beucken, Sander Leeuwenburgh, and John Jansen. Surface Engineering for Bone Implants: A Trend from Passive to Active Surfaces. *Coatings*, 2(4):95–119, jul 2012. ISSN 2079-6412. doi: 10.3390/coatings2030095. URL http://www.mdpi.com/2079-6412/2/3/95/.

[43] Joseph A. Lemire, Joe J. Harrison, and Raymond J. Turner. Antimicrobial activity of metals: mechanisms, molecular targets and applications. *Nature Reviews Microbiology*, 11(6):371–384, jun 2013. ISSN 1740-1526. doi: 10.1038/nrmicro3028. URL http://www.nature.com/articles/nrmicro3028.

[44] Yi-Yun Kao, Yi-Chun Chen, Tsun-Jen Cheng, Yin-Mei Chiung, and Pei-Shan Liu. Zinc Oxide Nanoparticles Interfere With Zinc Ion Homeostasis to Cause Cytotoxicity. *Toxicological Sciences*, 125(2):462–472, feb 2012. ISSN 1096-6080. doi: 10.1093/TOXSCI/KFR319. URL https://academic.oup.com/toxsci/article/125/2/462/1615354.

[45] Kristina Glenske, Phil Donkiewicz, Alexander Köwitsch, Nada Milosevic-Oljaca, Patrick Rider, Sven Rofall, Jörg Franke, Ole Jung, Ralf Smeets, Reinhard Schnettler, Sabine Wenisch, and Mike Barbeck. Applications of Metals for Bone Regeneration. *International Journal of Molecular Sciences 2018, Vol. 19, Page 826*, 19 (3):826, mar 2018. doi: 10.3390/IJMS19030826. URL https://www.mdpi.com/1422-0067/19/3/826/htmhttps://www.mdpi.com/1422-0067/19/3/826.

[46] Joe J. Harrison, Howard Ceri, Carol A. Stremick, and Raymond J. Turner. Biofilm susceptibility to metal toxicity. *Environmental Microbiology*, 6(12):1220–1227, dec 2004. ISSN 1462-2912. doi: 10.1111/j.1462-2920.2004.00656.x. URL http://doi.wiley.com/10.1111/j.1462-2920.2004.00656.x.

[47] Chengyun Ning, Xiaolan Wang, Lihua Li, Ye Zhu, Mei Li, Peng Yu, Lei Zhou, Zhengnan Zhou, Junqi Chen, Guoxin Tan, Yu Zhang, Yingjun Wang, and Chuan-

bin Mao. Concentration Ranges of Antibacterial Cations for Showing the Highest Antibacterial Efficacy but the Least Cytotoxicity against Mammalian Cells: Implications for a New Antibacterial Mechanism. *Chemical Research in Toxicology*, 28(9):1815–1822, sep 2015. ISSN 15205010. doi: 10.1021/acs.chemrestox.5b00258. URL http://www.ncbi.nlm.nih.gov/pubmed/26258952http://www.pubmedcentral.nih.gov/articlerender.fcgi?artid=PMC4925100.

[48] J Ruben Morones-Ramirez, Jonathan A Winkler, Catherine S Spina, and James J Collins. Silver enhances antibiotic activity against gram-negative bacteria. *Science translational medicine*, 5(190):190ra81, jun 2013. ISSN 1946-6242. doi: 10.1126/scitranslmed.3006276. URL http://www.ncbi.nlm.nih.gov/pubmed/23785037http://www.pubmedcentral.nih.gov/articlerender.fcgi?artid=PMC3771099.

[49] Pavel Dibrov, Judith Dzioba, Khoosheh K Gosink, and Claudia C Häse. Chemiosmotic mechanism of antimicrobial activity of Ag(+) in Vibrio cholerae. *Antimicrobial agents and chemotherapy*, 46(8):2668–70, aug 2002. ISSN 0066-4804. doi: 10.1128/AAC.46.8.2668-2670.2002. URL http://www.ncbi.nlm.nih.gov/pubmed/12121953http://www.pubmedcentral.nih.gov/articlerender.fcgi?artid=PMC127333.

[50] Katherine B. Holt and Allen J. Bard. Interaction of silver(I) ions with the respiratory chain of Escherichia coli: An electrochemical and scanning electrochemical microscopy study of the antimicrobial mechanism of micromolar Ag. *Biochemistry*, 44(39):13214–13223, 2005. ISSN 00062960. doi: 10.1021/bi0508542. URL https://pubs.acs.org/doi/full/10.1021/bi0508542.

[51] Hee-Jin Park, Jee Yeon Kim, Jaeeun Kim, Joon-Hee Lee, Ji-Sook Hahn, Man Bock Gu, and Jeyong Yoon. Silver-ion-mediated reactive oxygen species generation affecting bactericidal activity. *Water Research*, 43(4):1027–1032, mar 2009. ISSN 0043-1354. doi: 10.1016/J.WATRES.2008.12.002. URL https://www.sciencedirect.com/science/article/pii/S0043135408006039?via{\%}3Dihub.

[52] Hua Geng, Gowsihan Poologasundarampillai, Naomi Todd, Aine Devlin-Mullin, Katie L. Moore, Zahra Golrokhi, James B. Gilchrist, Eric Jones, Richard J. Potter, Chris Sutcliffe, Marie O'Brien, David W.L. Hukins, Sarah Cartmell, Christopher A. Mitchell, and Peter D. Lee. Biotransformation of Silver Released from Nanoparticle Coated Titanium Implants Revealed in Regenerating Bone. *ACS Applied Materials & Interfaces*, 9(25):21169–21180, jun 2017. ISSN 1944-8244. doi: 10.1021/acsami.7b05150. URL http://pubs.acs.org/doi/10.1021/acsami.7b05150.

[53] Joe A. Lemire, Lindsay Kalan, Alexandru Bradu, and Raymond J. Turner. Silver Oxynitrate, an Unexplored Silver Compound with Antimicrobial and Antibiofilm Activity. *Antimicrobial Agents and Chemotherapy*, 59(7):4031–4039, jul 2015. ISSN 0066-4804. doi: 10.1128/AAC.05177-14. URL http://www.ncbi.nlm.nih.gov/pubmed/25918137http://www.pubmedcentral.nih.gov/articlerender.fcgi?artid=PMC4468715.

[54] J. A. McMillan. Higher Oxidation States of Silver. *Chemical Reviews*, 62(1):65–80, feb 1962. ISSN 0009-2665. doi: 10.1021/cr60215a004. URL http://pubs.acs.org/cgi-bin/doilookup/?10.1021/cr60215a004.

[55] Wilson Sim, Ross Barnard, M.A.T. Blaskovich, and Zyta Ziora. Antimicrobial Silver in Medicinal and Consumer Applications: A Patent Review of the Past Decade (20072017). *Antibiotics*, 7(4):93, oct 2018. ISSN 2079-6382. doi: 10.3390/antibiotics7040093. URL http://www.mdpi.com/2079-6382/7/4/93.

[56] David J. Barillo and David E. Marx. Silver in medicine: A brief history BC 335 to present. *Burns*, 40(S1):S3–S8, dec 2014. ISSN 0305-4179. doi: 10.1016/J.BURNS.2014.09.009.

[57] Simon Silver, Le T. Phung, and Gregg Silver. Silver as biocides in burn and wound dressings and bacterial resistance to silver compounds. In *Journal of Industrial Microbiology and Biotechnology*, volume 33, pages 627–634, jul 2006. doi: 10.1007/s10295-006-0139-7.

[58] Simon Silver. Bacterial silver resistance: molecular biology and uses and misuses of silver compounds. *FEMS Microbiology Reviews*, 27(2-3):341–353, jun 2003. ISSN 1574-6976. doi: 10.1016/S0168-6445(03)00047-0. URL https://academic.oup.com/femsre/article-lookup/doi/10.1016/S0168-6445(03)00047-0.

[59] Gail Larkin Mchugh, RobertC. Moellering, CyrusC. Hopkins, and MortonN. Swartz. SALMONELLA TYPHIMURIUM RESISTANT TO SILVER NITRATE, CHLORAMPHENICOL, AND AMPICILLIN: A New Threat in Burn Units ? *The Lancet*, 305(7901):235–240, feb 1975. ISSN 0140-6736. doi: 10.1016/S0140-6736(75)91138-1. URL https://www.sciencedirect.com/science/article/pii/S0140673675911381?via{\%}3Dihub.

[60] Le T. Phung, Simon Silver, Amit Gupta, and Diane E. Taylor. Diversity of silver resistance genes in IncH incompatibility group plasmids. *Microbiology*, 147(12):3393–3402, dec 2001. ISSN 1350-0872. doi: 10.1099/

00221287-147-12-3393. URL http://mic.microbiologyresearch.org/content/journal/micro/10.1099/00221287-147-12-3393.

[61] C. P. Randall, A. Gupta, N. Jackson, D. Busse, and A. J. O'Neill. Silver resistance in Gram-negative bacteria: a dissection of endogenous and exogenous mechanisms. *Journal of Antimicrobial Chemotherapy*, 70(4):1037–1046, jan 2015. ISSN 0305-7453. doi: 10.1093/jac/dku523. URL https://academic.oup.com/jac/article-lookup/doi/10.1093/jac/dku523.

[62] Amit Gupta, Kazuaki Matsui, Jeng-Fan Lo, and Simon Silver. Molecular basis for resistance to silver cations in Salmonella. *Nature Medicine*, 5(2):183–188, feb 1999. ISSN 1078-8956. doi: 10.1038/5545. URL http://www.nature.com/articles/nm0299{_}183.

[63] Phillip J Finley, Rhy Norton, Cindy Austin, Amber Mitchell, Sara Zank, and Paul Durham. Unprecedented Silver Resistance in Clinically Isolated Enterobacteriaceae: Major Implications for Burn and Wound Management. *Antimicrobial agents and chemotherapy*, 59(8):4734–41, aug 2015. ISSN 1098-6596. doi: 10.1128/AAC.00026-15. URL http://www.ncbi.nlm.nih.gov/pubmed/26014954http://www.pubmedcentral.nih.gov/articlerender.fcgi?artid=PMC4505248.

[64] Jia V Loh, Steven L Percival, Emma J Woods, Nicola J Williams, and Christine A Cochrane. Silver resistance in MRSA isolated from wound and nasal sources in humans and animals. *International Wound Journal*, 6(1):32–38, feb 2009. ISSN 17424801. doi: 10.1111/j.1742-481X.2008.00563.x. URL http://doi.wiley.com/10.1111/j.1742-481X.2008.00563.x.

[65] C. P. Randall, L. B. Oyama, J. M. Bostock, I. Chopra, and A. J. O'Neill. The silver cation (Ag+): antistaphylococcal activity, mode of action and resistance studies. *Journal of Antimicrobial Chemotherapy*, 68(1):131–138, jan 2013. ISSN 0305-7453. doi: 10.1093/jac/dks372. URL https://academic.oup.com/jac/article-lookup/doi/10.1093/jac/dks372.

[66] Jendrik Hardes, Marcel P. Henrichs, Gregor Hauschild, Markus Nottrott, Wiebke Guder, and Arne Streitbuerger. Silver-Coated Megaprosthesis of the Proximal Tibia in Patients With Sarcoma. *Journal of Arthroplasty*, 2017. ISSN 15328406. doi: 10.1016/j.arth.2017.02.054.

[67] H. Wafa, R. J. Grimer, K. Reddy, L. Jeys, A. Abudu, S. R. Carter, and R. M. Tillman. Retrospective evaluation of the incidence of early periprosthetic infection

with silver-treated endoprostheses in high-risk patients: Case-control study. *Bone and Joint Journal*, 2015. ISSN 20494408. doi: 10.1302/0301-620X.97B2.34554.

[68] Ping Li, Juan Li, Changzhu Wu, Qingsheng Wu, and Jian Li. Synergistic antibacterial effects of β-lactam antibiotic combined with silver nanoparticles. *Nanotechnology*, 16(9):1912–1917, sep 2005. ISSN 0957-4484. doi: 10.1088/0957-4484/16/9/082. URL http://stacks.iop.org/0957-4484/16/i=9/a=082?key=crossref.1f9651ed1c3ea96d6b820e6213df23b1.

[69] Aleš Panáček, Monika Smékalová, Renata Večeová, Kateina Bogdanová, Magdaléna Röderová, Milan Kolá, Martina Kilianová, Šárka Hradilová, Jens P. Froning, Markéta Havrdová, Robert Prucek, Radek Zboil, and Libor Kvítek. Silver nanoparticles strongly enhance and restore bactericidal activity of inactive antibiotics against multiresistant Enterobacteriaceae. *Colloids and Surfaces B: Biointerfaces*, 142:392–399, jun 2016. ISSN 0927-7765. doi: 10.1016/J.COLSURFB.2016.03.007. URL https://www.sciencedirect.com/science/article/pii/S0927776516301515.

[70] Jaeeun Kim, Betsey Pitts, Philip S Stewart, Anne Camper, and Jeyong Yoon. Comparison of the antimicrobial effects of chlorine, silver ion, and tobramycin on biofilm. *Antimicrobial agents and chemotherapy*, 52(4):1446–53, apr 2008. ISSN 0066-4804. doi: 10.1128/AAC.00054-07. URL http://www.ncbi.nlm.nih.gov/pubmed/18195062http://www.pubmedcentral.nih.gov/articlerender.fcgi?artid=PMC2292569.

[71] K C Chaw, M Manimaran, and Francis E H Tay. Role of silver ions in destabilization of intermolecular adhesion forces measured by atomic force microscopy in Staphylococcus epidermidis biofilms. *Antimicrobial agents and chemotherapy*, 49(12):4853–9, dec 2005. ISSN 0066-4804. doi: 10.1128/AAC.49.12.4853-4859.2005. URL http://www.ncbi.nlm.nih.gov/pubmed/16304145http://www.pubmedcentral.nih.gov/articlerender.fcgi?artid=PMC1315927.

[72] Hee-Jin Park, Soomin Park, Jinkyu Roh, Sujin Kim, Kyunghee Choi, Jongheop Yi, Younghun Kim, and Jeyong Yoon. Biofilm-inactivating activity of silver nanoparticles: A comparison with silver ions. *Journal of Industrial and Engineering Chemistry*, 19(2):614–619, mar 2013. ISSN 1226-086X. doi: 10.1016/J.JIEC.2012.09.013. URL https://www.sciencedirect.com/science/article/pii/S1226086X12003073{\#}sec0065.

[73] G. Perrelli and G. Piolatto. Tentative reference values for gold, silver and platinum: literature data analysis. *Science of The Total Environment*, 120(1-2):93–96, jun

1992. ISSN 0048-9697. doi: 10.1016/0048-9697(92)90219-I. URL https://www.sciencedirect.com/science/article/pii/004896979290219I.

[74] Guido Scoccianti, Filippo Frenos, Giovanni Beltrami, Domenico Andrea Campanacci, and Rodolfo Capanna. Levels of silver ions in body fluids and clinical results in silver-coated megaprostheses after tumour, trauma or failed arthroplasty. *Injury*, 2016. ISSN 18790267. doi: 10.1016/j.injury.2016.07.042.

[75] M. Glehr, A. Leithner, J. Friesenbichler, W. Goessler, A. Avian, D. Andreou, W. Maurer-Ertl, R. Windhager, and P-U. Tunn. Argyria following the use of silver-coated megaprostheses. *The Bone & Joint Journal*, 95-B(7):988–992, jul 2013. ISSN 2049-4394. doi: 10.1302/0301-620X.95B7.31124. URL http://online.boneandjoint.org.uk/doi/10.1302/0301-620X.95B7.31124.

[76] E Sudmann, H Vik, M Rait, K Todnem, K J Andersen, K Julsham, O Flesland, and J Rungby. Systemic and local silver accumulation after total hip replacement using silver-impregnated bone cement. *Medical progress through technology*, 20(3-4):179–84, 1994. ISSN 0047-6552. URL http://www.ncbi.nlm.nih.gov/pubmed/7877562.

[77] Mohamed Gouda. Nano-zirconium oxide and nano-silver oxide/cotton gauze fabrics for antimicrobial and wound healing acceleration:. *http://dx.doi.org/10.1177/1528083711414960*, 41(3):222–240, aug 2011. doi: 10.1177/1528083711414960. URL https://journals.sagepub.com/doi/full/10.1177/1528083711414960?casa{_}token=mlFFBrTGEHIAAAAA{\%}3A7tlJkLrNvm5vsLLutnt1LyJYsS4lQNYVKLtcqhxVGU0YVNTDQOu3ROH9foeE{_}uWqmvqZnCWyXg5Ftg.

[78] Dagmar Chudobova, Lukas Nejdl, Jaromir Gumulec, Olga Krystofova, Miguel Angel Merlos Rodrigo, Jindrich Kynicky, Branislav Ruttkay-Nedecky, Pavel Kopel, Petr Babula, Vojtech Adam, and Rene Kizek. Complexes of Silver(I) Ions and Silver Phosphate Nanoparticles with Hyaluronic Acid and/or Chitosan as Promising Antimicrobial Agents for Vascular Grafts. *International Journal of Molecular Sciences 2013, Vol. 14, Pages 13592-13614*, 14(7):13592–13614, jun 2013. doi: 10.3390/IJMS140713592. URL https://www.mdpi.com/1422-0067/14/7/13592/htmhttps://www.mdpi.com/1422-0067/14/7/13592.

[79] Surapaneni Meghana, Prachi Kabra, Swati Chakraborty, and Nagarajan Padmavathy. Understanding the pathway of antibacterial activity of copper oxide nanoparticles. *RSC Advances*, 5(16):12293–12299, jan 2015. ISSN 20462069. doi: 10.1039/c4ra12163e. URL https:

//pubs.rsc.org/en/content/articlehtml/2015/ra/c4ra12163ehttps://pubs.rsc.org/en/content/articlelanding/2015/ra/c4ra12163e.

[80] Azhwar Raghunath and Ekambaram Perumal. Metal oxide nanoparticles as antimicrobial agents: a promise for the future. *International Journal of Antimicrobial Agents*, 49(2):137–152, feb 2017. ISSN 0924-8579. doi: 10.1016/J.IJANTIMICAG.2016.11.011.

[81] Marcel F. Kunrath and Maria M. Campos. Metallic-nanoparticle release systems for biomedical implant surfaces: effectiveness and safety. *https://doi.org/10.1080/17435390.2021.1915401*, 15(6):721–739, 2021. doi: 10.1080/17435390.2021.1915401. URL https://www.tandfonline.com/doi/abs/10.1080/17435390.2021.1915401.

[82] Aoxue Zhang, Kuiyu Meng, Yuda Liu, Yuanhu Pan, Wei Qu, Dongmei Chen, and Shuyu Xie. Absorption, distribution, metabolism, and excretion of nanocarriers in vivo and their influences. *Advances in Colloid and Interface Science*, 284:102261, oct 2020. ISSN 0001-8686. doi: 10.1016/J.CIS.2020.102261.

[83] J. Sawai, H. Kojima, H. Igarashi, A. Hashimoto, S. Shoji, T. Sawaki, A. Hakoda, E. Kawada, T. Kokugan, and M. Shimizu. Antibacterial characteristics of magnesium oxide powder. *World Journal of Microbiology and Biotechnology*, 16(2):187–194, 2000. ISSN 09593993. doi: 10.1023/A:1008916209784. URL http://link.springer.com/10.1023/A:1008916209784.

[84] Erum Dilshad, Mehmoona Bibi, Nadeem Ahmed Sheikh, Khairul Fikri Tamrin, Qaisar Mansoor, Qaisar Maqbool, and Muhammad Nawaz. Synthesis of Functional Silver Nanoparticles and Microparticles with Modifiers and Evaluation of Their Antimicrobial, Anticancer, and Antioxidant Activity. *Journal of Functional Biomaterials 2020, Vol. 11, Page 76*, 11(4):76, oct 2020. doi: 10.3390/JFB11040076. URL https://www.mdpi.com/2079-4983/11/4/76/htmhttps://www.mdpi.com/2079-4983/11/4/76.

[85] M. Turalija, P. Merschak, B. Redl, U. Griesser, H. Duelli, and T. Bechtold. Copper(I)oxide microparticles synthesis and antimicrobial finishing of textiles. *Journal of Materials Chemistry B*, 3(28):5886–5892, jul 2015. ISSN 2050-7518. doi: 10.1039/C5TB01049G. URL https://pubs.rsc.org/en/content/articlehtml/2015/tb/c5tb01049ghttps://pubs.rsc.org/en/content/articlelanding/2015/tb/c5tb01049g.

[86] Su-Eon Jin and Hyo-Eon Jin. Antimicrobial Activity of Zinc Oxide Nano/Microparticles and Their Combinations against Pathogenic Microorganisms for Biomedical Applications: From Physicochemical Characteristics to Pharmacological Aspects. *Nanomaterials 2021, Vol. 11, Page 263*, 11(2):263, jan 2021. doi: 10.3390/NANO11020263. URL https://www.mdpi.com/2079-4991/11/2/263/htmhttps://www.mdpi.com/2079-4991/11/2/263.

[87] Maria Pau Ginebra, Cristina Canal, Montserrat Espanol, David Pastorino, and Edgar B. Montufar. Calcium phosphate cements as drug delivery materials, sep 2012. ISSN 0169409X.

[88] Maryam Nabiyouni, Theresa Brückner, Huan Zhou, Uwe Gbureck, and Sarit B. Bhaduri. Magnesium-based bioceramics in orthopedic applications, jan 2018. ISSN 18787568.

[89] *ASTM ISO/ASTM52900-15 Standard Terminology for Additive Manufacturing General Principles Terminology*. ASTM International, 2015.

[90] Fei Cao, Tiantian Zhang, Matthew A. Ryder, and Diana A. Lados. A Review of the Fatigue Properties of Additively Manufactured Ti-6Al-4V. *JOM*, 70(3):349–357, mar 2018. ISSN 1047-4838. doi: 10.1007/s11837-017-2728-5. URL http://link.springer.com/10.1007/s11837-017-2728-5.

[91] Dirk Herzog, Vanessa Seyda, Eric Wycisk, and Claus Emmelmann. Additive manufacturing of metals. *Acta Materialia*, 117:371–392, sep 2016. ISSN 1359-6454. doi: 10.1016/J.ACTAMAT.2016.07.019. URL https://www.sciencedirect.com/science/article/pii/S1359645416305158?via{\%}3Dihub{\#}bib90.

[92] Stéphane Gorsse, Christopher Hutchinson, Mohamed Gouné, and Rajarshi Banerjee. Additive manufacturing of metals: a brief review of the characteristic microstructures and properties of steels, Ti-6Al-4V and high-entropy alloys. *Science and Technology of Advanced Materials*, 18(1):584–610, dec 2017. ISSN 1468-6996. doi: 10.1080/14686996.2017.1361305. URL https://www.tandfonline.com/doi/full/10.1080/14686996.2017.1361305.

[93] Richard Bibb, Dominic Eggbeer, Peter Evans, Alan Bocca, and Adrian Sugar. Rapid manufacture of customfitting surgical guides. *Rapid Prototyping Journal*, 15(5):346–354, sep 2009. ISSN 1355-2546. doi: 10.1108/13552540910993879. URL http://www.emeraldinsight.com/doi/10.1108/13552540910993879.

[94] Matthew D Tam, Stephen D Laycock, Duncan Bell, and Adrian Chojnowski. 3-D printout of a DICOM file to aid surgical planning in a 6 year old patient with a

large scapular osteochondroma complicating congenital diaphyseal aclasia. *Journal of radiology case reports*, 6(1):31–7, jan 2012. ISSN 1943-0922. doi: 10.3941/jrcr.v6i1.889. URL http://www.ncbi.nlm.nih.gov/pubmed/22690278http://www.pubmedcentral.nih.gov/articlerender.fcgi?artid=PMC3370704.

[95] Renishaw. Digital evolution of cranial surgery, may 2017. URL http://www.renishaw.com/en/digital-evolution-of-cranial-surgery--38602.

[96] Philip Tack, Jan Victor, Paul Gemmel, and Lieven Annemans. 3D-printing techniques in a medical setting: a systematic literature review. *BioMedical Engineering OnLine*, 15(1):115, dec 2016. ISSN 1475-925X. doi: 10.1186/s12938-016-0236-4. URL http://biomedical-engineering-online.biomedcentral.com/articles/10.1186/s12938-016-0236-4.

[97] Timothy D Jackson, Jeffrey J Wannares, R Todd Lancaster, David W Rattner, and Matthew M Hutter. Does speed matter? The impact of operative time on outcome in laparoscopic surgery. *Surgical endoscopy*, 25(7):2288–95, jul 2011. ISSN 1432-2218. doi: 10.1007/s00464-010-1550-8. URL http://www.ncbi.nlm.nih.gov/pubmed/21298533http://www.pubmedcentral.nih.gov/articlerender.fcgi?artid=PMC3676304.

[98] Kevin Phan, Jun S Kim, Joung Heon Kim, Sulaiman Somani, John Di'Capua, James E Dowdell, and Samuel K Cho. Anesthesia Duration as an Independent Risk Factor for Early Postoperative Complications in Adults Undergoing Elective ACDF. *Global spine journal*, 7(8):727–734, dec 2017. ISSN 2192-5682. doi: 10.1177/2192568217701105. URL http://www.ncbi.nlm.nih.gov/pubmed/29238635http://www.pubmedcentral.nih.gov/articlerender.fcgi?artid=PMC5721997.

[99] Minxun Lu, Yongjiang Li, Yi Luo, Wenli Zhang, Yong Zhou, and Chongqi Tu. Uncemented three-dimensional-printed prosthetic reconstruction for massive bone defects of the proximal tibia. *World Journal of Surgical Oncology*, 16(1):47, dec 2018. ISSN 1477-7819. doi: 10.1186/s12957-018-1333-6. URL https://wjso.biomedcentral.com/articles/10.1186/s12957-018-1333-6.

[100] Horatiu Rotaru, Ralf Schumacher, Seong-Gon Kim, and Cristian Dinu. Selective laser melted titanium implants: a new technique for the reconstruction of extensive zygomatic complex defects. *Maxillofacial Plastic and Reconstructive Surgery*, 37 (1):1, dec 2015. ISSN 2288-8586. doi: 10.1186/s40902-015-0001-9. URL http://www.jkamprs.com/content/37/1/1.

[101] Wenbin Luo, Lanfeng Huang, He Liu, Wenrui Qu, Xin Zhao, Chenyu Wang, Chen Li, Tao Yu, Qing Han, Jincheng Wang, and Yanguo Qin. Customized Knee Prosthesis in Treatment of Giant Cell Tumors of the Proximal Tibia: Application of 3-Dimensional Printing Technology in Surgical Design. *Medical science monitor : international medical journal of experimental and clinical research*, 23:1691–1700, apr 2017. ISSN 1643-3750. doi: 10.12659/MSM.901436. URL http://www.ncbi.nlm.nih.gov/pubmed/28388595http://www.pubmedcentral.nih.gov/articlerender.fcgi?artid=PMC5391808.

[102] Mitsuo Niinomi, Masaaki Nakai, and Junko Hieda. Development of new metallic alloys for biomedical applications. *Acta Biomaterialia*, 8(11):3888–3903, nov 2012. ISSN 1742-7061. doi: 10.1016/J.ACTBIO.2012.06.037. URL https://www.sciencedirect.com/science/article/pii/S1742706112002942.

[103] Mohammad Elahinia, Narges Shayesteh Moghaddam, Mohsen Taheri Andani, Amirhesam Amerinatanzi, Beth A. Bimber, and Reginald F. Hamilton. Fabrication of NiTi through additive manufacturing: A review. *Progress in Materials Science*, 83:630–663, oct 2016. ISSN 0079-6425. doi: 10.1016/J.PMATSCI.2016.08.001. URL https://www.sciencedirect.com/science/article/pii/S0079642516300469.

[104] I. Yadroitsev, P. Krakhmalev, and I. Yadroitsava. Titanium Alloys Manufactured by In Situ Alloying During Laser Powder Bed Fusion. *JOM*, 69(12):2725–2730, dec 2017. ISSN 15431851. doi: 10.1007/s11837-017-2600-7. URL http://link.springer.com/10.1007/s11837-017-2600-7.

[105] Xiao Lin, Shaofeng Yang, Kalyn Lai, Huilin Yang, Thomas J. Webster, and Lei Yang. Orthopedic implant biomaterials with both osteogenic and anti-infection capacities and associated in vivo evaluation methods. *Nanomedicine: Nanotechnology, Biology and Medicine*, 13(1):123–142, jan 2017. ISSN 15499634. doi: 10.1016/j.nano.2016.08.003. URL http://linkinghub.elsevier.com/retrieve/pii/S1549963416301113.

[106] Qingsong Wei, Shuai Li, Changjun Han, Wei Li, Lingyu Cheng, Liang Hao, and Yusheng Shi. Selective laser melting of stainless-steel/nano-hydroxyapatite composites for medical applications: Microstructure, element distribution, crack and mechanical properties. *Journal of Materials Processing Technology*, 222:444–453, aug 2015. ISSN 0924-0136. doi: 10.1016/J.JMATPROTEC.2015.02.010. URL https://www.sciencedirect.com/science/article/pii/S0924013615000539.

[107] L. Hao, S. Dadbakhsh, O. Seaman, and M. Felstead. Selective laser melting of a stainless steel and hydroxyapatite composite for load-bearing implant de-

velopment. *Journal of Materials Processing Technology*, 209(17):5793–5801, aug 2009. ISSN 0924-0136. doi: 10.1016/J.JMATPROTEC.2009.06.012. URL https://www.sciencedirect.com/science/article/pii/S0924013609002398.

[108] Changjun Han, Qian Wang, Bo Song, Wei Li, Qingsong Wei, Shifeng Wen, Jie Liu, and Yusheng Shi. Microstructure and property evolutions of titanium/nano-hydroxyapatite composites in-situ prepared by selective laser melting. *Journal of the Mechanical Behavior of Biomedical Materials*, 71:85–94, jul 2017. ISSN 1751-6161. doi: 10.1016/J.JMBBM.2017.02.021. URL https://www.sciencedirect.com/science/article/pii/S1751616117300784.

[109] Changjun Han, Yan Li, Qian Wang, Daosheng Cai, Qingsong Wei, Li Yang, Shifeng Wen, Jie Liu, and Yusheng Shi. Titanium/hydroxyapatite (Ti/HA) gradient materials with quasi-continuous ratios fabricated by SLM: Material interface and fracture toughness. *Materials & Design*, 141:256–266, mar 2018. ISSN 0264-1275. doi: 10.1016/J.MATDES.2017.12.037. URL https://www.sciencedirect.com/science/article/pii/S0264127517311425.

[110] Teodora Marcu, Cinzia Menapace, Luca Girardini, Dan Leordean, and Catalin Popa. Selective laser melting of Ti6Al7Nb with hydroxyapatite addition. *Rapid Prototyping Journal*, 20(4):301–310, 2014. URL https://doi.org/10.1108/RPJ-09-2012-0083.

[111] I. V. Shishkovskii, I. A. Yadroitsev, and I. Yu. Smurov. Selective laser sintering/melting of nitinolhydroxyapatite composite for medical applications. *Powder Metallurgy and Metal Ceramics*, 50(5-6):275–283, sep 2011. ISSN 1068-1302. doi: 10.1007/s11106-011-9329-6. URL http://link.springer.com/10.1007/s11106-011-9329-6.

[112] Cijun Shuai, Yuanzhuo Zhou, Youwen Yang, Pei Feng, Long Liu, Chongxian He, Mingchun Zhao, Sheng Yang, Chengde Gao, and Ping Wu. Biodegradation Resistance and Bioactivity of Hydroxyapatite Enhanced Mg-Zn Composites via Selective Laser Melting. *Materials*, 10(3):307, mar 2017. ISSN 1996-1944. doi: 10.3390/ma10030307. URL http://www.mdpi.com/1996-1944/10/3/307.

[113] Qiang Wang, Ling Ren, Xiaopeng Li, Shuyuan Zhang, Timothy B. Sercombe, and Ke Yang. Antimicrobial Cu-bearing stainless steel scaffolds. *Materials Science and Engineering: C*, 68:519–522, nov 2016. ISSN 0928-4931. doi: 10.1016/J.MSEC.2016.06.038. URL http://www.sciencedirect.com/science/article/pii/S0928493116306075.

[114] Tong Xi, M. Babar Shahzad, Dake Xu, Ziqing Sun, Jinlong Zhao, Chunguang Yang, Min Qi, and Ke Yang. Effect of copper addition on mechanical properties, corrosion resistance and antibacterial property of 316L stainless steel. *Materials Science and Engineering: C*, 71:1079–1085, feb 2017. ISSN 0928-4931. doi: 10.1016/J.MSEC.2016.11.022. URL https://www.sciencedirect.com/science/article/pii/S0928493116311304.

[115] Pavel Krakhmalev, Igor Yadroitsev, Ina Yadroitsava, and Olga de Smidt. Functionalization of Biomedical Ti6Al4V via In Situ Alloying by Cu during Laser Powder Bed Fusion Manufacturing. *Materials*, 10(10):1154, oct 2017. ISSN 1996-1944. doi: 10.3390/ma10101154. URL http://www.mdpi.com/1996-1944/10/10/1154.

[116] Andrew Macpherson, Xiaopeng Li, Paul McCormick, Ling Ren, Ke Yang, and Timothy B. Sercombe. Antibacterial Titanium Produced Using Selective Laser Melting. *JOM*, pages 1–6, sep 2017. ISSN 1047-4838. doi: 10.1007/s11837-017-2589-y. URL http://link.springer.com/10.1007/s11837-017-2589-y.

[117] Sai Guo, Yanjin Lu, Songquan Wu, Lingling Liu, Mengjiao He, Chaoqian Zhao, Yiliang Gan, Junjie Lin, Jiasi Luo, Xiongcheng Xu, and Jinxin Lin. Preliminary study on the corrosion resistance, antibacterial activity and cytotoxicity of selective-laser-melted Ti6Al4V-xCu alloys. *Materials Science and Engineering: C*, 72:631–640, mar 2017. ISSN 0928-4931. doi: 10.1016/J.MSEC.2016.11.126. URL https://www.sciencedirect.com/science/article/pii/S0928493116309365.

[118] Jiasi Luo, Sai Guo, Yanjin Lu, Xiongcheng Xu, Chaoqian Zhao, Songquan Wu, and Jinxin Lin. Cytocompatibility of Cu-bearing Ti6Al4V alloys manufactured by selective laser melting. *Materials Characterization*, dec 2017. ISSN 1044-5803. doi: 10.1016/J.MATCHAR.2017.12.003. URL https://www.sciencedirect.com/science/article/pii/S1044580317325305.

[119] Yanjin Lu, Ling Ren, Songquan Wu, Chunguang Yang, Wenlie Lin, Suli Xiao, Yang Yang, Ke Yang, and Jinxin Lin. CoCrWCu alloy with antibacterial activity fabricated by selective laser melting: Densification, mechanical properties and microstructural analysis. *Powder Technology*, 325:289–300, feb 2018. ISSN 0032-5910. doi: 10.1016/J.POWTEC.2017.11.018. URL https://www.sciencedirect.com/science/article/pii/S0032591017308860.

[120] Jiasi Luo, Songquan Wu, Yanjin Lu, Sai Guo, Yang Yang, Chaoqian Zhao, Junjie Lin, Tingting Huang, and Jinxin Lin. The effect of 3wt.% Cu addition on the microstructure, tribological property and corrosion resistance of CoCrW alloys

fabricated by selective laser melting. *Journal of Materials Science: Materials in Medicine*, 29(4):37, apr 2018. ISSN 0957-4530. doi: 10.1007/s10856-018-6043-7. URL http://link.springer.com/10.1007/s10856-018-6043-7.

[121] Ling Ren, Kaveh Memarzadeh, Shuyuan Zhang, Ziqing Sun, Chunguang Yang, Guogang Ren, Robert P. Allaker, and Ke Yang. A novel coping metal material CoCrCu alloy fabricated by selective laser melting with antimicrobial and antibiofilm properties. *Materials Science and Engineering: C*, 67:461–467, oct 2016. ISSN 0928-4931. doi: 10.1016/J.MSEC.2016.05.069. URL https://www.sciencedirect.com/science/article/pii/S0928493116305021.

[122] Cijun Shuai, Long Liu, Mingchun Zhao, Pei Feng, Youwen Yang, Wang Guo, Chengde Gao, and Fulai Yuan. Microstructure, biodegradation, antibacterial and mechanical properties of ZK60-Cu alloys prepared by selective laser melting technique. *Journal of Materials Science & Technology*, 34(10):1944–1952, oct 2018. ISSN 1005-0302. doi: 10.1016/J.JMST.2018.02.006. URL https://www.sciencedirect.com/science/article/pii/S100503021830029X.

[123] Cijun Shuai, Yuanzhuo Zhou, Youwen Yang, Chengde Gao, Shuping Peng, and Guoyong Wang. Ag-Introduced Antibacterial Ability and Corrosion Resistance for Bio-Mg Alloys. *BioMed Research International*, 2018:1–13, jul 2018. ISSN 2314-6133. doi: 10.1155/2018/6023460. URL https://www.hindawi.com/journals/bmri/2018/6023460/.

[124] Mian Chen, Lei Yang, Lan Zhang, Yong Han, Zheng Lu, Gaowu Qin, and Erlin Zhang. Effect of nano/micro-Ag compound particles on the bio-corrosion, antibacterial properties and cell biocompatibility of Ti-Ag alloys. *Materials Science and Engineering: C*, 75:906–917, jun 2017. ISSN 09284931. doi: 10.1016/j.msec.2017.02.142. URL http://www.sciencedirect.com/science/article/pii/S0928493116319981http://linkinghub.elsevier.com/retrieve/pii/S0928493116319981.

[125] Patrik Stenlund, Shingo Kurosu, Yuichiro Koizumi, Felicia Suska, Hiroaki Matsumoto, Akihiko Chiba, and Anders Palmquist. Osseointegration Enhancement by Zr doping of Co-Cr-Mo Implants Fabricated by Electron Beam Melting. *Additive Manufacturing*, 6:6–15, apr 2015. ISSN 2214-8604. doi: 10.1016/J.ADDMA.2015.02.002. URL https://www.sciencedirect.com/science/article/pii/S2214860415000123?via{\%}3Dihub.

[126] Furqan A. Shah, Edvin Jergéus, Akihiko Chiba, and Anders Palmquist. Osseointegration of 3D printed microalloyed CoCr implants-Addition of 0.04% Zr to CoCr

does not alter bone material properties. *Journal of Biomedical Materials Research Part A*, 106(6):1655–1663, jun 2018. ISSN 15493296. doi: 10.1002/jbm.a.36366. URL http://doi.wiley.com/10.1002/jbm.a.36366.

[127] Mark I Froimson, Jonathan Garino, Alan Machenaud, and J P Vidalain. Minimum 10-year results of a tapered, titanium, hydroxyapatite-coated hip stem: an independent review. *The Journal of arthroplasty*, 22(1):1–7, jan 2007. ISSN 0883-5403. doi: 10.1016/j.arth.2006.03.003. URL http://www.ncbi.nlm.nih.gov/pubmed/17197301.

[128] Jean-Alain Epinette. Long lasting outcome of hydroxyapatite-coated implants in primary knee arthroplasty: a continuous series of two hundred and seventy total knee arthroplasties at fifteen to twenty two years of clinical follow-up. *International Orthopaedics*, 38(2):305–311, feb 2014. ISSN 0341-2695. doi: 10.1007/s00264-013-2246-1. URL http://link.springer.com/10.1007/s00264-013-2246-1.

[129] S.M. Giannitelli, P. Mozetic, M. Trombetta, and A. Rainer. Combined additive manufacturing approaches in tissue engineering. *Acta Biomaterialia*, 24:1–11, sep 2015. ISSN 1742-7061. doi: 10.1016/J.ACTBIO.2015.06.032. URL https://www.sciencedirect.com/science/article/pii/S1742706115300040.

[130] V Mager. RESEARCH ON INFILTRATING BIOCOMPATIBLE FILLERS TO PRODUCE COMPOSITE IMPLANTS. *ACADEMIC JOURNAL OF MANUFACTURING ENGINEERING*, 11(4), 2013. URL http://www.auif.utcluj.ro/images/v11{_}4/18-MagerV.pdf.

[131] Hao Liu, Wei Li, Can Liu, Jie Tan, Hong Wang, Bao Hai, Hong Cai, Hui-Jie Leng, Zhong-Jun Liu, and Chun-Li Song. Incorporating simvastatin/poloxamer 407 hydrogel into 3D-printed porous Ti ₆ Al ₄ V scaffolds for the promotion of angiogenesis, osseointegration and bone ingrowth. *Biofabrication*, 8(4):045012, oct 2016. ISSN 1758-5090. doi: 10.1088/1758-5090/8/4/045012. URL http://stacks.iop.org/1758-5090/8/i=4/a=045012?key=crossref.09199eb85374c68d93013b0fe94834cc.

[132] Sophie C. Cox, Parastoo Jamshidi, Neil M. Eisenstein, Mark A. Webber, Hany Hassanin, Moataz M. Attallah, Duncan E.T. Shepherd, Owen Addison, and Liam M. Grover. Adding functionality with additive manufacturing: Fabrication of titanium-based antibiotic eluting implants. *Materials Science and Engineering: C*, 64:407–415, jul 2016. ISSN 09284931. doi: 10.1016/j.msec.

2016.04.006. URL http://dx.doi.org/10.1016/j.msec.2016.04.006http://linkinghub.elsevier.com/retrieve/pii/S0928493116303046.

[133] Hany Hassanin, Laurane Finet, Sophie C. Cox, Parastoo Jamshidi, Liam M. Grover, Duncan E.T. Shepherd, Owen Addison, and Moataz M. Attallah. Tailoring selective laser melting process for titanium drug-delivering implants with releasing micro-channels. *Additive Manufacturing*, 20:144–155, mar 2018. ISSN 22148604. doi: 10.1016/j.addma.2018.01.005. URL https://www.sciencedirect.com/science/article/pii/S2214860417305778https://linkinghub.elsevier.com/retrieve/pii/S2214860417305778.

[134] Martin B. Bezuidenhout, Anton D. van Staden, Gert A. Oosthuizen, Dimitar M. Dimitrov, and Leon M. T. Dicks. Delivery of Antibiotics from Cementless Titanium-Alloy Cubes May Be a Novel Way to Control Postoperative Infections. *BioMed Research International*, 2015:1–7, 2015. ISSN 2314-6133. doi: 10.1155/2015/856859. URL http://www.hindawi.com/journals/bmri/2015/856859/.

[135] Chunmei Li, Chengchen Guo, Vincent Fitzpatrick, Ahmed Ibrahim, Myrthe Jasmijn Zwierstra, Philip Hanna, Aron Lechtig, Ara Nazarian, Samuel J. Lin, and David L. Kaplan. Design of biodegradable, implantable devices towards clinical translation. *Nature Reviews Materials*, 5(1):61–81, 2020. ISSN 20588437. doi: 10.1038/s41578-019-0150-z. URL http://dx.doi.org/10.1038/s41578-019-0150-z.

[136] Jim. O'Neill. Review on Antimicrobial Resistance. Tackling drug-resistant infections globally. *Who*, (May):11, 2016. ISSN 00351334.

[137] David M. Livermore. Antibiotic resistance in staphylococci. In *International Journal of Antimicrobial Agents*, volume 16, pages 3–10. Elsevier, 2000. doi: 10.1016/s0924-8579(00)00299-5.

[138] Jon Iredell, Jeremy Brown, and Kaitlin Tagg. Antibiotic resistance in Enterobacteriaceae: Mechanisms and clinical implications, feb 2016. ISSN 17561833.

[139] Zheng Pang, Renee Raudonis, Bernard R. Glick, Tong Jun Lin, and Zhenyu Cheng. Antibiotic resistance in Pseudomonas aeruginosa: mechanisms and alternative therapeutic strategies, jan 2019. ISSN 07349750.

[140] K Schwach-Abdellaoui, N Vivien-Castioni, and R Gurny. Local delivery of antimicrobial agents for the treatment of periodontal diseases. *European journal of pharmaceutics and biopharmaceutics : official journal of Arbeitsgemeinschaft*

fur Pharmazeutische Verfahrenstechnik e.V, 50(1):83–99, jul 2000. ISSN 0939-6411. doi: 10.1016/s0939-6411(00)00086-2. URL http://www.ncbi.nlm.nih.gov/pubmed/10840194.

[141] Eric J. Tobin. Recent coating developments for combination devices in orthopedic and dental applications: A literature review. *Advanced Drug Delivery Reviews*, 112:88–100, mar 2017. ISSN 0169409X. doi: 10.1016/j.addr.2017.01.007. URL http://dx.doi.org/10.1016/j.addr.2017.01.007http://linkinghub.elsevier.com/retrieve/pii/S0169409X17300261.

[142] C. L. Romanò, H. Tsuchiya, I. Morelli, A. G. Battaglia, and L. Drago. Antibacterial coating of implants: are we missing something? *Bone & Joint Research*, 8(5):199–206, may 2019. ISSN 2046-3758. doi: 10.1302/2046-3758.85.BJR-2018-0316. URL https://online.boneandjoint.org.uk/doi/10.1302/2046-3758.85.BJR-2018-0316.

[143] Vasilios Athans, Michael P. Veve, and Susan L. Davis. Trowels and Tribulations: Review of Antimicrobial-Impregnated Bone Cements in Prosthetic Joint Surgery. *Pharmacotherapy*, 37(12):1565–1577, dec 2017. ISSN 18759114. doi: 10.1002/phar.2040. URL http://doi.wiley.com/10.1002/phar.2040.

[144] Erik A.B. Hughes, Thomas E. Robinson, David B. Bassett, Sophie C. Cox, and Liam M. Grover. Critical and diverse roles of phosphates in human bone formation, 2019. ISSN 20507518.

[145] Faleh Tamimi, Zeeshan Sheikh, and Jake Barralet. Dicalcium phosphate cements: Brushite and monetite, feb 2012. ISSN 17427061.

[146] Raymond J Turner. Metal-based antimicrobial strategies. *Microbial biotechnology*, 10(5):1062–1065, sep 2017. ISSN 1751-7915. doi: 10.1111/1751-7915.12785. URL http://www.ncbi.nlm.nih.gov/pubmed/28745454http://www.pubmedcentral.nih.gov/articlerender.fcgi?artid=PMC5609261.

[147] Andrea Ewald, Daniel Hösel, Sarika Patel, Liam M. Grover, Jake E. Barralet, and Uwe Gbureck. Silver-doped calcium phosphate cements with antimicrobial activity. *Acta Biomaterialia*, 7(11):4064–4070, nov 2011. ISSN 17427061. doi: 10.1016/j.actbio.2011.06.049. URL https://linkinghub.elsevier.com/retrieve/pii/S1742706111002959.

[148] Volker Alt, Thorsten Bechert, Peter Steinrücke, Michael Wagener, Peter Seidel, Elvira Dingeldein, Eugen Domann, and Reinhard Schnettler. In vitro testing

of antimicrobial activity of bone cement. *Antimicrobial agents and chemotherapy*, 48(11):4084–8, nov 2004. ISSN 0066-4804. doi: 10.1128/AAC.48.11.4084-4088.2004. URL http://www.ncbi.nlm.nih.gov/pubmed/15504825http://www.pubmedcentral.nih.gov/articlerender.fcgi?artid=PMC525460.

[149] Masaya Ueno, Hiroshi Miyamoto, Masatsugu Tsukamoto, Shuichi Eto, Iwao Noda, Takeo Shobuike, Tomoki Kobatake, Motoki Sonohata, and Masaaki Mawatari. Silver-Containing Hydroxyapatite Coating Reduces Biofilm Formation by Methicillin-Resistant Staphylococcus aureus In Vitro and In Vivo. *BioMed Research International*, 2016:1–7, 2016. ISSN 2314-6133. doi: 10.1155/2016/8070597. URL https://www.hindawi.com/journals/bmri/2016/8070597/.

[150] Catarina C. Coelho, Rita Araújo, Paulo A. Quadros, Susana R. Sousa, and Fernando J. Monteiro. Antibacterial bone substitute of hydroxyapatite and magnesium oxide to prevent dental and orthopaedic infections. *Materials Science and Engineering: C*, 97:529–538, apr 2019. ISSN 0928-4931. doi: 10.1016/J.MSEC.2018.12.059. URL https://www.sciencedirect.com/science/article/pii/S092849311831230X?via{\%}3Dihub.

[151] G. Mestres, M. Abdolhosseini, W. Bowles, S. H. Huang, C. Aparicio, S. U. Gorr, and M. P. Ginebra. Antimicrobial properties and dentin bonding strength of magnesium phosphate cements. *Acta Biomaterialia*, 9(9):8384–8393, sep 2013. ISSN 17427061. doi: 10.1016/j.actbio.2013.05.032. URL https://www.sciencedirect.com/science/article/pii/S174270611300281Xhttps://linkinghub.elsevier.com/retrieve/pii/S174270611300281X.

[152] Wei-xin Zheng, Xue-ying Xiao, Cheng-gong Chang, Jin-mei Dong, Jing Wen, Qing Huang, Yuan Zhou, and Ying Li. Characterizing properties of magnesium oxychloride cement concrete pavement. *Journal of Central South University*, 26(12):3410–3419, dec 2019. ISSN 2095-2899. doi: 10.1007/s11771-019-4263-8. URL http://link.springer.com/10.1007/s11771-019-4263-8.

[153] Yichao Wang, Linzhuo Wei, Jiangtao Yu, and Kequan Yu. Mechanical properties of high ductile magnesium oxychloride cement-based composites after water soaking. *Cement and Concrete Composites*, 97:248–258, mar 2019. ISSN 09589465. doi: 10.1016/j.cemconcomp.2018.12.028.

[154] Shengwen Tang, Yang Hu, Wang Ren, Peng Yu, Qing Huang, Xiaoying Qi, Ying Li, and E. Chen. Modeling on the hydration and leaching of eco-friendly magnesium oxychloride cement paste at the microscale. *Construction and Building Materials*, 204:684–690, apr 2019.

ISSN 09500618. doi: 10.1016/j.conbuildmat.2019.01.232. URL https://www.sciencedirect.com/science/article/pii/S095006181930279Xhttps://linkinghub.elsevier.com/retrieve/pii/S095006181930279X.

[155] Xiaoyang Chen, Tingting Zhang, Wanli Bi, and Christopher Cheeseman. Effect of tartaric acid and phosphoric acid on the water resistance of magnesium oxychloride (MOC) cement. *Construction and Building Materials*, 213:528–536, jul 2019. ISSN 0950-0618. doi: 10.1016/J.CONBUILDMAT.2019.04.086. URL https://www.sciencedirect.com/science/article/pii/S095006181930916X.

[156] Deng Dehua and Zhang Chuanmei. The formation mechanism of the hydrate phases in magnesium oxychloride cement. *Cement and Concrete Research*, 29(9):1365–1371, sep 2002. ISSN 00088846. doi: 10.1016/s0008-8846(98)00247-6. URL https://www.sciencedirect.com/science/article/pii/S0008884698002476.

[157] Katerina Ioannidou, Matej Kanduč, Lunna Li, Daan Frenkel, Jure Dobnikar, and Emanuela Del Gado. The crucial effect of early-stage gelation on the mechanical properties of cement hydrates. *Nature Communications*, 7(1):1–9, jul 2016. ISSN 20411723. doi: 10.1038/ncomms12106.

[158] Liam M. Grover, Uwe Gbureck, Anne M. Young, Adrian J. Wright, and Jake E. Barralet. Temperature dependent setting kinetics and mechanical properties of β-TCPpyrophosphoric acid bone cement. *Journal of Materials Chemistry*, 15(46):4955, dec 2005. ISSN 0959-9428. doi: 10.1039/b507056m. URL http://xlink.rsc.org/?DOI=b507056m.

[159] Francesca Ridi, Emiliano Fratini, and Piero Baglioni. Fractal structure evolution during cement hydration by differential scanning calorimetry: Effect of organic additives. *Journal of Physical Chemistry C*, 117(48):25478–25487, dec 2013. ISSN 19327447. doi: 10.1021/jp406268p.

[160] Roque Góchez, Jim Wambaugh, Brett Rochner, and Christopher L. Kitchens. Kinetic study of the magnesium oxychloride cement cure reaction. *Journal of Materials Science*, 52(13):7637–7646, jul 2017. ISSN 0022-2461. doi: 10.1007/s10853-017-1013-x. URL http://link.springer.com/10.1007/s10853-017-1013-x.

[161] Hengjing Ba and Hui Guan. Influence of MgO/MgCl2 molar ratio on phase stability of magnesium oxychloride cement. *Journal of Wuhan University of Technology-Mater. Sci. Ed.*, 24(3):476–481, jun 2009. ISSN 1000-2413.

doi: 10.1007/s11595-009-3476-3. URL http://link.springer.com/10.1007/s11595-009-3476-3.

[162] M. Bohner and U. Gbureck. Thermal reactions of brushite cements. *Journal of Biomedical Materials Research Part B: Applied Biomaterials*, 84B(2):375–385, feb 2008. ISSN 15524973. doi: 10.1002/jbm.b.30881. URL http://doi.wiley.com/10.1002/jbm.b.30881.

[163] Vincenzo M. Sglavo, Francesca De Genua, Alexia Conci, Riccardo Ceccato, and Roberto Cavallini. Influence of curing temperature on the evolution of magnesium oxychloride cement. *Journal of Materials Science*, 46(20):6726–6733, oct 2011. ISSN 00222461. doi: 10.1007/s10853-011-5628-z. URL http://link.springer.com/10.1007/s10853-011-5628-z.

[164] LADAWAN URWONGSE and CHARLES A. SORRELL. The System MgO-MgCl2-H2O at 23oC. *Journal of the American Ceramic Society*, 63(9-10):501–504, sep 1980. ISSN 0002-7820. doi: 10.1111/j.1151-2916.1980.tb10752.x. URL http://doi.wiley.com/10.1111/j.1151-2916.1980.tb10752.x.

[165] H. X. Qiao, B. R. Zhu, Y. Y. Shi, J. M. Dong, and M. Elizabeth Wanjiru. Strength development and micro-mechanism of magnesium oxychloride cement concrete. *Materials Research Innovations*, 19(sup1):S1–185–S1–190, apr 2015. ISSN 1432-8917. doi: 10.1179/1432891715Z.0000000001401. URL https://www.tandfonline.com/doi/full/10.1179/1432891715Z.0000000001401.

[166] Zongjin Li and C. K. Chau. Influence of molar ratios on properties of magnesium oxychloride cement. *Cement and Concrete Research*, 37(6):866–870, jun 2007. ISSN 00088846. doi: 10.1016/j.cemconres.2007.03.015.

[167] Jorge Stolfi. MgO-MgCl2-H2O phase diagram 23 C PDF, nov 2018. URL https://commons.wikimedia.org/wiki/File:MgO-MgCl2-H2O{_}phase{_}diagram{_}23{_}C{_}PDF.pdf.

[168] Chengyou Wu, Huifang Zhang, and Hongfa Yu. The effects of alumina-leached coal fly ash residue on magnesium oxychloride cement. *Advances in Cement Research*, 25(5):254–261, oct 2013. ISSN 0951-7197. doi: 10.1680/adcr.12.00019. URL http://www.icevirtuallibrary.com/doi/10.1680/adcr.12.00019.

[169] Chuanmei Zhang and Dehua Deng. The Effect of Aluminate Minerals on Magnesium Oxychloride Cement. *Chinese Science Abstracts Series B*, 14(5 Part B):6, 1995.

[170] Dehua Deng. The mechanism for soluble phosphates to improve the water resistance of magnesium oxychloride cement. *Cement and Concrete Research*, 33(9):1311–1317, sep 2003. ISSN 00088846. doi: 10.1016/S0008-8846(03)00043-7. URL https://linkinghub.elsevier.com/retrieve/pii/S0008884603000437.

[171] Ying Li, Zongjin Li, Huafu Pei, and Hongfa Yu. The influence of FeSO4 and KH2PO4 on the performance of magnesium oxychloride cement. *Construction and Building Materials*, 102:233–238, jan 2016. ISSN 09500618. doi: 10.1016/j.conbuildmat.2015.10.186. URL https://linkinghub.elsevier.com/retrieve/pii/S0950061815306073.

[172] Jing Wen, Hong-fa Yu, Ying Li, Cheng-you Wu, Jin-mei Dong, and Li-na Zheng. Effects of H3PO4 and Ca(H2PO4)2 on mechanical properties and water resistance of thermally decomposed magnesium oxychloride cement. *Journal of Central South University*, 20(12):3729–3735, dec 2013. ISSN 2095-2899. doi: 10.1007/s11771-013-1901-4. URL http://link.springer.com/10.1007/s11771-013-1901-4.

[173] Yanni Tan, Yong Liu, Zhongwei Zhao, Jennifer Z Paxton, and Liam M Grover. Synthesis and in vitro degradation of a novel magnesium oxychloride cement. *Journal of Biomedical Materials Research Part A*, 103(1):194–202, jan 2015. ISSN 15493296. doi: 10.1002/jbm.a.35166. URL https://onlinelibrary.wiley.com/doi/pdf/10.1002/jbm.a.35166http://doi.wiley.com/10.1002/jbm.a.35166.

[174] Xiali Guan, Gang Zhou, Yangyang Cui, Jingjng Fei, and Yubo Fan. Effect of different-sizes of hydroxyapatite on the water resistance of magnesium oxychloride cement for bone repair. *RSC Advances*, 9(66):38619–38628, 2019. ISSN 2046-2069. doi: 10.1039/C9RA08200J. URL http://xlink.rsc.org/?DOI=C9RA08200J.

[175] Nhu Y.Thi Nguyen, Nathaniel Grelling, Cheyann Lee Wetteland, Romeo Rosario, and Huinan Liu. Antimicrobial Activities and Mechanisms of Magnesium Oxide Nanoparticles (nMgO) against Pathogenic Bacteria, Yeasts, and Biofilms. *Scientific Reports*, 8(1), dec 2018. ISSN 20452322. doi: 10.1038/s41598-018-34567-5.

[176] Tingjie Huang, Qiang Yuan, and Dehua Deng. The role of phosphoric acid in improving the strength of magnesium oxychloride cement pastes with large molar ratios of H 2 O/MgCl 2. *Cement and Concrete Composites*, 97:379–386, mar 2019. ISSN 09589465. doi: 10.1016/j.cemconcomp.2019.01.013.

[177] E. ahin and M. Çiftçiolu. Monetite promoting effect of citric acid on brushite cement setting kinetics. *Materials Research Innovations*, 18(3):138–145, apr 2014.

ISSN 1432-8917. doi: 10.1179/1433075X13Y.0000000175. URL https://www.tandfonline.com/doi/full/10.1179/1433075X13Y.0000000175.

[178] R. P. Howlin, M. J. Brayford, J. S. Webb, J. J. Cooper, S. S. Aiken, and P. Stoodley. Antibiotic-loaded synthetic calcium sulfate beads for prevention of bacterial colonization and biofilm formation in periprosthetic infections. *Antimicrobial Agents and Chemotherapy*, 59(1):111–120, jan 2015. ISSN 10986596. doi: 10.1128/AAC.03676-14.

[179] ASTM. *ASTM C 266-08: Standard Test Method for Time of Setting of Hydraulic-Cement Paste by Gillmore Needles*. ASTM International, 2008. doi: 10.1520/C0266-18. URL www.astm.org,.

[180] Thomas E. Robinson, Erik A. B. Hughes, Neil M. Eisenstein, Liam M. Grover, and Sophie C. Cox. The Quantification of Injectability by Mechanical Testing. *JoVE (Journal of Visualized Experiments)*, (159):e61417, may 2020. ISSN 1940-087X. doi: 10.3791/61417.

[181] Janet B. Quinn and George D. Quinn. A practical and systematic review of Weibull statistics for reporting strengths of dental materials. *Dental Materials*, 26(2):135–147, feb 2010. ISSN 01095641. doi: 10.1016/j.dental.2009.09.006. URL https://linkinghub.elsevier.com/retrieve/pii/S0109564109003108.

[182] Rakesh Kumar and Bishwa Bhattacharjee. Porosity, pore size distribution and in situ strength of concrete. *Cement and Concrete Research*, 33(1):155–164, jan 2003. ISSN 00088846. doi: 10.1016/S0008-8846(02)00942-0.

[183] R. W. Reed and G. B. Reed. "DROP PLATE" METHOD OF COUNTING VIABLE BACTERIA. *Canadian Journal of Research*, 26e(6):317–326, dec 1948. ISSN 1923-4287. doi: 10.1139/cjr48e-020.

[184] J Sawai, E Kawada, F Kanou, H Igarashi, A Hashimoto, T Kokugan, and M Shimizu. Detection of active oxygen generated from ceramic powders having antibacterial activity. *JOURNAL OF CHEMICAL ENGINEERING OF JAPAN*, 29(4):627–633, 1996. ISSN 0021-9592. doi: 10.1252/jcej.29.627. URL http://joi.jlc.jst.go.jp/JST.JSTAGE/jcej/29.627?from=CrossRef.

[185] K. Loza, C. Sengstock, S. Chernousova, M. Köller, and M. Epple. The predominant species of ionic silver in biological media is colloidally dispersed nanoparticulate silver chloride. *RSC Advances*, 4(67):35290–35297, 2014. ISSN 20462069. doi: 10.1039/c4ra04764h.

[186] M. Bohner, P. Van Landuyt, H. P. Merkle, and J. Lemaitre. Composition effects on the pH of a hydraulic calcium phosphate cement. *Journal of Materials Science: Materials in Medicine*, 8(11):675–681, nov 1997. ISSN 09574530. doi: 10.1023/A:1018583706335.

[187] Francesca M. L. Bushell, Peter D. Tonner, Sara Jabbari, Amy K. Schmid, and Peter A. Lund. Synergistic Impacts of Organic Acids and pH on Growth of Pseudomonas aeruginosa: A Comparison of Parametric and Bayesian Non-parametric Methods to Model Growth. *Frontiers in Microbiology*, 9(JAN):3196, jan 2019. ISSN 1664-302X. doi: 10.3389/fmicb.2018.03196. URL https://www.frontiersin.org/article/10.3389/fmicb.2018.03196/full.

[188] Davide Campoccia, Lucio Montanaro, and Carla Renata Arciola. A review of the biomaterials technologies for infection-resistant surfaces. *Biomaterials*, 34(34):8533–8554, nov 2013. ISSN 01429612. doi: 10.1016/j.biomaterials.2013.07.089. URL http://www.sciencedirect.com/science/article/pii/S0142961213009174http://linkinghub.elsevier.com/retrieve/pii/S0142961213009174.

[189] David R Lide, editor. *CRC Handbook of Chemistry and Physics, 84th Edition Edited by David R. Lide (National Institute of Standards and Technology). CRC Press LLC: Boca Raton. 2003. 2616 pp. $139.95. ISBN 0-8493-0484-9.*, volume 126. American Chemical Society (ACS), feb 2004. doi: 10.1021/ja0336372. URL https://pubs.acs.org/doi/10.1021/ja0336372.

[190] Aleksander Trummal, Lauri Lipping, Ivari Kaljurand, Ilmar A. Koppel, and Ivo Leito. Acidity of Strong Acids in Water and Dimethyl Sulfoxide. *The Journal of Physical Chemistry A*, 120(20):3663–3669, may 2016. ISSN 1089-5639. doi: 10.1021/acs.jpca.6b02253. URL https://pubs.acs.org/doi/10.1021/acs.jpca.6b02253.

[191] Samuel F. Etris and C. Robert Cappel. Silver Compounds. In *Kirk-Othmer Encyclopedia of Chemical Technology*. John Wiley & Sons, Inc., Hoboken, NJ, USA, may 2003. doi: 10.1002/0471238961.1909122203011616.a01.pub2. URL http://doi.wiley.com/10.1002/0471238961.1909122203011616.a01.pub2.

[192] Egon Wiberg, A. F. Holleman, and Nils Wiberg. *Holleman-Wiberg Inorganic Chemistry*. Academic Press, 2001. ISBN 0-12-352651-5. URL https://books.google.co.uk/books?id=Mtth5g59dEIC{\&}printsec=frontcover{\&}dq=isbn:0123526515{\&}hl=en{\&}sa=X{\&}ved=

0ahUKEwjik5rkmfvpAhVyTxUIHYtKBhsQ6AEIKDAA{\#}v=onepage{\&}q{\&}f=false.

[193] James D. Kretlow, Leda Klouda, and Antonios G. Mikos. Injectable matrices and scaffolds for drug delivery in tissue engineering, may 2007. ISSN 0169409X.

[194] Thomas E. Robinson, Erik A. B. Hughes, Aniruddha Bose, Elizabeth A. Cornish, Jun Y. Teo, Neil M. Eisenstein, Liam M. Grover, and Sophie C. Cox. Filling the Gap: A Correlation between Objective and Subjective Measures of Injectability. *Advanced Healthcare Materials*, page 1901521, jan 2020. ISSN 2192-2640. doi: 10.1002/adhm.201901521. URL https://onlinelibrary.wiley.com/doi/abs/10.1002/adhm.201901521.

[195] Sophie C. Cox, Sarika Patel, Uwe Gbureck, Adrian J. Wright, and Liam M. Grover. A cohesive premixed monetite biocement. *Journal of the American Ceramic Society*, 100(3):1241–1249, mar 2017. ISSN 00027820. doi: 10.1111/jace.14699. URL http://doi.wiley.com/10.1111/jace.14699.

[196] Uwe Gbureck, Jake E. Barralet, Kerstin Spatz, Liam M. Grover, and Roger Thull. Ionic modification of calcium phosphate cement viscosity. Part I: hypodermic injection and strength improvement of apatite cement. *Biomaterials*, 25(11):2187–2195, may 2004. ISSN 01429612. doi: 10.1016/j.biomaterials.2003.08.066. URL https://linkinghub.elsevier.com/retrieve/pii/S0142961203007233.

[197] Ingrid Ajaxon, Alice Acciaioli, Giacomo Lionello, Maria Pau Ginebra, Caroline Öhman-Mägi, Massimiliano Baleani, and Cecilia Persson. Elastic properties and strain-to-crack-initiation of calcium phosphate bone cements: Revelations of a high-resolution measurement technique. *Journal of the Mechanical Behavior of Biomedical Materials*, 74:428–437, oct 2017. ISSN 18780180. doi: 10.1016/j.jmbbm.2017.06.023.

[198] J. E. Barralet, L. Grover, T. Gaunt, A. J. Wright, and I. R. Gibson. Preparation of macroporous calcium phosphate cement tissue engineering scaffold. *Biomaterials*, 23(15):3063–3072, aug 2002. ISSN 01429612. doi: 10.1016/S0142-9612(01)00401-X.

[199] Jingtao Zhang, Weizhen Liu, Verena Schnitzler, Franck Tancret, and Jean-Michel Bouler. Calcium phosphate cements for bone substitution: Chemistry, handling and mechanical properties. *Acta Biomaterialia*, 10(3):1035–1049, mar 2014. ISSN 17427061. doi: 10.1016/j.actbio.2013.11.001. URL https://linkinghub.elsevier.com/retrieve/pii/S1742706113005576.

[200] I. Hervas, A. Montagne, A. Van Gorp, M. Bentoumi, A. Thuault, and A. Iost. Fracture toughness of glasses and hydroxyapatite: A comparative study of 7 methods by using Vickers indenter. *Ceramics International*, 42(11):12740–12750, aug 2016. ISSN 02728842. doi: 10.1016/j.ceramint.2016.05.030. URL `https://linkinghub.elsevier.com/retrieve/pii/S0272884216306198`.

[201] Hanan Moussa, Wenge Jiang, Ammar Alsheghri, Alaa Mansour, Amir El Hadad, Haihua Pan, Ruikang Tang, Jun Song, Javier Vargas, Marc D. McKee, and Faleh Tamimi. High strength brushite bioceramics obtained by selective regulation of crystal growth with chiral biomolecules. *Acta Biomaterialia*, feb 2020. ISSN 17427061. doi: 10.1016/j.actbio.2020.01.047. URL `https://linkinghub.elsevier.com/retrieve/pii/S1742706120300659`.

[202] Linzhuo Wei, Yichao Wang, Jiangtao Yu, Jianzhuang Xiao, and Shilang Xu. Feasibility study of strain hardening magnesium oxychloride cement-based composites. *Construction and Building Materials*, 165:750–760, mar 2018. ISSN 09500618. doi: 10.1016/j.conbuildmat.2018.01.041.

[203] J. J. Kruzic, D. K. Kim, K. J. Koester, and R. O. Ritchie. Indentation techniques for evaluating the fracture toughness of biomaterials and hard tissues, aug 2009. ISSN 17516161.

[204] K. T. Faber and A. G. Evans. Crack deflection processes-I. Theory. *Acta Metallurgica*, 31(4):565–576, apr 1983. ISSN 00016160. doi: 10.1016/0001-6160(83)90046-9.

[205] Volker Alt, Thorsten Bechert, Peter Steinrücke, Michael Wagener, Peter Seidel, Elvira Dingeldein, Eugen Domann, and Reinhard Schnettler. An in vitro assessment of the antibacterial properties and cytotoxicity of nanoparticulate silver bone cement. *Biomaterials*, 25(18):4383–4391, aug 2004. ISSN 01429612. doi: 10.1016/j.biomaterials.2003.10.078. URL `https://linkinghub.elsevier.com/retrieve/pii/S0142961203010196`.

[206] Yuntao Xie and Lihua Yang. Calcium and Magnesium Ions Are Membrane-Active against Stationary-Phase Staphylococcus aureus with High Specificity. *Scientific Reports*, 6(1):1–8, feb 2016. ISSN 20452322. doi: 10.1038/srep20628.

[207] G. Wirtanen and S. Salo. Biofilm Risks. In *Handbook of Hygiene Control in the Food Industry: Second Edition*, pages 55–79. Elsevier Inc., jun 2016. ISBN 9780081001974. doi: 10.1016/B978-0-08-100155-4.00005-4.

[208] A. Bannerman, R. L. Williams, S. C. Cox, and L. M. Grover. Visualising phase change in a brushite-based calcium phosphate ceramic. *Scientific Reports*, 6(1):

32671, dec 2016. ISSN 2045-2322. doi: 10.1038/srep32671. URL http://www.nature.com/articles/srep32671.

[209] M. P. Ginebra, T. Traykova, and J. A. Planell. Calcium phosphate cements as bone drug delivery systems: A review, jun 2006. ISSN 01683659.

[210] Yongliang Xiong, Haoran Deng, Martin Nemer, and Shelly Johnsen. Experimental determination of the solubility constant for magnesium chloride hydroxide hydrate (Mg3Cl(OH)5·4H2O, phase 5) at room temperature, and its importance to nuclear waste isolation in geological repositories in salt formations. *Geochimica et Cosmochimica Acta*, 74(16):4605–4611, aug 2010. ISSN 00167037. doi: 10.1016/j.gca.2010.05.029. URL https://linkinghub.elsevier.com/retrieve/pii/S0016703710003078.

[211] Harry Chisholm. Magnesium oxychloride cements, apr 1957.

[212] E. G. Brodie, A. E. Medvedev, J. E. Frith, M. S. Dargusch, H. L. Fraser, and A. Molotnikov. Remelt processing and microstructure of selective laser melted Ti25Ta. *Journal of Alloys and Compounds*, 820:153082, apr 2020. ISSN 09258388. doi: 10.1016/j.jallcom.2019.153082.

[213] M. Fischer, D. Joguet, G. Robin, L. Peltier, and P. Laheurte. In situ elaboration of a binary Ti26Nb alloy by selective laser melting of elemental titanium and niobium mixed powders. *Materials Science and Engineering: C*, 62:852–859, may 2016. ISSN 09284931. doi: 10.1016/j.msec.2016.02.033. URL http://linkinghub.elsevier.com/retrieve/pii/S0928493116301254.

[214] J. C. Wang, Y. J. Liu, P. Qin, S. X. Liang, T. B. Sercombe, and L. C. Zhang. Selective laser melting of Ti35Nb composite from elemental powder mixture: Microstructure, mechanical behavior and corrosion behavior. *Materials Science and Engineering A*, 760:214–224, jul 2019. ISSN 09215093. doi: 10.1016/j.msea.2019.06.001.

[215] Jan T. Sehrt, Stefan Kleszczynski, and Christian Notthoff. Nanoparticle improved metal materials for additive manufacturing. *Progress in Additive Manufacturing*, 2(4):179–191, dec 2017. ISSN 2363-9512. doi: 10.1007/s40964-017-0028-9. URL http://link.springer.com/10.1007/s40964-017-0028-9.

[216] Roberto Sorci, Oriana Tassa, Alessandro Colaneri, Alessandro Astri, Daphne Mirabile, Simon Iwnicki, and Ali Gökhan Demir. Design of an Innovative Oxide Dispersion Strengthened Al Alloy for Selective Laser Melting to Produce Lighter

Components for the Railway Sector. *Journal of Materials Engineering and Performance*, pages 1–11, apr 2021. ISSN 1059-9495. doi: 10.1007/s11665-021-05693-5. URL https://doi.org/10.1007/s11665-021-05693-5.

[217] Marziyeh Ajdary, Mohammad Amin Moosavi, Marveh Rahmati, Mojtaba Falahati, Mohammad Mahboubi, Ali Mandegary, Saranaz Jangjoo, Reza Mohammadinejad, and Rajender S. Varma. Health concerns of various nanoparticles: A review of their in vitro and in vivo toxicity, sep 2018. ISSN 20794991. URL www.mdpi.com/journal/nanomaterials.

[218] Giulio Caracciolo, Omid C. Farokhzad, and Morteza Mahmoudi. Biological Identity of Nanoparticles In Vivo: Clinical Implications of the Protein Corona, mar 2017. ISSN 18793096.

[219] Darrell R. Boverhof, Christina M. Bramante, John H. Butala, Shaun F. Clancy, William M. Lafranconi, Jay West, and Steve C. Gordon. Comparative assessment of nanomaterial definitions and safety evaluation considerations. *Regulatory Toxicology and Pharmacology*, 73(1):137–150, oct 2015. ISSN 10960295. doi: 10.1016/j.yrtph.2015.06.001.

[220] Marie Louise Kirkegaard, Pete Kines, Katharina Christiane Jeschke, and Keld Alstrup Jensen. Risk Perceptions and Safety Cultures in the Handling of Nanomaterials in Academia and Industry. *Annals of Work Exposures and Health*, 64 (5):479–489, jun 2020. ISSN 23987316. doi: 10.1093/annweh/wxaa022. URL https://academic.oup.com/annweh/article/64/5/479/5802558.

[221] Thomas J. Fiske, Sudhir B. Railkar, and Dilhan M. Kalyon. Effects of segregation on the packing of spherical and nonspherical particles. *Powder Technology*, 81 (1):57–64, oct 1994. ISSN 0032-5910. doi: 10.1016/0032-5910(94)02862-1. URL https://www.sciencedirect.com/science/article/pii/0032591094028621.

[222] Anchal Jain, Matthew J. Metzger, and Benjamin J. Glasser. Effect of particle size distribution on segregation in vibrated systems. *Powder Technology*, 237:543–553, mar 2013. ISSN 00325910. doi: 10.1016/j.powtec.2012.12.044.

[223] John Robinson, Mark Stanford, and Arun Arjunan. Stable formation of powder bed laser fused 99.9% silver. *Materials Today Communications*, 24:101195, sep 2020. ISSN 23524928. doi: 10.1016/j.mtcomm.2020.101195. URL https://linkinghub.elsevier.com/retrieve/pii/S2352492819303058.

[224] Dongdong Gu, Yves-Christian Hagedorn, Wilhelm Meiners, Guangbin Meng, Rui João Santos Batista, Konrad Wissenbach, and Reinhart Poprawe. Densification

behavior, microstructure evolution, and wear performance of selective laser melting processed commercially pure titanium. *Acta Materialia*, 60(9):3849–3860, may 2012. ISSN 1359-6454. doi: 10.1016/J.ACTAMAT.2012.04.006. URL https://www.sciencedirect.com/science/article/pii/S1359645412002522{\#}s0010.

[225] Krzysztof Ziewiec, Zbigniew Kędzierski, Anna Zielińska-Lipiec, Janusz Stępiński, and Sławomir Kąc. Formation, properties and microstructure of amorphous/crystalline composite Ag20Cu30Ti50 alloy using miscibility gap. *Journal of Alloys and Compounds*, 482(1-2):114–117, aug 2009. ISSN 0925-8388. doi: 10.1016/J.JALLCOM.2009.04.049. URL https://www.sciencedirect.com/science/article/pii/S0925838809007518.

[226] Paul A. Hooper. Melt pool temperature and cooling rates in laser powder bed fusion. *Additive Manufacturing*, 22:548–559, aug 2018. ISSN 22148604. doi: 10.1016/j.addma.2018.05.032.

[227] Masatoshi TAKAHASHI, Masafumi KIKUCHI, and Yukyo TAKADA. Mechanical properties of dental Ti-Ag alloys with 22.5, 25, 27.5, and 30 mass% Ag. *Dental Materials Journal*, 34(4):503–507, jul 2015. ISSN 0287-4547. doi: 10.4012/dmj.2015-075. URL https://www.jstage.jst.go.jp/article/dmj/34/4/34{_}2015-075/{_}article.

[228] Keun-Taek Oh, Hyung-Min Shim, and Kyoung-Nam Kim. Properties of titanium-silver alloys for dental application. *Journal of Biomedical Materials Research Part B: Applied Biomaterials*, 74B(1):649–658, jul 2005. ISSN 1552-4973. doi: 10.1002/jbm.b.30259. URL http://doi.wiley.com/10.1002/jbm.b.30259.

[229] Anqi Shi, Chenshun Zhu, Shan Fu, Renxian Wang, Gaowu Qin, Dafu Chen, and Erlin Zhang. What controls the antibacterial activity of Ti-Ag alloy, Ag ion or Ti2Ag particles? *Materials Science and Engineering C*, 109:110548, apr 2020. ISSN 18730191. doi: 10.1016/j.msec.2019.110548.

[230] E. O. Olakanmi, R. F. Cochrane, and K. W. Dalgarno. A review on selective laser sintering/melting (SLS/SLM) of aluminium alloy powders: Processing, microstructure, and properties, aug 2015. ISSN 00796425.

[231] Il Hyuk Ahn. Determination of a process window with consideration of effective layer thickness in SLM process. *International Journal of Advanced Manufacturing Technology*, 105(10):4181–4191, dec 2019. ISSN 14333015. doi: 10.1007/s00170-019-04402-w. URL https://doi.org/10.1007/s00170-019-04402-w.

[232] Claire Bruna-Rosso, Ali Gökhan Demir, and Barbara Previtali. Selective laser melting finite element modeling: Validation with high-speed imaging and lack of fusion defects prediction. *Materials and Design*, 156:143–153, oct 2018. ISSN 18734197. doi: 10.1016/j.matdes.2018.06.037.

[233] Tesfaye Moges, Gaurav Ameta, and Paul Witherell. A Review of Model Inaccuracy and Parameter Uncertainty in Laser Powder Bed Fusion Models and Simulations. *Journal of Manufacturing Science and Engineering, Transactions of the ASME*, 141(4), apr 2019. ISSN 15288935. doi: 10.1115/1.4042789/475003. URL http://asmedigitalcollection.asme.org/manufacturingscience/article-pdf/141/4/040801/6406826/manu{_}141{_}4{_}040801.pdf.

[234] Kurian Antony and T Reghunathan Rakeshnath. Study on selective laser melting of commercially pure titanium powder. *Proceedings of the Institution of Mechanical Engineers, Part B: Journal of Engineering Manufacture*, 233(7):1794–1807, may 2019. ISSN 0954-4054. doi: 10.1177/0954405418798862. URL http://journals.sagepub.com/doi/10.1177/0954405418798862.

[235] X.P. Li, J. Van Humbeeck, and J.P. Kruth. Selective laser melting of weak-textured commercially pure titanium with high strength and ductility: A study from laser power perspective. *Materials & Design*, 116:352–358, feb 2017. ISSN 0264-1275. doi: 10.1016/J.MATDES.2016.12.019. URL https://www.sciencedirect.com/science/article/pii/S0264127516315349.

[236] D.W. Wang, Y.H. Zhou, J. Shen, Y. Liu, D.F. Li, Q. Zhou, G. Sha, P. Xu, T. Ebel, and M. Yan. Selective laser melting under the reactive atmosphere: A convenient and efficient approach to fabricate ultrahigh strength commercially pure titanium without sacrificing ductility. *Materials Science and Engineering: A*, 762:138078, aug 2019. ISSN 09215093. doi: 10.1016/j.msea.2019.138078. URL https://linkinghub.elsevier.com/retrieve/pii/S0921509319308640.

[237] Hooyar Attar, Shima Ehtemam-Haghighi, Damon Kent, Xinhua Wu, and Matthew S. Dargusch. Comparative study of commercially pure titanium produced by laser engineered net shaping, selective laser melting and casting processes. *Materials Science and Engineering: A*, 705:385–393, sep 2017. ISSN 0921-5093. doi: 10.1016/J.MSEA.2017.08.103. URL https://www.sciencedirect.com/science/article/pii/S0921509317311085?via{\%}3Dihub.

[238] Yali Li and Dongdong Gu. Thermal behavior during selective laser melting of commercially pure titanium powder: Numerical simulation and experimental

study. *Additive Manufacturing*, 1-4:99–109, oct 2014. ISSN 2214-8604. doi: 10.1016/J.ADDMA.2014.09.001. URL https://www.sciencedirect.com/science/article/pii/S2214860414000116{\#}sec0035.

[239] Pei Wei, Zhengying Wei, Zhen Chen, Jun Du, Yuyang He, Junfeng Li, and Yatong Zhou. The AlSi10Mg samples produced by selective laser melting: single track, densification, microstructure and mechanical behavior. *Applied Surface Science*, 408:38–50, jun 2017. ISSN 01694332. doi: 10.1016/j.apsusc.2017.02.215.

[240] Jie Liu, Dong dong Gu, Hong yu Chen, Dong hua Dai, and Han Zhang. Influence of substrate surface morphology on wetting behavior of tracks during selective laser melting of aluminum-based alloys. *Journal of Zhejiang University: Science A*, 19 (2):111–121, feb 2018. ISSN 18621775. doi: 10.1631/jzus.A1700599. URL https://doi.org/10.1631/jzus.A1700599.

[241] Curtis T. Rueden, Johannes Schindelin, Mark C. Hiner, Barry E. DeZonia, Alison E. Walter, Ellen T. Arena, and Kevin W. Eliceiri. ImageJ2: ImageJ for the next generation of scientific image data. *BMC Bioinformatics*, 18(1):529, dec 2017. ISSN 1471-2105. doi: 10.1186/s12859-017-1934-z. URL https://bmcbioinformatics.biomedcentral.com/articles/10.1186/s12859-017-1934-z.

[242] Johannes Schindelin, Ignacio Arganda-Carreras, Erwin Frise, Verena Kaynig, Mark Longair, Tobias Pietzsch, Stephan Preibisch, Curtis Rueden, Stephan Saalfeld, Benjamin Schmid, Jean-Yves Tinevez, Daniel James White, Volker Hartenstein, Kevin Eliceiri, Pavel Tomancak, and Albert Cardona. Fiji: an open-source platform for biological-image analysis. *Nature Methods*, 9(7):676–682, jul 2012. ISSN 1548-7091. doi: 10.1038/nmeth.2019. URL http://www.ncbi.nlm.nih.gov/pubmed/22743772http://www.pubmedcentral.nih.gov/articlerender.fcgi?artid=PMC3855844http://www.nature.com/articles/nmeth.2019.

[243] Laura Cordova, Ton Bor, Marc de Smit, Mónica Campos, and Tiedo Tinga. Measuring the spreadability of pre-treated and moisturized powders for laser powder bed fusion. *Additive Manufacturing*, 32:101082, mar 2020. ISSN 22148604. doi: 10.1016/j.addma.2020.101082.

[244] P. B. Johnson, R. W. Christy, and P. B. Johnson and R. W. Christy. Optical Constant of the Noble Metals. *Physica L Re View B*, 6(12):4370–4379, dec 1972. ISSN 01631829. doi: 10.1103/PhysRevB.6.4370. URL https://journals.aps.org/prb/abstract/10.1103/PhysRevB.6.4370.

[245] Yajie Jiang, Supriya Pillai, and Martin A. Green. Realistic Silver Optical Constants for Plasmonics. *Scientific Reports*, 6(1):1–7, jul 2016. ISSN 20452322. doi: 10.1038/srep30605. URL www.nature.com/scientificreports.

[246] P. B. Johnson, R. W. Christy, P. B. Johnson, and R. W. Christy. Optical constants of transition metals. *Physical Review B*, 9(12):5056–5070, jun 1974. ISSN 0556-2805. doi: 10.1103/PhysRevB.9.5056. URL https://journals.aps.org/prb/abstract/10.1103/PhysRevB.9.5056.

[247] Dmitrij A. Belousov, Vadim S. Terent'ev, Evgeny V. Spesivtsev, and Victor P. Korolkov. Spectral data of refractive index and extinction coefficient for thin films of titanium group metals used for fabrication of optical microstructures. *Data in Brief*, 28:104903, feb 2020. ISSN 23523409. doi: 10.1016/j.dib.2019.104903.

[248] C. D. Boley, Saad A. Khairallah, and Alexander M. Rubenchik. Calculation of laser absorption by metal powders in additive manufacturing. *Applied Optics*, 54 (9):2477, mar 2015. ISSN 1559-128X. doi: 10.1364/AO.54.002477. URL https://www.osapublishing.org/abstract.cfm?URI=ao-54-9-2477.

[249] B Wilthan, C Cagran, and G Pottlacher. Combined DSC and Pulse-Heating Measurements of Electrical Resistivity and Enthalpy of Tungsten, Niobium, and Titanium 1. *International Journal of Thermophysics*, 26(4), 2005. doi: 10.1007/s10765-005-6682-z.

[250] J. W. Arblaster. Thermodynamic Properties of Silver. *Journal of Phase Equilibria and Diffusion*, 36(6):573–591, dec 2015. ISSN 15477037. doi: 10.1007/s11669-015-0411-5. URL https://link.springer.com/article/10.1007/s11669-015-0411-5.

[251] T. Mukherjee, H. L. Wei, A. De, and T. DebRoy. Heat and fluid flow in additive manufacturingPart I: Modeling of powder bed fusion. *Computational Materials Science*, 150:304–313, jul 2018. ISSN 09270256. doi: 10.1016/j.commatsci.2018.04.022.

[252] C Y Ho, R W Powell, and P E Liley. Thermal Conductivity of Selected Materials, Part 2. *Nsrds-Nbs 16*, page 168, 1968.

[253] A.D. Kirshenbaum, J.A. Cahill, and A.V. Grosse. The density of liquid silver from its melting point to its normal boiling point 2450K. *Journal of Inorganic and Nuclear Chemistry*, 24(3):333–336, mar 1962. ISSN 00221902. doi: 10.1016/0022-1902(62)80188-2. URL https://linkinghub.elsevier.com/retrieve/pii/0022190262801882.

[254] B. Giordanengo, N. Benazzi, J. Vinckel, J. G. Gasser, and L. Roubi. Thermal conductivity of liquid metals and metallic alloys. *Journal of Non-Crystalline Solids*, 250 (I):377–383, aug 1999. ISSN 00223093. doi: 10.1016/S0022-3093(99)00268-9.

[255] K. Zhou, H. P. Wang, J. Chang, and B. Wei. Experimental study of surface tension, specific heat and thermal diffusivity of liquid and solid titanium. *Chemical Physics Letters*, 639:105–108, oct 2015. ISSN 00092614. doi: 10.1016/j.cplett.2015.09.014.

[256] J. Spreadborough and J. W. Christian. The measurement of the lattice expansions and debye temperatures of titanium and silver by X-ray methods. *Proceedings of the Physical Society*, 74(5):609–615, nov 1959. ISSN 03701328. doi: 10.1088/0370-1328/74/5/314. URL https://iopscience.iop.org/article/10.1088/0370-1328/74/5/314https://iopscience.iop.org/article/10.1088/0370-1328/74/5/314/meta.

[257] Paul-François Paradis and Won-Kyu Rhim. Non-contact measurements of thermophysical properties of titanium at high temperature. *The Journal of Chemical Thermodynamics*, 32(1):123–133, jan 2000. ISSN 00219614. doi: 10.1006/jcht.1999.0576. URL https://linkinghub.elsevier.com/retrieve/pii/S0021961499905761.

[258] Manabu Watanabe, Masayoshi Adachi, and Hiroyuki Fukuyama. Heat capacities and thermal conductivities of palladium and titanium melts and correlation between thermal diffusivity and density of states for transition metals in a liquid state. *Journal of Molecular Liquids*, 324:115138, feb 2021. ISSN 01677322. doi: 10.1016/j.molliq.2020.115138.

[259] Manabu Watanabe, Masayoshi Adachi, and Hiroyuki Fukuyama. Density measurement of TiX (X = Cu, Ni) melts and thermodynamic correlations. *Journal of Materials Science*, 54(5):4306–4313, mar 2019. ISSN 15734803. doi: 10.1007/s10853-018-3098-2. URL https://doi.org/10.1007/s10853-018-3098-2.

[260] James H. VanSant. Conduction heat transfer solutions. Technical report, Lawrence Livermore National Laboratory (LLNL), Livermore, CA (United States), mar 1980. URL http://www.osti.gov/servlets/purl/7035199/.

[261] L L Aráujo and M Behar. Al and Ag diffusion study in α-titanium. *Appl. Phys. A*, 71:169–174, 2000. doi: 10.1007/s003390000485. URL https://link.springer.com/content/pdf/10.1007{\%}2FPL00021114.pdf.

[262] Sung-Yul Lee, Yoshiaki Iijima, Osamu Taguchi, and Ken-Ichi Hirano. Diffusion of Copper and Silver in β-Titanium, 1990.

[263] Fujio Makuta, Yoshiaki Iijima, and Ken ichi Hirano. Diffusion of Titanium, Vanadium, Chromium and Manganese in Silver., 1979. ISSN 00214434.

[264] Arden Phua, Christian Doblin, Phil Owen, Chris H.J. Davies, and Gary W. Delaney. The effect of recoater geometry and speed on granular convection and size segregation in powder bed fusion. *Powder Technology*, 394:632–644, dec 2021. ISSN 00325910. doi: 10.1016/j.powtec.2021.08.058. URL `https://linkinghub.elsevier.com/retrieve/pii/S0032591021007452`.

[265] Mohamad Yousef Shaheen, Anthony R. Thornton, Stefan Luding, and Thomas Weinhart. The influence of material and process parameters on powder spreading in additive manufacturing. *Powder Technology*, 383:564–583, may 2021. ISSN 0032-5910. doi: 10.1016/J.POWTEC.2021.01.058.

[266] Andre Mussatto, Robert Groarke, Aidan O'Neill, Muhannad Ahmed Obeidi, Yan Delaure, and Dermot Brabazon. Influences of powder morphology and spreading parameters on the powder bed topography uniformity in powder bed fusion metal additive manufacturing. *Additive Manufacturing*, 38:101807, feb 2021. ISSN 2214-8604. doi: 10.1016/J.ADDMA.2020.101807.

[267] Christoph Meier, Reimar Weissbach, Johannes Weinberg, Wolfgang A. Wall, and A. John Hart. Modeling and characterization of cohesion in fine metal powders with a focus on additive manufacturing process simulations. *Powder Technology*, 343:855–866, feb 2019. ISSN 00325910. doi: 10.1016/j.powtec.2018.11.072. URL `https://linkinghub.elsevier.com/retrieve/pii/S0032591018309884`.

[268] Christoph Meier, Reimar Weissbach, Johannes Weinberg, Wolfgang A. Wall, and A. John Hart. Critical influences of particle size and adhesion on the powder layer uniformity in metal additive manufacturing. *Journal of Materials Processing Technology*, 266:484–501, apr 2019. ISSN 09240136. doi: 10.1016/j.jmatprotec.2018.10.037.

[269] Christopher Paul Randall. *The Silver Cation (Ag +): Antibacterial Mode of Action and Mechanisms of Resistance*. PhD thesis, University of Leeds, 2013. URL `http://etheses.whiterose.ac.uk/5915/1/ChristopherRandall200360180eThesis.pdf`.

[270] Marius Colin, Flora Klingelschmitt, Emilie Charpentier, Jérôme Josse, Lukshe Kanagaratnam, Christophe De Champs, and Sophie C. Gangloff. Copper Alloy Touch Surfaces in Healthcare Facilities: An Effective Solution to Prevent Bacterial Spreading. *Materials 2018, Vol. 11, Page 2479*, 11(12):2479, dec 2018. doi: 10.3390/

MA11122479. URL https://www.mdpi.com/1996-1944/11/12/2479/htmhttps://www.mdpi.com/1996-1944/11/12/2479.

[271] A. L. Casey, D. Adams, T. J. Karpanen, P. A. Lambert, B. D. Cookson, P. Nightingale, L. Miruszenko, R. Shillam, P. Christian, and T. S.J. Elliott. Role of copper in reducing hospital environment contamination. *Journal of Hospital Infection*, 74(1): 72–77, jan 2010. ISSN 0195-6701. doi: 10.1016/J.JHIN.2009.08.018.

[272] J. O. Noyce, H. Michels, and C. W. Keevil. Potential use of copper surfaces to reduce survival of epidemic meticillin-resistant Staphylococcus aureus in the healthcare environment. *Journal of Hospital Infection*, 63(3):289–297, jul 2006. ISSN 0195-6701. doi: 10.1016/J.JHIN.2005.12.008.

[273] Lydia Finney, Stefan Vogt, Tohru Fukai, and David Glesne. COPPER AND ANGIOGENESIS: UNRAVELLING A RELATIONSHIP KEY TO CANCER PROGRESSION. *Clinical and Experimental Pharmacology and Physiology*, 36(1): 88–94, jan 2009. ISSN 1440-1681. doi: 10.1111/J.1440-1681.2008.04969.X. URL https://onlinelibrary.wiley.com/doi/full/10.1111/j.1440-1681.2008.04969.xhttps://onlinelibrary.wiley.com/doi/abs/10.1111/j.1440-1681.2008.04969.xhttps://onlinelibrary.wiley.com/doi/10.1111/j.1440-1681.2008.04969.x.

[274] Sarah A Lowndes and Adrian L Harris. The Role of Copper in Tumour Angiogenesis. 2006. doi: 10.1007/s10911-006-9003-7.

[275] María Cecilia Cortizo and Mónica Fernández Lorenzo de Mele. Cytotoxicity of copper ions released from metal. *Biological Trace Element Research 2004 102:1*, 102(1):129–141, dec 2004. ISSN 1559-0720. doi: 10.1385/BTER:102:1-3:129. URL https://link.springer.com/article/10.1385/BTER:102:1-3:129.

[276] Michael C Wyatt, Michael Foxall-Smith, Andrew Roberton, Andrew Beswick, David C Kieser, and Michael R Whitehouse. The use of silver coating in hip megaprostheses: a systematic review. *Hip international : the journal of clinical and experimental research on hip pathology and therapy*, 29(1):7–20, jan 2019. ISSN 1724-6067. doi: 10.1177/1120700018811070. URL http://www.ncbi.nlm.nih.gov/pubmed/30442019.

[277] Ramesh Bharti, Kulvinder Kaur Wadhwani, Aseem Prakash Tikku, and Anil Chandra. Dental amalgam: An update. *Journal of Conservative Dentistry : JCD*, 13(4):204, sep 2010. ISSN 07340338. doi: 10.4103/0972-0707.

73380. URL /pmc/articles/PMC3010024//pmc/articles/PMC3010024/?report=abstracthttps://www.ncbi.nlm.nih.gov/pmc/articles/PMC3010024/.

[278] Feilong Jiang, Weiwei Zhu, Cancan Zhao, Yulei Li, Pengbo Wei, Tian Wan, Haixia Ye, Shuai Pan, and Fuzeng Ren. A strong, wear- and corrosion-resistant, and antibacterial Co30 at.% Cr5 at.% Ag ternary alloy for medical implants. *Materials & Design*, 184:108190, dec 2019. ISSN 0264-1275. doi: 10.1016/J.MATDES.2019.108190. URL https://www.sciencedirect.com/science/article/pii/S0264127519306288.

[279] Xiaotian Liu, Shuyang Chen, James K.H. Tsoi, and Jukka Pekka Matinlinna. Binary titanium alloys as dental implant materialsa review. *Regenerative Biomaterials*, 4 (5):315–323, oct 2017. ISSN 2056-3418. doi: 10.1093/RB/RBX027. URL https://academic.oup.com/rb/article/4/5/315/4210443.

[280] Olivier Dezellus, Raymundo Arroyave, and Suzana G. Fries. Thermodynamic modelling of the Ag-Cu-Ti ternary system. *International Journal of Materials Research*, 102(3):286–297, 2011. doi: 10.3139/146.110472. URL https://hal.archives-ouvertes.fr/hal-00623284/document.

[281] Jung Gu Lee and Min-Ku Lee. Microstructure and mechanical behavior of a titanium-to-stainless steel dissimilar joint brazed with Ag-Cu alloy filler and an Ag interlayer. *Materials Characterization*, 129:98–103, jul 2017. ISSN 1044-5803. doi: 10.1016/J.MATCHAR.2017.04.032. URL https://www.sciencedirect.com/science/article/pii/S1044580317304229{\#}f0030.

[282] R. H. Shiue and S. K. Wu. Infrared brazing of Ti50Ni50 shape memory alloy using two AgCuTi active braze alloys. *Intermetallics*, 14(6):630–638, jun 2006. ISSN 0966-9795. doi: 10.1016/J.INTERMET.2005.10.012.

[283] A. Fraser-Moodie. Sensitivity to silver in a patient treated with silver sulphadiazine (Flamazine). *Burns*, 18(1):74–75, feb 1992. ISSN 0305-4179. doi: 10.1016/0305-4179(92)90128-H.

[284] Marija Trop, Michael Novak, Siegfried Rodl, Bengt Hellbom, Wolfgang Kroell, and Walter Goessler. Silver-coated dressing acticoat caused raised liver enzymes and argyria-like symptoms in burn patient. *Journal of Trauma - Injury, Infection and Critical Care*, 60(3):648–652, mar 2006. doi: 10.1097/01.TA.0000208126.22089.B6. URL https://journals.lww.com/jtrauma/Fulltext/2006/03000/Silver{_}Coated{_}Dressing{_}Acticoat{_}Caused{_}Raised.28.aspx.

[285] J. Fong, F. Wood, and B. Fowler. A silver coated dressing reduces the incidence of early burn wound cellulitis and associated costs of inpatient treatment: Comparative patient care audits. *Burns*, 31(5):562–567, aug 2005. ISSN 0305-4179. doi: 10.1016/J.BURNS.2004.12.009.

[286] Mian Chen, Erlin Zhang, and Lan Zhang. Microstructure, mechanical properties, bio-corrosion properties and antibacterial properties of TiAg sintered alloys. *Materials Science and Engineering: C*, 62:350–360, may 2016. ISSN 09284931. doi: 10.1016/j.msec.2016.01.081. URL http://www.sciencedirect.com/science/article/pii/S0928493116300789http://linkinghub.elsevier.com/retrieve/pii/S0928493116300789.

[287] B.B. Zhang, Y.F. Zheng, and Y. Liu. Effect of Ag on the corrosion behavior of TiAg alloys in artificial saliva solutions. *Dental Materials*, 25(5):672–677, may 2009. ISSN 0109-5641. doi: 10.1016/J.DENTAL.2008.10.016. URL https://www.sciencedirect.com/science/article/pii/S010956410800287X{\#}fig4.

[288] Hyung-Min Shim, Keun-Taek Oh, Jae-Young Woo, Chung-Ju Hwang, and Kyoung-Nam Kim. Corrosion resistance of titanium-silver alloys in an artificial saliva containing fluoride ions. *Journal of Biomedical Materials Research Part B: Applied Biomaterials*, 73B(2):252–259, may 2005. ISSN 1552-4973. doi: 10.1002/jbm.b.30206. URL http://doi.wiley.com/10.1002/jbm.b.30206.

[289] Barbara Szaraniec and Tomasz Goryczka. Structure and properties of Ti-Ag alloys produced by powder metallurgy. *Journal of Alloys and Compounds*, 709:464–472, jun 2017. ISSN 09258388. doi: 10.1016/j.jallcom.2017.03.155. URL https://www.sciencedirect.com/science/article/pii/S0925838817309386https://linkinghub.elsevier.com/retrieve/pii/S0925838817309386.

[290] Keng-Liang Ou, Chao-Chia Weng, Yun-Ho Lin, and Mao-Suan Huang. A promising of alloying modified beta-type Titanium-Niobium implant for biomedical applications: Microstructural characteristics, in vitro biocompatibility and antibacterial performance. *Journal of Alloys and Compounds*, 697:231–238, mar 2017. ISSN 09258388. doi: 10.1016/j.jallcom.2016.12.120. URL http://dx.doi.org/10.1016/j.jallcom.2016.12.120http://linkinghub.elsevier.com/retrieve/pii/S0925838816340385.

[291] D. Wojcieszak, M. Mazur, D. Kaczmarek, P. Mazur, B. Szponar, J. Domaradzki, and L. Kepinski. Influence of the surface properties on bactericidal and fungicidal activity of magnetron sputtered TiAg and NbAg thin films. *Materials Science and Engineering: C*, 62:86–95, may 2016. ISSN 0928-4931. doi: 10.1016/J.

MSEC.2016.01.029. URL https://www.sciencedirect.com/science/article/pii/S092849311630025X.

[292] Yiwen Zhang, Kangjie Chu, Shan He, Bi Wang, Weiwei Zhu, and Fuzeng Ren. Fabrication of high strength, antibacterial and biocompatible Ti-5Mo-5Ag alloy for medical and surgical implant applications. *Materials Science and Engineering: C*, 106:110165, jan 2020. ISSN 0928-4931. doi: 10.1016/J.MSEC.2019.110165. URL https://www.sciencedirect.com/science/article/pii/S092849311832352X.

[293] Zeming Lei, Hangzhou Zhang, Erlin Zhang, Junhua You, Xiaoxue Ma, and Xizhuang Bai. Antibacterial activities and biocompatibilities of Ti-Ag alloys prepared by spark plasma sintering and acid etching. *Materials Science and Engineering: C*, 92:121–131, nov 2018. ISSN 0928-4931. doi: 10.1016/J.MSEC.2018.06.024. URL https://www.sciencedirect.com/science/article/pii/S0928493117335270?via{\%}3Dihub.

[294] Takeshi Nagase, Megumi Matsumoto, and Yoshikazu Fujii. Microstructure of Ti-Ag immiscible alloys with liquid phase separation. *Journal of Alloys and Compounds*, 738:440–447, mar 2018. ISSN 0925-8388. doi: 10.1016/J.JALLCOM.2017.12.138. URL https://www.sciencedirect.com/science/article/pii/S0925838817343347.

[295] J. Zemann. Crystal structures, 2nd edition. Vol. 1 by R. W. G. Wyckoff. *Acta Crystallographica*, 18(1):139–139, jan 1965. ISSN 0365-110X. doi: 10.1107/S0365110X65000361. URL https://onlinelibrary.wiley.com/doi/full/10.1107/S0365110X65000361https://onlinelibrary.wiley.com/doi/abs/10.1107/S0365110X65000361https://onlinelibrary.wiley.com/doi/10.1107/S0365110X65000361.

[296] A. Vaitkus, A. Merkys, S. Gražulis, and IUCr. Validation of the Crystallography Open Database using the Crystallographic Information Framework. *urn:issn:1600-5767*, 54(2):661–672, feb 2021. ISSN 1600-5767. doi: 10.1107/S1600576720016532. URL http://scripts.iucr.org/cgi-bin/paper?yr5065https://journals.iucr.org/j/issues/2021/02/00/yr5065/.

[297] Anubhav Jain, Shyue Ping Ong, Geoffroy Hautier, Wei Chen, William Davidson Richards, Stephen Dacek, Shreyas Cholia, Dan Gunter, David Skinner, Gerbrand Ceder, and Kristin A. Persson. Commentary: The materials project: A materials genome approach to accelerating materials innovation, jul 2013. ISSN 2166532X. URL http://aip.scitation.org/doi/10.1063/1.4812323.

[298] M.R Plichta, H.I Aaronson, and J.H Perepezko. The thermodynamics and kinetics of the $\beta \rightarrow \alpha$m transformation in three Ti-X systems. *Acta Metallurgica*, 26(8):1293–1305, aug 1978. ISSN 0001-6160. doi: 10.1016/0001-6160(78)90014-7. URL https://www.sciencedirect.com/science/article/pii/0001616078900147https://www.sciencedirect.com/science/article/pii/0001616078900147?via{\%}3Dihub.

[299] C. Fleißner-Rieger, T. Pogrielz, D. Obersteiner, T. Pfeifer, H. Clemens, and S. Mayer. An Additively Manufactured Titanium Alloy in the Focus of Metallography. *Practical Metallography*, 58(1):4–31, jan 2021. ISSN 2195-8599. doi: 10.1515/PM-2020-0001. URL https://www.degruyter.com/document/doi/10.1515/pm-2020-0001/html.

[300] Ertuan Zhao, Shichen Sun, and Yu Zhang. Recent advances in silicon containing high temperature titanium alloys. *Journal of Materials Research and Technology*, 14:3029–3042, sep 2021. ISSN 2238-7854. doi: 10.1016/J.JMRT.2021.08.117.

[301] G. W. Franti, J. C. Williams, and H. I. Aaronson. A survey of eutectoid decomposition in ten Ti-X systems. *Metallurgical Transactions A 1978 9:11*, 9 (11):1641–1649, nov 1978. ISSN 1543-1940. doi: 10.1007/BF02661947. URL https://link.springer.com/article/10.1007/BF02661947.

[302] R. J. Contieri, E. S.N. Lopes, R. Caram, A. Devaraj, S. Nag, and R. Banerjee. Effects of cooling rate on the microstructure and solute partitioning in near eutectoid Ti-Cu alloys. *Philosophical Magazine*, 94(21):2350–2371, jul 2014. ISSN 14786443. doi: 10.1080/14786435.2014.913113. URL https://www.tandfonline.com/doi/abs/10.1080/14786435.2014.913113.

[303] Yuan Tsung Wang, Yoshitaka Adachi, Kiyomi Nakajima, and Yoshimasa Sugimoto. Quantitative three-dimensional characterization of pearlite spheroidization. *Acta Materialia*, 58(14):4849–4858, aug 2010. ISSN 1359-6454. doi: 10.1016/J.ACTAMAT.2010.05.023.

[304] Yong Lai Tian and R. Wayne Kraft. Mechanisms of Pearlite Spheroidization. *Metallurgical Transactions A 1987 18:8*, 18(8):1403–1414, aug 1987. ISSN 1543-1940. doi: 10.1007/BF02646654. URL https://link.springer.com/article/10.1007/BF02646654.

[305] V. A. Lubarda. On the effective lattice parameter of binary alloys. *Mechanics of Materials*, 35(1-2):53–68, jan 2003. ISSN 0167-6636. doi: 10.1016/S0167-6636(02)00196-5.

[306] Frederick Seitz. Color centers in alkali halide crystals. *Reviews of Modern Physics*, 18(3):384–408, 1946. ISSN 00346861. doi: 10.1103/RevModPhys.18.384.

[307] J. Cermak and L. Kral. Carbon diffusion in carbon-supersaturated ferrite and austenite. *Journal of Alloys and Compounds*, 586:129–135, feb 2014. ISSN 0925-8388. doi: 10.1016/J.JALLCOM.2013.10.058.

[308] Christian Herzig, Ralf Willecke, and Klaus Vieregge. Self-diffusion and fast cobalt impurity diffusion in the bulk and in grain boundaries of hexagonal titanium. *https://doi.org/10.1080/01418619108213927*, 63(5):949–958, 1991. ISSN 01418610. doi: 10.1080/01418619108213927. URL `https://www.tandfonline.com/doi/abs/10.1080/01418619108213927`.

[309] Joseph I Goldstein, Dale E Newbury, P. Echlin, David C Joy, C. Fiori, and E. Lifshin. *Scanning Electron Microscopy and X-ray Microanalysis: a text for Biologists, Materials Scientists, and Geologists.* Plenum Press, New York, second edition, 1992. ISBN 9781461304913.

[310] Yoshiaki Okajima. Estimation of sputtering rate by bombardment with argon gas ions. *Journal of Applied Physics*, 51(1):715–717, jul 1980. ISSN 00218979. doi: 10.1063/1.327331. URL `https://doi.org/10.1063/1.327331`.

[311] Eteri Svanidze, Tiglet Besara, M. Fevsi Ozaydin, Chandra Sekhar Tiwary, Jiakui K. Wang, Sruthi Radhakrishnan, Sendurai Mani, Yan Xin, Ke Han, Hong Liang, Theo Siegrist, Pulickel M. Ajayan, and E. Morosan. High hardness in the biocompatible intermetallic compound b-Ti3Au. *Science Advances*, 2(7), 2016. ISSN 23752548. doi: 10.1126/sciadv.1600319. URL `/pmc/articles/PMC4956191/?report=abstracthttps://www.ncbi.nlm.nih.gov/pmc/articles/PMC4956191/`.

[312] Sara Axelsson, Yu Cao, and Uta Klement. Surface Characterization of Titanium Powders with X-ray Photoelectron Spectroscopy Diploma work in the Master Programme Advanced Engineering Materials. Technical report.

[313] Doo-Hoon Song, Soo-Hyuk Uhm, Sang-Bae Lee, Jeon-Geon Han, and Kyoung-Nam Kim. Antimicrobial silver-containing titanium oxide nanocomposite coatings by a reactive magnetron sputtering. *Thin Solid Films*, 519(20):7079–7085, aug 2011. ISSN 0040-6090. doi: 10.1016/J.TSF.2011.01.385. URL `https://www.sciencedirect.com/science/article/pii/S0040609011004524`.

[314] Monica Thukkaram, Pieter Cools, Anton Nikiforov, Petra Rigole, Tom Coenye, Pascal Van Der Voort, Gijs Du Laing, Chris Vercruysse, Heidi Declercq, Rino

Morent, Lieven De Wilde, Patrick De Baets, Kim Verbeken, and Nathalie De Geyter. Antibacterial activity of a porous silver doped TiO2 coating on titanium substrates synthesized by plasma electrolytic oxidation. *Applied Surface Science*, 500:144235, jan 2020. ISSN 0169-4332. doi: 10.1016/J.APSUSC.2019.144235. URL https://www.sciencedirect.com/science/article/pii/S016943321933051X.

[315] Erik Unosson, Daniel Rodriguez, Ken Welch, and Håkan Engqvist. Reactive combinatorial synthesis and characterization of a gradient AgTi oxide thin film with antibacterial properties. *Acta Biomaterialia*, 11:503–510, jan 2015. ISSN 1742-7061. doi: 10.1016/J.ACTBIO.2014.09.048. URL http://www.sciencedirect.com/science/article/pii/S1742706114004401{\#}b0230.

[316] Yunzhi Yang, Renee Cavin, and Joo L Ong. Protein adsorption on titanium surfaces and their effect on osteoblast attachment. *Journal of Biomedical Materials Research*, 67A(1):344–349, oct 2003. ISSN 0021-9304. doi: 10.1002/jbm.a.10578. URL http://doi.wiley.com/10.1002/jbm.a.10578.

[317] N. Hori, W. Att, T. Ueno, N. Sato, M. Yamada, L. Saruwatari, T. Suzuki, and T. Ogawa. Age-dependent degradation of the protein adsorption capacity of titanium. *Journal of Dental Research*, 88(7):663–667, jul 2009. ISSN 00220345. doi: 10.1177/0022034509339567. URL https://journals.sagepub.com/doi/abs/10.1177/0022034509339567.

[318] Bengt Wälivaara, Björn Owe Aronsson, Michael Rodahl, Jukka Lausmaa, and Pentti Tengvall. Titanium with different oxides: in vitro studies of protein adsorption and contact activation. *Biomaterials*, 15(10):827–834, aug 1994. ISSN 0142-9612. doi: 10.1016/0142-9612(94)90038-8.

[319] Kaiyong Cai, Jörg Bossert, and Klaus D. Jandt. Does the nanometre scale topography of titanium influence protein adsorption and cell proliferation? *Colloids and Surfaces B: Biointerfaces*, 49(2):136–144, may 2006. ISSN 0927-7765. doi: 10.1016/J.COLSURFB.2006.02.016. URL http://www.sciencedirect.com/science/article/pii/S0927776506000750.

[320] Marcus Jäger, Herbert P. Jennissen, Marcel Haversath, André Busch, Thomas Grupp, Andrea Sowislok, and Monika Herten. Intrasurgical Protein Layer on Titanium Arthroplasty Explants: From the Big Twelve to the Implant Proteome. *Proteomics - Clinical Applications*, 13(2):1800168, mar 2019. ISSN 18628354. doi: 10.1002/prca.201800168. URL https://onlinelibrary.wiley.com/doi/abs/10.1002/prca.201800168.

[321] Elsa F. Vieira, Joana Carvalho, Edgar Pinto, Sara Cunha, Agostinho A. Almeida, and Isabel M.P.L.V.O. Ferreira. Nutritive value, antioxidant activity and phenolic compounds profile of brewer's spent yeast extract. *Journal of Food Composition and Analysis*, 52:44–51, sep 2016. ISSN 0889-1575. doi: 10.1016/J.JFCA.2016.07.006.

[322] Artyom Shchelokov, Nadezhda Palko, Vladimir Potemkin, Maria Grishina, Roman Morozov, Elena Korina, Danil Uchaev, Igor Krivtsov, and Oleg Bol'Shakov. Adsorption of Native Amino Acids on Nanocrystalline TiO 2 : Physical Chemistry, QSPR, and Theoretical Modeling. *Langmuir*, 35(2):538–550, jan 2019. ISSN 15205827. doi: 10.1021/ACS.LANGMUIR.8B02007/SUPPL_FILE/LA8B02007_SI_001.PDF. URL https://pubs.acs.org/doi/full/10.1021/acs.langmuir.8b02007.

[323] M. A. Khan, R. L. Williams, and D. F. Williams. The corrosion behaviour of Ti6Al4V, Ti6Al7Nb and Ti13Nb13Zr in protein solutions. *Biomaterials*, 20(7):631–637, apr 1999. ISSN 0142-9612. doi: 10.1016/S0142-9612(98)00217-8.

[324] Mohd Talha, Yucong Ma, Pardeep Kumar, Yuanhua Lin, and Ambrish Singh. Role of protein adsorption in the bio corrosion of metallic implants A review. *Colloids and Surfaces B: Biointerfaces*, 176:494–506, apr 2019. ISSN 0927-7765. doi: 10.1016/J.COLSURFB.2019.01.038.

[325] Moon-Jin Hwang, Eun-Jin Park, Won-Jin Moon, Ho-Jun Song, and Yeong-Joon Park. Characterization of passive layers formed on Ti10wt% (Ag, Au, Pd, or Pt) binary alloys and their effects on galvanic corrosion. *Corrosion Science*, 96:152–159, jul 2015. ISSN 0010-938X. doi: 10.1016/J.CORSCI.2015.04.007. URL https://www.sciencedirect.com/science/article/pii/S0010938X15001675?via{\%}3Dihub.

[326] Wislei R. Osório, Celia M. Freire, Rubens Caram, and Amauri Garcia. The role of Cu-based intermetallics on the pitting corrosion behavior of SnCu, TiCu and AlCu alloys. *Electrochimica Acta*, 77:189–197, aug 2012. ISSN 0013-4686. doi: 10.1016/J.ELECTACTA.2012.05.106.

[327] J. A. Dean. Lange's handbook of chemistry. *Materials and Manufacturing Processes*, 5(4):687–688, 1990. ISSN 15322475. doi: 10.1080/10426919008953291. URL https://www.tandfonline.com/doi/abs/10.1080/10426919008953291http://fptl.ru/biblioteka/spravo4niki/dean.pdf.

[328] S. Smoes, F. Mandy, A. Vander AuweraMahieu, and J. Drowart. Determination by the mass spectrometric knudsen cell method of the dissociation energies of the group IB chalcogenides. *Bulletin des Sociétés Chimiques Belges*, 81(1):45–56,

jan 1972. ISSN 0037-9646. doi: 10.1002/BSCB.19720810103. URL https://onlinelibrary.wiley.com/doi/full/10.1002/bscb.19720810103https://onlinelibrary.wiley.com/doi/abs/10.1002/bscb.19720810103https://onlinelibrary.wiley.com/doi/10.1002/bscb.19720810103.

[329] Nicole Ciacotich, Rameez Ud Din, Jens J. Sloth, Per Møller, and Lone Gram. An electroplated coppersilver alloy as antibacterial coating on stainless steel. *Surface and Coatings Technology*, 345:96–104, jul 2018. ISSN 0257-8972. doi: 10.1016/J.SURFCOAT.2018.04.007.

[330] Ignasi Puigdomenech. Hydra/Medusa Chemical Equilibrium Database and Plotting Software, 2004. URL https://scholar.google.com/scholar?hl=en{\&}as{_}sdt=0{\%}2C5{\&}q=Puigdomenech{\%}2C+Ignasi.+{\%}22Hydra{\%}2FMedusa+chemical+equilibrium+database+and+plotting+software.{\%}22+KTH+Royal+Institute+of+Technology+{\%}282004{\%}29.{\&}btnG=http://www.kemi.kth.se/medusa/.

[331] Haibo Wang, Aixin Yan, Zhigang Liu, Xinming Yang, Zeling Xu, Yuchuan Wang, Runming Wang, Mohamad Koohi-Moghadam, Ligang Hu, Wei Xia, Huiru Tang, Yulan Wang, Hongyan Li, and Hongzhe Sun. Deciphering molecular mechanism of silver by integrated omic approaches enables enhancing its antimicrobial efficacy in E. Coli. *PLoS Biology*, 17(6):e3000292, jun 2019. ISSN 15457885. doi: 10.1371/journal.pbio.3000292. URL https://doi.org/10.1371/journal.pbio.3000292.

[332] T. S. Rao, Aruna Jyothi Kora, B. Anupkumar, S. V. Narasimhan, and R. Feser. Pitting corrosion of titanium by a freshwater strain of sulphate reducing bacteria (Desulfovibrio vulgaris). *Corrosion Science*, 47(5):1071–1084, may 2005. ISSN 0010-938X. doi: 10.1016/J.CORSCI.2004.07.025.

[333] Tingru Chang, R. Prasath Babu, Weijie Zhao, C. Magnus Johnson, Peter Hedström, Inger Odnevall, and Christofer Leygraf. High-Resolution Microscopical Studies of Contact Killing Mechanisms on Copper-Based Surfaces. *ACS Applied Materials & Interfaces*, 13(41):49402–49413, oct 2021. ISSN 1944-8244. doi: 10.1021/ACSAMI.1C11236/SUPPL_FILE/AM1C11236_SI_001.PDF. URL https://pubs.acs.org/doi/full/10.1021/acsami.1c11236.

[334] S. Amin Yavari, L. Loozen, F. L. Paganelli, S. Bakhshandeh, K. Lietaert, J. A. Groot, A. C. Fluit, C. H. E. Boel, J. Alblas, H. C. Vogely, H. Weinans, and A. A. Zadpoor. Antibacterial Behavior of Additively Manufactured Porous Titanium with Nanotubular Surfaces Releasing Silver Ions. *ACS Applied Materials & Interfaces*,

8(27):17080–17089, jul 2016. ISSN 1944-8244. doi: 10.1021/acsami.6b03152. URL http://pubs.acs.org/doi/abs/10.1021/acsami.6b03152.

[335] Matias D. Campos, Paola C. Zucchi, Ann Phung, Steven N. Leonard, and Elizabeth B. Hirsch. The activity of antimicrobial surfaces varies by testing protocol utilized. *PLoS ONE*, 11(8), aug 2016. ISSN 19326203. doi: 10.1371/journal.pone.0160728. URL /pmc/articles/PMC4975443/?report=abstracthttps://www.ncbi.nlm.nih.gov/pmc/articles/PMC4975443/.

[336] M. Ojeil, C. Jermann, J. Holah, S. P. Denyer, and J. Y. Maillard. Evaluation of new invitro efficacy test for antimicrobial surface activity reflecting UK hospital conditions. *Journal of Hospital Infection*, 85(4):274–281, dec 2013. ISSN 0195-6701. doi: 10.1016/J.JHIN.2013.08.007.

[337] Yuting Guo, Sabine Baumgart, Hans Joachim Stärk, Hauke Harms, and Susann Müller. Mass cytometry for detection of silver at the bacterial single cell level. *Frontiers in Microbiology*, 8(JUL):1326, jul 2017. ISSN 1664302X. doi: 10.3389/fmicb.2017.01326. URL www.frontiersin.org.

[338] Suraj Dinkar Jadhav, Pushkar Prakash Dhekne, Sasan Dadbakhsh, Jean Pierre Kruth, Jan Van Humbeeck, and Kim Vanmeensel. Surface Modified Copper Alloy Powder for Reliable Laser-based Additive Manufacturing. *Additive Manufacturing*, 35:101418, oct 2020. ISSN 22148604. doi: 10.1016/j.addma.2020.101418.

[339] Suraj Dinkar Jadhav, Dongmei Fu, Maxim Deprez, Kristof Ramharter, Denise Willems, Brecht Van Hooreweder, and Kim Vanmeensel. Highly conductive and strong CuSn0.3 alloy processed via laser powder bed fusion starting from a tin-coated copper powder. *Additive Manufacturing*, 36:101607, dec 2020. ISSN 22148604. doi: 10.1016/j.addma.2020.101607.

[340] S. F. Li, K. Geng, R. D.K. Misra, J. Y. Cui, D. Ye, Y. Liu, and Y. F. Yang. Commercial Scale Uniform Powder Coating for Metal Additive Manufacturing. *JOM*, 72 (12):4639–4647, dec 2020. ISSN 15431851. doi: 10.1007/s11837-020-04386-z. URL https://doi.org/10.1007/s11837-020-04386-z.

APPENDIX A

MATHEMATICAL DERIVATIONS

A.1 Solutions to Fick's Law

A.1.1 One dimensional case

For a one dimensional case, Fick's second law given by

$$\frac{\delta C}{\delta t} = D\left\{\frac{\delta^2 C}{\delta x^2}\right\} \tag{A.1}$$

where C is the concentration of solute, t is time, D the diffusion coefficient, and x distance.

For a fixed quantity of solute diffusing into a semi-infinite bar, boundary conditions are as follows:

- Inside the bar, initial solute concentration is zero; $C\{x, t = 0\} = C_0$
- The amount of solute within the system is constant, i.e. $\int_0^\infty C\{x, t\}\, dx = B$, where B is a constant.

Solution for the boundary conditions given by

$$C\{x, t\} = \frac{B}{\sqrt{\pi D t}} exp\left\{\frac{-x^2}{4Dt}\right\} \tag{A.2}$$

Considering an infinite source, i.e. that in the diffusion time assessed solute will not be depleted at the far end of the source, a sequence of the thin sources described above can be summated. Boundary conditions:

- Solute concentration within the bar is C_0 initially, i.e. $C\{x, t = 0\} = C_0$
- At the end of the bar, solute concentration remains constant, therefore $C\{x = 0, t\} = C_s$

Using the above boundary conditions, the solution given is

$$C\{x,t\} = C_s - (C_s - C_0)erf\left\{\frac{x}{2\sqrt{Dt}}\right\} \tag{A.3}$$

where $erf(x)$ is the error function. Analytical solutions to the $erf(x)$ are not possible, but accurate numerical solutions can be calculated.

A.1.2 Three dimensional case

$$Multiple\,dimensional\,case = \frac{\delta C}{\delta t} = D\left\{\nabla^2 C\right\} \tag{A.4}$$

where C is the concentration of solute, t is time, D the diffusion coefficient, and x distance.

A.2 Optical properties of materials

The key optical characteristics of a material can be represented by the complex refractive index, $\underline{n} = n + ik$ where n is the refractive index and k is the extinction coefficient.

Using a naive model of normally incident, unpolarised radiation travelling from one medium to another, the Fresnel equations provide a reflectance, R, given by:

$$R = \left[\frac{n_1 - n_2}{n_1 + n_2}\right]^2 \tag{A.5}$$

where n_1 and n_2 are the refractive indices of the materials.

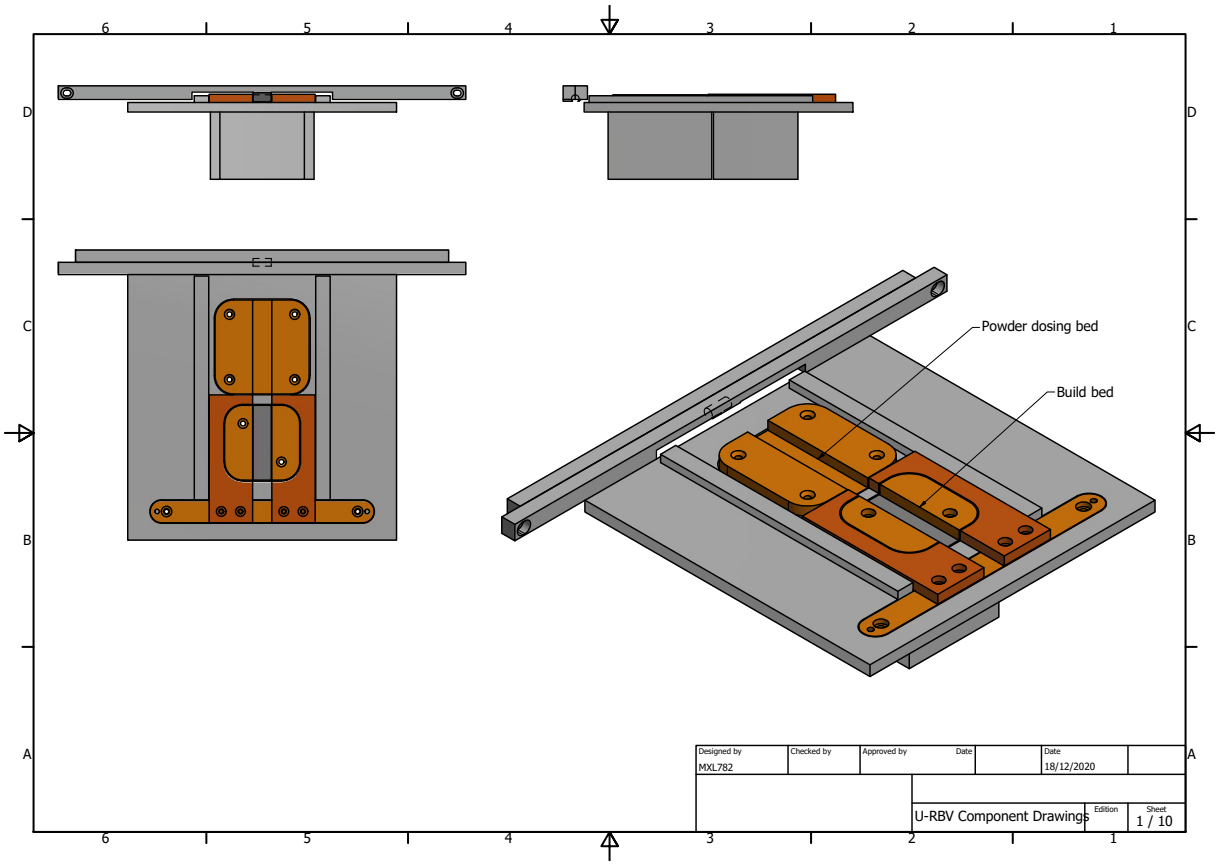
Where the Beer-Lambert law applies, the penetration depth δ_p at which intensity of penetrating electromagnetic radiation falls to $\frac{1}{e}$ of the incident intensity, is inversely related to the attenuation constant, α:

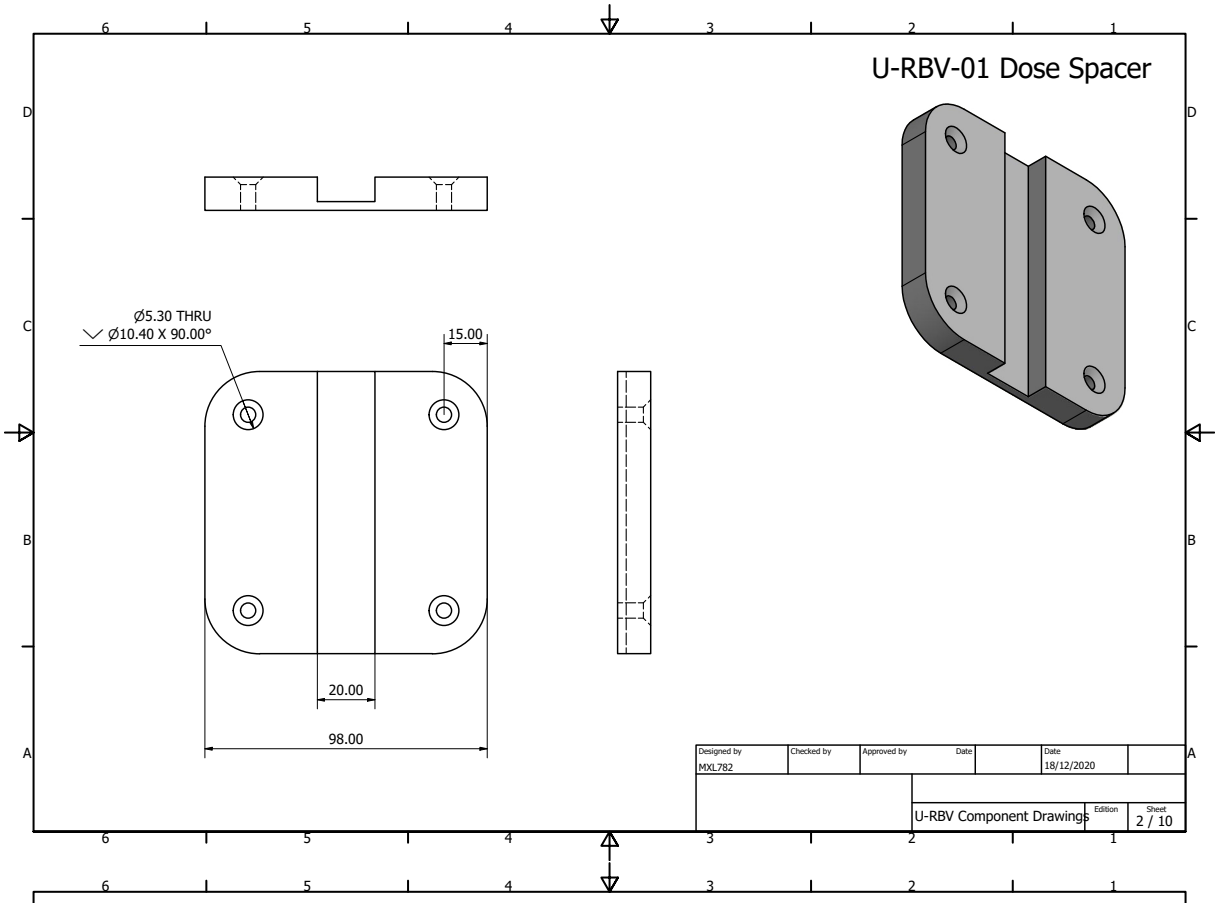
$$\delta_p = \frac{1}{\alpha} = \frac{\lambda}{4\pi k} \tag{A.6}$$

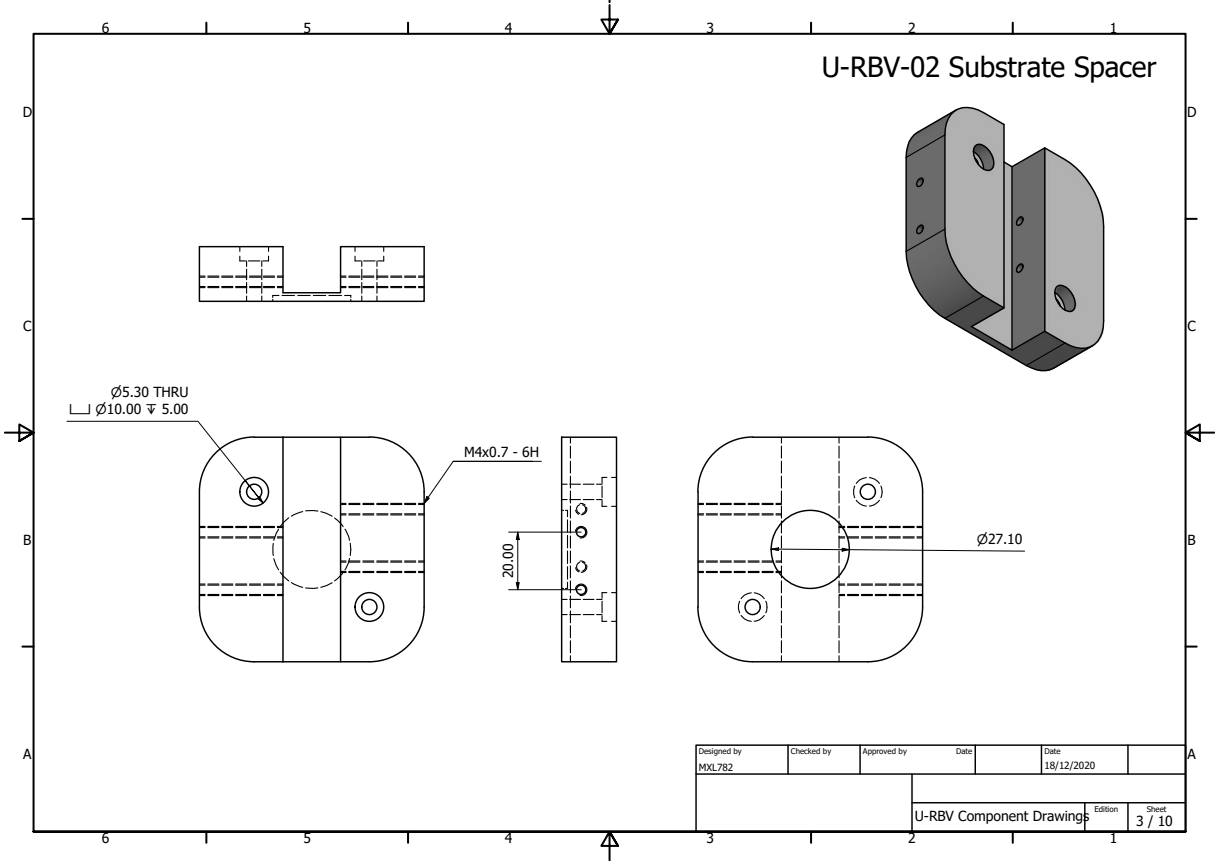
where λ is the wavelength of incident radiation and k is the extinction coefficient.

APPENDIX B

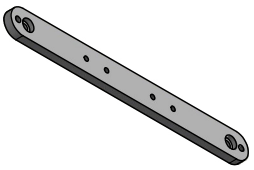
DESIGN AND SPECIFICATION OF U-RBV REDUCED BUILD ANCILLARY

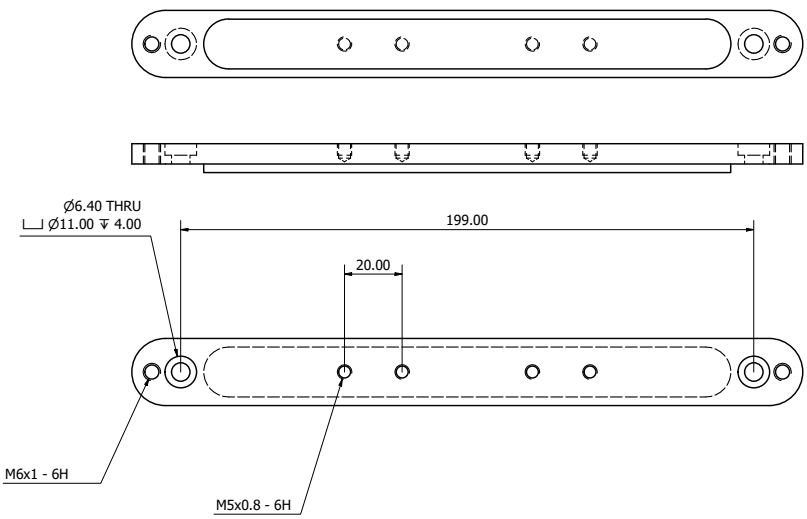



U-RBV-01 Dose Spacer
Ø5.30 THRU
Ø10.40 X 90.00°
15.00
20.00
98.00
Designed by
MXL782
Checked by
Approved by
Date
Date
18/12/2020
U-RBV Component Drawings
Edition
Sheet
2 / 10


U-RBV-02 Substrate Spacer
Ø5.30 THRU
Ø10.00 ↧ 5.00
M4x0.7 - 6H
20.00
Ø27.10
Designed by
MXL782
Checked by
Approved by
Date
Date
18/12/2020
U-RBV Component Drawings
Edition
Sheet
3 / 10

U-RBV-03A Blank

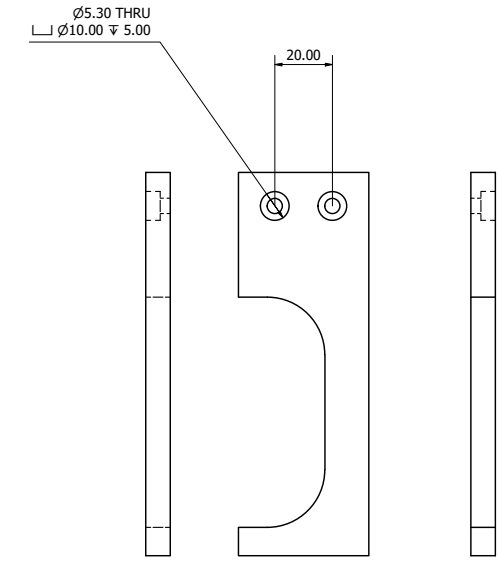


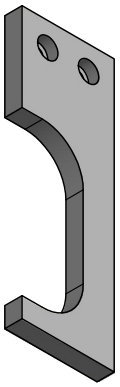


Designed by	Checked by	Approved by	Date		Date
MXL782					18/12/2020

U-RBV Component Drawings | Edition | Sheet 4 / 10

U-RBV-03B Track Left

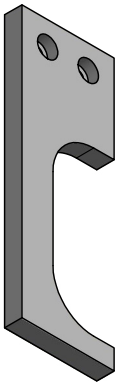


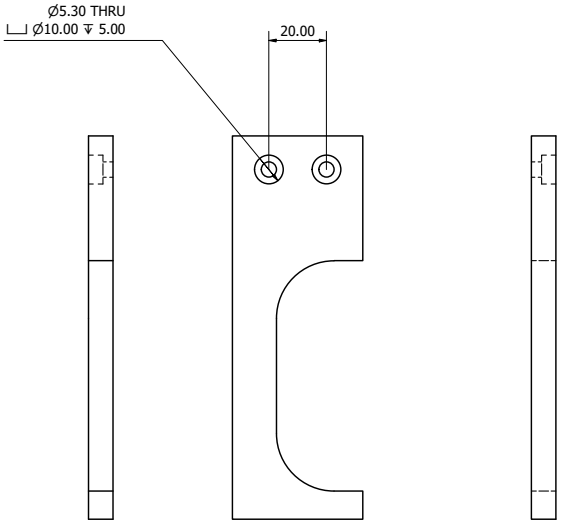


Designed by	Checked by	Approved by	Date		Date
MXL782					18/12/2020

U-RBV Component Drawings | Edition | Sheet 5 / 10

U-RBV-03C Track Right

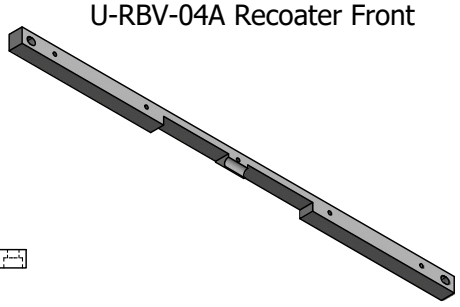


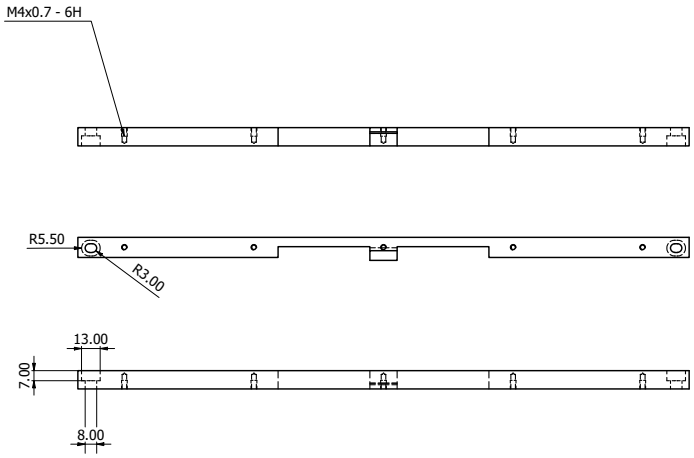


Designed by	Checked by	Approved by	Date		Date
MXL782					18/12/2020

U-RBV Component Drawings	Edition	Sheet
		6 / 10

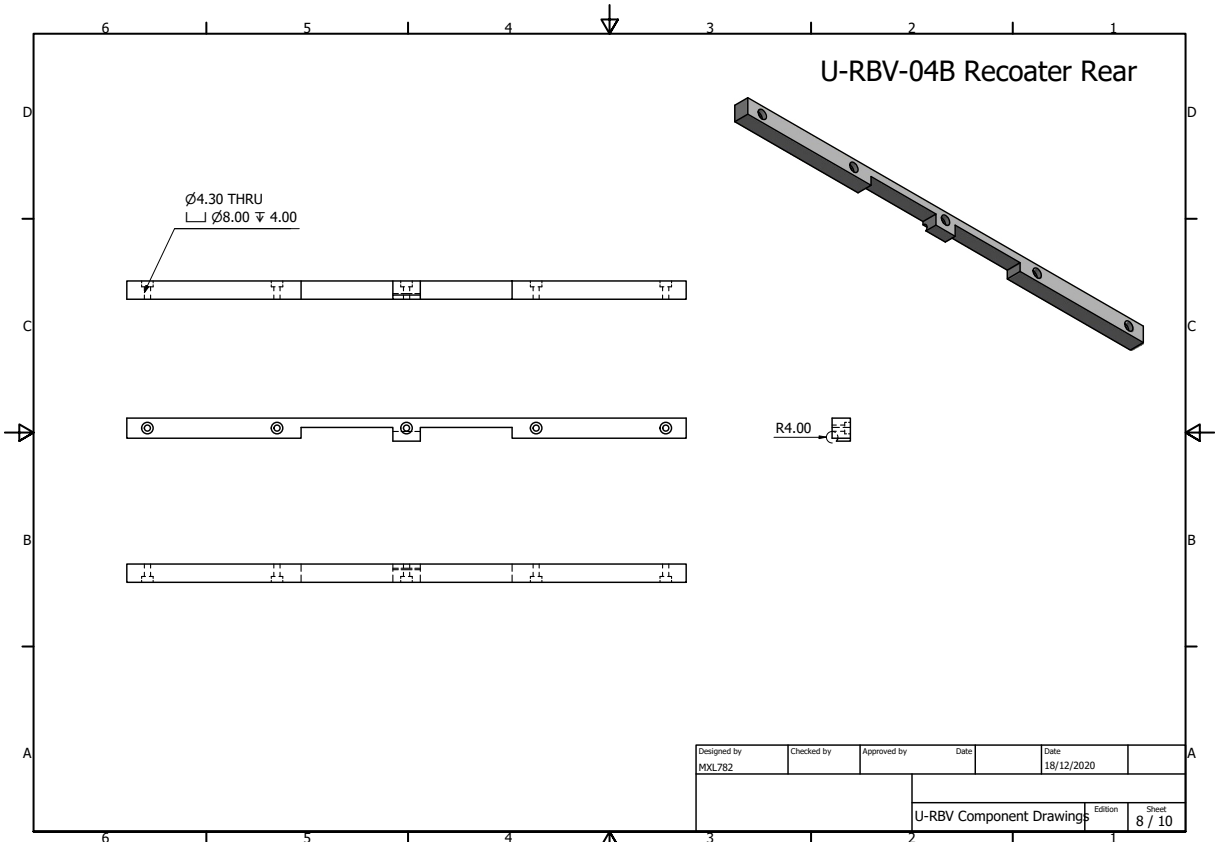
U-RBV-04A Recoater Front

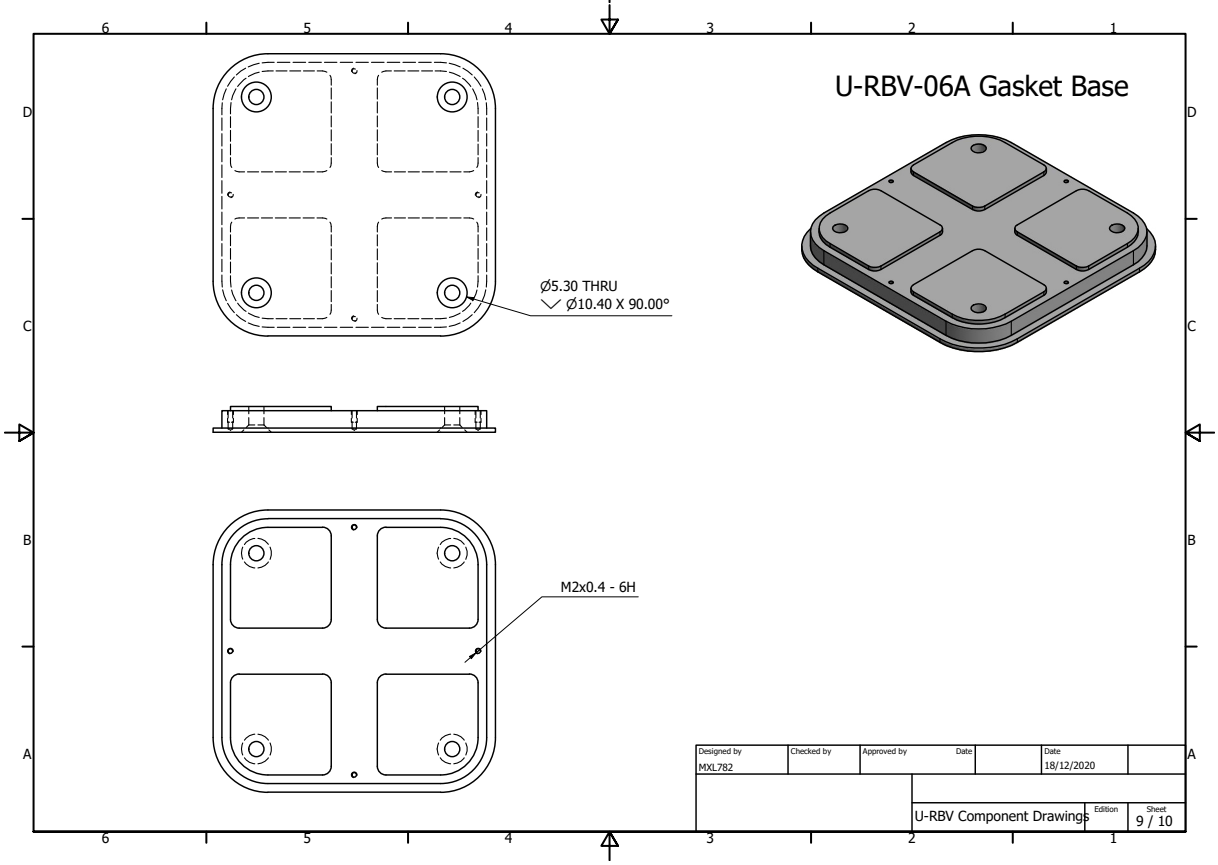


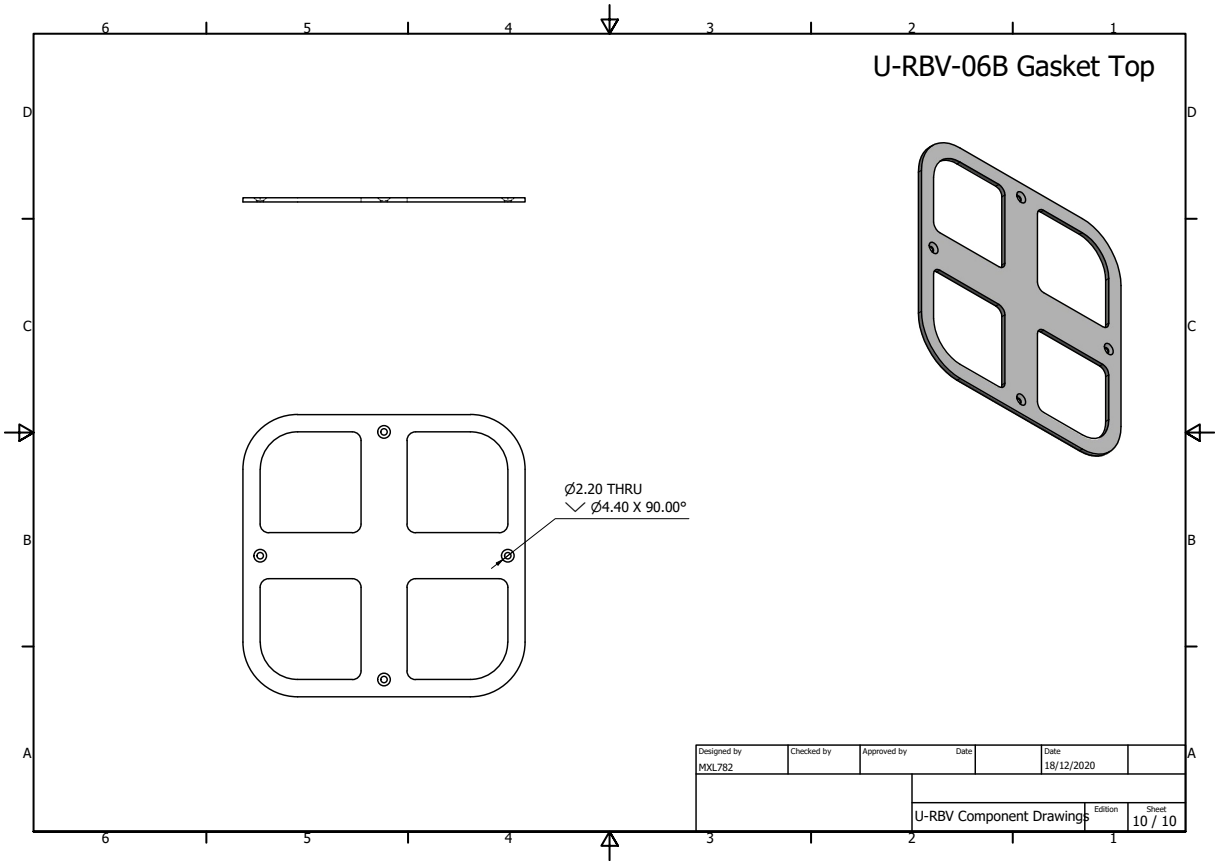


Designed by	Checked by	Approved by	Date		Date
MXL782					18/12/2020

U-RBV Component Drawings	Edition	Sheet
		7 / 10


U-RBV-04B Recoater Rear
Ø4.30 THRU
⌴ Ø8.00 ↧ 4.00
R4.00
Designed by
MXL782
Checked by
Approved by
Date
Date
18/12/2020
U-RBV Component Drawings
Edition
Sheet
8 / 10


U-RBV-06A Gasket Base
Ø5.30 THRU
⌵ Ø10.40 X 90.00°
M2x0.4 - 6H
Designed by
MXL782
Checked by
Approved by
Date
Date
18/12/2020
U-RBV Component Drawings
Edition
Sheet
9 / 10


U-RBV-06B Gasket Top
Ø2.20 THRU
Ø4.40 X 90.00°
Designed by
MXL782
Checked by
Approved by
Date
Date
18/12/2020
U-RBV Component Drawings
Edition
Sheet
10 / 10